

Spectroscopic analysis of the benchmark system α Aurigae

Daniel P. Sablowski



Univ.-Diss.

Kumulative Dissertation zur Erlangung des akademischen Grades
“doctor rerum naturalium” (Dr. rer. nat.) in der Wissenschaftsdisziplin
Astrophysik

eingereicht an der Mathematisch-Naturwissenschaftlichen Fakultät der
Universität Potsdam

und

Leibniz-Institut für Astrophysik Potsdam (AIP)



Disputation: Potsdam den 11.07.2019

Hauptbetreuer:

Prof. Dr. Klaus G. Strassmeier

Betreuer:

Priv. Doz. Axel Schwöpe

Dr. Michael Weber

Gutachter:

Prof. Dr. Klaus G. Strassmeier

Priv. Doz. Axel Schwöpe

Prof. Dr. Ulrich Heber

Published online at the

Institutional Repository of the University of Potsdam:

<https://doi.org/10.25932/publishup-43239>

<https://nbn-resolving.org/urn:nbn:de:kobv:517-opus4-432396>

Abstract (English/Deutsch) Binaries play an important role in observational and theoretical astrophysics. Since the mass and the chemical composition are key ingredients for stellar evolution, high-resolution spectroscopy is an important and necessary tool to derive those parameters to high confidence in binaries. This involves carefully measured orbital motion by the determination of radial velocity (RV) shifts and sophisticated techniques to derive the abundances of elements within the stellar atmosphere.

A technique superior to conventional cross-correlation methods to determine RV shifts is known as spectral disentangling. Hence, a major task of this thesis was the design of a sophisticated software package for this approach. In order to investigate secondary effects, such as flux and line-profile variations, imprinting changes on the spectrum the behavior of spectral disentangling on such variability is a key to understand the derived values, to improve them, and to get information about the variability itself. Therefore, the spectral disentangling code presented in this thesis and available to the community combines multiple advantages: separation of the spectra for detailed chemical analysis, derivation of orbital elements, derivation of individual RVs in order to investigate distorted systems (either by third body interaction or relativistic effects), the suppression of telluric contaminations, the derivation of variability, and the possibility to apply the technique to eclipsing binaries (important for orbital inclination) or in general to systems that undergo flux-variations.

This code in combination with the spectral synthesis codes MOOG and SME was used in order to derive the carbon $^{12}\text{C}/^{13}\text{C}$ isotope ratio (CIR) of the benchmark binary Capella. The observational result will be set into context with theoretical evolution by the use of MESA models and resolves the discrepancy of theory and observations existing since the first measurement of Capella's CIR in 1976.

The spectral disentangling code has been made available to the community and its applicability to completely different behaving systems, Wolf-Rayet stars, have also been investigated and resulted in a published article (see Appendix C).

Additionally, since this technique relies strongly on data quality, continues development of scientific instruments to achieve best observational data is of great importance in observational astrophysics. That is the reason why there has also been effort in astronomical instrumentation during the work on this thesis (see Appendix A).

Doppelsterne spielen eine wichtige Rolle in der beobachtenden und theoretischen Astrophysik. Die Massen und die chemische Zusammensetzung der Sterne sind dabei ausschlaggebende Parameter. Die wichtige und notwendige Methode um diese zu bestimmen ist hochaufgelöste Spektroskopie. Dies beinhaltet eine penible Bestimmung der orbitalen Bewegung durch die Vermessung von Radialgeschwindigkeitsverschiebungen (RV) und fortgeschrittene Techniken zur Bestimmung der Häufigkeiten der in der Sternatmosphäre vorhandenen Elemente.

Gegenüber der konventionellen Kreuzkorrelation zur Bestimmung der RV-Verschiebungen, gilt die Methode des sogenannten 'spectral disentangling' als überlegen. Daher bestand ein Großteil der vorliegenden Arbeit darin, eine solche Methode in einem weiterentwickelten Softwarepaket zu realisieren. Um sekundäre Effekte zu verstehen, welche zu weiteren Änderungen im Spektrum führen, also insbesondere solche wie Fluss- und Linienprofilvariationen, ist es von zentraler Bedeutung das Verhalten des spectral disentangling durch solche Variabilitäten zu verstehen, sodass die ermittelten Größen besser interpretiert und verbessert, sowie Informationen über die Variabilität selbst abgeleitet werden können. Daher vereint der in dieser Arbeit vorgestellte und der Allgemeinheit offen stehende Algorith-

mus für das spectral disentangling mehrere Vorteile: Separation der Spektren für detaillierte chemische Analysen, Ableitung der orbitalen Bahnelemente, Ableitung der einzelnen RV-Verschiebungen um auch gestörte Systeme (z.B. durch einen dritten Körper oder relativistische Effekte) analysieren zu können, die Reduktion des Einflusses tellurischer Kontamination, Ableitung der Variabilität und die Möglichkeit der Anwendung auf Bedeckungsveränderliche (wichtig zur Bestimmung der Inklination) bzw. allgemeiner auf Systeme mit Flussvariationen.

Der vorgestellte Algorithmus wurde zusammen mit MOOG und SME zur Erzeugung synthetischer Spektren verwendet um das Kohlenstoff- $^{12}\text{C}/^{13}\text{C}$ Isotopen-Verhältnis (KIV) des Referenzsystems Capella zu bestimmen. Dieses Ergebnis aus Beobachtungen wird in Kontext zur theoretischen Entwicklung durch Verwendung von MESA Modellen gesetzt und löst die Unstimmigkeit zwischen Beobachtung und Theorie die bereits seit der ersten Messung des KIV von Kapella von 1976 existiert.

Der Algorithmus für das spectral disentangling ist der Allgemeinheit zugänglich gemacht und wurde auf vollkommen anders verhaltende Objekte, den Wolf-Rayet-Sternen, angewendet, was in einer publizierten Arbeit resultierte (siehe Anhang C).

Da die Methode stark von der Qualität der Beobachtungsdaten abhängt, ist eine kontinuierliche Weiterentwicklung der wissenschaftlichen Messtechnik der beobachtenden Astrophysik sehr wichtig um die bestmöglichen Beobachtungsdaten gewinnen zu können. Daher wurden auch große Anstrengungen in der astronomischen Instrumentierung während dieser Arbeit unternommen (siehe Anhang A).

This page has been intentionally left blank.

Contents

1. Introduction	9
1.1. Stellar evolution with focus on Capella	10
1.2. Overview of the Manuscripts	16
1.2.1. Manuscript I	16
1.2.2. Manuscript II	16
1.2.3. Manuscript III	16
1.2.4. Manuscript AI	16
1.2.5. Manuscript AII	17
1.2.6. Manuscript AIII	17
2. Spectral Disentangling with Spectangular (Manuscript I)	18
2.1. Introduction	18
2.2. Method of disentangling in λ -space	19
2.2.1. Formulation of the problem	19
2.2.2. The procedure	20
2.2.3. Details on Downhill Simplex Implementation	23
2.2.4. Error Estimation	24
2.3. Test with artificial data	25
2.3.1. Performance	25
2.3.2. SB1 and static lines	25
2.3.3. Artificial SB2 system	28
2.4. Application to Capella	32
2.4.1. The ideal minimum case	34
2.4.2. Data at quadrature - a non-ideal case	35
2.4.3. The realistic ideal case	41
2.5. Conclusion	41
3. Spectangular: Disentangling variable Spectra (Manuscript II)	44
3.1. Introduction	44
3.2. Code modifications and procedures	45
3.2.1. Handling broad wavelength ranges	46
3.2.2. Influence and correction of telluric lines	47
3.2.3. Signal-to-noise ratio and flux ratio	47
3.3. Disentangling variable spectra	49
3.3.1. General remarks	49
3.3.2. Radial pulsations	50
3.3.3. Flares	51
3.3.4. Eclipsing binaries	52
3.3.4.1. Light curve model	52
3.3.4.2. Artificial eclipsing binary	55
3.3.4.3. Extracting the flux ratios	56
3.3.5. Surface spots	57
3.3.6. Impact of variability on disentangling results	60

3.4. Summary	62
4. Carbon $^{12}\text{C}/^{13}\text{C}$ isotope ratio of α Aurigae revised (Manuscript III)	65
4.1. Introduction	65
4.2. Observations	66
4.3. Data reduction and spectral disentangling	67
4.4. Analysis	69
4.5. Summary and conclusion	73
5. Discussion	76
5.1. Evolution	76
5.1.1. Overshooting	76
5.1.2. Model grid	77
5.1.3. Optimised model	78
5.2. Rotation	82
5.2.1. Observations, Data Reduction, and Disentanglement	82
5.2.2. Frequency Analysis	84
6. Summary and Outlook	88
A. Contributions to Instrument Developments	92
A.1. SILENT: Spectrograph sImuLation and EmulatioN Tool (Manuscript AI)	92
A.1.1. Introduction	92
A.1.2. Basic equations	93
A.1.2.1. Basic design considerations	94
A.1.2.2. Aperture sizes	95
A.1.2.3. Target and telescope specification	99
A.1.2.4. Efficiency calculation	99
A.1.2.5. Detector	100
A.1.3. Main systems	100
A.1.4. The classical spectrograph	100
A.1.5. The echelle spectrograph	103
A.1.6. The 3D spectrograph	105
A.1.7. Additional tools	106
A.1.7.1. Volume phase holographic grating	106
A.1.7.2. Optical fibres	109
A.1.7.3. Telescope spectrograph interface	109
A.1.7.4. Fabry perot etalon	109
A.1.7.5. Czerny Turner	110
A.1.7.6. Petzval lens	111
A.1.7.7. Glass tool	112
A.1.7.8. Peltier tool	115
A.1.8. A Design Example	115
A.1.9. Conclusion and Outlook	117
A.2. A study of white-pupil configurations for high-resolution échelle spectrographs (Manuscript AII)	120
A.2.1. Introduction	120
A.2.1.1. Main parameters	121
A.2.1.2. Design constraints	122
A.2.2. White pupil arrangements	123

A.2.3. Design example	130
A.2.4. Conclusion	136
A.3. PEPSI-feed: linking PEPSI to the Vatican Advanced Technology Telescope using a 450m long fibre (Manuscript AIII)	138
A.3.1. Introduction	138
A.3.2. The measurement chain	139
A.3.2.1. Fibre link	139
A.3.2.2. Guding and PEPSI interface	144
A.3.3. Observations	149
A.3.4. Future work and conclusion	150
B. Appendix of Manuscript III	152
B.1. Correction of tellurics and flux ratio	152
B.2. Spectrum of the secondary	152
C. Contributions to the high-mass regime	157
C.1. The Tarantula Massive Binary Monitoring project: II. A first SB2 orbital and spectroscopic analysis for the Wolf-Rayet binary R145	157
C.2. The Wolf-Rayet binaries of the nitrogen sequence in the Large Magellanic Cloud - Spectroscopy, orbital analysis, formation, and evolution	157
D. Individual lines and periods	160
D.1. Individual lines	160
D.1.1. Ca II IRT	160
D.1.2. H α and H β	160
D.1.3. Mg I b triplet and 4571 Å line	160
D.1.4. Na I D resonance doublet	162
D.1.5. Li I λ 6708 Å and photospheric lines	162
D.2. Periods	163
E. MESA Inlist-file for Capella	167

1. Introduction

According to the Vogt-Russell theorem, stellar structure and evolution are described by the mass and chemical composition of the star if rotation and magnetic fields can be neglected. It is therefore of primary interest to determine the mass of stars, which can be done most precisely within binary systems¹. In addition, one can assume that the components of a binary were formed at the same time and from the same cloud-collapse. Therefore, it can be assumed that they had identical initial chemical composition. Hence, the study of binaries is of major importance for stellar physics. An ideal case to study modern evolution models is a binary consisting of a non-evolved object showing still the initial chemical composition and an evolved component. In addition, to circumvent complications due to binary interaction, the orbital period should be sufficiently large so that the components are not affected by their winds, tidal forces, and mass transfer. Observations of such a system would reveal the difference in chemical composition which can be attributed to stellar evolution. Hence, having two components that fulfil these criteria, the difference in evolution is due to their difference in mass. Capella in itself is very close to such an ideal study case. The more massive primary is an evolved clump giant while the secondary is on its short way through the Hertzsprung gap, meaning that it just left the main sequence (Fig. 1.1).

From an observational point of view, one needs to analyse the spectra of the components to obtain the chemical composition. Usually, and also in the case of Capella, we can not separate the components in the focal plane of the telescope. Such stars, showing the lines of both components in the spectra, are referred to as spectroscopic binaries (SB2). It is immediately clear that analysis of chemical composition and stellar parameters would benefit strongly from a technique to separate the spectra, to carry out template-independent analysis. This technique is known as spectral separation. Despite confusion in literature, there is a clear distinction between two approaches:

1. simple separation and
2. spectral disentangling

While the former often depends on template and always on prior knowledge of the orbital elements of the SB2 system, the latter is independent from templates and connected to an optimization algorithm which acts on the orbital parameters. Hence, it outputs both, the separated spectra and the orbital elements best fitting the data. Therefore, a major task of the thesis was the development of a scientific software package for spectral disentangling (Manuscript I). However, since some codes on that topic exists², they are often difficult to run, accessible, and limited to the needs of the developer.

¹Another method is asteroseismology. However, in that approach the results strongly depend on the stellar model used. Despite its great success, the Keplerian orbit (or even relativistic orbits) is considered here as a safer source to derive absolute masses (see Brogaard et al., 2018).

²See Manuscript I;

KOREL: <http://www.asu.cas.cz/~had/korel.html>

FDBinary: <http://sail.zpf.fer.hr/fdbinary/>

CRES: <http://sail.zpf.fer.hr/cres/>

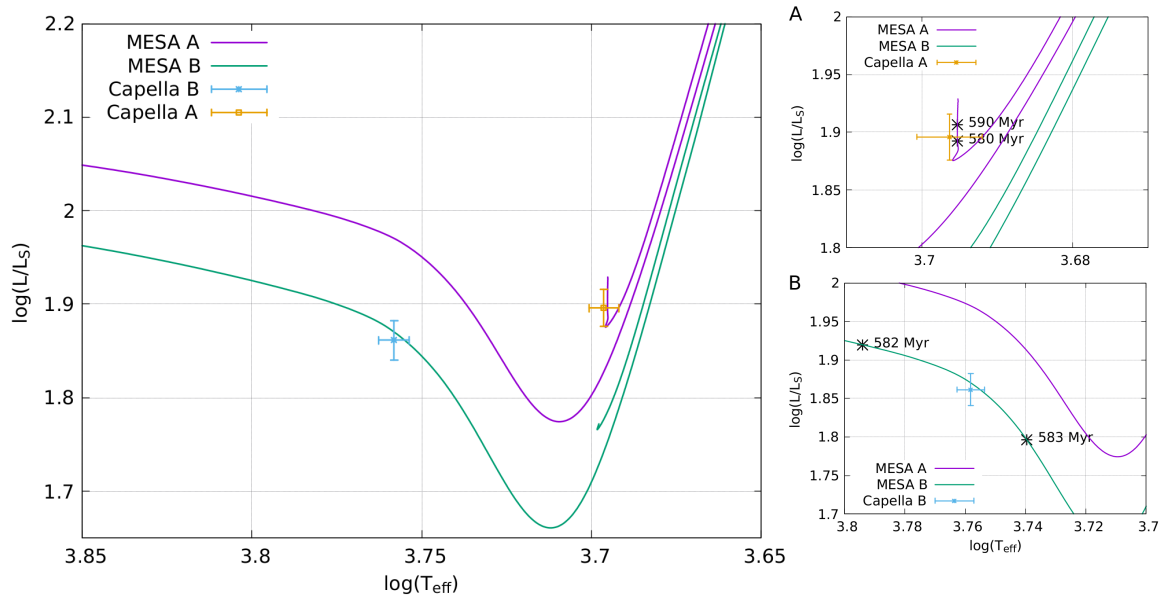


Figure 1.1.: Evolutionary tracks from MESA for both components of Capella and their positions in the HRD. Component A (orange and purple) is at the clump and B (blue and green) is moving into the gap. More details follow in Sect. 5.1.

One important addition to the spectral disentangling code is the possibility to derive the relative component strengths of the two companions. This becomes important for close eclipsing or even interacting binaries. These aspects and the influence of spectral variability to the disentanglement is discussed in Manuscript II. Another advantage which distinguishes the presented code from the others is the possibility to optimize on the individual radial velocities (RVs) rather than orbital parameters. This can be of advantage in several cases:

1. unknown third body object
2. relativistic effects
3. data calibration errors.

Outside the work on Capella, the code was used on WR stars (see Chap. C).

1.1. Stellar evolution with focus on Capella

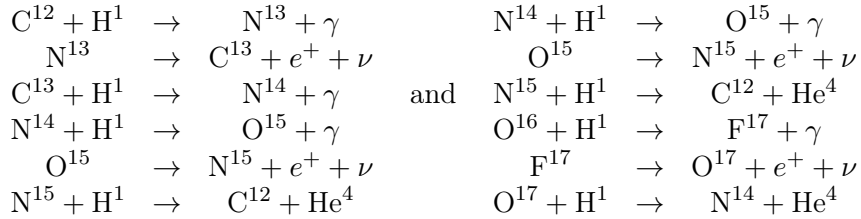
The overall parameters of Capella are summarized in Tables 1.1 and 1.2. The mass M of the two components differ only by $\approx 4\%$ but places them at two distinct positions on the Hertzsprung-Russell diagram (HRD). The tracks within the HRD for both components which will be discussed in more detail in Sect. 5.1 are shown in Fig. 1.1. They were computed with the stellar evolution code Modules for Experiments in Stellar Astrophysics (Paxton et al., 2010, 2018, MESA).

Stars more massive than the Sun (solar mass, M_{\odot}) have convective cores and radiative

Quantity	Torres et al. (2009)	Weber & Strassmeier (2011a)	Torres et al. (2015)
Spectrum	G8III + G0III	-	G8III + G0III
P [days]	104.02173±0.00022		104.02128±0.00016
T_0 [HJD 24+]	47,528.514±0,016	54,389±2.8	48,147,6±2.6
γ [kms ⁻¹]	29,653±0.035	29.9378±0.0026	29.9387±0.0032
K_A [km/s]	26.005±0.036	25.960±0,0065	25.9611±0.0044
K_B [km/s]	26.260±0.087	26.840±0.024	26.860±0.017
e	0.0	0.00087±0.00013	0.00089±0.00011
ω [deg]	-	345±9.7	342.6±9.0
$a \sin(i)$ [10^6 km/s]		37.134±0.0093	
$a \sin(i)$ [10^6 km/s]		38.392±0.034	
$M_A \sin^3(i)$ [M_\odot]		0.8064±0.0014	
$M_B \sin^3(i)$ [M_\odot]		0.7800±0.0008	
M_B/M_A	0.9903±0.0036	0.9673±0.0020	0.96653±0.00062
i [deg]	137.21±0.05	137.21±0.05	137.156±0.046
M_A [M_\odot]	2.466±0.018	2.573±0.009	2.5687±0.0074
M_B [M_\odot]	2.442±0.013	2.488±0.008	2.4828±0.0067
R_A [R_\odot]	11.87		
R_B [R_\odot]	8.75		

Table 1.1.: Summary of main parameters of the Capella binary from Torres et al. (2009); Weber & Strassmeier (2011a); Torres et al. (2015). Continued in Table 1.2.

envelopes. They gain their energy primarily from the catalytic CNO cycle:



This cycle is very sensitive to the temperature ($\propto T^{16}$) and the energy production rate is determined by the slowest reaction (Prialnik, 2010, p. 59-61). Since the beta-decay is independent from environmental conditions, the rate is determined by the proton capture reactions. However, for very high temperatures this inverts and the beta-decay determines the burning rate (explosive burning). In late state of the main sequence phase (H burning in the core), the H depleted core grows while the burning happens in a shell. The mass-limit of the core capable to balance gravity is the Schönberg-Chandrasekhar limit (or instability, Schönberg & Chandrasekhar, 1942). This limit is exceeded by stars more massive than $2 M_\odot$. Hence, the core starts to contract and will cool while collapsing (on a thermal time scale), see Fig. 1.2. At this stage, the luminosity of the star decreases and it starts its way through the Hertzsprung gap. However, a layer around the core is heated in which H-shell burning will ignite. That leads to a new increase of the luminosity. Since this period of the evolution happens rather fast, the probability to find a star in that gap is very small – the HRD is poorly populated in that region \rightarrow gap. Hence, these objects are worth to be observed. The secondary of Capella is in such a stage. Another known case is the single star 31 Com.

The core will reach again a stable configuration and H-shell burning will further increase.

	(Fuhrmann, 2011)		Torres et al. (2015)		(Takeda et al., 2018)	
	Primary	Secondary	Primary	Secondary	Primary	Secondary
a'' [mas]			56.442±0.023			
Ω_{J2000} [deg]			40.522±0.039			
a''_{phot} [mas]			2.14±0.70			
$\Delta\alpha^*$ [mas]			-0.53±0.81			
$\Delta\delta$ [mas]			-0.37±0.57			
$\Delta\mu_\alpha \cos(\delta)$ [mas/yr]			0.33±1.00			
$\Delta\mu_\delta$ [mas/yr]			-0.04±0.60			
f_p^b			1.0400±0.0032			
a [10^6 km/s]			111.11±0.10			
a [R_\odot]			159.72±0.15			
a [A.E.]			0.74272±0.00069			
π_{orb}			75.994±0.089			
Distance [pc]			13.159±0.015			
$\log(g)_A$ dex[cgs]			2.691±0.041	2.941±0.032	2.52±0.08	2.88±0.17
T_{eff}			4970±50	5730±60	4943±23	5694±73
L_\odot			78.7±4.2	72.7±3.6		
M_V			0.296±0.016	0.167±0.015		
$\mu_\alpha \cos \delta$			75.85±1.00			
μ_δ			-427.17±0.60			
$(l_B/l_A)H_p^d$			1.204±0.060			
$v \sin(i)$ [km/s]			4.1±0.4	35.0±0.5		
P_{rot} [d]			104±3	8.5±0.2		
A(Li)			1.08±0.11	3.28±0.13		
[Fe/H]	+0.07		-0.04±0.06		+0.10±0.05	-0.08±0.08
Age [Myr]			590 - 650			
$^{12}\text{C}/^{13}\text{C}$			27±4			
C/N			0.57±0.06	3.30±0.16		
ζ_{RT} [km s^{-1}]	5.0	7.0	6.6±0.13			
ξ_t [km s^{-1}]	1.40	1.80	1.48±0.08	1.55±0.11	1.47±0.13	2.29±0.38

Table 1.2.: Continued summary of Capella parameters.

The increase of energy production leads to a convective instability of the envelope and causes it to expand. Since convection will trigger magnetic activity and the expansion of the star was moderate during the gap phase, its rotational velocity is still high. This is why the star will undergo a sudden ignition of strong activity. The star moves up the red giant branch in the HRD. Convection will finally occur in the whole envelope, bringing processed material to the observable surface of the star (first dredge-up). As can be seen by the first reaction chain of the CNO cycle, one product is ^{13}C . It is created from a beta-decay after the first fusion process. We can therefore expect an increase of that isotope at the surface (Manuscript III). This scenario assumes no mixing during the main sequence. Nevertheless, stars (e.g. 37 Com, α Ori, α Sco, ξ Pup, and ϵ Gem) which show a very low carbon isotope ratio ($^{12}\text{C}/^{13}\text{C}$, CIR) cannot be explained by that picture. Further mixing processes such as diffusion and meridional induced mixing are needed. Meridional mixing is induced by rotation of the star. In addition, strong wind during the main sequence phase reduces the mass of the envelope and can result in a higher relative abundance of ^{13}C . In that context, mass transfer in close binaries can also lead to a lower CIR. Also a second

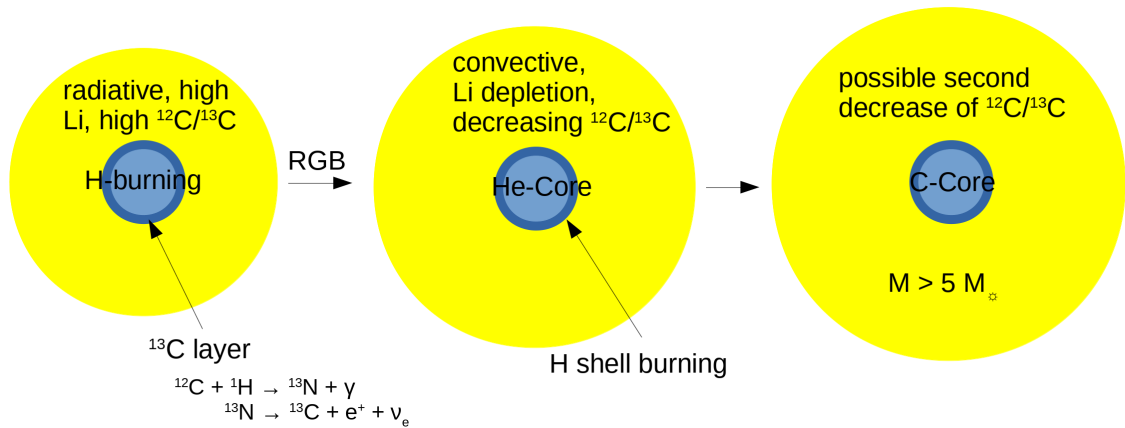


Figure 1.2.: Not to scale sketch of the evolutionary track for a star more massive than $2M_{\odot}$. A ^{13}C layer is produced around the core by the CNO-cycle. This is brought to the surface when the star expands and develops a convective envelope after it has left the main sequence.

dredge-up after the He- core burning phase is possible (e.g., Boothroyd & Sackmann, 1999; Karakas et al., 2002).

As the sixth brightest star in the night sky, the literature about Capella (primary G8III at end of core helium-burning clump star + secondary G0III in the Hertzsprung gap), HD34029 is very numerous. Although the studies date back almost a century, Alpha Aurigae remains an interesting target for stellar physicists due to the state of evolution of the components. Since the orbital parameters, and with that, the masses of both components are very precisely measured, Torres et al. (2015) were able to determine the evolutionary state of both main components to high confidence. However, this was only possible using the revisited orbit determined by Weber & Strassmeier (2011a) with the use of long-term spectroscopic observations and demonstrates the potential and benefit of observations on bright targets.

The pin-down of the orbital parameters of Capella has a long history as well, starting with interferometric observations (Anderson, 1920; Hummel et al., 1994), continuing over proper motions and parallaxes, (e.g. Heintz, 1975), to radial velocities (e.g. Batten & Erceg, 1975; Weber & Strassmeier, 2011a), and several combined and revisited determinations (e.g. McAlister, 1981; Shen et al., 1985; Branham, 2008). Capella may be associated to a wide multiple system of up to eight components including of a M star binary GJ 195 A & B, 51 Per and HD25893, the latter two being binaries themselves (see Fuhrmann, 2011, and references therein).

The activity of Capella has been extensively studied within the X-ray, EUV, UV, and NUV by many authors (e.g. Haisch & Linsky, 1976; Ayres & Linsky, 1980; Ayres et al., 1993; Dupree et al., 1993; Wood & Ayres, 1995; Linsky et al., 1995; Brickhouse et al., 2000; Phillips et al., 2001; Audard et al., 2001; Johnson et al., 2002; Gu et al., 2006; Raassen & Kaastra, 2007). Johnson et al. (2002) suggest that the bulk coronal variability originates from the cooler clump giant. They connect their observations with post main-sequence evolution, when convection enhances magnetic activity which also brakes the rotation steeply at the red end of the Hertzsprung gap. Furthermore, it is believed that the contraction and spin-up of the core increases differential rotation of the convective envelope and further supports a dynamo effect. On the contrary, the spin-down of the gap giant by enhanced activity and evolutionary caused expansion causes the magnetic activity

to decline again. An excellent review of the topic of chromospheric activity can be found in Linsky (2017, 1980) and Hall (2008).

There has also been strong effort in determining the rotational period of the Capella components. Especially the period of the gap star challenged several authors (e.g. Katsova & Scherbakov, 1998; Strassmeier et al., 2001; Fuhrmann, 2011). To summarise, all period estimates are in agreement according to the assigned errors. Additionally, Shcherbakov et al. (1990) and Katsova & Shcherbakov (1998) analysed the chromospheric He I λ 10830 line. They found a periodicity of that line connected to the orbital period and, due to the RV, which follow the photospheric radial velocities (RV) of the primary, they contribute the variability to a small and hot spot on the gap giant. Furthermore, the latter authors found a six year cycle of the He I λ 10830 line.

Capella was also used for tests of tidal theory. The expansion of the primary has led to the circularization of the orbit and to its synchronisation of the rotation (Torres et al., 2009; Torres et al., 2015). However, the time of circularisation determined by Torres et al. (2009) of 563.6 Myr is larger than the age of the system from their model predictions. Torres et al. (2015) pointed out that a mass-transfer scenario is not in agreement with their calculated Roche lobe filling factor of 0.63. However, that idea would explain the nearly equal masses of the components as pointed out by Fuhrmann (2011).

Chapter 2 describes the mathematical background of the developed disentangling code as well as its implementation. Furthermore, its application to artificial SB1 and SB2 systems is demonstrated. It also includes the treatment of an additional static component (telluric or emission, e.g., from emission nebulae). The applicability of the code on variable spectra is presented in Chap. 3. It involves telluric lines, flares, pulsation, surface spots and flux-variations. In Chap. 4, this code is used to disentangle high-resolution spectra of Capella to determine the carbon isotope ratio of Capella A. The results will be set into context with stellar evolution in Chap. 5. The summary and an outlook is given in Chap. 4.5.

References

- Anderson, J. A. 1920, Contributions from the Mount Wilson Observatory / Carnegie Institution of Washington, 185, 1
- Audard, M., Behar, E., Güdel, M., et al. 2001, A&A, 365, L329
- Ayres, T. R., Brown, A., Gayley, K. G., & Linsky, J. L. 1993, ApJ, 402, 710
- Ayres, T. R. & Linsky, J. L. 1980, ApJ, 241, 279
- Batten, A. H. & Erceg, V. 1975, MNRAS, 171, 47P
- Boothroyd, A. I. & Sackmann, I.-J. 1999, ApJ, 510, 232
- Branham, R. L. 2008, AJ, 136, 963
- Brickhouse, N. S., Dupree, A. K., Edgar, R. J., et al. 2000, ApJ, 530, 387
- Brogaard, K., Hansen, C. J., Miglio, A., et al. 2018, MNRAS, 476, 3729
- Dupree, A. K., Brickhouse, N. S., Doschek, G. A., Green, J. C., & Raymond, J. C. 1993, ApJL, 418, L41
- Fuhrmann, K. 2011, ApJ, 742, 42
- Gu, M. F., Gupta, R., Peterson, J. R., Sako, M., & Kahn, S. M. 2006, ApJ, 649, 979

- Haisch, B. M. & Linsky, J. L. 1976, *ApJL*, 205, L39
- Hall, J. C. 2008, *Living Reviews in Solar Physics*, 5, 2
- Heintz, W. D. 1975, *ApJ*, 195, 411
- Hummel, C. A., Armstrong, J. T., Quirrenbach, A., et al. 1994, *AJ*, 107, 1859
- Johnson, O., Drake, J. J., Kashyap, V., et al. 2002, *ApJL*, 565, L97
- Karakas, A. I., Lattanzio, J. C., & Pols, O. R. 2002, *Pub. Astro Soc. Australia*, 19, 515
- Katsova, M. M. & Scherbakov, A. G. 1998, *Astronomy Reports*, 42, 485
- Katsova, M. M. & Shcherbakov, A. G. 1998, *A&A*, 329, 1080
- Linsky, J. L. 1980, *ARAA*, 18, 439
- Linsky, J. L. 2017, *ARAA*, 55, null
- Linsky, J. L., Wood, B. E., Judge, P., et al. 1995, *ApJ*, 442, 381
- McAlister, H. A. 1981, *AJ*, 86, 795
- Paxton, B., Bildsten, L., Dotter, A., et al. 2010, *ApJS*, 192, 3
- Paxton, B., Schwab, J., Bauer, E. B., et al. 2018, *ApJS*, 234, 34
- Phillips, K., Mathioudakis, M., Huenemoerder, D., et al. 2001, *MNRAS*, 325, 1500
- Prialnik, D. 2010, *An Introduction to the Theory of Stellar Structure and Evolution*, 2nd edn. (Cambridge University Press)
- Raassen, A. J. J. & Kaastra, J. S. 2007, *A&A*, 461, 679
- Schönberg, M. & Chandrasekhar, S. 1942, *ApJ*, 96, 161
- Shcherbakov, A. G., Tuominen, I., Jetsu, L., Katsova, M. M., & Poutanen, M. 1990, *A&A*, 235, 205
- Shen, L.-Z., Beavers, W. I., Eitter, J. J., & Salzer, J. J. 1985, *AJ*, 90, 1503
- Strassmeier, K., Reegen, P., & Granzer, T. 2001, *AN*, 322, 115
- Takeda, Y., Hashimoto, O., & Honda, S. 2018, *ApJ*, 862, 57
- Torres, G., Claret, A., Pavlovski, K., & Dotter, A. 2015, *ApJ*, 807, 26
- Torres, G., Claret, A., & Young, P. A. 2009, *ApJ*, 700, 1349
- Weber, M. & Strassmeier, K. G. 2011a, *A&A*, 531, A89
- Wood, B. E. & Ayres, T. R. 1995, *ApJ*, 443, 329

1.2. Overview of the Manuscripts

The published or accepted manuscripts are as after language editing. The layout, figure size, and citation style was adapted for the overall appearance of the document. The appendix of manuscript III was moved to Appendix B.

1.2.1. Manuscript I

Status: published 2017 in *Astronomy & Astrophysics*, Vol. 597, A125

Title: Spectral disentangling with Spectangular

Authors: D. P. Sablowski and M. Weber

Aims: The developed code for spectral disentangling has been presented in that article.

Own contributions: Full coding of the software, generating artificial data for code testing, and code testing. I wrote the complete publication text.

1.2.2. Manuscript II

Status: accepted 2019 for publication in *Astronomy & Astrophysics*

Title: Spectangular: Disentangling variable spectra

Authors: D. P. Sablowski, S. Järvinen, M. Weber

Aims: Quantitative analysis of the behavior of spectral disentangling with spectra from variable objects.

Own contributions: I did the modifications/additions of the code, created the artificial test data, did the code testing. The analysis apart from the calculation of the Doppler maps and the writing was also my part.

1.2.3. Manuscript III

Status: published 2019 in *Astronomy & Astrophysics Letter to the Editor*, 622, L11

Title: Carbon $^{12}\text{C}/^{13}\text{C}$ isotope ratio of α Aurigae revised

Authors: D. P. Sablowski, S. Järvinen, I. Ilyin, K. G. Strassmeier

Aims: Determination of the carbon isotope ratio of Capella from disentangled spectrum.

Own contributions: I performed the data preparation, disentangling, spectral synthesis analysis, and wrote much of the text.

1.2.4. Manuscript AI

Status: submitted 2019 to *New Astronomy*.

Title: SILENT: Spectrograph sImuLation and EmulatioN Tool

Authors: D. P. Sablowski and Klaus Vollmann

Aims: Software for pre-design of spectroscopic systems like classical, 3D (multi-object) and echelle. Also additional design tools for the design and peripheral sub-systems. First open-source software for such tasks.

Own contributions: Full coding of the software, with exception of subsection 2.2 the text was written entirely by myself.

1.2.5. Manuscript All

Status: published 2018 in Conference Proceedings of SPIE, Vol. 10706
Non-refereed conference proceeding

Title: A study of white pupil configurations for high-resolution échelle spectrographs

Authors: D. P. Sablowski, M. Woche, M. Weber, A. Järvinen, K. G. Strassmeier

Aims: The optical performance of the collimating and transfer-collimating optics were studied and compared for different well-known optical set-ups. A new configuration resulted from these investigations which is superior to all others in terms of homogeneity of the spots in the image plane.

Own contributions: I carried out the whole optical design and analysis. The text of the article was entirely written by myself.

1.2.6. Manuscript AllI

Status: published 2016 in Conference Proceedings of SPIE, Vol. 9912
Non-refereed conference proceeding

Title: PEPSI-feed: Linking PEPSI to the Vatican-Advanced-Technology Telescope using a 450m long fiber

Authors: D. P. Sablowski, M. Weber, M. Woche, I. Ilyin, A. Järvinen, K. G. Strassmeier, P. Gabor

Aims: Study and presentation of the fibre-link from the VATT to PEPSI at the LBT.

Own contributions: Assembled the unit, first (and further observations). With exception of section 2.2, the text was written by myself.

2. Spectral Disentangling with Spectangular (Manuscript I)

Daniel P. Sablowski¹ and Michael Weber¹

Astronomy & Astrophysics, 2017, Volume 597, A125

1: Leibniz Institute for Astrophysics Potsdam (AIP), An der Sternwarte 16, 14482 Potsdam, Germany

Abstract

The paper introduces the software *Spectangular* for spectral disentangling via singular value decomposition with global optimisation of the orbital parameters of the stellar system or radial velocities of the individual observations. We will describe the procedure and the different options implemented in our program. Furthermore, we will demonstrate the performance and the applicability using tests on artificial data. Additionally, we use high-resolution spectra of Capella to demonstrate the performance of our code on real-world data. The novelty of this package is the implemented global optimisation algorithm and the graphical user interface (GUI) for ease of use. We have implemented the code to tackle SB1 and SB2 systems with the option of also dealing with telluric (static) lines.

2.1. Introduction

Since stellar evolution depends critical on the mass of the object, measurement of radial velocities of binary stars is, besides the measurement of the inclination, an important step for stellar evolution studies. It was shown, e. g. by Gallenne et al. (2016) and Holmgren (2004), that disentangling the spectra helps to improve the orbit determination of binaries. Furthermore, it allows detailed chemical analysis of the component spectra (Pavlovski & Hensberge, 2005).

We note first, that decomposition methods like direct and iterative subtraction (e.g. González & Levato, 2006) are not understood as disentangling techniques. These subtraction methods rely on a fully analytical approach which is not fulfilled by real (noisy) measurements. Their procedure is to use as many spectra as components present in the stellar system obtained at different phase positions. This would yield an analytically determined system of equations as long as noise (and further errors, e.g. from wavelength calibration) would be negligible. Solving this set of spectra results in decomposed spectra for each component. The result is commonly an average of solutions from several sets to reduce the noise of the decomposed spectra. Disentangling to the contrary uses a larger set of observations spread over the whole orbit of the system, and identifies moving contributions of each component in the composite spectra. Its strength is derived from an overdetermined situation, which makes noise a less degrading factor. As long as all data

are of equal quality, the result will have a significantly higher signal-to-noise ratio. Furthermore, disentangling does not assume information about the radial velocities since the result is coupled to an optimisation on the orbital elements.

Spectral disentangling can also be defined as template independent separation of different contributions of sources to an observed composite spectrum. These contributions are mainly the components of multiple stellar systems. However, also telluric lines and time-dependent line variability (e.g. Harmanec et al., 2004; Hadrava et al., 2009) can be extracted from composite spectra. The first application of a decomposition procedure was published by Bagnuolo & Gies (1991) where they used a tomographic method to separate the spectra of the binary AO Cas. Simon & Sturm (1994) published the disentangling method based on singular value decomposition (SVD). They also implemented a global optimisation (Downhill-Simplex, Nelder & Mead, 1965) method to find the best orbital fits to their observations. Independently, Hadrava (1995) developed his famous code based on Fourier transform of the composed spectra. Further development resulted in KOREL (e.g., Hadrava, 1997), FDBinary (and fd3, see Ilijic et al., 2004) and CRES (see Ilijic, 2004). CRES uses SVD but it does not optimise the radial velocities of the observations.

A comparison between disentangling in Fourier and λ -space is given by Ilijic et al. (2002). The disentangling in the λ -space is more flexible in the sense that (1) each spectra can have its own sampling, (2) each data point can have its own weight and (3) the output can be extended due to the radial velocities of the observations. In Fourier-disentangling all spectra need to have equal binning, weight and the output is a periodic function of the wavelength. Our code is written to elevate point (3). Hence, the solution will cover an extended wavelength range, defined by the radial velocities of the observations. It should be noted that point (2) could in both cases Fourier and λ -space be achieved by rebinning all spectra to the same grid. However, one may really want to use different sampled data without resampling them to a common grid.

In Sect. 2.2 we collect all necessary basics of spectral disentangling in the λ -space and describe the procedure. We present tests of the code with artificial data in Sect. 2.3. An application to observations is presented in Sect. 2.4 and the conclusion follows in Sect. 2.5.

2.2. Method of disentangling in λ -space

2.2.1. Formulation of the problem

The time-series of spectra, spread over the orbital phase, needs to be carefully normalised. To account for the relative flux ratio of the components, additional data are required (e.g., from photometry). We also note, that disentangling is applicable only to well-detached systems. However, the components can have different spectral types.

At first, we assume that the flux is constant with phase, i.e. the spectra from a possible eclipse are not used. The spectra are furthermore corrected to the heliocentric system and rebinned to a logarithmic wavelength scale

$$p = A \log(\lambda) + B, \quad (2.1)$$

where A and B are constant and p is the pixel number of the new scale. A given shift of the spectra by the Doppler effect yields a constant shift of p . If we assume, that the resolution of the observations is sufficiently high (in first approximation given by the rotational velocity of the components) we can apply a linear transformation between observations and individual spectra. The solution vector

$$\vec{x} = (x_1, \dots, x_k)^t \quad (2.2)$$

is given by the individual spectra of the k components of the multiple system. If we collect all n observations in

$$\vec{\sigma} = (\vec{\sigma}_1, \dots, \vec{\sigma}_n)^t \quad (2.3)$$

the problem to be solved is given by

$$\underline{M} \cdot \vec{x} = \vec{\sigma} \quad (2.4)$$

where \underline{M} is the transformation matrix containing the radial velocity information of all spectra. This matrix can be further separated to

$$\underline{M} = \begin{pmatrix} \underline{N}_{1,1} & \cdots & \underline{N}_{k,1} \\ \vdots & \ddots & \vdots \\ \underline{N}_{1,n} & \cdots & \underline{N}_{k,n} \end{pmatrix}, \quad (2.5)$$

where each of the sets $\underline{N}_{1,j}, \dots, \underline{N}_{k,j}$ images the component spectra to one observation and contains the RV information

$$\underline{N}_{i,j} = \begin{pmatrix} \overbrace{0 \dots 1}^{v_{i,j}} & \dots & 0 \\ \vdots & \ddots & \vdots \\ 0 & \dots & 1 \end{pmatrix}, \quad (2.6)$$

where $v_{i,j}$ is the velocity in observation j of component i . As long as SVD is applied to rank deficient and overdetermined systems, the solution behaves as a least square fit, i.e., it gives the solution of smallest residuum, which is

$$r = \|\underline{M}\vec{x} - \vec{\sigma}\|. \quad (2.7)$$

This residuum can be used as the value to be minimised during the optimisation procedure. However, Simon & Sturm (1994) optimised on the orbit fit to the RVs from the optimisation algorithm. To fulfil the criterion of an overdetermined system we need at least one more observation as components are to be disentangled, $n_{min} = k + 1$, at different phases of the system.

If static lines, e.g., tellurics, are present, we add an additional column of matrices, $\underline{N}_{k+1,j}$, without shifting the diagonal. Since telluric lines vary in strength from observation to observation, we need to take this into account. This can be done by using the relative line-depths as the elements for this matrix. Furthermore, heliocentric correction should not be applied since the static matrix does not account for shifts. In this case, the velocities are given by $v_{i,j} = RV_{i,j} + h_j$ the sum of the radial velocities and the heliocentric correction. It is worth noting, that the minimum number of necessary observations $n_{min} = k + 2$ increases by one.

2.2.2. The procedure

We assume that the observations are carefully normalised and corrected for the heliocentric velocity, which should be applied by the spectroscopic data reduction. However, heliocentric correction is not necessary if one is not interested to the orbital motion or if the velocities will be corrected afterwards. Moreover, in regions where telluric lines are present, no heliocentric correction should be applied. We have created an additional C++ GUI¹ application (*CroCo*) for logarithmic rebinning and 2-dimensional cross-correlation, i.e., this tool

¹We are using the Qt library for GUI programming: www.qt.io

is used to prepare the input data. The data are resampled to a new grid in the logarithmic scale. The step size I is set by the user in parts of the smallest $\delta = \min(\log(\lambda_{\ell+1}) - \log(\lambda_{\ell}))$ difference between the sampling points on the logarithmic scale, such that the new sampling is $\delta' = I \cdot \delta$. This sampling is also applied to the templates and all data will be cropped to an identical wavelength region for the cross-correlation. It is also possible to choose the spectral region of interest, in case that processing the whole spectral range is not necessary. Linear interpolation is applied to find the values of the spectra on the new wavelength scale. Furthermore, the continuum value is subtracted since we perform the cross-correlation for zero-normalised spectra. The cross-correlation sum for such data is

$$C(n) = \frac{1}{N\sigma_{s,t}} \sum_m^N (s(m) - \bar{s}(m))(t(m-n) - \bar{t}(m)), \quad (2.8)$$

where \bar{s} and \bar{t} are the mean values and

$$\sigma_{s,t} \equiv \sigma_s \sigma_t = \frac{1}{N-1} \sqrt{\sum_m^N (s(m) - \bar{s}(m))^2 (t(m-n) - \bar{t}(m))^2} \quad (2.9)$$

the standard deviation product of the spectrum and template, respectively. Based on the new wavelength-sampling, *CroCo* performs the cross-correlation of all possible combinations of the templates in the specified velocity ranges with the observed spectrum. These ranges are defined by a value for maximum separation of the templates and maximum shift against the rest wavelength. In Fig. 2.1 we show an example of a cross-correlation for one spectrum (a) and the whole set (b) around the Li I $\lambda 6708 \text{ \AA}$ line of an artificial binary. All performed 2-dimensional cross-correlations are shown. The program picks out the one with the maximum value. In regions where no overlap between template and observation exists, we add 0 to the cross-correlation sum. Cross-correlation was performed using the templates from which the spectra themselves were constructed. More details on these data follow in Sect. 2.3.3.

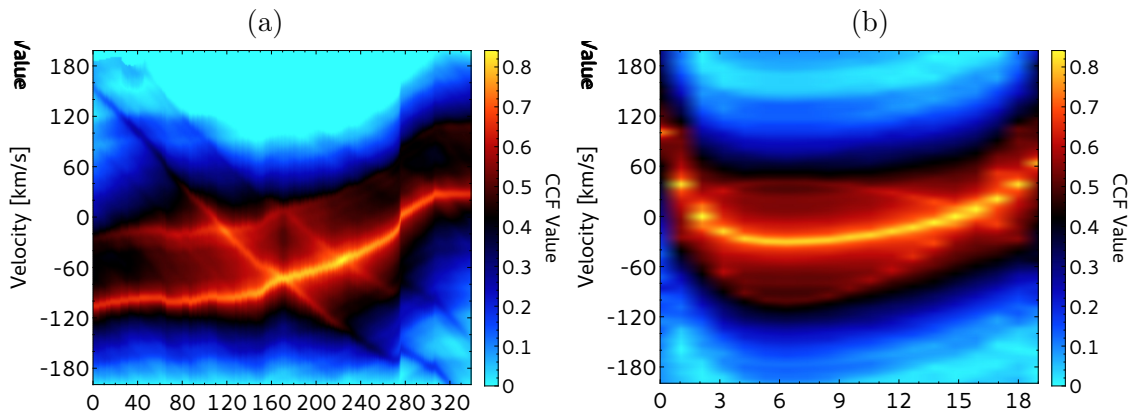


Figure 2.1.: An example of the 2-dim cross-correlation as provided by *CroCo*. (a): All cross-correlations (340) performed on one spectrum; (b): The cross-correlations with maximum peak value for all (20) spectra equidistantly spread in phase of our artificial data.

For this artificial binary we applied an orbit comparable to Mizar (ζ UMa) with an eccentricity of $e = 0.537$, systemic velocity $\gamma = -5.6 \text{ km/s}$ and amplitudes of $K_1 = 68.6 \text{ km/s}$ and $K_2 = 67.6 \text{ km/s}$ for the primary and secondary, respectively. With the “Binary Tool” implemented in *CroCo*, two template-spectra can be combined to a composite

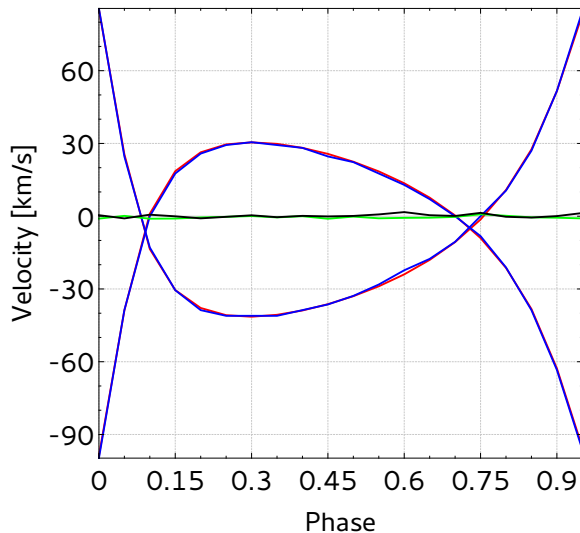


Figure 2.2: The orbit of our test system, red is calculated and blue is the result from the cross-correlation. Green and black shows the differences between calculated and cross-correlation for both components. The velocity sampling was about 1.17 km/s and we have not fitted the CCF peak.

spectra covering the specified orbit. These data can be used to find systematic errors and to cross-check with the results of the observations. The orbit and the result from the cross-correlation are shown in Fig. 2.2. We note here, that we do not fit the correlation peak for a more precise determination because these values will be optimised during the disentangling procedure. However, the cross-correlation data are stored as ASCII files for further processing. The velocities from the cross-correlation can be used for the disentangling in case that a preliminary orbit is not known. As we will describe below, optimisation can be performed directly on the RVs of each component and each observation or on the orbital parameters. Optimisation on the velocities can be advantageous in case of orbital distortions, e.g, a third component.

During the orbital motion, the wavelength window will vary according to the RV value. This leads to slight differences of the wavelength range each individual observation covers. In order to prevent edge errors and to gather the maximum wavelength information, we construct the matrices in Eq. (2.6) such that they cover the maximum wavelength range. This in turn will enlarge the wavelength range of the solution vectors (Eq. (2.7)). As described in the introduction, this would not be possible using a procedure based on Fourier-transform.

The disentangling code *Spectangular* uses the *Armadillo* C++ linear algebra library (see Sanderson, 2010) for efficient matrix and vector operations. It also provides three different algorithms for the SVD, the classical full SVD, an economical solution (ECON) and divide-and-conquer (DaC) method. For most data sizes DaC is by far the fastest procedure and is implemented in the global optimisation algorithm. Nevertheless, for very small data sets the classical SVD could be faster since it does not need any pre-calculations, e.g., DaC needs to separate the large transformation matrix \underline{M} into smaller ones and treats them separately. Disentangling without any optimisation can also be performed with all three methods. Furthermore, we use the *OpenBLAS* library which provides parallel computing routines. This is especially advantageous for matrix operations, since it reduces the time for these calculations by approximately the reciprocal of the number of used threads.

The most time-consuming part of the optimisation algorithm is the initiation. In this first step, it creates the initial simplex which has $(kn + 1)$ points, i.e., the SVD is performed $(kn + 1)$ -times for the whole data set. This initial data is saved in case one wants to start the optimisation again. Note that the variation of the RV values to create this simplex is not random, i.e., for a given set of input RVs (or orbital parameters) the initial

simplex will always be the same. This will be described in more detail in Sect. 2.2.3. After that initiation the algorithm performs as many iterations as specified by the user. Depending upon the data and initial values, the SVD is performed multiple times during one iteration. The most time-intensive transformation of the simplex is a total contraction, where kn points need to be re-calculated, i.e., it takes almost as long as the initiation itself. We have implemented direct optimisation on the radial velocities and on the orbital elements. When optimised on orbital elements, the initiation will take only eight (seven orbit elements) evaluations and in general this procedure leads to faster convergence. The value to be minimised in both cases is the residuum between result and observations given by Eq. (2.7). Additionally, it is also implemented to optimise on the peak-deviation, i.e., the maximum deviation of a single spectral bin to the disentangling result. This criterion, however, is not recommended since it is very sensitive to remaining cosmics, pixel errors, etc.

The resulting optimisation data are saved again to a local file and can be used in case that the optimisation needs to be continued. If the residuum r was reduced after a transformation, the result can be plotted in the main window of the program as a live view to control the procedure. After each evaluation of the SVD the optimisation can be aborted in case that r is not longer minimised. Currently, the code is implemented for SB1 and SB2 data and the user can choose whether telluric (static) lines are present or not.

2.2.3. Details on Downhill Simplex Implementation

For the downhill simplex method, it is common to use the standard deviation of all $(kn+1)$ function values (the residuum of the SVD in our case) of the simplex as the abort criterion for the optimisation. However, we have implemented to set the number of iterations of the downhill simplex algorithm (DSA). The mean as well as the standard deviation of all residua of the simplex are calculated and written to the logfile after each iteration.

As already mentioned, the DSA performs transformations of the initial simplex. There is no general rule to construct this initial simplex. In the case of optimisation on each RV, the initial simplex is constructed as

$$\vec{P}_i = \vec{P}_0 + \delta RV \cdot \vec{e}, \quad i = 1 \dots N, \quad (2.10)$$

where P_0 is the point defined by the initial values, δRV is the change, \vec{e} is the unit vector, i.e., only one of the values differ from point to point and $N = kn$ is the number of variables. The change in RV can be set by the user in fractions of the binning B_v of the spectra in velocity space, i.e., $\delta RV = SB_v$, where S is the user-defined step size. In the case of optimisation on the orbital parameters the step of each parameter is user-defined and $N = 7$ for the number of orbital parameters of an SB2 system and with the relation $\omega_2 = \omega_1 + \pi$ for the longitude of periastron for the secondary.

Furthermore, the coefficients for the transformations can also be changed. There are four transformations: (1) reflection

$$\vec{R} = \vec{Z} + \alpha(\vec{Z} - \vec{P}_w), \quad (2.11)$$

of the worst point P_w (corresponds to highest r) over the centroid \vec{Z} of the simplex, where $\alpha = 1$ is the reflection coefficient. (2) expansion

$$\vec{E} = \vec{Z} + \gamma(\vec{Z} - \vec{R}), \quad (2.12)$$

over the reflected point, where $\gamma = 2$ is the expansion coefficient. (3) single contraction

$$\vec{C} = \vec{Z} + \beta(\vec{P}_w - \vec{Z}), \quad (2.13)$$

of the worst point towards the centroid, where $\beta = 0.5$ is the contraction coefficient. (4) total contraction

$$\vec{P}'_i = \vec{P}_b + \beta_{tot}(\vec{P}_i - \vec{P}_b), \quad i \neq b, \quad (2.14)$$

towards the best point \vec{P}_b , where $\beta_{tot} = 0.5$ is the total contraction coefficient. All given values for the coefficients are defaults and used if user values are not defined.

We note here, that the DSA could stagnate and minimisation of the residuum is not achieved even after many iterations. In such a case the optimisation should be aborted. The current best values for the parameters should be used as the new start values to start a new optimisation. To cover this case, an automatic re-initiation option is implemented such that optimisation will be reinitiated after DSA has passed two iterations without a change in mean and STD values of the simplex points. Another complication can occur in computing the correct residuum between solution and observations at the edges of the spectra. The solution can lose its overdetermination, i.e., the solution is poorly defined at the edges. In this region the entries of the solution vector $\vec{x}(edge)$ (more precise: the corresponding singular values) do only represent rounding errors. Computing the residuum against the whole spectra would yield wrong (higher) values of the residuum. Hence, there is the option to calculate the residuum in a (smaller) user-defined wavelength range.

2.2.4. Error Estimation

The common way (e.g. Phillips & Eyring, 1988; Nelder & Mead, 1965) is to compute the curvature matrix

$$\Gamma_{ij} = \frac{\partial^2 \chi^2}{\partial p_i \partial p_j}, \quad (2.15)$$

where $\chi^2 = \sum w_i (y_i - f_i)^2$. From this matrix one obtains the variance-covariance matrix according to

$$\epsilon_{ij} = s^2 (\Gamma^{-1})_{ij}, \quad (2.16)$$

where $s^2 = \chi^2 / (n - N)$. In the case that the off-diagonal elements of ϵ can be neglected, the standard deviation of parameter i is given by $\sigma_{p_i} = \sqrt{\epsilon_{ii}}$. To fit a quadratic function to the error surface additional points $\vec{P}_{ij} = (\vec{P}_i + \vec{P}_j) / 2$, $i \neq j$ are required. This leads to an additional $(N + 1)N/2$ necessary SVDs, i.e., Eq. (2.4) needs to be solved $28 \times$ in case of an SB2 system to estimate the error. It becomes computational expensive in case of large data sets and optimisation on the individual RVs, e.g. 10 spectra of an SB2 system would require 210 SVDs of Eq. (2.4). However, it is an acceptable and necessary effort in case of orbital parameters and the advantage is that no numerical increments for the derivatives need to be assumed (Eq.(2.15)).

Nevertheless, there are two cases in which the quadratic fit is not applicable. Firstly, the final simplex could be too small, i.e., the error estimation is dominated by rounding errors. Secondly, the opposite case were the final simplex is too large for a quadratic fit. As pointed out by Phillips & Eyring (1988) the former case is the more important one. Indeed, if the optimisation is performed with already good parameters, it is possible that one of them is only changed by a small value or, even worse, not changed at all. This will make it impossible to compute the curvature matrix, since inversions are involved and they would be singular. In such a case. the critical parameter is varied in one vertex of the simplex and the residuum recalculated. However, this decision requires user-input and one should be aware that there is also the possibility to create new optimisation data by using the best parameters and starting the optimisation again only for a few iterations.

Finally, according to experience, we note that a good alternative is to perform the optimisation on individual RVs and apply an orbit fit to the optimised RVs. This provides

errors for the orbital parameters. Furthermore, errors introduced by a third component and uncertainties on the wavelength axis of the spectra (e.g. due to calibration errors) will have a smaller effect on the resulting spectra.

2.3. Test with artificial data

2.3.1. Performance

We used artificial data with different sampling to test the computation time in dependence of data size. In Fig. 2.3 we show a comparison between single core and eight logical cores. The spectra had a length of around 2,000 points after rebinning to the logarithmic wavelength scale. Hence, the different data size comes from the number of used spectra. The time depends on both number of rows u and columns v of the $u \times v$ transformation matrix. For a rectangular matrix, $v < u$, it is sufficient to calculate only v singular values. The singular matrix is then a quadratic $v \times v$ matrix and only these column vectors need to be considered (this is one of three economical SVD methods - thin SVD).

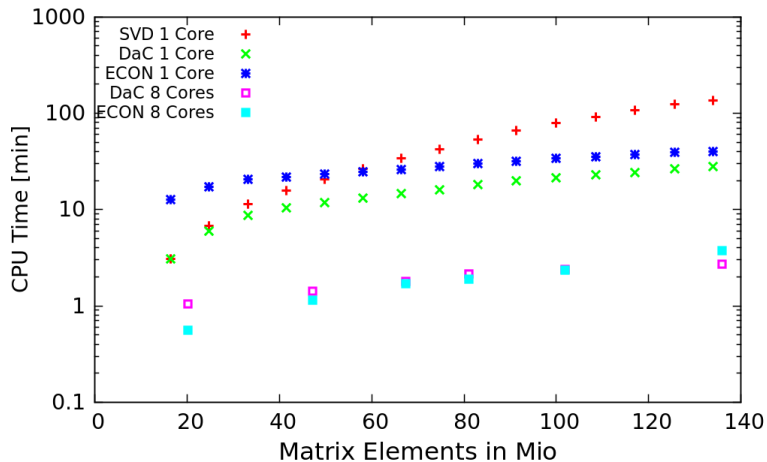


Figure 2.3.: CPU time vs. data size for the three SVD methods for computation on one and eight cores. SVD is the standard full SVD, ECON the economical SVD and DaC is for SVD with divide-and-conquer method.

We note that our code-development workstation had four physical cores and we enabled hyperthreading to split these to eight logical cores. Using eight threads, the computing-time is reduced by a factor of eight.

The memory consumption can be estimated by the number of elements of the transformation matrix \underline{M} . Let l_p be the number of spectral bins on the logarithmic scale. Neglecting the additional columns due to the velocity shift we get $v = 2l_p$ and $u = nl_p$ for the number of columns and rows, respectively. SVD decomposes \underline{M} into three matrices of dimensions $v \times v$, $u \times v$ and $u \times u$, respectively. We therefore get the following relation for the memory usage: $f(n) = l_p^2(n(n+2) + 4) \cdot 8 \cdot 10^{-9}$ [GB]. We show this dependence together with collected data for ECON and DaC in Fig. 2.4.

2.3.2. SB1 and static lines

Here we demonstrate the disentangling of lines of SB1 systems which are blended, e.g. from telluric features. This is the case for the KI $\lambda 7699$ Å line, e.g., in ϵ Aurigae (Strassmeier

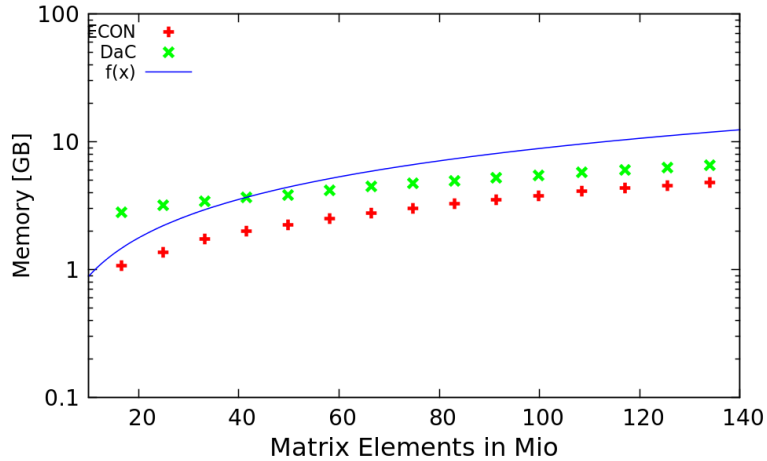


Figure 2.4.: Memory vs. data size for the economical (ECON) SVD, SVD with divide-and-conquer method (DaC) and the memory estimation $f(n)$ (see text).

et al., 2014) which is hidden in the A-band of O_2 around $\lambda 7600 \text{ \AA}$. To demonstrate this, we have created artificial data with an absorption at the K I line wavelength and applied the orbital parameters as described in Sect. 2.2.2 and the time-series is shown in Fig. 2.5. To get more realistic data we added Gaussian noise resulting in a signal-to-noise ratio of 100. Furthermore, we varied the line-strength of the telluric features and assume that the ratios are measured and known. Hence, the matrix $\underline{N}_{k+1,j}$ is filled with these ratios. We alternately changed the line-strength from spectrum to spectrum by a factor of 0.5. Disentangling was performed with three iterations of the optimisation algorithm. The result of the disentangling is shown in Fig. 2.6. The top panel in Fig. 2.6 (a) shows the disentangled SB1 line and the telluric lines. Fig. 2.6 (b) at the bottom shows the differences between the disentangled result and the composite spectra. These differences are computed with all composite spectra according to $\underline{M}\vec{x} - \vec{d}$. We note here, that the telluric features would also be successfully disentangled if the ratios are not given. In that case, the variation of line strength would be present in the differences between observations and result. This is shown in the bottom panel of Fig. 2.6

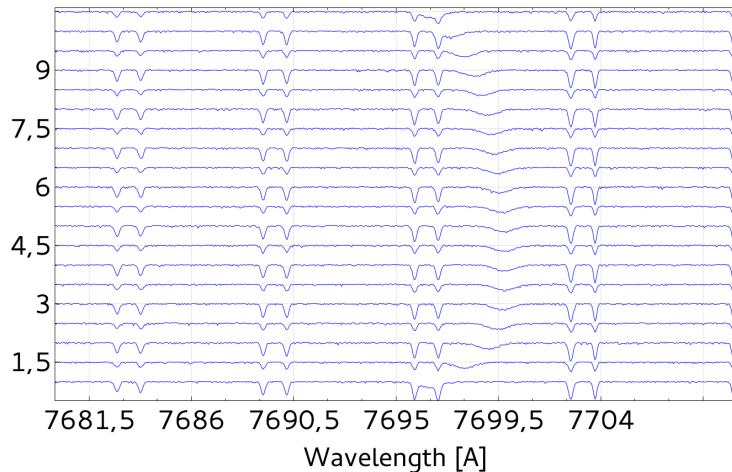


Figure 2.5.: The artificial time-series of our SB1 system with the stellar K I $\lambda 7699 \text{ \AA}$ line in the variable A-band of O_2 .

As described previously, the result vectors (2.2) cover a slightly larger wavelength range due to the orbital motion. This can also be seen in Fig. 2.6a between the telluric and the stellar spectrum.

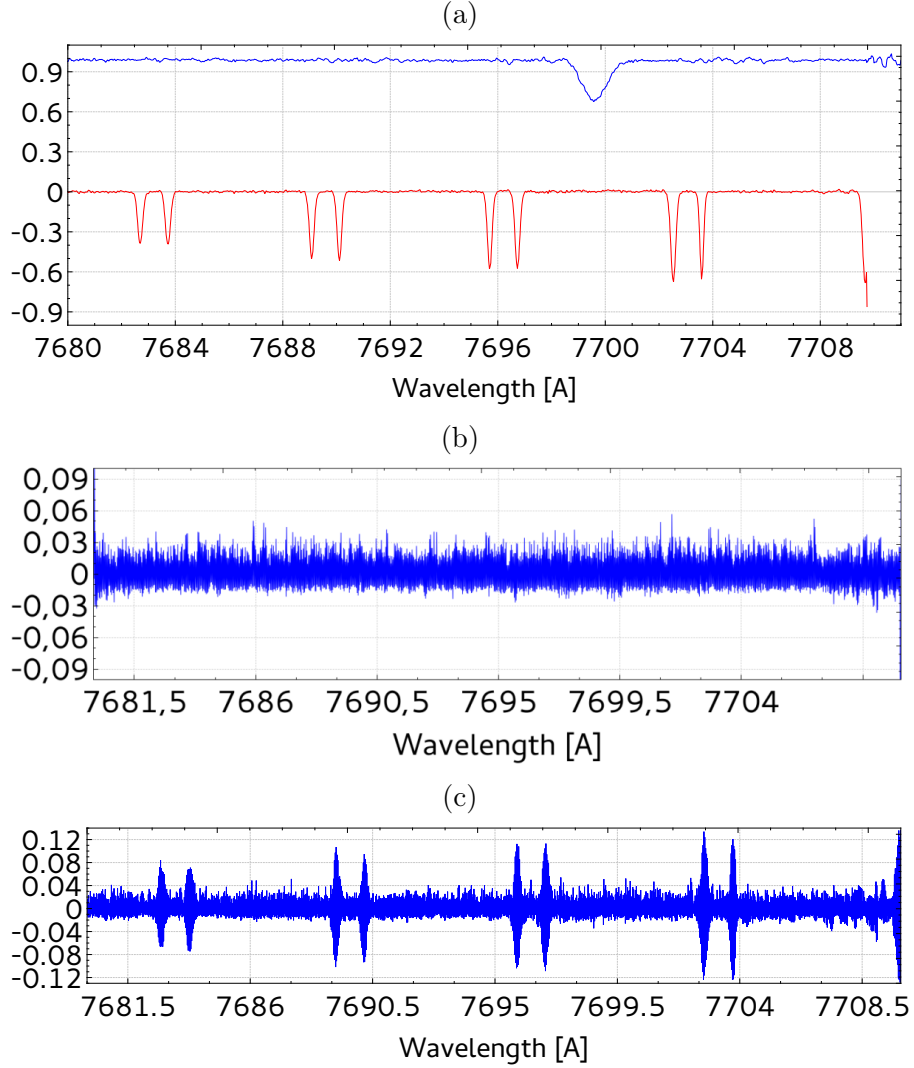


Figure 2.6.: Result of the disentangling with optimisation of our SB1 system with the stellar K I $\lambda 7699$ Å line in the variable A-band of O₂. (a): Absorptions from the SB1 line and variable telluric lines; (b): Differences between all spectra and result; (c): Differences between all spectra and result without accounting for line strength variation.

Additionally, we have generated spectra with superimposed emission lines to simulate stars embedded in emission nebulae. We used emission line data from Osterbrock et al. (1992) of M42 and added Gaussian noise to our data. Again, we used the same orbit parameters as described in Sect. 2.2.2 to model an absorption crossing a static emission. We show the time-series of these data in Fig. 2.7, where we have created two sets of data. These sets differ in the width of the emission line compared to the width of the absorption line.

The disentangling-results after three iterations of optimisation are shown in Fig. 2.8 for the broad emission and in Fig. 2.9 for the narrow emission line, respectively. The wavelength range of the result for the absorption spectra is again slightly larger than the one for the static lines, as expected. The residuum is of the order of $4.8 \cdot 10^{-5}$ in both

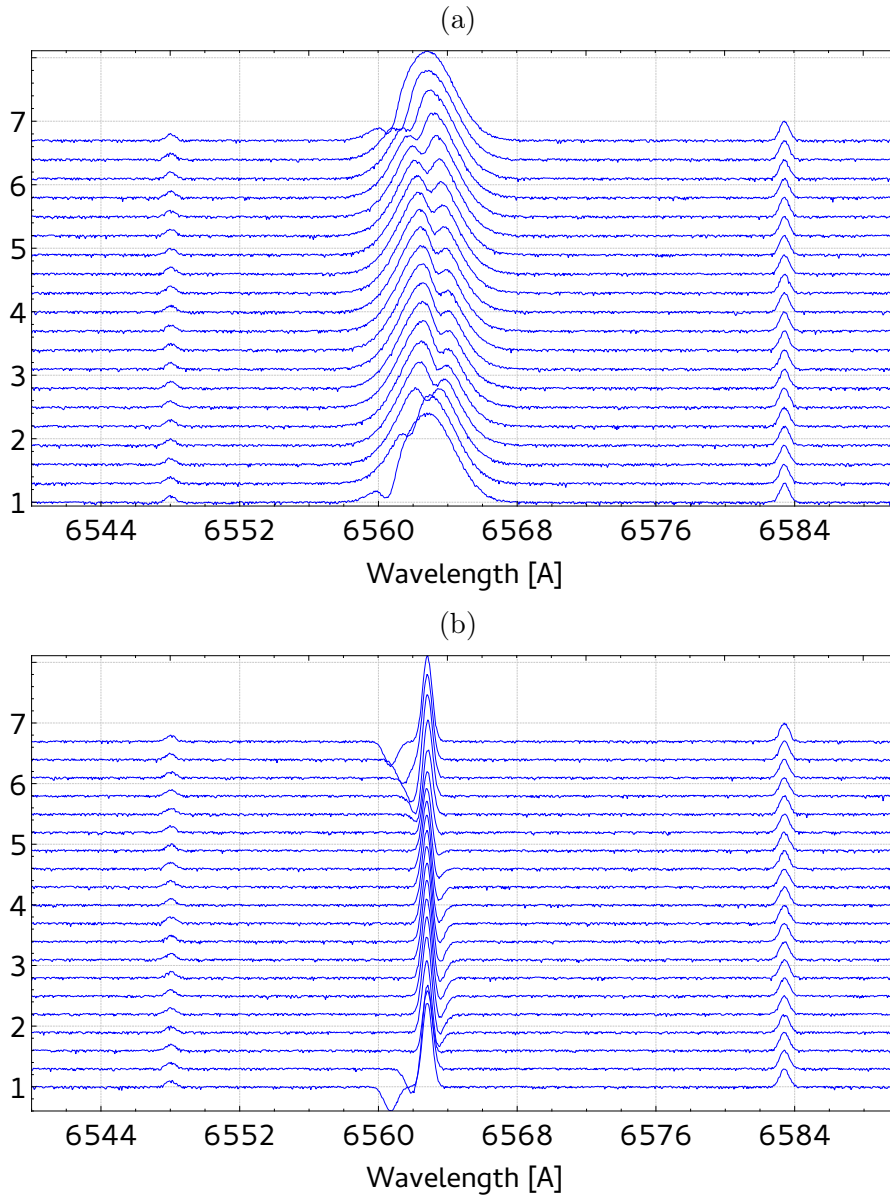


Figure 2.7.: The artificial time-series of our SB1 system with the superimposed broad (a) and narrow (b) emission.

cases.

2.3.3. Artificial SB2 system

We will use time-series of artificial spectra with different noise levels (SNR of 10, 20, 40, 60, 80 and 100) to demonstrate the optimisation and error estimation. One time-series with applied SNR of 100 is shown in Fig. 2.10. The $v \sin(i)$ for the sharp-lined and broad-lined component is 5 km/s and 20 km/s, respectively. The corresponding results from disentangling with best parameters and the differences between these results and the artificial spectra are shown in Figs. 2.11a and 2.11b, respectively. As mentioned in Sect. 2.2.3, poor definition at the edges can influence the residuum. The plot of the differences in Fig. 2.11b shows such a case for the lower three spectra. Hence, the differences are not

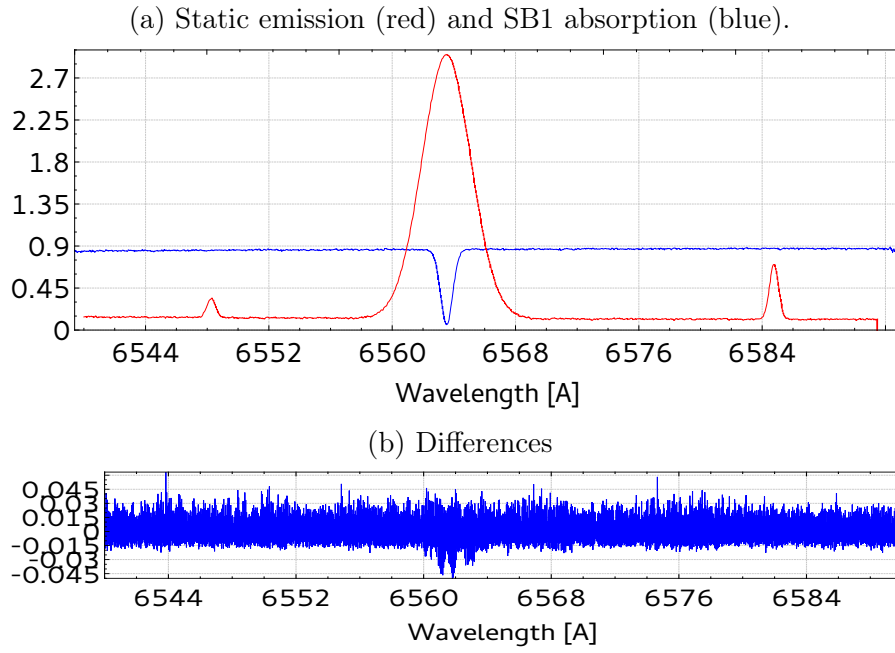


Figure 2.8.: Disentangling result of the superimposed broad emission line of the data shown in Fig. 2.7 (a).

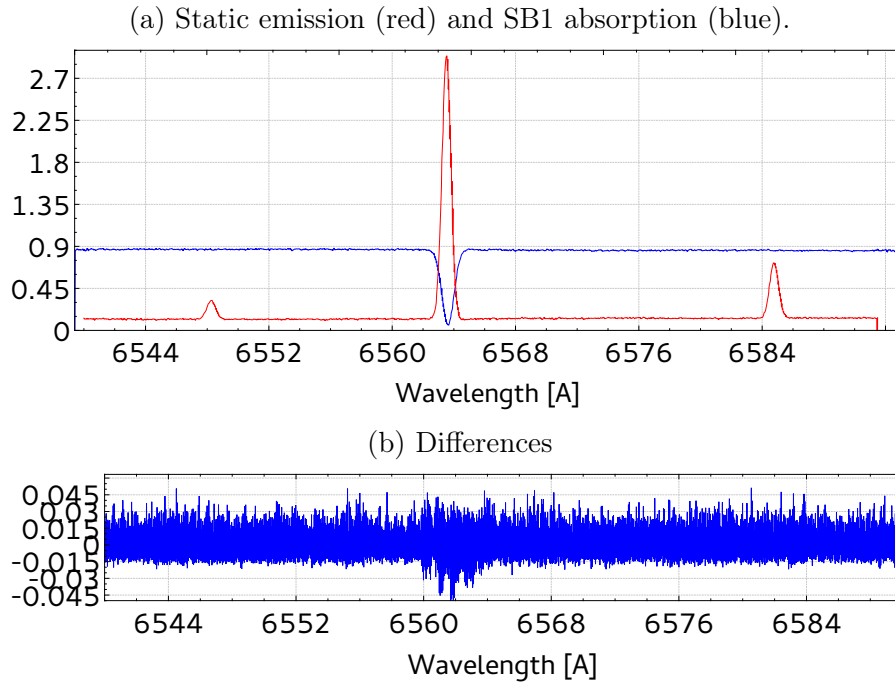


Figure 2.9.: Disentangling result of the superimposed narrow emission line of the data shown on bottom in Fig. 2.7 (b).

computed for the whole wavelength range at the red end.

Tab. 2.1 summarises the data before and after optimisation. The first row lists the SNR values of the result for the sharp-lined component spectra measured in two wavelength regions. σ_A^{opt} and σ_B^{opt} are the summed least squares between calculated RVs and the optimised values for the primary and secondary, respectively. We also list the summed

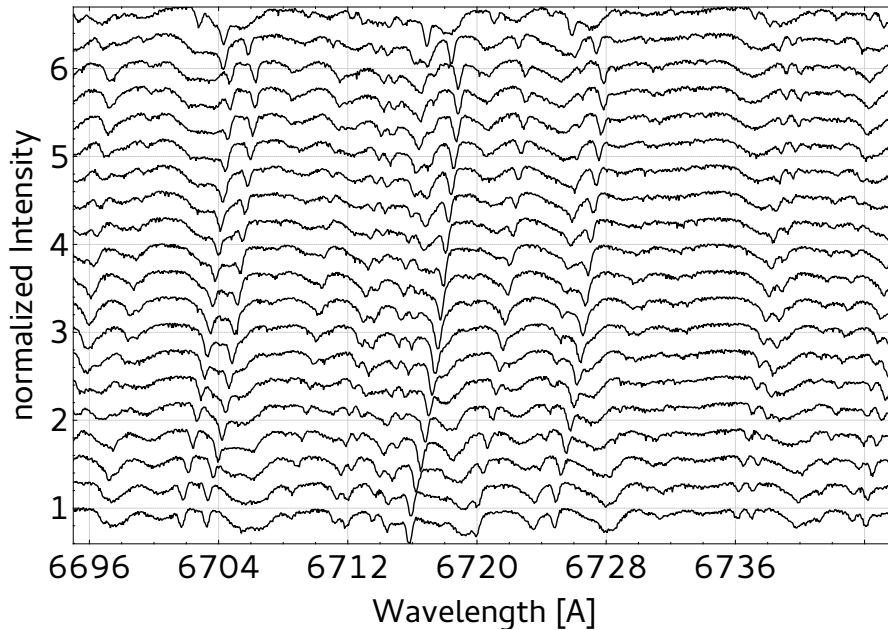


Figure 2.10.: All 20 spectra of our artificial binary around the Li i $\lambda 6708$ Å line with SNR of 80.

least squares, σ_A and σ_B , between calculated RVs and those from the cross-correlation with *CroCo*. These values were used to start the optimisation. We’ve performed 120 iterations of the optimisation on the RV values and fitted the orbit afterwards. The errors from the fit are also listed in Tab. 2.1.

In all cases, the resulting spectra show a significantly higher SNR compared to the input data by at least a factor of two. Additionally, the resulting RVs from cross-correlation and from optimisation of disentangling improve with increasing SNR. From the errors for the masses of the components, which we are most likely interested in, one can see a significant reduction of the errors. These errors could be further reduced by continuing with the optimisation. We note that we have used ideal input data, equally normalised, identical quality and equidistantly spread over the orbital phase. This itself yields good results for the cross-correlation method. However, disentangling has further improved the results.

How unequal noise-levels in a time-series influence the result is shown in Fig. 2.12. We have replaced two spectra from the SN100 set by those from the SN10 set. The continuum is now less well determined and the noise in the resulting spectra is increased (compared to Fig. 2.11 (a)). Only a few spectra with significant higher noise will make line-profile analysis difficult. Additionally, in Fig. 2.13 we show the result for unequal normalisation levels. Therefore, we have set the continuum of spectrum 2 to 0.98, spectrum 14 to 1.05 and spectrum 19 to 0.9. There is only a slight change of the continuum level in the results.

Furthermore, we show a comparison of the disentangling result between the minimum case, where we used three spectra, and the result from all 20 spectra in Fig. 2.14. One can see, that the contributions of the components are correctly separated. However, the noise level in the result is high and will make detailed line-profile analysis difficult.

Table 2.1.: Data for SB2 time-series for all 6 data sets. SNR1 and SNR2 is the signal-to-noise ratio measured in the result of the sharp-lined component between $[\lambda 6734.2:6737]$ and $[\lambda 6700:6702.5]$, respectively. The σ -values are the summed least squares between the calculated RVs and the optimised RVs and between calculated and those from *CroCo*. Furthermore we list all the errors for the orbital parameters before and after optimisation.

Data:	SN10	SN20	SN40	SN60	SN80	SN100
SNR1/SNR2:	27/28	58/61	106/115	173/136	231/200	252/273
σ_A [km/s]	1.571	0.807	0.783	0.775	0.745	0.752
σ_A^{opt} [km/s]	1.540	0.760	0.748	0.680	0.643	0.520
σ_B [km/s]	5.930	2.779	2.166	2.146	2.206	2.025
σ_B^{opt} [km/s]	4.146	1.831	1.566	1.514	1.351	1.525
$\delta(P)$ [days]	$\pm 8.7 \times 10^{-6}$	$\pm 3.6 \times 10^{-6}$	$\pm 2.8 \times 10^{-6}$	$\pm 3.1 \times 10^{-6}$	$\pm 2.9 \times 10^{-6}$	$\pm 2.5 \times 10^{-6}$
$\delta(P^{opt})$ [days]	$\pm 7.6 \times 10^{-6}$	$\pm 3.8 \times 10^{-6}$	$\pm 3.0 \times 10^{-6}$	$\pm 2.8 \times 10^{-6}$	$\pm 2.6 \times 10^{-6}$	$\pm 2.3 \times 10^{-6}$
$\delta(e)$	± 0.0077	± 0.0035	± 0.0027	± 0.0031	± 0.0029	± 0.0025
$\delta(e^{opt})$	± 0.0076	± 0.0040	± 0.0030	± 0.0028	± 0.0026	± 0.0023
$\delta(K_A)$ [km/s]	± 0.56	± 0.26	± 0.21	± 0.24	± 0.22	± 0.19
$\delta(K_A^{opt})$ [km/s]	± 0.58	± 0.31	± 0.25	± 0.23	± 0.21	± 0.17
$\delta(K_B)$ [km/s]	± 1.9	± 0.78	± 0.52	± 0.59	± 0.58	± 0.46
$\delta(K_B^{opt})$ [km/s]	± 1.4	± 0.68	± 0.47	± 0.46	± 0.41	± 0.45
$\delta(\gamma)$ [km/s]	± 0.38	± 0.16	± 0.13	± 0.14	± 0.14	± 0.11
$\delta(\gamma^{opt})$ [km/s]	± 0.35	± 0.18	± 0.14	± 0.13	± 0.12	± 0.11
$\delta(T_0)$	± 0.00088	± 0.00037	± 0.00029	± 0.00032	± 0.00030	± 0.00026
$\delta(T_0^{opt})$	± 0.00079	± 0.00040	± 0.00032	± 0.00029	± 0.00027	± 0.00024
$\delta(\omega_A)$	± 0.95	± 0.44	± 0.35	± 0.40	± 0.36	± 0.32
$\delta(\omega_A^{opt})$	± 0.95	± 0.51	± 0.39	± 0.36	± 0.34	± 0.29
$\delta(M_A \sin^3 i)$ [M_\odot]	± 0.00081	$\pm \pm 0.00037$	± 0.00025	± 0.00029	± 0.00028	± 0.00022
$\delta(M_A^{opt} \sin^3 i)$ [M_\odot]	± 0.00064	± 0.00034	± 0.00024	± 0.00023	± 0.00021	± 0.00022
$\delta(M_B \sin^3 i)$ [M_\odot]	± 0.00054	± 0.00024	± 0.00018	± 0.00020	± 0.00019	± 0.00016
$\delta(M_B^{opt} \sin^3 i)$ [M_\odot]	± 0.00048	± 0.00025	± 0.00019	± 0.00018	± 0.00016	± 0.00015

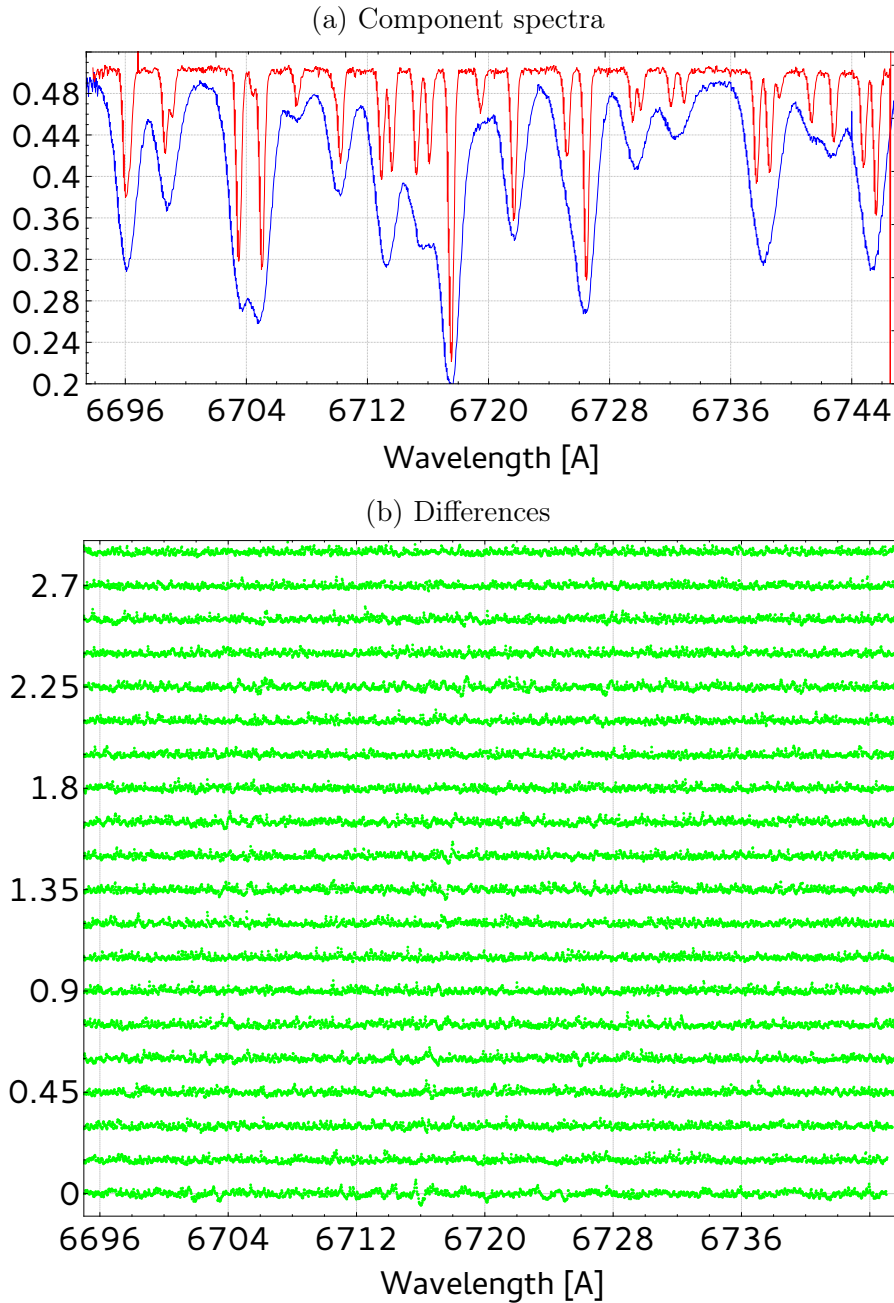


Figure 2.11.: (a) Disentangling result of our artificial binary with SNR of 80. (b) Differences between result and all spectra.

2.4. Application to Capella

This system is somehow unique due to its very precisely determined masses (Weber & Strassmeier, 2011) and evolutionary state (Torres et al., 2015). From our STELLA (see Weber et al., 2008) telescopes on Tenerife, there are lots of spectroscopic data available for Capella. We selected some for our disentangling-study, which are listed in Tab. 2.2.

Table 2.2.: Spectra used for the studies in Sect. 2.4. The x in the last three columns indicate which spectra are used in the respective subsections. The SNR of these spectra is $\gtrsim 100$.

No.	HJD 2456+	RV A	RV B	Sect.		
		[km/s]	[km/s]	2.4.1	2.4.2	2.4.3
0	347.591	34.97	25.01			x
1	364.534	54.33	4.82	x	x	x
2	366.344	55.20	3.92		x	x
3	366.520	55.22	3.86		x	
4	369.340	55.86	3.15		x	
5	370.387	55.91	3.08		x	
6	371.341	55.86	3.12		x	
7	372.341	55.72	3.25		x	
8	373.246	55.48	3.48		x	
9	377.343	53.62	5.34	x	x	x
10	378.526	52.78	6.17		x	x
11	379.523	52.01	6.97		x	
12	381.344	50.38	8.63		x	x
13	381.524	50.22	8.81		x	
14	382.529	49.18	9.86		x	
15	383.515	48.11	10.95		x	x
16	398.420	26.72	32.99	x	x	x
17	399.412	25.19	34.57			x
18	414.369	6.95	53.57		x	x
19	415.368	6.29	54.27		x	
20	416.369	5.69	54.91		x	
21	417.386	5.17	55.46		x	
22	418.370	4.76	55.91		x	
23	420.364	4.19	56.53		x	
24	515.669	9.26	51.15		x	x
25	518.661	6.78	53.75		x	x
26	528.663	4.23	56.56	x	x	x
27	531.621	5.26	55.54	x	x	x
28	538.635	10.73	49.98			x
29	544.605	18.14	42.39			x
30	549.752	25.78	34.51			x
31	570.578	53.05	6.17			x

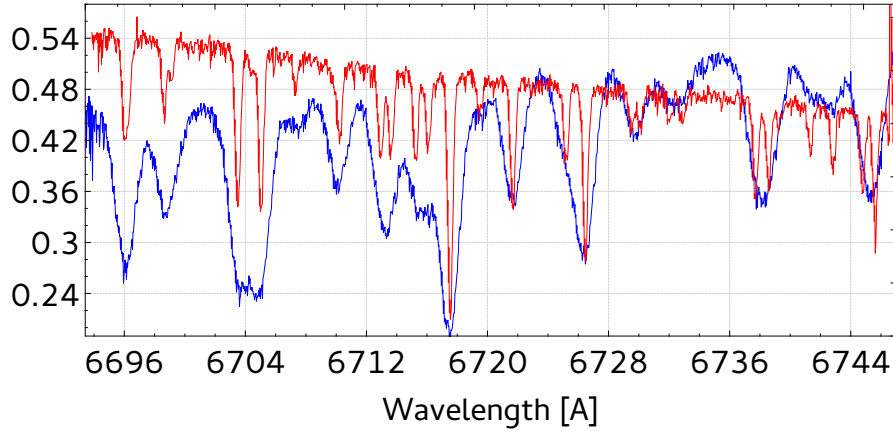


Figure 2.12.: Result from disentangling of the SN100 set with two spectra replaced from the SN10 set. The continuum is less well determined and the noise in the result is increased.

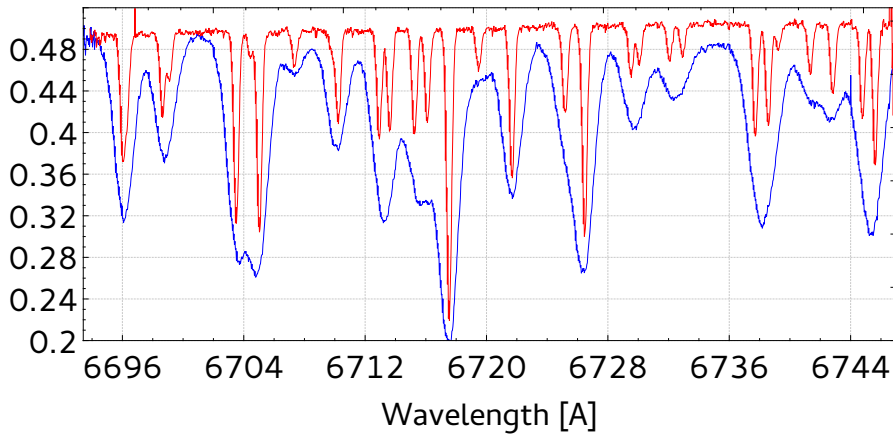


Figure 2.13.: Result from the disentangling of SN100 set with three spectra on different continuum levels. Compared to the results in Fig. 2.11a there is only a slight change of the continuum level of the results.

2.4.1. The ideal minimum case

To show the reliability of the code, we have decided to use only a small data set. As described, as long as SVD is applied to overdetermined and rank deficient systems it yields the solution of smallest residuum. The system of a binary without telluric lines has therefore two unknowns and to fulfil the criterion of overdetermination we need three independent spectra. The time-series of spectra is shown in Fig. 2.16 and the radial velocity curve with the measurements in Fig. 2.15 (a). We used different combinations of the spectra 2, 9, 16, 26 and 27 as listed in Tab. 2.2. The additional two spectra are used to show, how they can help to reduce the noise in the result.

With these data we will study the minimum case for disentangling. The determined case where we used two spectra from following quadratures (spectra 9 & 26 in Tab. 2.2) is shown in Fig. 2.17 (a). Due to the noise in the data it is not possible for the code to distinguish fully between the two components. Only strong lines in the secondary spectrum (blue) like the Li I itself and Ca I $\lambda 6718$ Å are visible. The minimum case is shown in Fig. 2.17 (b), where we had included an observation near conjunction (spectrum 16 in Tab. 2.2). These

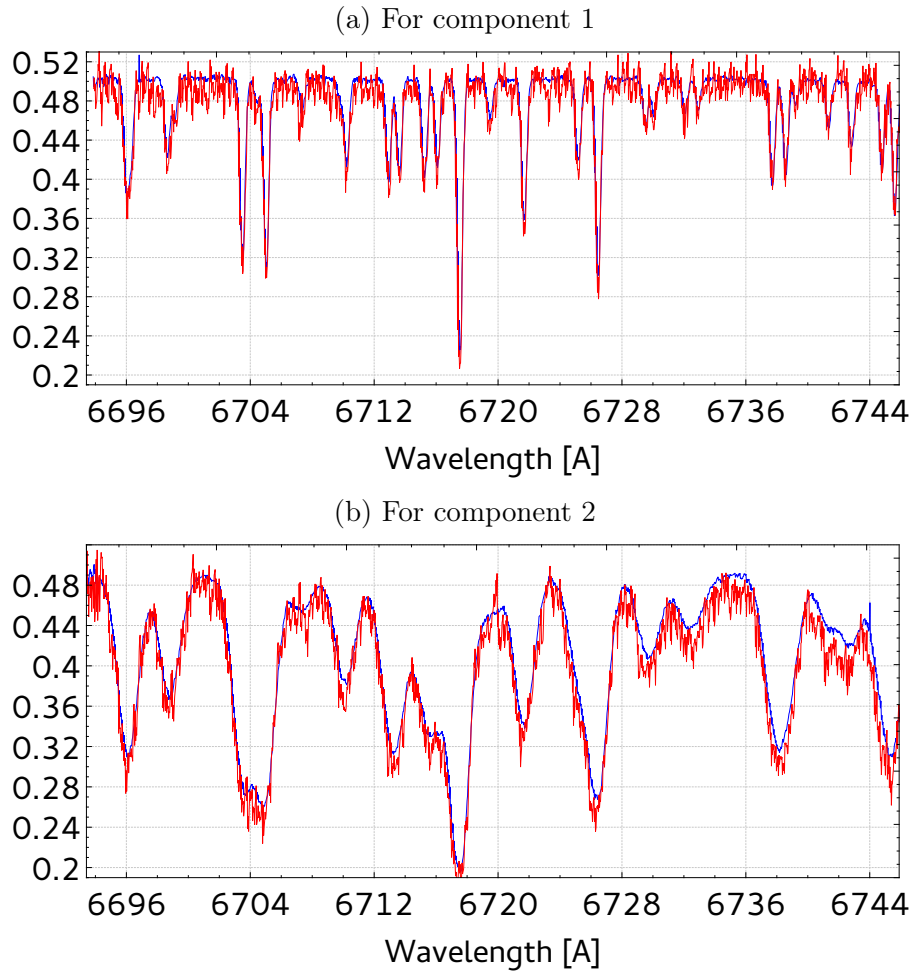


Figure 2.14.: Overplot of results for SN100 minimum case (three spectra) and all (20 spectra). (a) for the narrow-lined component and (b) for the broad-lined component.

three spectra yield an overdetermined system and the solution is less affected by noise as it is the case for the only determined system.

The next example (Fig. 2.17 c) shows the result, when all four spectra from the two consecutive quadratures are used (spectra 1, 2, 26 & 27 in Tab. 2.2). If we compare this result with the one above, one can see that the jitter of the solution due to noise in the measurements is reduced. However, since the binning of these spectra correspond to a velocity of 1 km/s the two pixel resolution is around 2 km/s. A glance on the RV values in Tab. 2.2 shows that the two observations for each pair differ by less than 2 km/s. This will give the code a better estimate of the noise but not of the components, since we would need three independent conditions to get an overdetermined system. Fig. 2.17 (d) shows the result when we use all 5 spectra. Compared to the minimum case (Fig. 2.17 b), the noise is greatly reduced.

2.4.2. Data at quadrature - a non-ideal case

Observations at maximum separation of the components lead to minimum blending of equal lines of both components, and are therefore often used to study the properties of the individual components of spectroscopic binaries. The orbital distribution of the observations we chose for this test (marked in the sixth column of Tab. 2.2) are shown in Fig. 2.15

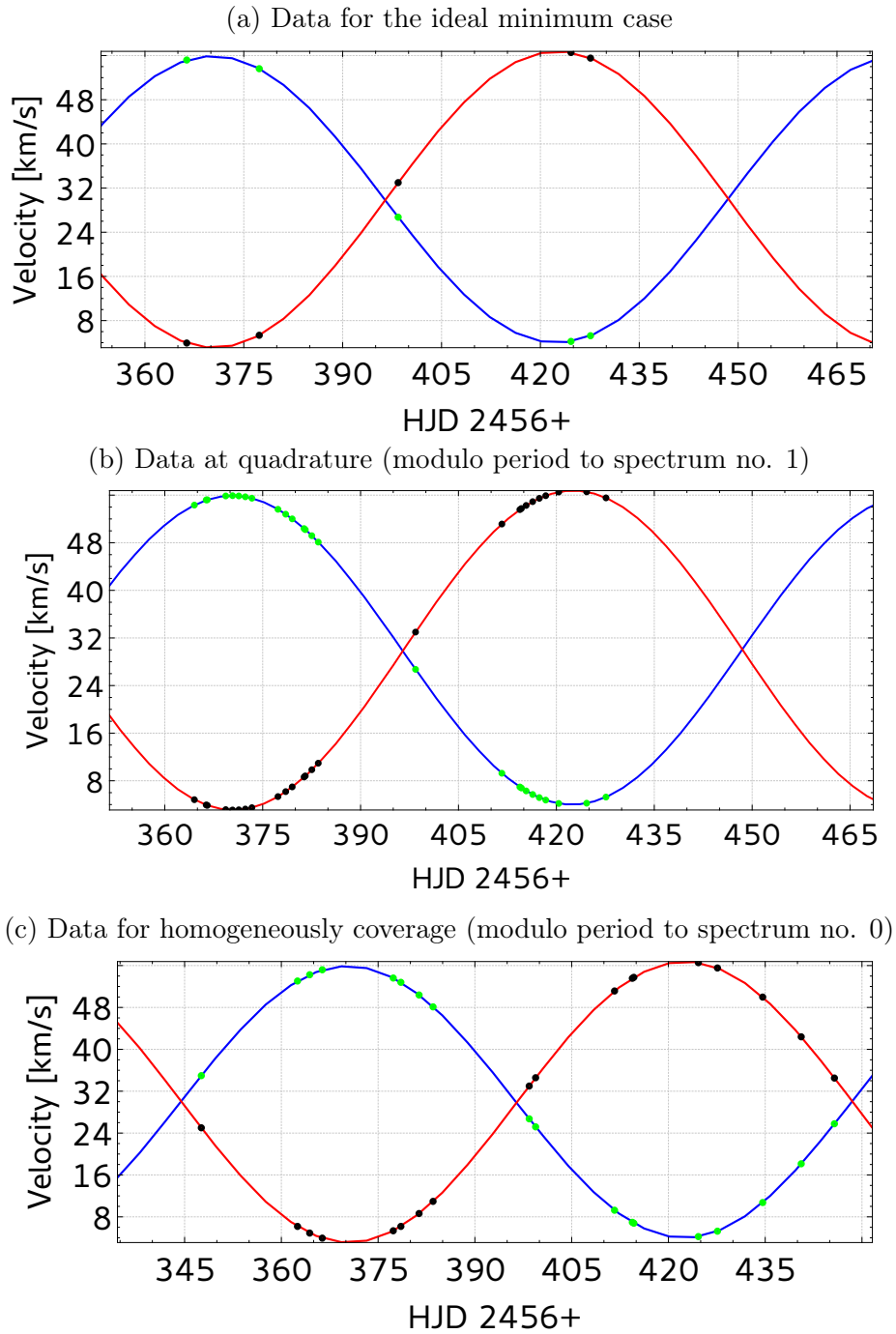


Figure 2.15.: Radial velocities from Tab. 2.2 for the three special cases studied. The blue (red) curve show the primary’s (secondary’s) orbital motion (computed from orbital parameters from Torres et al. (2015)), green (black) dots correspond to the primary (secondary) radial velocity of each spectrum.

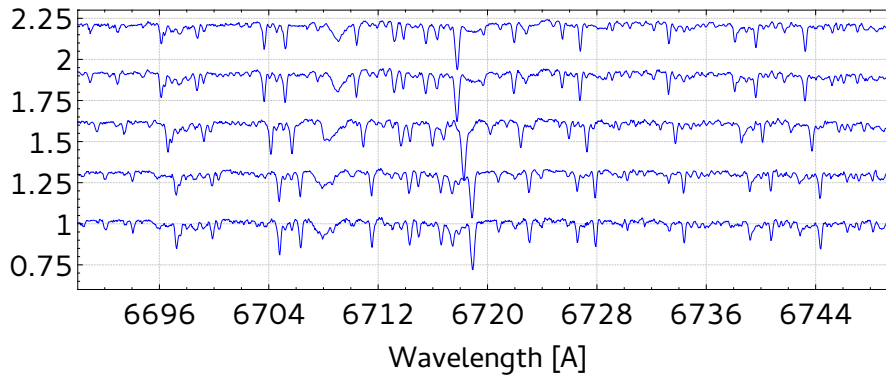


Figure 2.16.: The five spectra from Capella around the Li I 6708 Å line used for our investigations for the minimum ideal case. Spectrum 1 at the bottom, 5 at the top.

Table 2.3.: Data for the non-ideal case at quadrature. We list the time for a single SVD on 4 cores, the residuum r before/after optimisation, the size of the transformation matrix \underline{M} , the number of independent spectra N_{IS} and our quality factor Q_d .

Case	Time (min)	r 10^{-4}	\underline{M} $u \times v$	N_{IS}	Q_d
1	7.7	0.94/0.94	5752×42120	4	-0.021
2	12.4	1.24/0.95	5488×70225	8	-0.078
3	8.4	0.94/0.94	5798×44928	5	-0.018
4	13.2	1.48/1.45	5848×73034	9	-0.096
5	8.6	0.91/0.89	5840×44924	5	-0.018
6	9.7	0.91/0.91	5840×47736	6	-0.013

(b). Spectrum 16 is near conjunction and all the other of the 25 spectra are at quadrature.

We have studied six different cases: (1) The first one uses the spectra 1 to 15 from the first quadrature. (2) The second case is with spectra from both quadratures from 1 to 15 and 18 to 27. (3) The third case uses spectra from 1 to 16, i.e. all spectra from one quadrature, plus an additional spectrum near conjunction. (4) For the fourth case we used all 26 spectra. (5) For the fifth case we use all spectra from the first quadrature and spectrum 22 from the following quadrature. (6) As (5) but with spectrum 16 near conjunction. Since most of the spectra from the same quadrature differ little in their radial velocities, the overdetermination is weak for cases (1) and (2). As shown for the minimum ideal case, the spectrum near conjunction is advantageous to fulfil the criterion of an overdetermined system.

Spectrum 5 has the highest (lowest) RV for component A (B). The next spectra which have an RV difference of at least ≈ 2 km/s are 9, 12 and 15, i.e., these 15 spectra lead to a weakly overdetermined system. Two spectra for the determined case, another two spectra for overdetermination and the rest will help to reduce the noise in the result (case 1). The number of independent spectra, N_{IS} , for each case is listed in Tab. 2.3.

The results shown in Fig. 2.19 show that data sets which prefer particular phase positions and suffer from many non-independent spectra, will degrade the result. This can be seen especially from cases 2 (spectra from both quadratures) and 4 (all spectra). The other cases show a better separation of line pairs which are close together. However, it is visible that the red wings of these lines show smearing towards the continuum. This comes from regions where line-blending is present and the SVD is not able to fully distinguish between

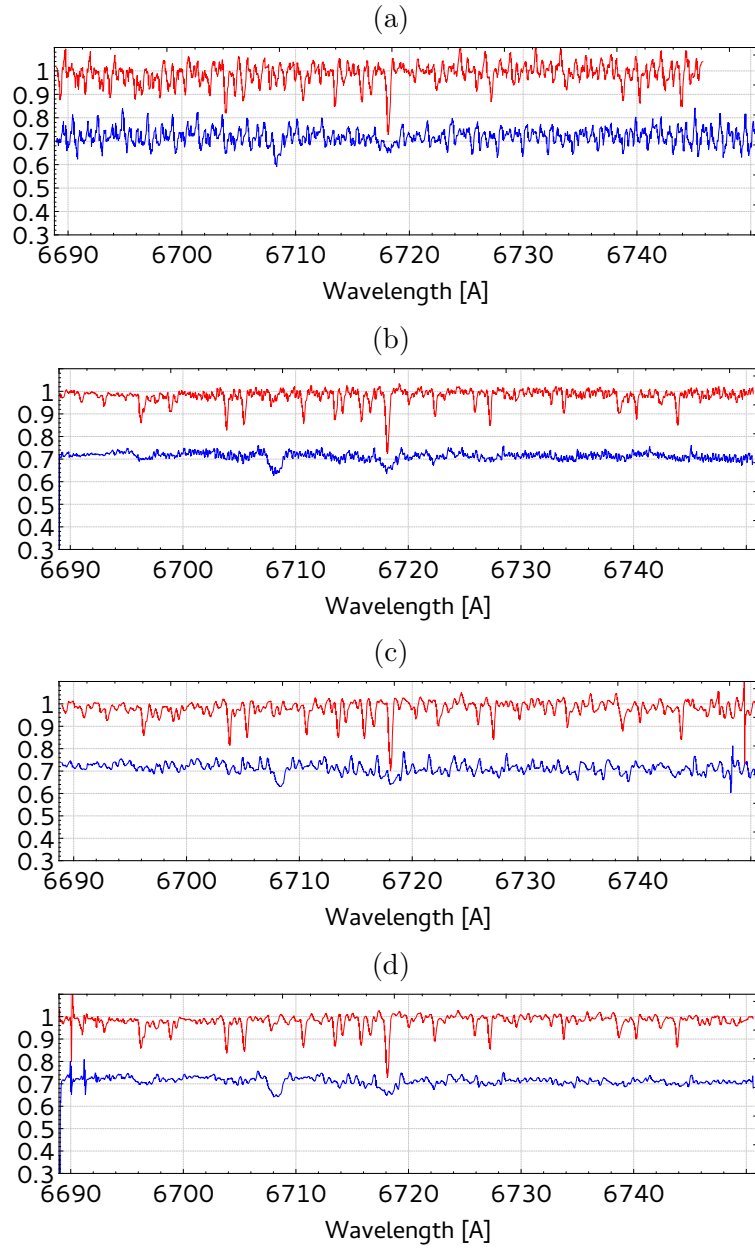


Figure 2.17.: Results from disentangling around the Li I 6708 Å line of Capella from the observations marked in Tab. 2.2. (a): Result for the determined situation with one spectrum per two consecutive quadratures; (b): As top but with an additional spectrum at conjunction, which is the minimal necessary set of required data; (c): Two spectra per two consecutive quadratures. This set yields only a determined system, which can better distinguish between noise and the signal of the components; (d): All five spectra yield a minimum overdetermined system with good noise reduction.

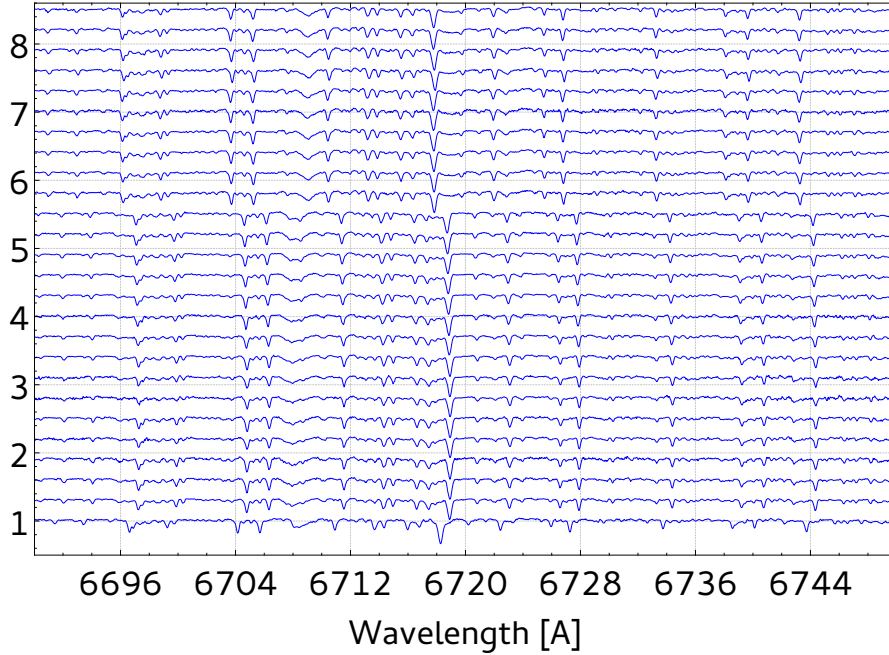


Figure 2.18.: All the spectra of the non-ideal case at quadrature. The spectrum at bottom is spectrum 16 near conjunction and all others are in order as in Tab. 2.2 from bottom to top.

the two components in these regions. This is even worse if data from both quadratures are used since all the information about the line-profile in between is missing. If precise measurements of line profiles and equivalent widths are to be made on the resulting spectra, a good phase coverage is indispensable.

We define a quality factor which relates the number of independent spectra, N_{IS} , to the total number of spectra used by their orbital coverage. Let \widehat{RV} denote the peak-to-peak value of the radial velocity curve, S_{RV} is the two pixel resolution in the velocity space, N_S the number of all spectra and $N_{RS} = N_S - N_{IS}$ is the number of reproductions, thus we define

$$Q_d \equiv N_{IS}/N_{max}(1 - N_{RS}/N_S - N_{RS}/N_{max}), \quad (2.17)$$

where $N_{max} = \widehat{RV}/S_{RV}$ is the maximum number of independent spectra. This factor is at maximum unity as long as redundant measurements are not counted, $N_S \leq N_{max}$. The bracket accounts for a statistical overweight of a specific phase position which leads to a negative Q_d . For the case that independent spectra compensate reproductions, $N_{RS} = N_{IS}$, the factor is zero, i.e., the independent spectra compensate preferred phase positions. We list this factor for all six cases in the last column of Tab. 2.3 and note that for all cases $Q_d < 0$ and case 6 indicates the best result. Moreover, we note that the quality factor is at 6% for the data set of only five spectra ($N_{IS} = 3$) used in Sect. 2.4.1. Hence, this small data set is superior to the larger set used here. This can be seen from a comparison of line-separation, e.g., of the two Fe i lines blue from the strong Ca i $\lambda 6717.68 \text{ \AA}$ in the disentangled spectra of the primary (Fig. 2.19 and Fig. 2.17 (d), $r = 0.83 \cdot 10^{-4}$).

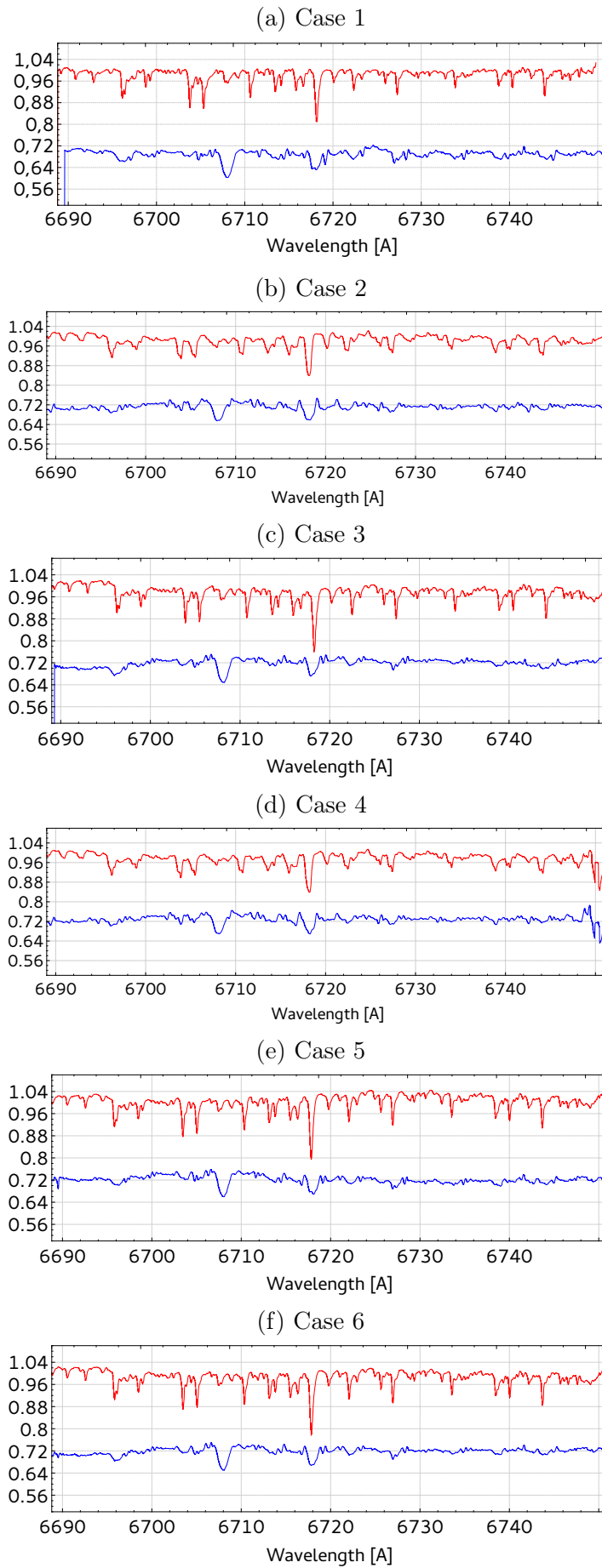


Figure 2.19.: Results for all six cases of the data from quadrature. See text and Tab. 2.3 for details.

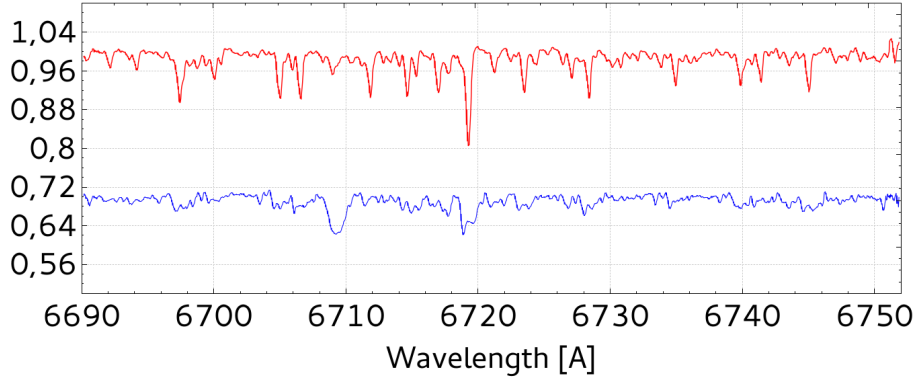


Figure 2.20.: Result of the disentangling of the data marked in the last column of Tab. 2.2.

2.4.3. The realistic ideal case

As shown in the previous two sections, data should be spread homogeneously over at least half the orbital period such that the SVD is able to identify the differential moving contributions. For this case we selected 18 spectra as marked in Tab. 2.2 to get a realistic data set spread over one orbit. The radial velocities are shown in Fig. 2.15c. Unlike the data set at quadrature, these data do not show any strong preference of any particular orbit section. The quality factor Q_d is approximately 20% and indicates much better coverage of the orbit information.

The result for this data is shown in Fig. 2.20, where better defined line-wings are visible when compared to the results from the previous section. Narrow lines are much better separated now.

2.5. Conclusion

Using artificial data, we have shown the applicability of disentangling and of the presented code in particular to a variety of spectroscopic data from SB1 as well as SB2 systems including static lines. Additionally, the application to high-resolution data from Capella shows that with well-sampled small data sets one can achieve good results. Due to the broad and compared to the primary shallow secondary lines, Capella is a very challenging object.

We conclude that the ideal case for observations is given by a set of spectra spread over one period with a difference of two times the spectrum sampling in radial velocities. This criterion is based on the Nyquist two-pixel-resolution. It requires only half of the data as the criterion given by Simon & Sturm (1994), where they suggest one spectra per a single velocity bin. However, our tests with Capella have shown that these data are helpful to reduce noise but they do not significantly contribute to determine the component spectra (increment of overdetermination). Furthermore, the data should not overweigh a specific phase position. The quality factor given by Eq. (2.17) should be used to plan the observations especially when the orbit is already known. We plot this relation in Fig. 2.21 for $N_{max} = 27$ and for different N_S in dependence of N_{IS} . It is $N_S = N_{max}$ for the purple curve and if all 27 spectra are independent, i.e., $N_{IS} = N_S = N_{max}$ it yields an $Q_d = 1$. For the green curve it is $N_S = 20 < N_{max}$, i.e., $Q_d < 1$ even if all observations are independent, $N_{IS} = N_S = 20$.

We also note that all the spectra within the data set need to be of equal quality with

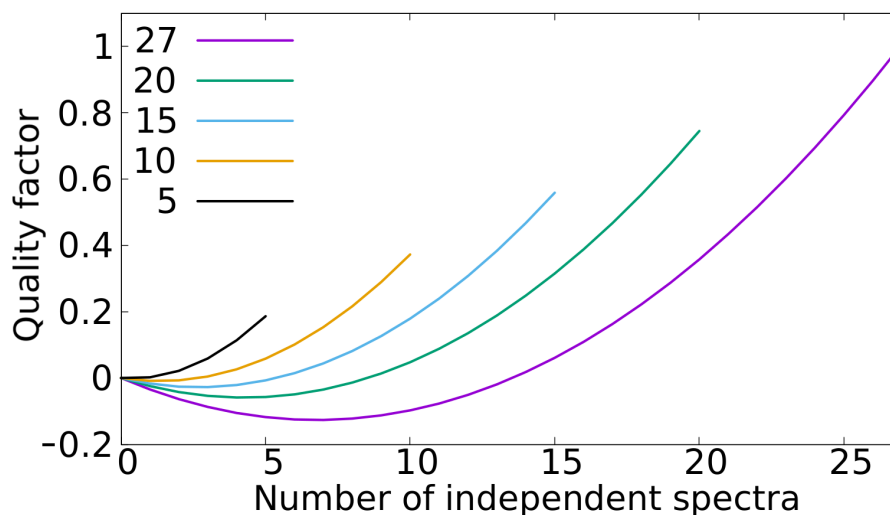


Figure 2.21.: Example of the quality factor in dependence of N_{IS} for $N_{max} = 27$ for different N_S as listed in the graph key.

respect to signal-to-noise and normalisation. A good example is the time-series shown in Fig. 2.18 where all the spectra are nicely normalised and have identical SNR values.

In the case that there is no initial information on the orbital parameters of a system, it is recommended to perform a cross-correlation first to get an estimate for the orbital parameters. The optimisation is then initiated with this orbit which helps to avoid stagnation of the DSA since it should be already in the vicinity of the best fit. However, optimisation of individual RVs instead of orbital parameters, could be preferable in case of presence of a third component or systematics, e.g. in wavelength calibration. The orbital parameters and the corresponding errors are then found by fitting to the optimised RVs.

Furthermore, *Spectangular* is able to disentangle telluric lines variable in time if relative ratios of the line depths are given. These ratios need to be measured for each of the spectra. As long as line depths can be measured from unblended lines, it is also possible to account for line-depth variability of the component spectra itself. This will also make it possible to use spectra from an eclipse if a light curve of the system is available. This could help to get better phase coverage. However, if the uncertainties of the flux ratios are high and eclipse is short compared to the orbital period, they can be rejected.

However, despite parallel computing, SVD is a time-consuming procedure. This is underlined when optimisation needs to be performed. Also, the amount of necessary memory is high, since the number of elements to be stored grows quadratically with the spectrum size. Further applications related to time-dependent variability of line-shape rather than depth need to be investigated.

We finally note, that we are working on the implementation of a third non-static component. However, we will not couple this to an equation of orbital motion. Hence, the optimisation will be performed in case of an SB3 system only on the individual RVs.

We will make the code available under the Apache 2.0 licence on github ASAP. This will include the disentangling program *Spectangular* as well as *CroCo* for data preparation. Furthermore, a support page on the www and manuals for both programs will be made available.

<https://github.com/DPSablowski/croco>

<https://github.com/DPSablowski/spectangular>

Acknowledgements

We thank the referee for his constructive comments which helped to improve the content and the readability of this paper.

References

- Bagnuolo, Jr., W. G. & Gies, D. R. 1991, *ApJ*, 376, 266
- Gallenne, A., Pietrzyński, G., Graczyk, D., et al. 2016, *A&A*, 586, A35
- González, J. F. & Levato, H. 2006, *A&A*, 448, 283
- Hadrava, P. 1995, *A&AS*, 114, 393
- Hadrava, P. 1997, *A&AS*, 122
- Hadrava, P., Šlechta, M., & Škoda, P. 2009, *A&A*, 507, 397
- Harmanec, P., Uytterhoeven, K., & Aerts, C. 2004, *A&A*, 422, 1013
- Holmgren, D. E. 2004, in *ASP Conference Series*, Vol. 318, *Spectroscopically and Spatially Resolving the Components of the Close Binary Stars*, ed. R. W. Hilditch, H. Hensberge, & K. Pavlovski, 95–102
- Ilijic, S. 2004, in *ASP Pacific Conference Series*, Vol. 318, *Spectroscopically and Spatially Resolving the Components of the Close Binary Stars*, ed. R. W. Hilditch, H. Hensberge, & K. Pavlovski, 107–110
- Ilijic, S., Hensberge, H., & Pavlovski, K. 2002, *FIZIKA B*, vol. 10, No. 4, p. 357-366, 10, 357
- Ilijic, S., Hensberge, H., Pavlovski, K., & Freyhammer, L. M. 2004, in *Astronomical Society of the Pacific Conference Series*, Vol. 318, *Spectroscopically and Spatially Resolving the Components of the Close Binary Stars*, ed. R. W. Hilditch, H. Hensberge, & K. Pavlovski, 111–113
- Nelder, J. A. & Mead, R. 1965, *The Computer Journal*, 7, 308
- Osterbrock, D. E., Tran, H. D., & Veilleux, S. 1992, *ApJ*, 389, 305
- Pavlovski, K. & Hensberge, H. 2005, *A&A*, 439, 309
- Phillips, G. R. & Eyring, E. M. 1988, *Analytical Chemistry*, 60, 738
- Sanderson, C. 2010, *Australia*
- Simon, K. P. & Sturm, E. 1994, *A&A*, 281, 286
- Strassmeier, K. G., Weber, M., Granzer, T., et al. 2014, *AN*, 335, 904
- Torres, G., Claret, A., Pavlovski, K., & Dotter, A. 2015, *ApJ*, 807, 26
- Weber, M., Granzer, T., Strassmeier, K. G., & Woche, M. 2008, in *Proc. SPIE*, Vol. 7019, 70190L–70190L–12
- Weber, M. & Strassmeier, K. G. 2011, *A&A*, 531, A89

3. Spectangular: Disentangling variable Spectra (Manuscript II)

Daniel P. Sablowski¹, Silva Järvinen¹ and Michael Weber¹

Astronomy & Astrophysics, 2019, accepted

1: Leibniz Institute for Astrophysics Potsdam (AIP), An der Sternwarte 16, 14482 Potsdam, Germany

Abstract

Spectangular is a GUI based software package written in C++ designed for spectral disentangling on the wavelength scale. The code disentangles spectra of SB1 and SB2 systems and can now also be used also for spectra showing variability. In this work, effects of variability caused by telluric lines, line profile, and continuum flux are being investigated. Also shown is the disentangling on spectra from an artificial eclipsing binary. It is now possible to optimize on the flux ratios of each spectrum, making the disentangling a technique for extracting photometric information from spectroscopic observations usually provided by additional photometry. Furthermore, we make some comments about changes to the code since it was first published.

3.1. Introduction

Spectral disentangling is a technique used to separate component spectra of spectroscopic binaries (SB2) and multiples. In comparison to separation techniques (e.g. Bagnuolo, 1983) which need prior knowledge of radial velocities (RVs), it only requires a set of spectra spread over the orbital period at known times. This is made possible by connecting the disentangling algorithm with a global optimization algorithm, working on the orbital elements (or individual radial velocities). The solution is a disentangled spectrum of the two components (in the case of SB2), which can be interpreted as an extracted average of all individual single spectra from the observations. In addition, the orbital elements best fitting the data are derived. However, many binaries are variable and the influence of the changes in spectral behaviour on the output of the disentangling needs to be investigated and properly understood.

This paper is dedicated to a discussion of procedures dealing with different kinds of variability and how to extract the information of variability from the result of the disentanglement.

Spectangular was published by Sablowski & Weber (2017) (hereafter Paper I); we point the reader to that article for the description of the program. The first application to highly variable Wolf-Rayet (WR) stars was presented in Shenar et al. (2017). **Spectangular** is based on singular value decomposition (SVD) and runs in a downhill simplex optimization. It differs significantly from another disentangling code, KOREL, which works in the frequency domain. Application of KOREL to variable spectra was presented in Harmanec et al. (2004) and Hadrava et al. (2009).

In Sect. 3.2 we summarize improvements to the code since it was first published. The SVD leads to results of least-squares nature, hence random variability will be strongly

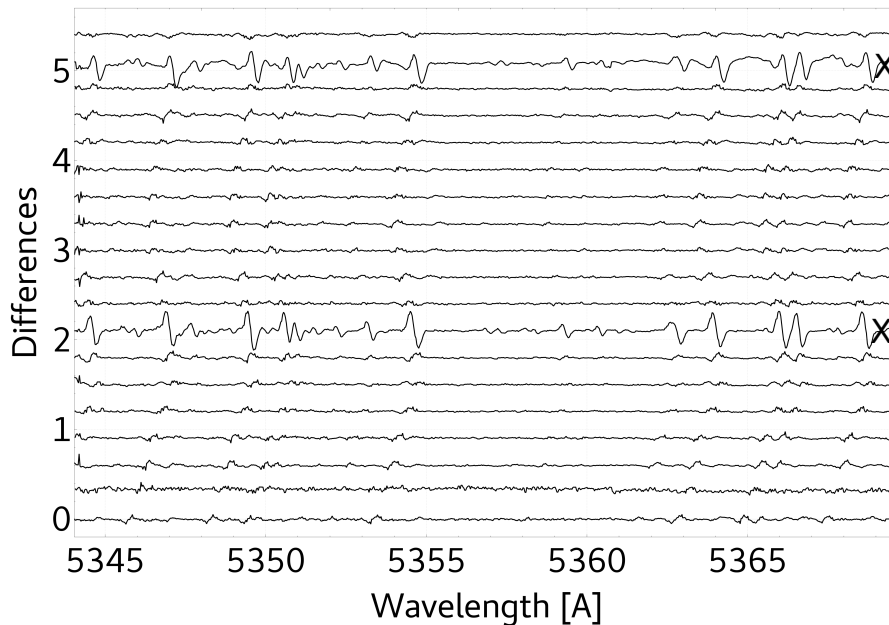


Figure 3.1.: Example of the differences between the disentangled spectra and 19 individual observations of Capella. The optimization has failed to find proper RV values for two spectra, which can be seen by the strong differences (black crosses). The spectra have been shifted by 0.3 on the y-axis for better visibility.

suppressed in the disentangled spectra. This is shown in Sect. 3.2.2, where we discuss the influence and a way to correct for telluric features by two-step disentangling. Section 3.3 concentrates on specific cases of variability of stellar origin. Section 3.3.2 shows a way to search for periodic line profile variations using the information in the spectrum-to-spectrum differences between the disentangled spectra and the individual observations. Continuum brightening has an effect on the extracted spectra as well, and is discussed in Sect.

3.3.3. Since eclipsing binaries play an important role in stellar physics, Sect. 3.3.4 is dedicated to demonstrating the applicability of the code to such systems. Surface spots imprint another periodic variability on the line profiles, and we investigate it in Sect. 3.3.5. The main results are summarized in Sect. 3.4.

3.2. Code modifications and procedures

For data preparation, we use the in-house developed code `CroCo` (see also Paper I). This code is used to re-sample the observations on a logarithmic wavelength scale and for two-dimensional cross-correlation (CC). The step size b_{log} for the logarithmic wavelength scale was set to be the minimum step size, $b_{log} = \min[b_{log,i}]$, $i = 0 \dots n$, found from all n spectra (multiplied by a user-set increment), where $b_{log,i}$, $i = 0 \dots n$. is the minimum step size in spectrum i (which usually refers to the bluest pixel). Since that can lead to a step size of zero length (data errors), we implemented a user definable step size. Alternatively, the median, $b_{log} = \text{median}[b_{log,i}]$, or the arithmetic mean, $b_{log} = \text{mean}[b_{log,i}]$, of all these minimum step sizes can be used. Furthermore, the interpolation of the spectra can now be performed with a cubed spline (or a linear) interpolation. The spline can lead to better approximations at larger step sizes, corresponding to less data on the logarithmic scale.

When running the optimization with `Spectangular` on the individual RVs, there can be

spectra for which the code does not find proper RVs. There can be three reasons for this: (i) the large number of variables, e.g. if 10 spectra of a SB2 system are used, we already have to deal with 20 variables; (ii) the noise level within the spectra; (iii) the selection of the initial values. In the case of non-convergence of optimization the disentangling fails. The SVD extracts a mean spectrum, best adapted to the data by the determined RVs. If the RVs are not realistic, the disentangled spectra are distorted. It is necessary now to identify these spectra and either remove them from the data set or change the initial RVs. This is usually best done during a first optimization run. The code writes some statistical information of the residual spectra (sum, mean, square sum) into a file (diffstatisic.dat) that can be used to identify the worst offenders. However, in most cases they can already be identified by visual inspection of the plotted differences in the GUI window. These differences are calculated by shifting the disentangled spectra by the determined RVs of each observation and subtracting these shifted disentangled spectra from the observations. As an example, we show the differences for such a case in Fig.3.1 where we can clearly identify two spectra with outlying RVs. User interaction is likely to be necessary.

A further way to increase the convergence to the global minimum is to change the transformation coefficients of the optimizer (see Paper I). Barton & Ivey (1991), among others, found that a higher value of the contraction coefficient (e.g. 0.75 instead of 0.5) can be advantageous. This leads to a slower contraction of the simplex and an increase in the possibility to escape from local minima.

The program can also be run without the GUI, in a cluster environment for example. Only some minor changes need to be made in the source code, which are described in the manual of the software.¹

3.2.1. Handling broad wavelength ranges

Since SVD is very time consuming, `Spectangular` is used in narrow wavelength ranges. In high-resolution spectroscopy, however, we have spectra with data points of the order of 100 000. Therefore, we have implemented a routine in `CroCo` to create whole data sequences. This routine creates several short re-sampled spectrum pieces written in separate files. From our experience with echelle spectra, it can be advantageous to constrain the spectrum pieces by the length of a spectral order. This prevents problems rising from order merging. The advantage of using echelle orders separately is also known from two-dimensional cross-correlation (see e.g. Zucker et al., 2003). Furthermore, for example in the case of hot stars, long pieces of pure continuum can be excluded since the disentangling relies on shifts of spectral lines.

In `Spectangular`, we implemented a function to disentangle such a sequence. To achieve this, the code needs a criterion to stop the optimization and to continue with the next wavelength range. The criterion for the optimization algorithm is the summed squares of differences, r , between the disentangled spectra and the observations (see Fig. 2.1). After each iteration of the optimization, the mean m and the standard deviation s of the simplex are calculated (see Paper I). At the end of an optimization run, the simplex has contracted to a small region around a single point. In that case, m (and s) do not change any more from one iteration to the next. This stage is defined here as stagnation of the optimization. When this stage is reached, the re-initiation function implemented will re-initiate the optimization. Hence, a complete optimization needs multiple re-initiations of the simplex. The end of the whole optimization is reached if the optimization stagnates and the minimal r corresponds to the initial parameter set. The auto-stop function implemented will stop

¹www.dpsablowski.wordpress.com/disentangling

the optimizer if that stage is reached. In the case where a sequence is specified, the code will load the next data set and start again with the optimization procedure.

3.2.2. Influence and correction of telluric lines

The tellurics can be removed by using the differences between the disentangled spectra and observations. An example is shown in Fig. 3.2 using the H α region of Capella. The telluric absorption appears as emission in the residuals (black = observation - RV-shifted disentangled spectra). Here, we use a spline to reproduce these features and correct the individual observations by that spline. In the same figure the uncorrected spectrum (blue) and the spectrum corrected from terrestrial absorption (purple) are shown. To avoid removing any variability by fitting the differences, special care should be taken in the line profiles under consideration to make sure that only known terrestrial lines were fitted and removed. To identify these lines we used the HITRAN data base (Gordon et al., 2017). However, when the disentanglement is repeated on these cleaned spectra we did not observe any differences between the resulting line profiles. This is due to the strong variability of the terrestrial line strengths from spectrum to spectrum (in many spectra they are hardly visible) such that their influence is negligible.

To support this statement, we show in Fig. 3.3 a zoomed-in image of an overplot of disentangled H α profiles of the primary of Capella (G8III). The purple line is the result from the cleaned spectrum and the blue from the raw spectrum. The black line at the bottom shows the difference between these two profiles. Hence, such a telluric-check (TC) should always be performed to prevent any influence on the disentangled profile from tellurics.

If these lines do not show such a strong variability (also in the case of the strong terrestrial O2 absorption bands) the procedure will fail. In this case, a more classical approach is necessary (by observed tellurics within a spectrum of a hot star or simulated spectrum) to remove these lines before the disentangling is performed.

In addition, a third static component can be taken into account by the code. However, this can further complicate the optimization and will increase the time for computation significantly. Finally, for all of these procedures to work, it is necessary to use non-heliocentric corrected spectra. Otherwise, we have to deal with a third moving and variable component.

3.2.3. Signal-to-noise ratio and flux ratio

A major advantage of the disentanglement (especially in contrast to simple separation methods) is the enhancement of the S/N in the resulting spectra (see Table 1 in Paper I). However, for this to work the data has to be of equal quality in the sense of S/N and normalization. Assuming that this is fulfilled by the measurements, the S/N in the results can be estimated by simple statistics,

$$SNR_{A,B} = SNR f_{A,B} \sqrt{N}, \quad (3.1)$$

where N is the number of observations,

$$f_{A,B} = \begin{cases} k/(1+k) & \text{for component A} \\ 1/(1+k) & \text{for component B} \end{cases} \quad (3.2)$$

the strengths of component A and B in normalized spectra ($f_A + f_B \equiv 1$), $SNR_{A,B}$ the estimated S/N of the disentangled spectra for component A and B, and k is the flux-ratio. Hence, to conserve the S/N of the observations, at least $N = 1/\min[f_{A,B}^2]$ spectra are

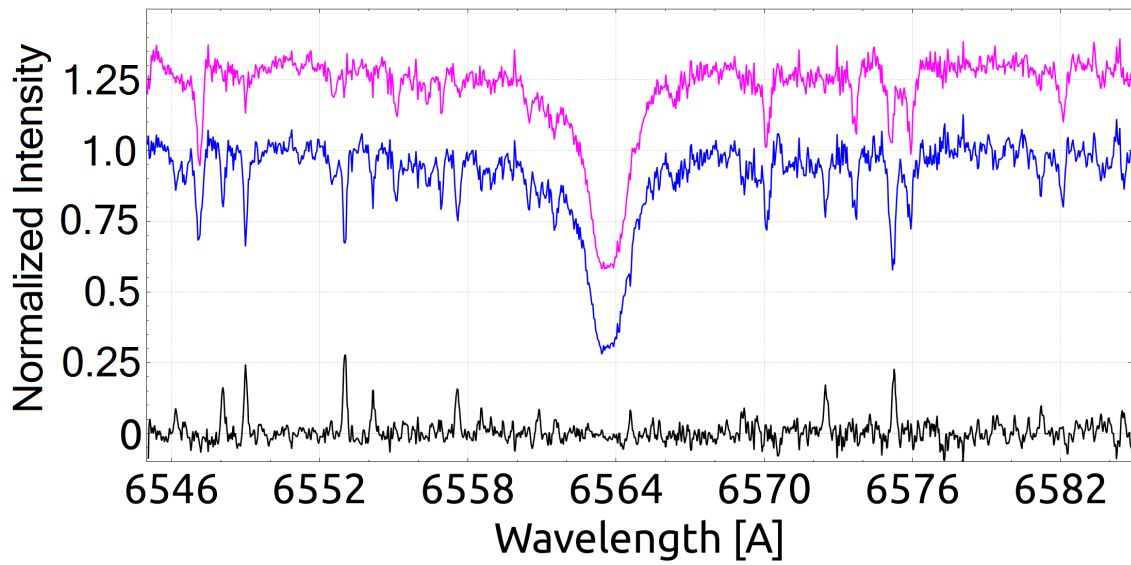


Figure 3.2.: Example of the remaining differences (black at bottom) from the disentanglement around the $H\alpha$ region used to remove the terrestrial absorption from the observation (blue at 1.0) to get a cleaned spectrum (purple, shifted to 1.25 for better visibility).

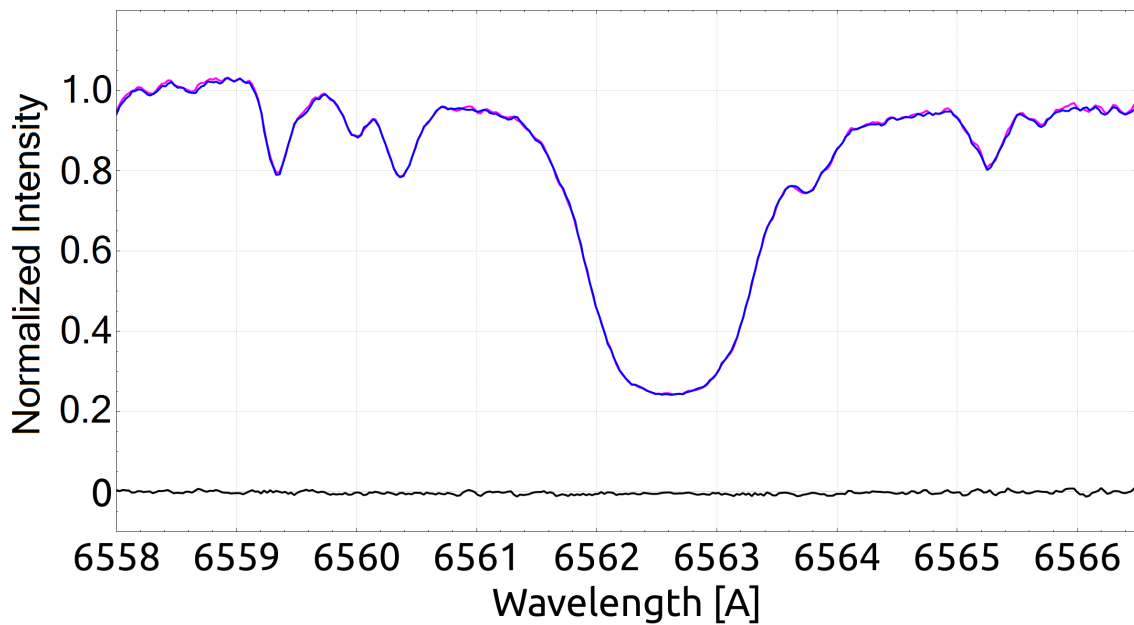


Figure 3.3.: Zoomed-in image of the disentangled $H\alpha$ profile of the primary of Capella when using spectra cleaned from terrestrial (purple) and non-cleaned (blue). Black is the difference between the two profiles.

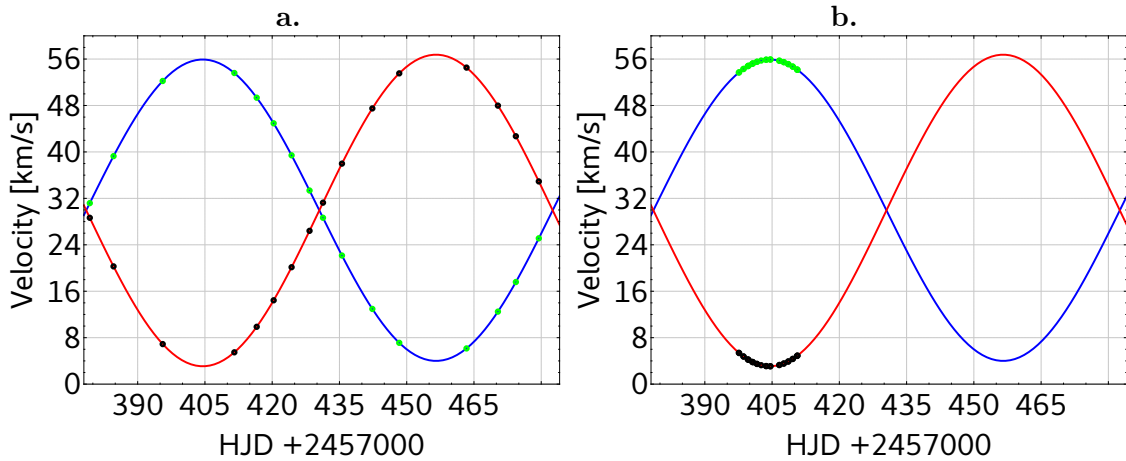


Figure 3.4.: **a:** Data set 1 (see text) spread over the whole orbital period to be used for disentangling. **b:** Data set 2 (see text) at orbital quadrature spread over the rotation period of the secondary used for rotational modulated line profile analysis.

required. For example, if $k = 1$ the two components have identical strength, $f_B = f_A = 0.5$, and at least $N = 4$ spectra are required to maintain the S/N in the disentangled spectra.

3.3. Disentangling variable spectra

3.3.1. General remarks

As stated in the previous section, the disentanglement results in a spectrum of each component which can be interpreted as an extracted mean from the individual composite observations. Hence, there are two general ways to investigate variability. First, the differences between the disentangled spectra and the individual observations (O-D) are affected by variability such as non-periodic line profile variability and telluric features with large variations from observation to observation. This variability can be reconstructed within the O-D spectra, and in the case of telluric lines corrected for in the observations (see Sect. 3.2.2). This approach is applied to periodic line variability in Sect. 3.3.2. Second, if one component can be treated as stable compared to a more variable component, the disentangled spectrum of that stable component can be subtracted from the individual observations. This will result in a time series of individual spectra of the variable component and makes more detailed line-profile analysis possible. This approach is used in Sect. 3.3.5.

However, especially in active binaries or systems with complex temporal changes, both components may show variability. Hence, the line-profile analysis need to be performed in the rest frame of the star of interest. Therefore, computing line moments, the interval of integration needs to be shifted according to the orbital motion of the component. The subtraction algorithm implemented uses the final RVs to shift the disentangled spectrum to be subtracted and, according to user preference, can also shift the resulting time series by the RVs of the non-subtracted component. This results in a time series of spectra with no (or constant) shift with respect to the rest frame.

In that context, in some binaries where the orbital period differs significantly from the rotational period, the following procedure may be applied if rotational effects (e.g. surface spots) are in the focus. Let us consider a binary with components A and B. The orbital period is P and the periods of rotation for the primary and secondary are $P_A = P$ and

Table 3.1.: Extracted period of pulsation for artificial SB2 data with one pulsating component. The extracted period corresponds to units of the orbital period (value to calculate the artificial data was six).

A_{pul} [km s ⁻¹]	A_{pul} % $v \sin(i)$	Extracted pulsations	Standard error
5	25	6.009	0.011
2	10	5.976	0.017
1	5	6.027	0.036
0.5	2.5	6.138	0.048

$P_B \ll P_A$, respectively. The spectra of the components can only be extracted if the orbital motion is well covered by observations at different orbital phases. For the analysis of the line profiles, however, it is advantageous to use spectra in quadrature (maximum separation of the two components in RVs). If we are interested in rotationally modulated effects of component B, two data sets are necessary, one set that covers the orbital period P (set 1, see Fig. 3.4a) and another set that covers the period of rotation of component B (set 2, see Fig. 3.4b), preferably around quadrature.

For rotation modulated analysis of the line profile of the secondary, the spectra of the components are disentangled by the use of data set 1 (data spread over orbital period) first. The disentangled spectra can then be used as templates to perform a two-dimensional CC with the spectra of set 2 covering the rotational period of component B. The obtained RVs from the CC can be used to subtract the disentangled spectrum of component A from data set 2. This method is applied in Sect. 3.3.5 to artificial data to create surface temperature maps.

3.3.2. Radial pulsations

As an example of a binary with a pulsating component, we generated 20 artificial SB2 spectra of a non-variable sharp-lined component ($v \sin i = 5 \text{ km s}^{-1}$) and a periodic pulsating (change in FWHM of the lines) broad-lined ($v \sin i = 20 \text{ km s}^{-1}$) component with different amplitudes of the pulsation and a S/N of 50. The period of pulsation was one-sixth of the orbital phase and we used a Mizar-like orbit to generate the data (see Behr et al., 2011).

The resulting spectra of the disentangling for this artificial data is shown in Fig. 3.5. Purple is a composite spectrum at orbital phase 0.05, blue is the disentangled mean spectrum of the pulsating component, and green shows the disentangled spectrum of the non-pulsating component (we note the strong noise suppression in the disentangled spectra). To detect the variability, we subtract the disentangled spectra from the composite spectra and summed up the differences over wavelength for each spectrum. These differences versus orbital phase are plotted in Fig. 3.6a (crosses) for the data with 2 km s^{-1} pulsational amplitude. The green curve is a sinusoidal fit to the data. Extracted periods of the pulsation are summarized in Table 3.1. Columns 1 and 2 list the amplitude of the pulsation in km s^{-1} and in per cent of the rotational velocity of the pulsating star (20 km s^{-1}), respectively. The extracted periods are inverse periods of the pulsation in fraction of the orbital period, that is, number of pulsation within the orbital period. As mentioned earlier, this value was set to six. The standard error results from a sin-fit to the data in least-squares minimization. As expected, the error increases with decreasing amplitude.

In the case of a similar variability of the two components, the differences can be used in an equivalent way. However, in any case, the signatures in these differences need to be

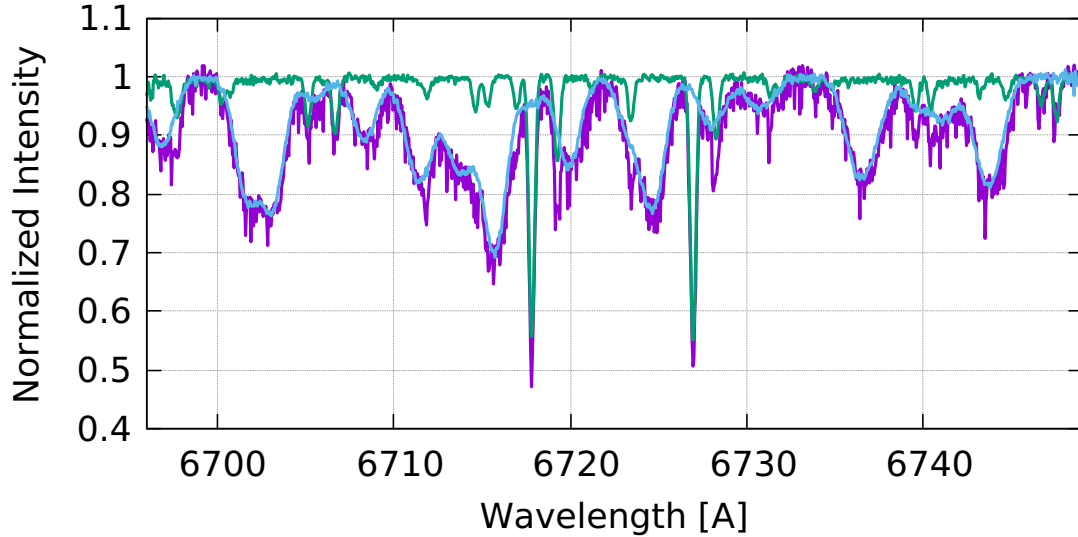


Figure 3.5.: Result from disentangling of the artificial SB2 with a broad-lined pulsating component. Blue: Disentangled mean spectrum of the pulsating component. Green: Same, but for the non-pulsating component. Purple: Artificial spectrum at orbital phase 0.05 for comparison.

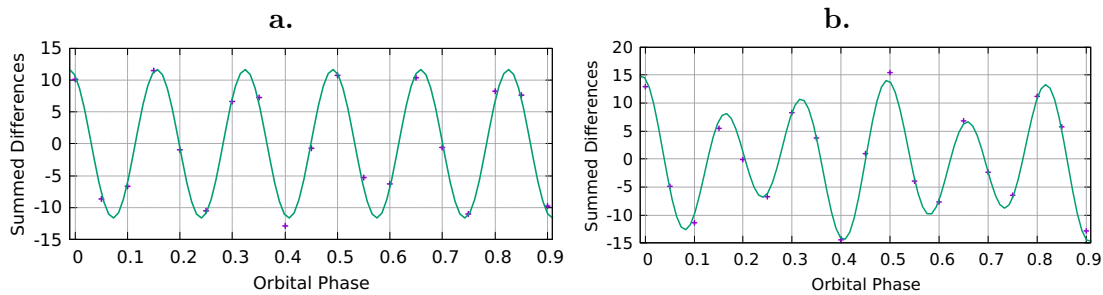


Figure 3.6.: Summed differences (crosses) and sin-fit (green line) vs orbital phase for the artificial SB2 data. **a:** With primary amplitude of pulsation of 2 km s^{-1} to extract the pulsational period. **b:** With amplitude of pulsation for the primary and secondary of 2 km s^{-1} and 1 km s^{-1} , respectively.

tracked in RVs in order to identify the component to which the variability is connected. With a single pulsation period of both components, we show the differences and a combined fit in Fig. 3.6b. Again, we used six pulsations within the orbital phase for the primary; we used four for the secondary, instead of none as in previous test set-up. The extracted number of pulsations from the differences for the primary and secondary are 6.028 ± 0.022 and 3.799 ± 0.054 , respectively.

3.3.3. Flares

In contrast to the variability by pulsations, flares are sudden non-periodic events. Hence, it is important to investigate how such changes in the spectra influence the extracted mean spectrum from the disentanglement. A flare also imprints changes in the radiated continuum of the star (e.g. Machado et al., 1980).

We generated a series of spectra (orbital elements, as used in Sect. 3.3.2) with one showing a flare as a brightening of the continuum of one component. This can be seen by a

significant increase in the squared summed differences for this spectrum. Such an event introduces a slope to the continuum of the resulting spectra. This slope further depends on the spectrum on which the flare event happened. We show three examples in Fig. 3.7. The disentangled spectra at the bottom correspond to a series of 20 spectra and the flare happened in spectrum number 5 (phase 0.25). In the middle graph, the flare happened in spectrum number 9 (phase 0.50) and at the top in spectrum number 15 (phase 0.75). If in the second data set (flare at phase 0.50) we exchange the flare spectrum with that at phase 0.00, we obtain the same result. Therefore, the tilt does not depend on the order of the spectra within the data set, but within the orbital motion. This also shows the importance of equally well-normalized spectra. Hence, in the case of strongly slanted disentangled spectra, the normalization of the observations needs to be checked and corrected.

The resulting slope cannot be corrected by re-normalization of the disentangled spectra by division of the continuum. It is a difference of fluxes between the two components. Therefore, the slope has to be corrected by subtracting the difference. Let the continuum be $c(\lambda)$ and the disentangled spectrum $s(\lambda)$. The disentangled spectra are assumed to be calculated with the correct flux ratio. The corrected disentangled spectrum is then

$$s'(\lambda) = s(\lambda) - (c(\lambda) - 1). \quad (3.3)$$

To conserve the flux in the resulting disentangled spectra, the continuum function $c(\lambda)$ is the same for both spectra,

$$s'_{A,B}(\lambda) = s(\lambda) \mp (c(\lambda) - 1), \quad (3.4)$$

such that what is subtracted in A has to be added to B.

As long as the difference in normalization is constant with wavelength, the slope is represented by a linear function, $c(\lambda) = m\lambda + b$. Hence, we have implemented a function to correct the resulting disentangled spectra from such a tilt.

3.3.4. Eclipsing binaries

The contribution of star A and B to the flux of the composite spectra of an eclipsing binary varies with phase. Hence, it is necessary for the disentanglement of such systems to know the light curve and a sufficient model.

3.3.4.1. Light curve model

In this section a simple spherical geometry model (no eccentricity and limb darkening) to generate a light curve is used to demonstrate how the disentanglement behaves with the data.

Let r be the vector distance between the two stars. From classical mechanics (see e.g. Goldstein et al., 2000) we know that the distance to the centre of mass is

$$\begin{aligned} r_A &= -r M_B / (M_A + M_B) = -r \beta_A, \\ r_B &= r M_A / (M_A + M_B) = r \beta_B. \end{aligned} \quad (3.5)$$

The geometry of the situation is sketched in Fig. 3.8a. From that figure we find

$$\begin{aligned} x &= r \sin(\phi), \quad y = r \cos(i) \cos(\phi), \\ \text{and } z &= r \sin(i) \cos(\phi), \end{aligned} \quad (3.6)$$

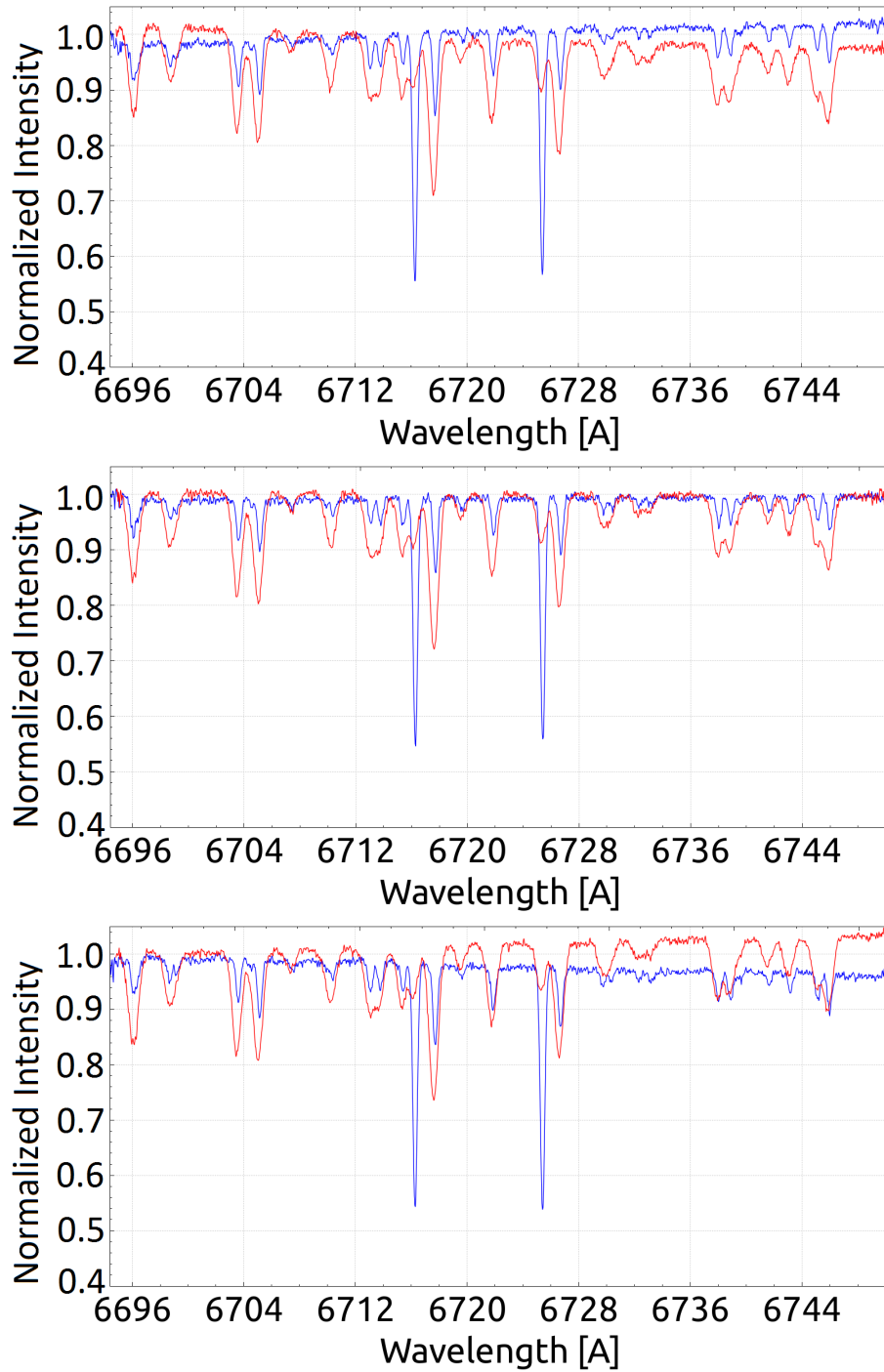


Figure 3.7.: Results from disentangled artificial spectra (time series of 20) showing a flare at phase 0.25 (bottom), 0.50 (centre), and 0.75 (top). The sign of the slope introduced in the results changes at the middle of such an equidistantly spread data set.

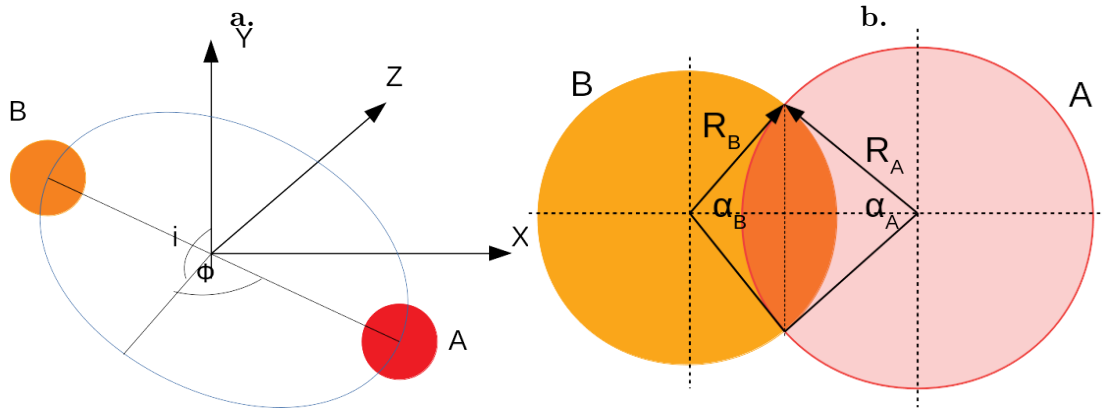


Figure 3.8.: **a:** Geometry of the binary model with spherical stars and orbit. The z -axis points towards the observer. **b:** Circle cross section of the stars during eclipse.

Quantity	value	Quantity	value
M_A	0.60	M_B	0.10
R_A	0.50	R_B	0.40
L_A	0.60	L_B	0.20
r	0.9	i	85 deg
n	5.00		

Table 3.2: Model values for the light curve shown in Fig. 3.9.

where ϕ is the phase angle and i the inclination. Substituting this into Eq. (3.5) yields the coordinates in the centre-of-mass system

$$x_A = -r \sin(\phi) \beta_A, \quad y_A = -r \cos(i) \cos(\phi) \beta_A, \quad (3.7)$$

$$\text{and } z_A = -r \sin(i) \cos(\phi) \beta_A$$

for component A and

$$x_B = r \sin(\phi) \beta_B, \quad y_B = r \cos(i) \cos(\phi) \beta_B, \quad (3.8)$$

$$\text{and } z_B = -r \sin(i) \cos(\phi) \beta_B$$

for component B. In addition, let be R_A and R_B the radii, A_A and A_B the unobscured areas, and L_A and L_B the luminosities of the stars. Hence, we can write

$$I(\phi) = n(L_A A_A / R_A^2 + L_B A_B / R_B^2) / (4\pi) \quad (3.9)$$

$$= I_A(\phi) + I_B(\phi)$$

for the brightness of the system, where n is a constant to normalize the light curve. The projected distance between the two stars in the plane perpendicular to the line of sight is

$$d_{AB} = \sqrt{(x_B - x_A)^2 + (y_B - y_A)^2}. \quad (3.10)$$

During an eclipse, the common cross section of the stars is described by circular segments of area $dA_{A,B} = R_{A,B}^2 (\alpha_{A,B} - \sin \alpha_{A,B}) / 2$. The angle α , the segment extents (see Fig. 3.8b), is found by the projected distance in the plane perpendicular to the line of sight by $\alpha_{A,B} = 2 \arccos[(\mp(R_B^2 - R_A^2) + d_{AB}^2) / (2R_{A,B} d_{AB})]$. For example, in the case that $z_A > z_B$ star A is in front of star B. Hence the areas are $A_A = \pi R_A^2$ and $A_B = \pi R_B^2 - (dA_A + dA_B)$.

An example light curve of this simple model is shown in Fig. 3.9.

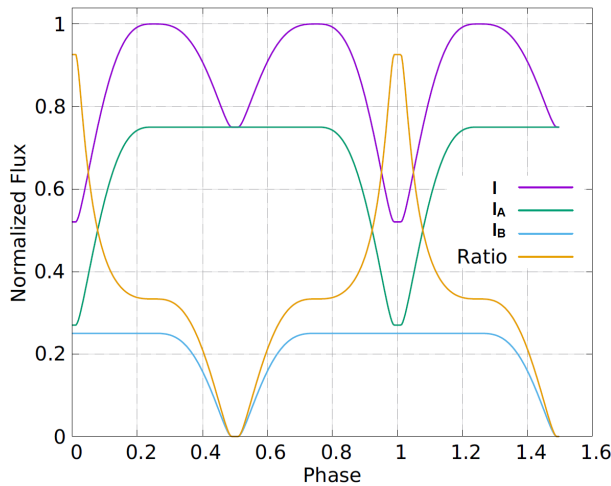


Figure 3.9: Example of a light curve modelled by the equations presented here. I is the (measurable) combined brightness of I_A and I_B and Ratio is the brightness (or light) ratio between the two components, I_B/I_A .

3.3.4.2. Artificial eclipsing binary

The values used for the model are summarized in Table 3.3.4.1. This model was used to create a set of 20 spectra equidistantly spread over the orbital phase (orbital parameters as in Sect. 3.3.2). From an observational point, the disentangling of such a set of data would be possible by using the spectra at phase 0.5 since the system shows a total eclipse; that is, only the signal of the primary is present in that spectrum. In wide eclipsing binaries, the disentangling can be performed with out-of-eclipse spectra. However, in close binaries the eclipses can cover a significant fraction of the orbital period (see Fig. 3.9). Furthermore, it is necessary for the disentanglement to use spectra that cover the orbital motion well. In the case of close binaries, spectra taken only out-of-eclipse may be insufficient for the disentangling. Hence, it is necessary to also use the spectra obtained during eclipse.

The light ratio necessary for the disentangling can be computed by

$$k(\phi) = 1/f_B(\phi) - 1 = f_A(\phi)/[1 - f_A(\phi)], \quad (3.11)$$

where

$$f_A(\phi) = I_A(\phi)/I(\phi) \text{ and } f_B(\phi) = I_B(\phi)/I(\phi). \quad (3.12)$$

From Sect. 3.3.3, we expect to see a slope in the continuum of the disentangled spectra if the phase dependent flux ratios are not taken into account. The result, where a constant ratio of $k(\phi) = 1$ is applied to this data, is shown in Fig. 3.10a. The appearance of such a slope gives a hint either to a variable flux of the system or to incorrect normalization. Therefore, if the case of bad normalization can be excluded, additional data (photometry) is necessary for a proper disentangling of the system. On the other hand, if we can exclude variability of the system, the normalization of the data needs to be corrected. In the same figure, we can also see that the line strengths are wrong (negative values for component A). It is therefore obvious that using the correct flux ratio (also if constant) is of major importance for any further analysis of the disentangled spectra.

The disentangled spectra with the correct flux ratios are shown in Fig. 3.10b together with the template spectra for both stars. They are shifted by 0.1 for A and -0.1 for B in the vertical direction for better visibility. In addition to the excellent agreement between disentangled spectra and templates, we can again see the enhancement of the signal-to-noise ratio.

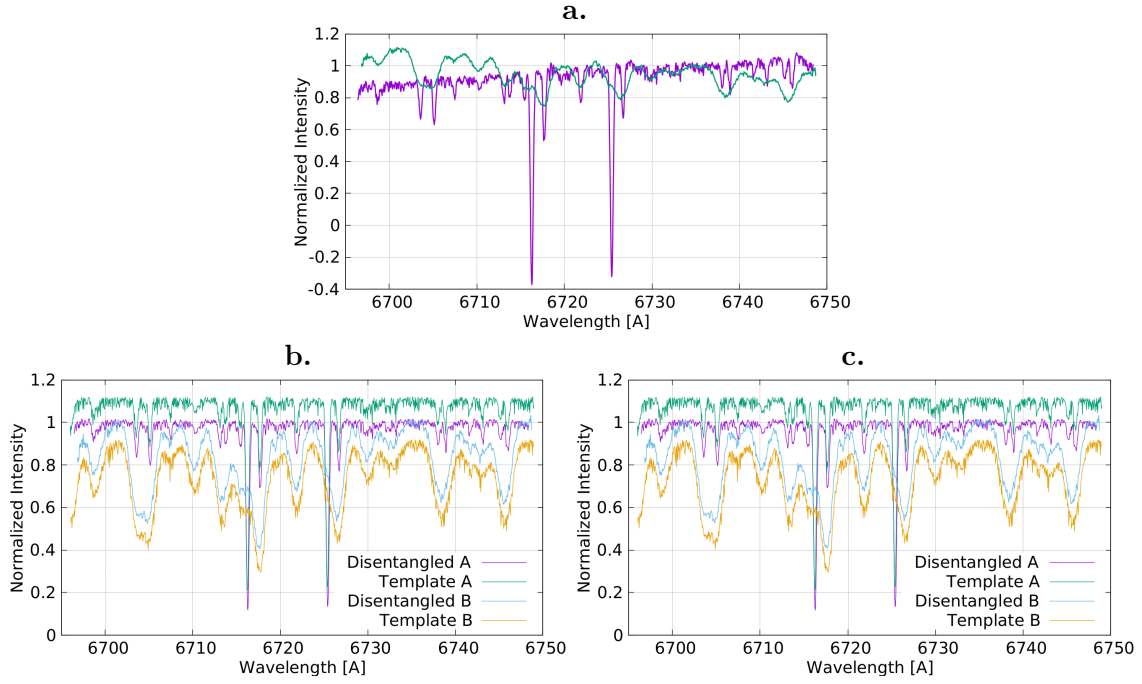


Figure 3.10.: Disentangled spectra of the artificial eclipsing binary. **a:** Phase dependent flux ratio has not been taken into account. As shown in the previous section, this introduces a slope to the disentangled spectra. Shown are the sharp-lined component A (purple) and B (green). **b:** Disentangled spectra with correct flux ratios used in comparison with the templates used to create the set of spectra. Template A and B are shifted by 0.1 and -0.1 on the y-axis for visibility. **c:** As **b**, but with flux ratios from the optimization with start ratio of $k = 1$ for all phases.

3.3.4.3. Extracting the flux ratios

As mentioned in Sect. 3.3.4.2, knowing the flux ratios is essential for disentanglement in eclipsing systems. Since the extracted spectrum is the mean spectrum present in all observations, the differences can also be used to optimize the flux ratio $k(\phi)$ in each spectrum. Therefore, we implemented a downhill simplex algorithm to find these flux ratios. This algorithm provides two targets for minimization: the summed squares of differences (as used for the spectral disentanglement) and the summed square of the slopes, $\sqrt{m_A^2 + m_B^2}$, of linear functions, $c_{A,B} = m_{A,B}\lambda + b_{A,B}$, representing the continuum of each disentangled spectrum (see also Sect. 3.3.3). The latter turned out, in our test runs, to be too insensitive. However, the minimization of the residuals with an initial constant $k(\phi) = 1$ lead to flux ratios plotted in Fig. 3.11 together with the values from the model, as described in Sect. 3.3.4.1. Furthermore, the resulting spectra in comparison with the templates used to create the data set are shown in Fig. 3.10c.

Knowing the correct RVs was assumed for that test run. They can be obtained, in a first step, by a CC. An iterative procedure alternating the optimization on flux ratios and RVs (or orbital elements) could be applied to such data with no information from photometry.

Knowing the flux ratio is not sufficient to get the light curve. However, if $I(\phi)$ is measured we can obtain the individual brightnesses of the two components from Eqs. (3.12). Therefore, the combination with photometry yields more information about the system, i.e. a separate light curve for both components.

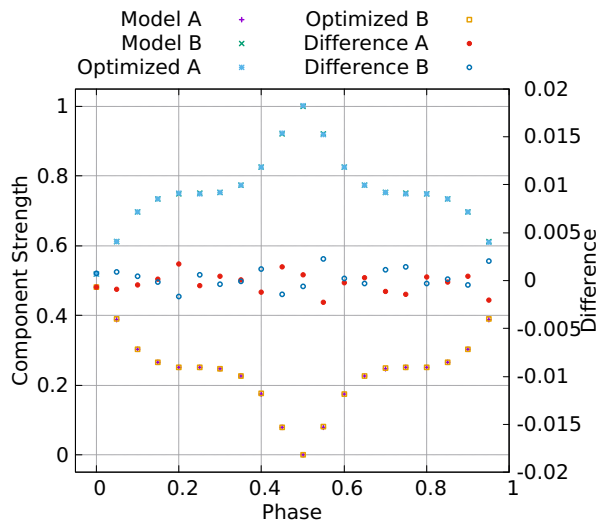


Figure 3.11: Comparison of the component strengths f_A and f_B from the model used (Model A and B) and after optimization (Optimized A and B) on flux ratio $k(\phi)$, Eq. 3.11, of the two components A and B. Also plotted are the differences of Model - Optimized.

3.3.5. Surface spots

Spots appear in the line-profiles as moving ‘bumps’ following the rotation of the star. Therefore, we constructed an artificial spotted star (A; see Fig. 3.15a) and calculated the spectra from this configuration (the same orbital parameters as used in Sect. 3.3.2) with two spot features at almost opposite sides of the stellar surface, and put that star in orbit with an unspotted component (B). The resulting line-profiles are illustrated in Fig. 3.12a. Then the spectra are disentangled and the component (B) without spots is subtracted from the composite spectra using the RVs from a CC with the disentangled spectra as templates (see Fig. 3.12b). The resulting spectra of component A are corrected for RV to have the line-profile at the same wavelength, which ideally would be the rest wavelength. Especially when subtracting a sharp-lined component, small mismatches between the disentangled and the composite cause artefacts in the resulting ‘cleaned’ spectrum. These artefacts are visible in Fig. 3.12b and follow the relative motion in wavelength between the two components. We show in Fig. 3.13a a zoom-in of a small spectral region where we subtracted the sharp-lined component and plot over the input spectrum at phase 0.05. In Fig. 3.13b is a further zoom-in of a single line, but for the whole spectral sequence to visualize the line-profile asymmetries caused by the spots.

As shown in Sect. 3.3.2, the residual spectra can be used to analyse variability and to search for periods. Therefore, we plot the summed differences in Fig. 3.14 together with a fit accounting for two spots crossing the surface. Hence, these differences can be used to search for the rotation period of the stars.

The stellar surface of the test star is reconstructed using the *iMap* code (for details, see Carroll et al., 2007, 2009, 2012). We note here that the two-temperature approximation used in the input map (Fig. 3.15a) is not ideal for inversions as shown in Fig. 3.15b, but is sufficient to investigate the differences between ideal spectra and disentangled spectra.

In the resulting maps shown in Fig. 3.15, we can see a small suppression of the temperature contrast. In the case of the ideal data (Fig. 3.15b), the coolest temperature recovered is 5121 K when the input value is 5000 K, whereas the disentangled spectra lead to the coolest temperature of 5210 K, see Fig. 3.15c. The shift of the spectra to the same wavelength after subtracting one component is crucial to recover the temperatures. This is demonstrated by the map in Fig. 3.15d. This map was computed from spectra shifted by RVs obtained from a CC without fitting the maximum of the CC function, but by manually adjusting the spectra. Therefore, this data set shows residual RV shifts between the spectra of the order

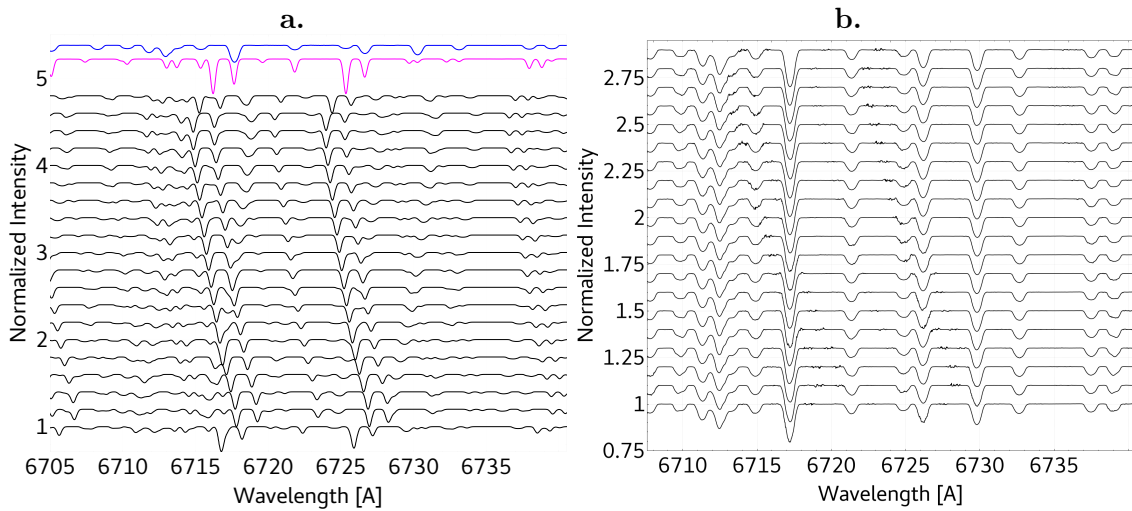


Figure 3.12.: **a:** Artificial data set of SB2 system with a spot on the broad-lined component. Disentangled profiles renormalized to one are shown at the top in blue and purple. **b:** The disentangled spectrum of the sharp-lined component is subtracted from the composite spectra and the result is shifted to the rest wavelength. These spectra were used to create the Doppler maps shown in Fig. 3.15c.

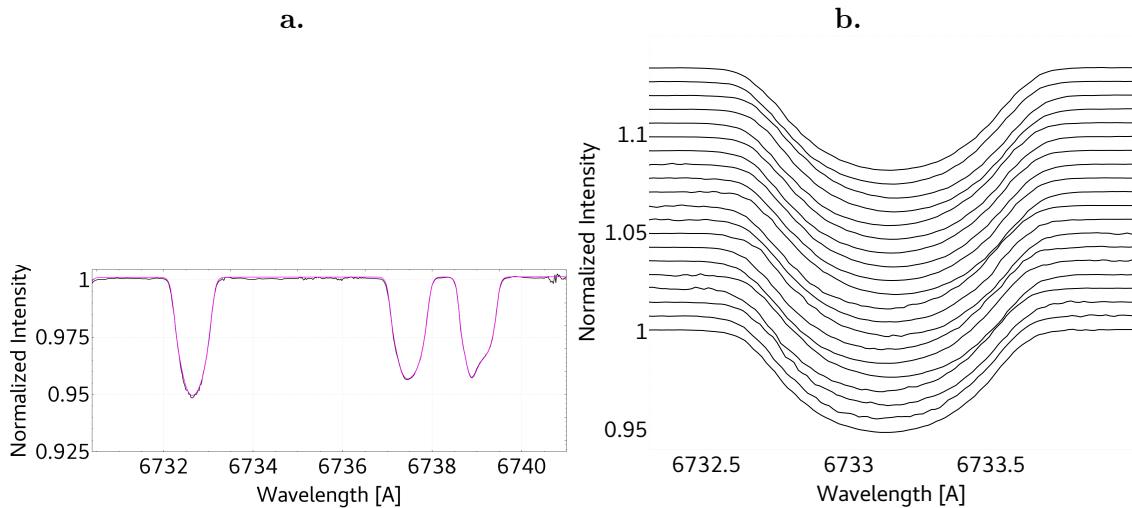


Figure 3.13.: **a:** Zoom-in of three lines of the spectra shown in Fig. 3.12b. Purple is the input spectra of the spotted component, black the spectra of the spotted component after subtraction of the disentangled non-spotted component used to calculate the map in Fig. 3.15c. **b:** Zoom-in of the leftmost line from panel a, but for all the spectra used to construct the maps.

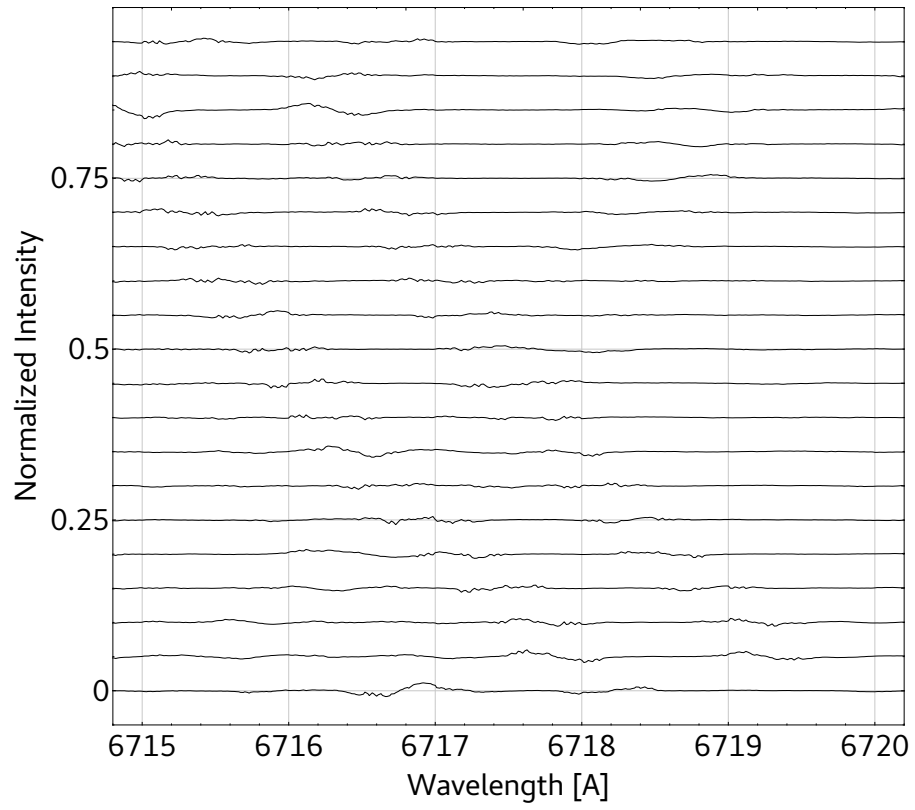


Figure 3.14.: Summed differences of the residuals from the artificial spot data (crosses). The solid line is a fit for two spots.

Table 3.3.: Orbital elements for the eclipsing binary after iterative optimization on orbital elements and flux ratios. Runs 2 and 4 belong to flux ratio optimization (orbital elements from previous optimization were used). Ideal values used to create the data are listed in Col. 1 and initial values for the optimization in Col. 2. The period P , systemic velocity γ , and time of periastron passage T_0 were fixed.

Elements	ideal	initial	Run 1	Run 3
P (days)	20.54	20.54	20.54	20.54
e	0.037	0.350	0.538	0.538
K_A km s $^{-1}$	68.6	40.0	69.0	68.8
K_B km s $^{-1}$	67.0	40.0	67.8	67.5
γ km s $^{-1}$	-5.6	-5.6	-5.6	-5.6
T_0 (days) 2436+	997	997	997	997
ω (deg)	106.16	80.0	106.35	106.14

of 0.05 pix (≈ 100 m/s), and the obtained coolest temperature (5257 K) is a bit higher than in the case of ideal RV shifts. We also note the presence of a very weak spot at phase 0.5 in these maps. We attribute the remaining difference in temperature to residuals of the subtraction and re-sampling effects.

Regardless of the small discrepancies in temperatures, the resulting Doppler maps in Fig. 3.15 display the two spots at correct positions. Hence, a proper analysis of a systematic suppression of the temperature difference of spot and stellar surface can be performed for an individual target.

3.3.6. Impact of variability on disentangling results

Since the actual errors on the orbital parameters determined by the optimization algorithm depend, in first order, on the data quality and the amplitude of the variability, only an idea of their magnitudes can be given here. In addition, in real-world applications we most likely have to deal with a combination of multiple effects.

In the case of eclipsing binaries, it was suggested in Sect. 3.3.4.3 to iteratively alter the optimization on flux ratios and orbital elements. To demonstrate this procedure, the data from Sect. 3.3.4.2 were used with an initial assumption of a constant flux ratio of $k(\phi) = 1$ and the orbital parameters as listed in Table 3.3 second column. The orbital elements used to create the data are listed in the first column. In runs 2 and 4 the flux ratios were optimized (no change in the orbital elements, therefore not listed). Since the period is often well determined, we fixed the period, P , and the time of periastron passage, T_0 . In addition, for this example we fixed the systemic velocity γ as well.

From the results, we can see that the amplitudes K_A and K_B show the strongest deviation. These amplitudes may be extremely important when it comes to the determination of masses. However, the overall solution after four runs is close to the ideal values especially if we consider the resolution of 1.7 km s $^{-1}$ of the spectra. Another optimization run on the orbital elements did not improved the results further.

Nevertheless, as was shown in Fig. 3.10a, incorrect flux ratios have a strong influence on the extracted spectra in the sense of line-depth. Hence, if spectral analyses are to be performed on the disentangled spectra, special care needs to be taken on the flux ratios.

The final precision of the flux ratios should be limited primarily by the S/N of the spectra. The RMS (between the ideal flux ratio used to create the data and the value obtained from optimization) from the 20 flux ratios obtained in Sect. 3.3.4.3 and obtained

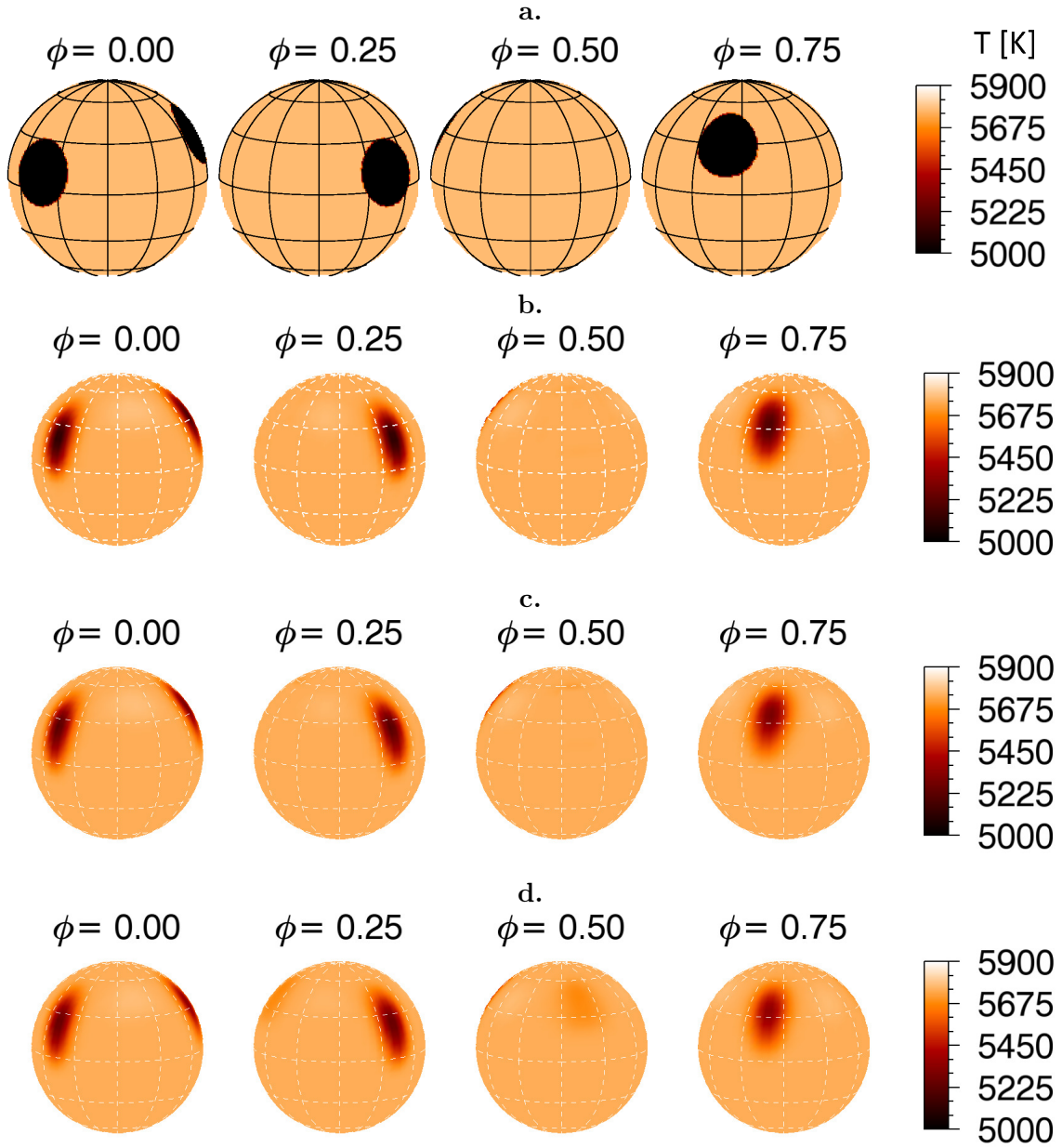


Figure 3.15.: **a:** Input map used to create artificial spot spectra shown from four different viewing angles. **b:** Surface map using the artificial spot spectra without a second component. **c:** Resulting surface map from the artificial spot data after subtraction of disentangled spectra. **d:** As **c**, but with RVs to align the spectra obtained by CC and manually adjusted.

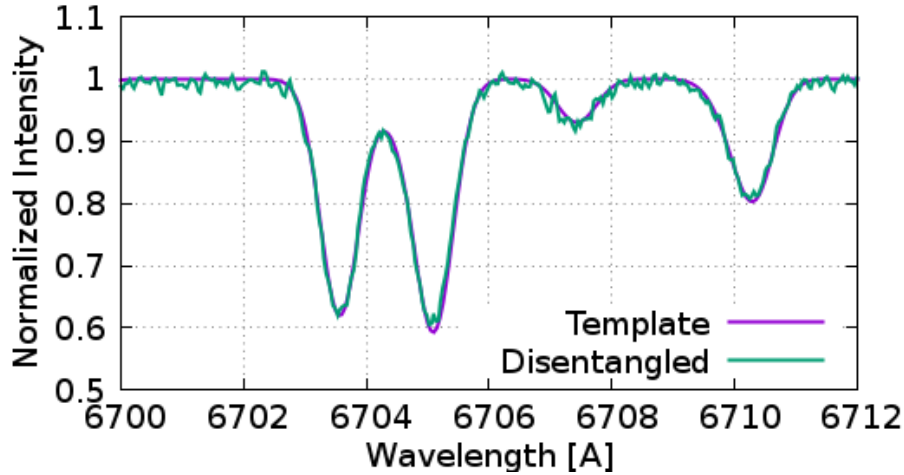


Figure 3.16.: Comparison of line-profiles between disentangled and template spectra using the same data as in Sect. 3.3.3.

here from run 4 are 0.0047 and 0.0046, respectively. From the 20 spectra with a S/N of 50, we get $1/(50\sqrt{20}) = 0.0045$, which is in agreement with the RMS values of the obtained flux ratios.

From this result we expect that a single flare spectrum has a negligible effect on the orbital parameters as long as the number of spectra without flares is much higher (>10). Figure 3.16 shows a comparison of the line-profiles of the disentangled spectrum with the template spectrum (as in Sect. 3.3.3). Noise was added to the template to construct the data. The continuum was a factor of three brighter during the flare. However, the disentangled spectra agrees very well with the template.

In Fig. 3.17 the equivalent width (EW) of the line at 6721.73\AA from Fig. 3.13 is shown for the data used in Sect. 3.3.5. The ideal data (green x) shows the periodicity as reflected by the summed differences shown in Fig. 3.14. Therefore, both measures could be used to search for the stellar rotation periods. Purple crosses are used for the EW of the line after the disentangled spectrum of the constant component was subtracted (Fig. 3.13b) and the blue square is the data point from the disentangled spectrum of the spotted component. The subtraction leads to scatter of the data points of the EW measured.

3.4. Summary

In this work we have investigated the influence of variability on the result of the disentanglement. This included tellurics and their correction, pulsations (change in FWHM of the lines), flare as continuum brightening, eclipsing binaries, and line profile variation by surface spots. The correction of tellurics is possible as long as they are highly variable in strength. In this case, the telluric features are strongly suppressed in the disentangled spectra. Furthermore, these lines can be reconstructed for each observation from the residuals by a spline approximation. In the case of strong variability from spectrum to spectrum, these tellurics do not influence the disentangled spectra.

We note that the code cannot account for wavelength dependent flux ratios. Therefore, temperature effects introducing a slope-change of the continuum may further affect the disentangling. However, since the wavelength ranges are rather narrow (in high-resolution spectra) the slope in such a small region may have a negligible effect. Since it also depends

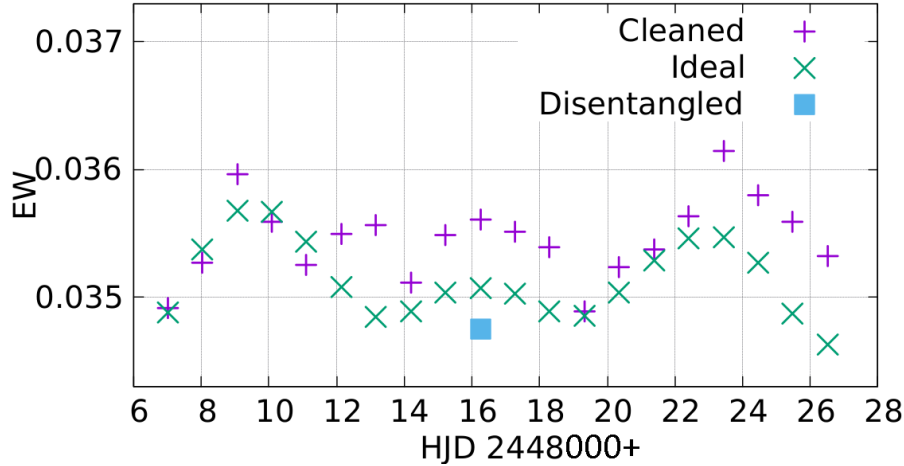


Figure 3.17.: Equivalent width (EW) [\AA] of the line at 6721.73\AA from the artificial spot data of Sect.3.3.5. Green is for the ideal single-component spectra used to create the composite binary spectra, purple (cleaned) is after subtraction of the constant component spectrum from the disentanglement, and the blue square corresponds to the EW of that line of the disentangled spectrum.

on the temperature difference, object-specific simulations should be performed. A wavelength dependent flux ratio to account for such effects (also from irradiation/heating) is a subject of future improvements to the code.

Two ways of treating the variability were presented. First, the analysis of the residuals between the disentangled spectra and the individual observations can be used to search for periodic changes. Second, subtracting the disentangled spectra of component B, for example, from the observations leads to a time series of spectra for component A which can be used for further analysis (e.g. Doppler imaging, line-profile analysis).

We also presented the disentanglement on artificial data of an eclipsing binary. The code allows the user to specify the contribution to the flux of each spectrum and each component. As long as the correct flux ratios are used, the disentangled spectra are in very good agreement with the templates. Furthermore, it is now possible to run an optimization on the flux ratios of each observed spectrum. This now provides a method for obtaining information about the flux variation. However, we assumed that the radial velocities are known, for example by an initial cross-correlation. Hence, the disentangling approach is also usable to extract light curve information from the spectroscopic data. A combination of light curve modelling, spectral disentangling, and solving for the flux ratios is beyond of the scope of this paper.

Additionally, since the flux-ratios are not bound to a light curve model, the variation in the brightness of the system from other effects (e.g. non-symmetry) can be accounted for. In this context, we note that a simultaneous solution from light- and RV-curves can help to further improve the results, for example as was implemented in FOTEL (see Hadrava, 1990). This coupling is beyond of the scope of this work and is the subject of future improvements of the code. Effects like apsidal motion, non-constant orbital period, and a third spectroscopically non-visible component can be taken into account by optimizing on the individual RVs.

Doppler imaging showed a sensitivity of the temperature difference between spot and surface to the alignment in wavelength of the time series of the spectra. This was shown by a comparison between maps obtained with spectra shifted by RVs from a CC and a

manually fine adjustment compared to a map with the RVs computed to create the binary spectra. In a science application a fit of the CC maximum can be performed, and an iterative approach using line profiles derived from the Doppler maps as templates can be used to improve the accuracy of the RVs.

It is important to note that a proper normalization of the observations needs to be done with special care. This can introduce a slope to the resulting spectra. This is also true for a brightening of the continuum (e.g. by flares). Therefore, we finally note that a proper preparation of the data for the disentanglement is of great importance since it can mimic variability.

Acknowledgements

We thank the anonymous referee for the constructive comments that helped to improve the content and readability of this work. Based in part on data obtained with the STELLA robotic telescope in Tenerife, an AIP facility jointly operated by AIP and IAC.

References

- Bagnuolo, Jr., W. G. 1983, *Lowell Observatory Bulletin*, 9, 180
- Barton, R. R. & Ivey, J. S. 1991, in *1991 Winter Simulation Conference Proceedings.*, 945–953
- Behr, B. B., Cenko, A. T., Hajian, A. R., et al. 2011, *AJ*, 142, 6
- Carroll, T. A., Kopf, M., Ilyin, I., & Strassmeier, K. G. 2007, *AN*, 328, 1043
- Carroll, T. A., Kopf, M., Strassmeier, K. G., & Ilyin, I. 2009, in *IAU Symposium*, ed. K. G. Strassmeier, A. G. Kosovichev, & J. E. Beckman, Vol. 259, 633
- Carroll, T. A., Strassmeier, K. G., Rice, J. B., & Künstler, A. 2012, *A&A*, 548, A95
- Goldstein, H., Poole, C., & Safko J. 2000, *Classical Mechanics*, 3rd edn. (Addison Wesley), p. 71
- Gordon, I., Rothman, L., Hill, C., et al. 2017, *JQSRT*, 203, 3, *hITRAN2016 Special Issue*
- Hadrava, P. 1990, *Contributions of the Astronomical Observatory Skalnaté Pleso*, 20, 23
- Hadrava, P., Slechta, M., & Skoda, P. 2009, *A&A*, 507, 397
- Harmanec, P., Uytterhoeven, K., & Aerts, C. 2004, *A&A*, 422, 1013
- Machado, M. E., Avrett, E. H., Vernazza, J. E., & Noyes, R. W. 1980, *ApJ*, 242, 336
- Sablowski, D. P. & Weber, M. 2017, *A&A*, 597, A125
- Shenar, T., Richardson, N. D., Sablowski, D. P., et al. 2017, *A&A*, 598, A85
- Zucker, S., Mazeh, T., Santos, N. C., Udry, S., & Mayor, M. 2003, *A&A*, 404, 775

4. Carbon $^{12}\text{C}/^{13}\text{C}$ isotope ratio of α Aurigae revised (Manuscript III)

Daniel P. Sablowski¹, Silva Järvinen¹, Ilya Ilyin¹ and Klaus G. Strassmeier¹

Astronomy & Astrophysics Letter to the Editor, 2019, Volume 622, L11

1: Leibniz Institute for Astrophysics Potsdam (AIP), An der Sternwarte 16, 14482 Potsdam, Germany

Abstract

Context. Capella (α Aur) is one of the few binaries in the sky with two cool giant stars. With spectral types of G8III and G0III, the two components appear at different but distinct stages in their evolution. The G0 secondary star is a Hertzsprung-gap giant, and the G8 primary star is thought to be a clump giant.

Aims. We present a new measure of the carbon $^{12}\text{C}/^{13}\text{C}$ isotope ratio of the primary component of Capella using high-resolution $R \approx 250\,000$ spectra obtained with the Potsdam Echelle Polarimetric and Spectroscopic Instrument (PEPSI) with both the Vatican Advanced Technology Telescope (VATT) and the Large Binocular Telescope (LBT).

Methods. Signal-to-noise ratios of up to 2700 were obtained by averaging nightly spectra. These average spectra were used to disentangle the two binary components. The isotope ratio was derived with the use of spectrum synthesis from the CN lines at 8004 Å.

Results. We found that the $^{12}\text{C}/^{13}\text{C}$ ratio of the primary component of Capella is 17.8 ± 1.9 . Our measurement precision is now primarily limited by the spectral-line data and by the grid-step size of the model atmospheres rather than the data. The separated spectrum of the secondary component does not show distinguishable ^{12}CN and ^{13}CN lines because of its $v \sin i$ and higher temperature.

Conclusions. Our new $^{12}\text{C}/^{13}\text{C}$ value is significantly lower than the previous value of 27 ± 4 but now agrees better with the recent model prediction of 18.8 - 20.7.

4.1. Introduction

Stellar evolution is traced by the carbon, nitrogen, and oxygen (CNO) abundances and in particular by the $^{12}\text{C}/^{13}\text{C}$ isotope ratio (e.g., Shetrone, 2003; Szigeti et al., 2018) because carbon will be converted into nitrogen and the $^{12}\text{C}/^{13}\text{C}$ ratio will be lowered over time by molecular CN processing (also CH and CO). The surface CNO abundances also depend on the mixing process (e.g., Mikolaitis et al., 2012; Drazdauskas et al., 2016; Tautvaisiene et al., 2016). Moreover, the abundances are not only scaled to stellar nucleosynthesis and mixing, but also to galactic chemical evolution (e.g., Allende Prieto et al., 2004). Previous isotopic measurements (see Lambert & Ries, 1981) indicate that the observed ratios for G–K giants are of about 10–30, which is significantly lower than the presumed initial (solar) ratio of about 90 (e.g. Anders & Grevesse, 1989; Jewitt et al., 1997). Iben (1964) made the first theoretical prediction of evolution-caused changes of isotopic abundances from the reaction $^{12}\text{C}(p, \gamma)^{13}\text{N}(\beta^+, \nu)^{13}\text{C}(p, \gamma)^{14}\text{N}$ (see also Henry et al., 2000; Yang et al., 2017). This reaction suggested that ^{13}C may be used as an observational tracer once it has been

brought up to the surface. It is therefore expected that the $^{12}\text{C}/^{13}\text{C}$ ratio decreases and the $^{14}\text{N}/^{15}\text{N}$ ratio increases with stellar evolution.

The main mechanism of mixing in stars is convection. However, stars that gain their energy primarily by the CNO cycle have radiative envelopes during their main-sequence lifetime. After hydrogen is exhausted in the core, the core contracts and heats the outer layers. A convection layer at the surface of the star is established and penetrates the interior of the star. As a consequence, processed material is transported to the surface. This is referred to as the first dredge-up, and it occurs when the star enters the Hertzsprung gap in the Hertzsprung-Russel (HR) diagram. To explain stars with very low carbon isotope ratios, additional mixing processes were suggested. The rotation-induced meridional mixing can provide mixing even during the main-sequence phase (e.g., Drazdauskas et al., 2016; Charbonnel, C. & Lagarde, N., 2010). The nature of further mixing processes after the first dredge-up is still debated (e.g., Pinsonneault, 1997; Charbonnel, C. & Lagarde, N., 2010; Hedrosa et al., 2013).

In this respect, binaries are of special interest because they consist of stars of the same age and same initial chemical composition that are at different stages of evolution, if of different mass. Capella (G8III is the primary and G0III is the secondary) is such a system. The combination of the many pieces known for this system, in particular stellar masses at the sub-percent precision (Weber & Strassmeier, 2011), resulted in rather detailed and precise models of stellar evolution for both components (Torres et al., 2015). In spite of the small mass difference of only about $3.5\pm 0.4\%$ between the two Capella components, they are at very different stages of evolution. The rapidly rotating secondary has just left the main sequence and is on its short path through the Hertzsprung gap, while the primary may be already near the end of the He-core burning phase. Hence, we expect to see significant differences in the CNO elements and their isotopes at the surface. The $^{12}\text{C}/^{13}\text{C}$ ratio of Capella was measured for the more evolved primary component by Tomkin et al. (1976) to be 27 ± 4 . This value is now over 40 years old, and its discrepancy compared to the model values presented by Torres et al. (2015) led to the present study.

We use the CN molecular lines around 8004 \AA for the isotope measurement. This region is the least blended and best accessible wavelength region in the optical for this type of analysis. It displays one line that is purely due to ^{12}CN and one line that is purely due to ^{13}CN . New observations are presented in Sect. 4.2, the data reduction and spectrum disentangling is described in Sect. 4.3, and our spectrum-synthesis analysis is given in Sect. 4.4. Our conclusions are summarized in Sect. 4.5.

4.2. Observations

The observations were carried out with the Potsdam Echelle Polarimetric and Spectroscopic Instrument (PEPSI; Strassmeier et al., 2015) installed on the pier of the $2 \times 8.4\text{ m}$ Large Binocular Telescope (LBT) on Mt. Graham, Arizona. Most of the spectra were obtained with the 1.83 m Vatican Advanced Technology Telescope (VATT), which has a 450 m fibre link to the PEPSI spectrograph at the LBT. A Cassegrain adapter on the VATT was used for target acquisition and guiding, and it also provides the feed for the entrance fibre (Sablowski et al., 2016).

PEPSI has three resolution modes related to the three fibre core diameters that feed it; see Strassmeier et al. (2018b) for a status and most recent mode description of the instrument. We used the ultra-high resolution mode with $R = \lambda/\Delta\lambda = 250\,000$ (2-pixel sampling and $0.74''$ sky aperture at LBT) with two pairs of $100\text{ }\mu\text{m}$ fibres and seven-slice image slicers. When fed from the VATT and used before mid-2016, PEPSI provided the

Table 4.1.: Overview of observations.

HJD (245+)	ϕ	Tel	R $\times 10^3$	t_{exp} (sec)	S/N	N
7354.73530	0.51	VATT	250	300	2047	9
7354.79351	0.51	VATT	250	300	1037	2
7354.81625	0.51	VATT	250	300	2121	8
7354.88761	0.51	VATT	250	300	2279	10
7354.96653	0.51	VATT	250	300	745	1
7663.00901	1.48	LBT	250	2.3	1740	10
7731.95117	2.14	VATT	200	2400	1377	1
7732.97880	2.15	VATT	200	700	1354	3
7820.72414	2.99	VATT	250	180	1616	4
7827.69544	3.06	VATT	250	180	2245	8
8028.00866	4.98	VATT	250	180	2638	7
8034.94472	5.05	VATT	250	180	2738	7

The S/N is given for the average spectrum from the N single exposures at orbital phase ϕ and about 8000 Å. The exposure time, t_{exp} , is given in seconds for single exposures.

same spectral resolution as when fed from the LBT, but with higher losses. After mid-2016, two new pairs of image slicers were implemented for the VATT feed. These provide an expected 2.6-pixel resolution of 200 000 with a single 3" sky aperture with a 200 μm fibre and a 9-slice image slicer for a 2-pixel resolution of 250 000 with the same aperture and a 9-slice image slicer, but smaller slice width. The respective wavelength coverage at LBT and VATT are always identical. PEPSI has blue and red arms with three cross-dispersers (CD) in each arm. One CD in each arm can be used simultaneously.

With the double-eyed LBT the light from the fibre pair of target and sky (optionally, it can be light from a Fabry-Pérot etalon) is rendered to four image slicers via respective octagonal fibres before it enters the spectrograph. Two 10k \times 10k STA1600LN CCDs with 9 μm pixel size and 16 amplifiers optimized for the blue and red arms are employed. When used with the VATT, only a single-eyed light path is available and no sky (but Fabry-Pérot light). The spectrograph is located in a pressure-controlled chamber at a constant temperature and humidity to keep the refractive index of the air inside constant. This provides a long-term radial velocity stability of about 5 m s^{-1} .

We acquired 70 spectra in total of Capella with the red-arm CD VI ($\lambda 7355 - 9137$ Å) between November 28, 2015 and March 15, 2017. The wavelength solution used about 3 000 ThAr lines and showed an error of the fit at the image center of 5 m s^{-1} . Consecutive single exposures obtained during the same night were averaged to obtain 12 spectra with high signal-to-noise ratio (S/N) that were then used to separate the two stellar components. These averaged spectra are listed in Table 4.1. The resolving power of the spectra varies according to the setup that was used, between 200k and 250k. The SN/ was measured to be about 8000 Å and is on average about 2 000:1. Figure 4.1 plots the 12 averaged spectra in the 8004 Å region.

4.3. Data reduction and spectral disentangling

The data were reduced on a generic software platform written in C++ under Linux, called the Spectroscopic Data System (SDS). The current image processing pipeline is specifically designed to handle the PEPSI data calibration flow and image specific content and is called

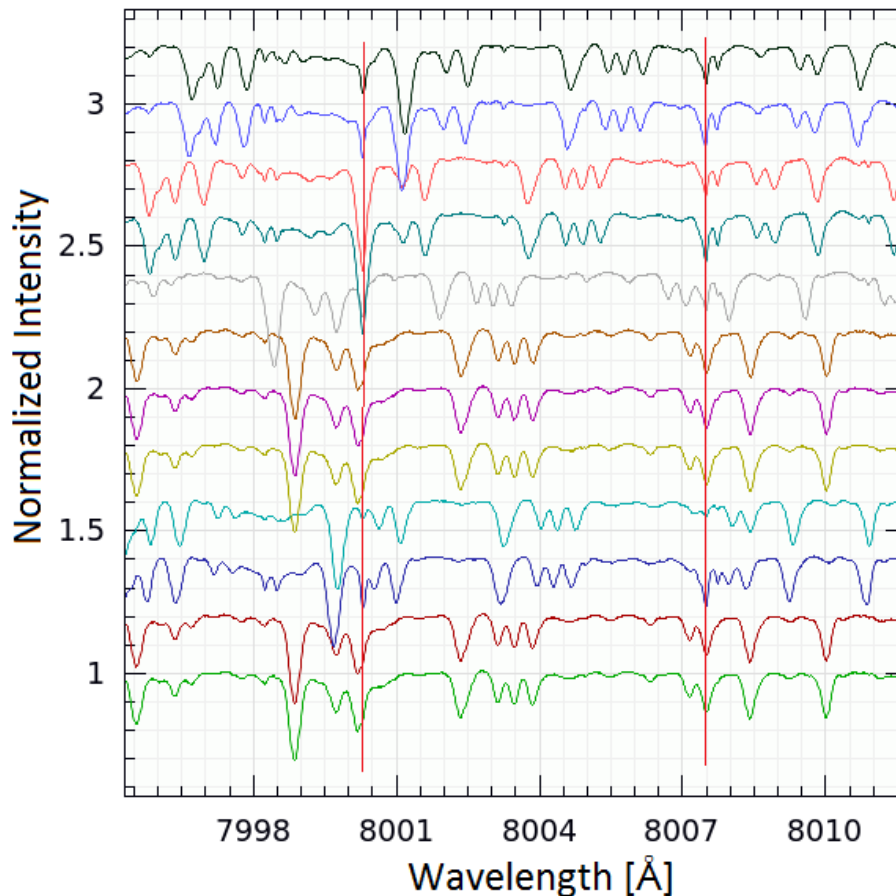


Figure 4.1.: Twelve Capella spectra that were used for the disentanglement. The bottom spectrum is the first spectrum listed in Table 4.1. The others are shifted in intensity by +0.2 for better visibility. The spectra are shown in laboratory wavelength scale (prior to heliocentric correction), and some telluric features are marked with vertical red lines.

SDS4PEPSI. The same SDS tools can be used for spectra that are obtained with different échelle spectrographs. It provides an automated pipeline without human interaction and relies on statistical inferences and robust statistics. The software numerical toolkit and graphical interface are designed based upon Ilyin (2000). Its application to PEPSI has initially been described in Strassmeier et al. (2018a), and its complete description will be presented in Ilyin (2019, in preparation).

The standard steps of image processing include the following: bias subtraction and variance estimation of the source images, super-master flat-field correction for the CCD spatial noise, échelle order definition from the tracing flats, scattered light subtraction, wavelength solution for the ThAr images, optimal extraction of image slicers and cosmic spike elimination of the target image, wavelength calibration and merging slices in each order, normalization to the master flat-field spectrum to remove CCD fringes and blaze function, a global 2D fit to the continuum of the normalized image, and rectification of all spectral orders in the image to a 1D spectrum for a given cross-disperser. The continuum of the final spectra in the time series was corrected for with the use of the mean spectrum. The weighted average of all spectra was normalized to the continuum to eliminate any residual effects in the continuum. The ratio of each individual spectrum and the mean is then used to fit a smoothing spline that constitutes the improved continuum for the

individual spectra.

The disentangling code `Spectangular` was presented by Sablowski & Weber (2017) and is based on singular-value decomposition (SVD) in the wavelength domain. It does not require correct input radial velocities (RVs) because it optimizes them during a full disentangling run. To apply this approach, it is necessary to use observations that are significantly spread over an orbital period. Because SVD requires an overdetermined set of equations, the minimum input is at least three spectra for two components. The Capella spectra used for the disentangling are shown in Fig. 4.1. Only a small wavelength fraction is plotted. These spectra are not well distributed throughout the orbit ($P_{\text{orb}} = 104$ d, see Table 4.1 for covered phases ϕ), but the small RV shifts between the spectra were sufficient for the algorithm to extract the individual components (see also Appendix B.2). The disentangling by the use of poorly sampled orbit was studied in Sablowski & Weber (2017). Furthermore, the disentangling code requires a priori knowledge of the light ratio of the two components in the wavelength range under consideration. We adopted the ratio of 1.118 (G8/G0) from Huby et al. (2013) (see also Appendix B.1).

An additional bonus from this disentangling process is that the telluric spectrum is removed. Water vapor lines, which we call tellurics, further complicate the analysis as well as the disentangling process because they can vary dramatically in strength (and they even slightly vary in RV). This is shown in Fig. 4.1 for a pair of telluric lines at wavelengths of about 8007.6 Å and for a line at 8000.3 Å. In order to preserve the flux in the wavelength pixels that are affected by tellurics, we did not apply the heliocentric correction before disentangling. This leads to a fixed position of tellurics in wavelength space. The high variability in the strength of these lines leads to a strong suppression in the separated spectra, which is due to the least-squares nature of the SVD solution. We then used the residuals from the separated spectra to identify the contribution of tellurics in each spectrum. These residuals were then approximated by a proper spline and corrected in the individual observed spectra. A second run of the entire disentangling process resulted in component spectra with negligible telluric contamination. For more details on this procedure, we refer to a forthcoming paper by Sablowski et al. (2019) and to the appendix. The final result of the separated spectra for the primary of Capella is shown in Fig. 4.2.

4.4. Analysis

For the carbon isotope ratio (CIR) we employed Spectroscopy Made Easy (SME; Valenti & Piskunov, 1996; Piskunov & Valenti, 2017) for a spectrum synthesis under local thermodynamical equilibrium (LTE) together with a grid of spherical model atmospheres from MARCS (Gustafsson et al., 2008) for giant stars as provided with the SME code. Because SME is not designed for individual isotope synthesis, we applied the following procedure. First, we fixed the stellar parameters to the values given in Table 4.2 (as derived by Takeda et al., 2018; Torres et al., 2015), but let the carbon abundance remain a free parameter. As a result of the high resolution of the spectra, the broadening values had to be reduced slightly compared to those determined by Takeda et al. (2018) and Torres et al. (2015). However, they are within the errors of the given values. These values were obtained by a synthesis of a few isolated lines, see Fig. 4.3. The orbital sampling in other wavelength regions is not sufficient for disentangling. We were therefore unable to determine the atmospheric parameters. Second, we fit the one line region that is solely due to ^{12}CN while masking out all the other nearby lines. Third, we fit the other line region that is solely due to ^{13}CN in the adjacent wavelength bin, again ignoring all the other lines (the fit regions are indicated as shaded areas in Fig. 4.2a). Based on these fits, we found a pseudo- ^{12}CN

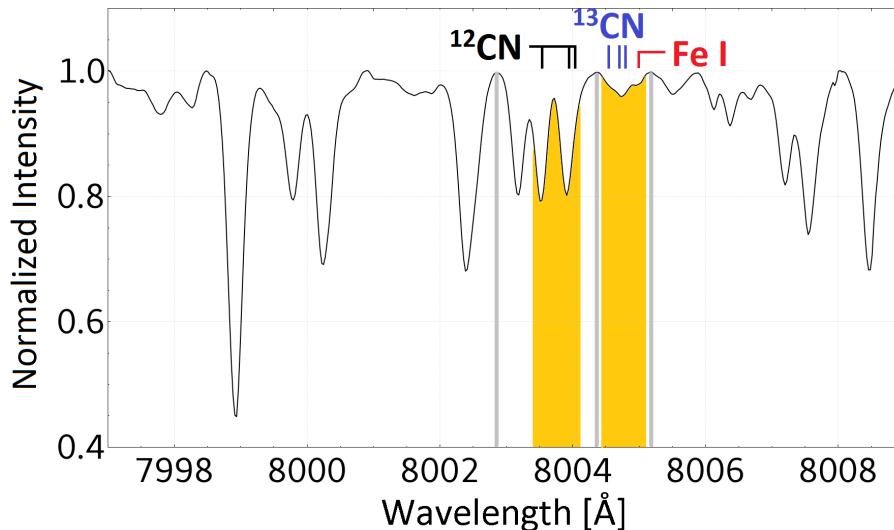


Figure 4.2.: Separated spectra of the G8III primary for the 8004 Å wavelength region of Capella. Light gray vertical lines define three continuum points, and the orange regions indicate the two fit regions for the spectrum synthesis.

Table 4.2.: Stellar parameters for the Capella primary.

Parameter	Primary	Secondary	MGS	Ref.
T_{eff} (K)	4943 ± 23	5694 ± 73	100	Takeda
$\log g$ (cgs)	2.52 ± 0.08	2.88 ± 0.17	0.5	Takeda
[Fe/H]	0.10 ± 0.05	-0.08 ± 0.08	var	Takeda
ξ_t (km s^{-1})	1.47 ± 0.13	2.29 ± 0.38	2.0	Takeda
ζ (km s^{-1})	6.6 ± 0.4	(7.0)*	...	Torres
$v \sin i$ (km s^{-1})	4.1 ± 0.5	35.0 ± 0.5	...	Torres

Takeda: Takeda et al. (2018). Torres: Torres et al. (2015). MGS: model-grid-step size of the used MARCS models. The microturbulence, ξ_t is fixed in the models. The metallicity, [Fe/H], has been varied. *The macroturbulent velocity for the secondary was set to 7.0 km s^{-1} .

and ^{13}CN abundance from which we obtained the carbon isotope ratio. The resulting best fits for both isotopes are shown in Fig. 4.4 along with their 3σ deviations.

We initially implemented the line list from Carlberg et al. (2012) for the SME synthesis. However, another small blend became obvious from our spectra. It is identified with a red thick mark in Fig. 4.2. This line is identified in VALD-3 as Fe I 8005.0490 Å (Kurucz, 2005) with an excitation potential $\chi=5.58$ eV and a transition probability $\log gf = -5.52$. We added it to the Carlberg et al. (2012) list and give the full line list and its parameters in Table 4.3.

We note that the precision of our isotope ratio is no longer limited by the data because of its high resolution, high S/N, and a continuum setting that is probably better than 0.1%. It turned out that the achievable precision is limited more by the atomic and molecular line data, and probably even more significantly, by the assumptions and grid resolutions of the model atmosphere. Tests were made by measuring the isotope ratio for synthetic spectra from multiple stellar parameters altered by the various grid resolutions and the measurement uncertainties given by Takeda et al. (2018) and Torres et al. (2015). SME provides the logarithmic abundances together with their errors, which for the best

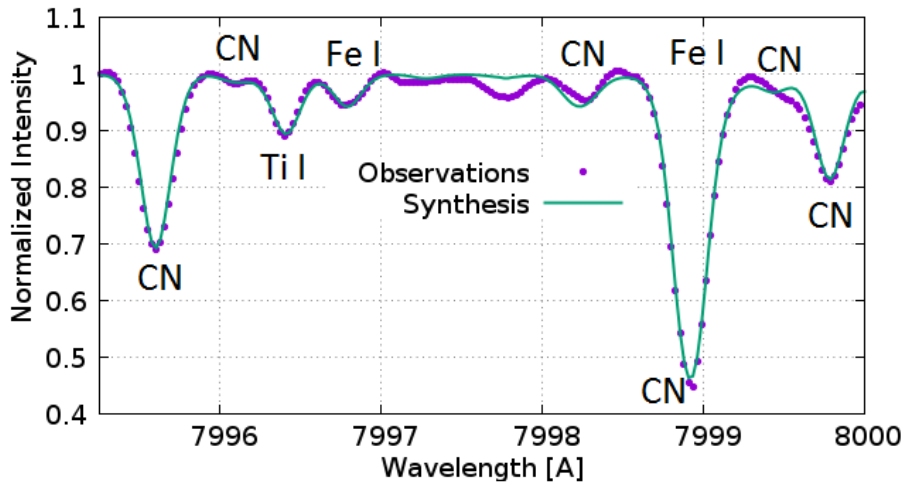


Figure 4.3.: Synthesis for refining the values of the broadening mechanisms by a few isolated lines within the separated region. The final values are $\xi_t = 1.39 \text{ km s}^{-1}$, $\zeta = 6.0 \text{ km s}^{-1}$, and $v \sin i = 3.8 \text{ km s}^{-1}$.

Species	λ (Å)	χ (eV)	$\log gf$ (cgs)
^{12}CN	8003.553	0.3109	-1.6440
^{12}CN	8003.910	0.3300	-1.6478
^{12}CN	8004.036	0.0600	-2.9245
^{13}CN	8004.550	0.1200	-1.5918
^{13}CN	8004.715	0.0700	-2.0814
^{13}CN	8004.801	0.1000	-1.6144
Fe I	8005.049	5.5869	-5.518
Zr I	8005.248	0.6230	-2.1901

Table 4.3: Line data for the synthesis.

fit (stellar parameters from Table 4.2) correspond to $\log A_{C_{12}} = -3.18 \pm 0.000658$ and $\log A_{C_{13}} = -4.43 \pm 0.04598$.

For a consistency check of the applied method in SME, we generated synthetic spectra with MOOG (Snedden, 1973), which can distinguish between the isotopes. These spectra were created with the same parameters as used in SME. Parameters of the MARCS model selected for the synthesis are $T_{\text{eff}} = 5000 \text{ K}$, $\log g = 2.5$, $[\text{Fe}/\text{H}] = 0.00$, and $\xi_t = 2.0 \text{ km s}^{-1}$. A good agreement is shown by the comparison with the observations in Fig. 4.4b. The slightly broader lines originate from the higher ξ_t of 2.0 km s^{-1} of this model. Therefore, we also used the model with $\xi_t = 1.0 \text{ km s}^{-1}$ and computed synthetic spectra with different carbon isotope ratios (CIR). The root mean square (RMS) between these spectra and the observations are shown in Fig. 4.5. The solid line represents a fit of an asymmetric parabola. The minima are in a very good agreement with the CIR value obtained by the fit with SME.

As described above, our analysis is limited to the models and line data. This is shown in Fig. 4.4c, where we plot the differences between the observations and the synthesis by MOOG with the obtained CIR.

Because the spectra from both codes agree well, we were confident to use the errors provided by the synthesis fitting in SME. The error of the isotope ratio was calculated according to the error propagation of the exponential function (e.g., Bevington & Robinson, 1992) $r = 10^u$ and $\sigma_r = \ln 10 \cdot r \sigma_u$, where r is the isotopic ratio, $u = \log A_{C_{12}} - \log A_{C_{13}}$

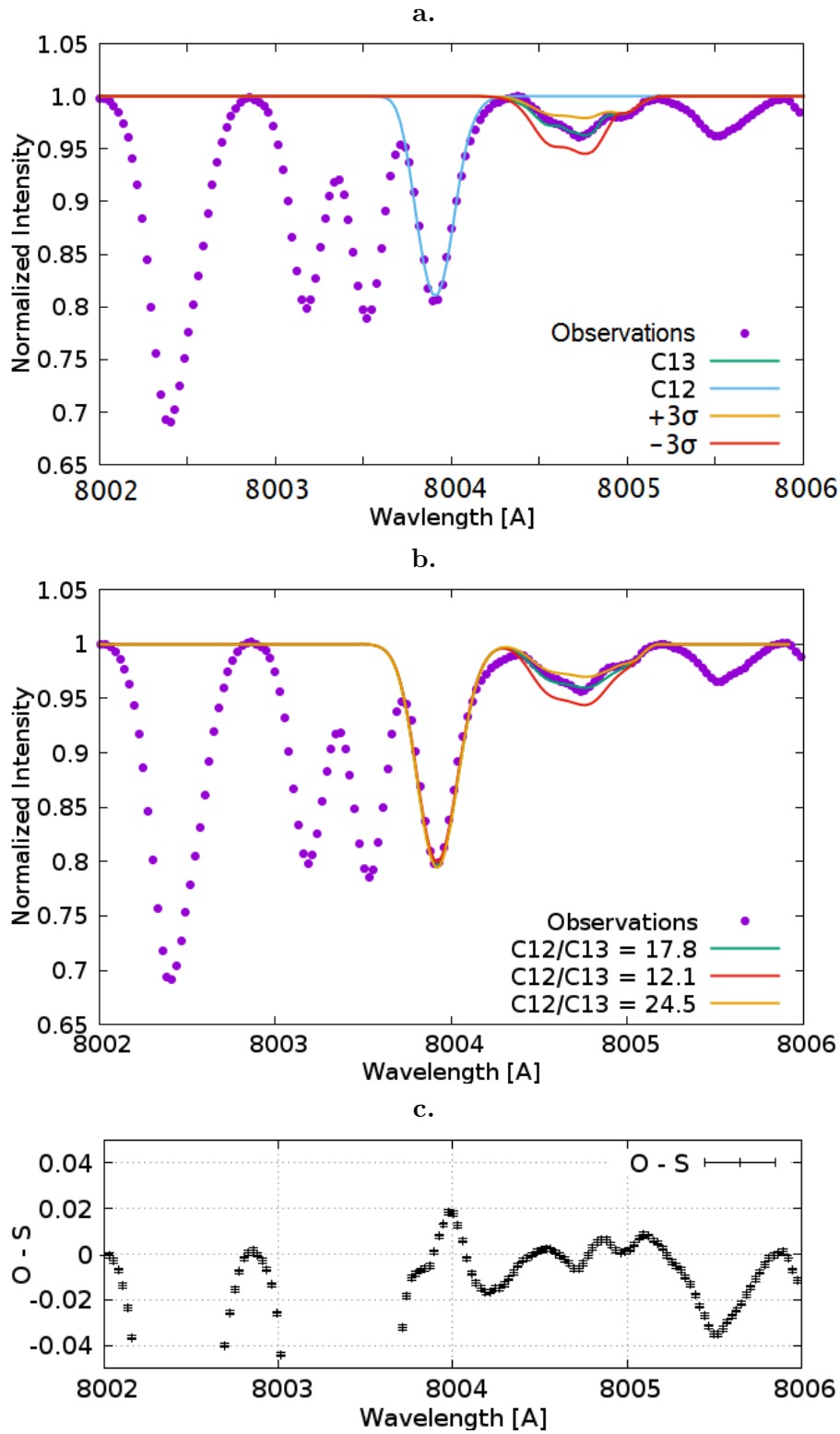


Figure 4.4.: **a:** Result from the spectrum synthesis fitting with SME. The observations are shown as dots, and we plot the best fits as blue and green lines for the ^{12}CN and ^{13}CN line region, respectively. This suggests an isotope ratio of 17.8 ± 1.9 . The synthetic spectra for $\pm 3\sigma$ deviations are shown as orange and red lines, respectively. **b:** Spectrum synthesis with MOOG for consistency of the spectral fitting by SME. See text for the parameters of the underlying MARCS model. **c:** Observations minus synthesis (O-S) for the MOOG synthesis. Error bars corresponds to an S/N of 1,000.

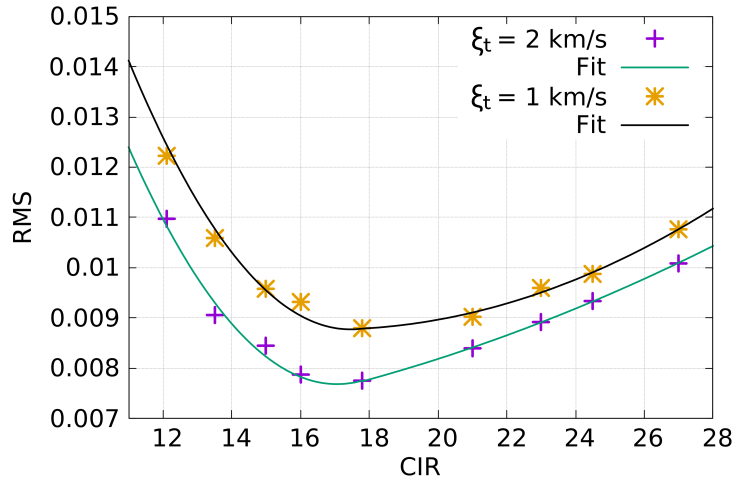


Figure 4.5.: RMS between synthesized spectra from MOOG vs. CIR with the use of MARCS models (see text) with $\xi_t = 1.0 \text{ km s}^{-1}$ and $\xi_t = 2.0 \text{ km s}^{-1}$, respectively.

and $\sigma_u^2 = \sigma_{C_{12}}^2 + \sigma_{C_{13}}^2$. The resulting value is $A_{C_{12}}/A_{C_{13}} = 17.8 \pm 1.9$.

The separated spectrum of the secondary (see Fig. B.3c) does not show separable signatures of the ^{12}CN and ^{13}CN 8004 Å lines. This is probably due to its higher temperature and much larger $v \sin i$ (see also Appendix B.2).

4.5. Summary and conclusion

We provided new measurement of the carbon $^{12}\text{C}/^{13}\text{C}$ isotope ratio of the Capella primary and found it to be 17.8 ± 1.9 . The assigned error is mostly due to uncertainties of the molecular line data and the grid-step-size of the underlying atmospheric models rather than the data. This new ratio is significantly lower than the value of 27 ± 4 originally measured by Tomkin et al. (1976) using a curve-of-growth analysis. Torres et al. (2009) have pointed out that Tomkin’s value was derived with an incorrect light ratio between the two stellar components. They estimated that the equivalent width measurements of the CN lines reported by Tomkin et al. (1976) were underestimated by about 6–11% as a result of this effect. Because the equivalent widths were used strictly differentially, we second the statement of Torres et al. (2009) that it introduced only a small error that is likely within the error bars already given. The difference to our new ratio therefore likely originates from the improvement of the data, the synthesis analysis, and better spectral-line data.

Although our new isotope ratio is now in a better agreement with theoretical expectations of 20.7 by Torres et al. (2015) based on MESA stellar evolution models, it is now (marginally) below the predictions if at an age of 588.5 Myr (see Paxton et al., 2013). The earlier prediction by Torres et al. (2009) was based on models from Claret (2004) and Young & Arnett (2005), which were all in the range of 18.88 to 19.60.

Acknowledgement

We thank the anonymous referee for the constructive comments that helped to improve the content of this study. We also thank our colleagues Gohar Harutyunyan, Arto Järvinen, and the developer of MOOG, Christopher A. Sneden, as well as the developers of SME, Nikolai Piskunov and Jeff Valenti, for their kind support to get the synthesis codes MOOG and SME running. This work is based on data acquired with PEPSI at the Large Binocular Telescope (LBT) and with the Vatican Advanced Technology Telescope (VATT). The LBT is an inter-

national collaboration among institutions in the United States, Italy, and Germany. LBT Corporation partners are the University of Arizona on behalf of the Arizona university system; Istituto Nazionale di Astrofisica, Italy; LBT Beteiligungsgesellschaft, Germany, representing the Max-Planck Society, the Leibniz-Institute for Astrophysics Potsdam (AIP), and Heidelberg University; the Ohio State University; and the Research Corporation, on behalf of the University of Notre Dame, University of Minnesota, and University of Virginia. This work has made use of the VALD database, operated at Uppsala University, the Institute of Astronomy RAS in Moscow, and the University of Vienna.

References

- Allende Prieto, C., Barklem, P. S., Lambert, D. L., & Cunha, K. 2004, *A&A*, 420, 183
- Anders, E. & Grevesse, N. 1989, *Geochimica et Cosmochimica Acta*, 53, 197
- Bevington, P. & Robinson, D. 1992, *Data Reduction and Error Analysis for the Physical Sciences*, 2nd edn. (McGraw-Hill: New York), p. 50
- Carlberg, J. K., Cunha, K., Smith, V. V., & Majewski, S. R. 2012, *ApJ*, 757, 109
- Charbonnel, C. & Lagarde, N. 2010, *A&A*, 522, A10
- Claret, A. 2004, *A&A*, 424, 919
- Drazdauskas, A., Tautvaisiene, G., Randich, S., et al. 2016, *A&A*, 589, A50
- Gustafsson, B., Edvardsson, B., Eriksson, K., et al. 2008, *A&A*, 486, 951
- Hedrosa, R. P., Abia, C., Busso, M., et al. 2013, *ApJL*, 768, L11
- Henry, R. B. C., Edmunds, M. G., & Köppen, J. 2000, *ApJ*, 541, 660
- Huby, E., Duchêne, G., Marchis, F., et al. 2013, *A&A*, 560, A113
- Iben, Jr., I. 1964, *ApJ*, 140, 1631
- Ilyin, I. 2000, PhD dissertation, University of Oulu, Finland
- Jewitt, D. C., Matthews, H. E., Owen, T., & Meier, R. 1997, *Science*, 278, 90
- Kurucz, R. L. 2005, *Memorie della Societa Astronomica Italiana Supplementi*, 8, 14
- Lambert, D. L. & Ries, L. M. 1981, *ApJ*, 248, 228
- Mikolaitis, S., Tautvaisiene, G., Gratton, R., Bragaglia, A., & Carretta, E. 2012, *A&A*, 541, A137
- Paxton, B., Cantiello, M., Arras, P., et al. 2013, *ApJS*, 208, 4
- Pinsonneault, M. 1997, *Annual Review of Astronomy and Astrophysics*, 35, 557
- Piskunov, N. & Valenti, J. A. 2017, *A&A*, 597, A16
- Sablowski, D., Järvinen, S., & Weber, M. 2019, *A&A*, accepted
- Sablowski, D. P. & Weber, M. 2017, *A&A*, 597, A125
- Sablowski, D. P., Weber, M., Woche, M., et al. 2016, in *Proc. SPIE*, Vol. 9912, 99125H

- Shetrone, M. D. 2003, *ApJL*, 585, L45
- Snedden, C. A. 1973, PhD dissertation, The University of Texas at Austin, USA
- Strassmeier, K., Ilyin, I., Järvinen, A., et al. 2015, *AN*, 336, 324
- Strassmeier, K. G., Ilyin, I., & Weber, M. 2018a, *A&A*, 612, A45
- Strassmeier, K. G., Ilyin, I., Weber, M., et al. 2018b, in *Proc. SPIE*, Vol. 10702, 1070212
- Szigeti, L., Mészáros, S., Smith, V. V., et al. 2018, *MNRAS*, 474, 4810
- Takeda, Y., Hashimoto, O., & Honda, S. 2018, *ApJ*, 862, 57
- Tautvaisiene, G., Drazdauskas, A., Bragaglia, A., Randich, S., & Zenoviene, R. 2016, *A&A*, 595, A16
- Tomkin, J., Luck, R. E., & Lambert, D. L. 1976, *ApJ*, 210, 694
- Torres, G., Claret, A., Pavlovski, K., & Dotter, A. 2015, *ApJ*, 807, 26
- Torres, G., Claret, A., & Young, P. A. 2009, *ApJ*, 700, 1349
- Valenti, J. A. & Piskunov, N. 1996, *AAS*, 118, 595
- Weber, M. & Strassmeier, K. G. 2011, *A&A*, 531, A89
- Yang, C., Wang, T., Ferland, G. J., et al. 2017, *ApJ*, 846, 150
- Young, P. A. & Arnett, D. 2005, *ApJ*, 618, 908

5. Discussion

The developed and released software packages `Spectangular` as well as `CroCo` were described in Chapters 2 and 3. The main advantage compared to other existing codes is the possibility to optimise on the individual radial velocities of the system. This circumvent the necessity that the RV curve in time follows an analytical equation. Hence, systems which undergo variations in their orbital motion due to third body interaction and relativistic effects can also be disentangled. Furthermore, that the applicability of the code goes beyond the work in this thesis, is shown by its application to WR stars in Appendix C. In addition, the applicability to variable spectra was studied. This also included the implementation of an algorithm to determine the light-ratio of the components in each observed spectrum. The continuum of the disentangled spectra are sensitive to (1) normalisation and (2) noise of the individual observations. Hence, besides sufficient coverage of the RV-curve, it is important that (1) all spectra have the same continuum level and (2) the noise should be equal in all spectra. Both effects lead to a less defined continuum in the disentangled spectra, resulting in a slope. This was shown in Fig. 2.12 and Fig. 3.7, respectively.

Understanding the evolution of stars is based strongly on the models used to calculate their tracks in the Hertzsprung-Russel diagram. Hence, it is important to determine all the observable (surface) parameters and to minimise the uncertainties on them. This can reveal the 'hidden' behavior within the interior of stars. One heavily discussed parameter is the overshooting of convective regions of stars. Hence, the section 5.1 will discuss this effect for Capella. In particular, the values for the overshooting and mixing length will be derived from a grid of tracks and by an optimisation algorithm. The derived carbon isotope ratio (Manuscript III) will also be set into context of these models.

Additionally, the determination of the rotation periods of the Capella components from long-term spectroscopy and the disentangling approach will be described in Sect. 5.2.

5.1. Evolution

5.1.1. Overshooting

As mentioned in the introduction, the time spend in the Hertzsprung gap is very short (about one per cent of the stellar live time). The absolute age the star has in the gap, however, depends mainly on the time spend on the main sequence. This time in turn, depends on the amount of fuel the star can burn during the H-core burning phase. This amount can be increased by convectional overshooting of the fully convective core into the radiative envelope. The overshoot parameter, f_{ov} , defines the overshoot in terms of pressure scale height. `MESA` (Paxton et al., 2010, 2018) uses two values to specify the overshooting. Since the mixing coefficient at the boundary is zero, the parameter f_0 defines how far from the boundary, the coefficient is used. A second parameter, f , defines the overshooting from that point, see also Fig. 5.1 left. Hence, $f = f_0 + f_{ov}$. For example, Torres et al. (2015) gave a $f_{ov} = 0.02$ for both components of Capella above the H-burning core¹. This can

¹The inlist file was provided via the `MESA` marketplace and adapted to a newer `MESA` release (r10398) used here. This list is given in Appendix E for completeness.

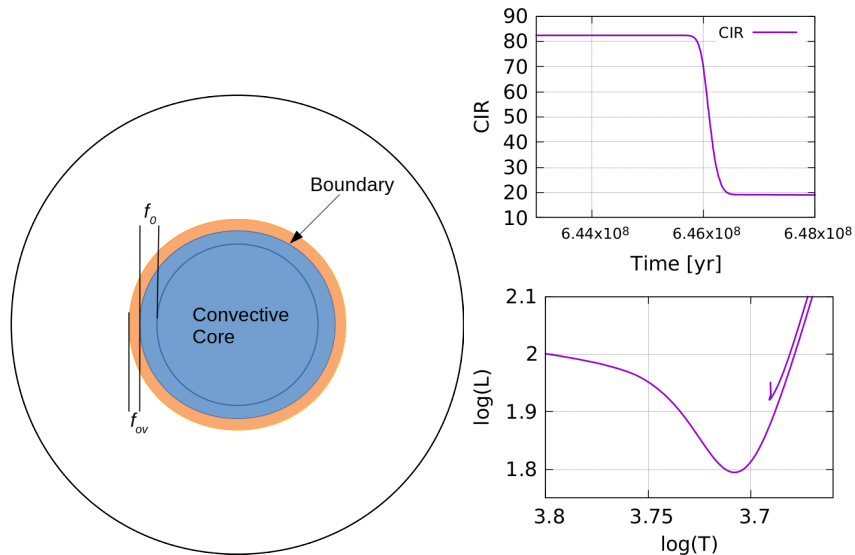


Figure 5.1.: Left: Definition of overshooting within MESA by the parameters $f = f_0 + f_{ov}$, see text. Right: drop of the carbon isotope ratio (CIR) and HRD showing the Hertzsprung gap and the clump for a star of about $2.5M_{\odot}$.

be obtained by $f_0 = 0.05$ and $f = 0.07$. However, giving f_{ov} is not sufficient to define the overshooting in MESA. Also the combination $f_0 = 0.01$ and $f = 0.03$ yields $f_{ov} = 0.02$. In fact, the first definition yields a much longer live time of the star on the main sequence, since more material is mixed to the core. For a sample of combinations of these parameters, the time until the first dredge-up (here defined as the time of the sudden decrease of the carbon isotope ratio, CIR, Fig. 5.1 right) for Capella is collected in Table 5.1.

Additionally, these parameters can be set for H-, He-, Z-burning above the core and above as well as below the burning shells and non-burning regions separately. However, due to the evolutionary stage of Capella, these definitions are not relevant here.

5.1.2. Model grid

A glance to Table 1.2 yields two metallicities determined for Capella. While Torres et al. (2015) determined sub-solar, Fuhrmann (2011) and Takeda et al. (2018) determined sub-solar for the secondary only. However, since the secondary should have undergone minor chemical evolution at the surface yet, its metallicity can be interpreted as the initial value for the computation of the evolutionary tracks. MESA uses the solar scale of Asplund et al. (2009), where $Z = 0.0134 \times 10^{[X/H]}$. This yields $Z_{\text{Torres}} = 0.0122$ and $Z_{\text{Takeda}} = 0.0112$. Mass loss was accounted for via Reimers (1975) with a scale factor of 0.2. The initial masses of the components were increased slightly (same as used in Torres et al., 2015, 0.0048 and 0.0027 M_{\odot} for A and B) to account for the mass-loss.

A series of tracks with a metallicity of 0.0122 are shown in Fig. 5.3. The model corresponding to the black line in Fig. 5.3 shows a good agreement with the positions of the stars in the HRD. However, the age difference is rather large with 28 Myr. Hence, from the grid computation, the model with $f_0 = 0.001$, $\alpha_{MLT} = 1.85$, and $f = 0.02$ with an age difference of 8.20 Myr is most confident. The predicted carbon isotope ratio (CIR) of the models are shown in Fig. 5.2. The measured value corresponds to the determination of the CIR from Chapter 4 and is in very good agreement with models for a initial ratio of 82.

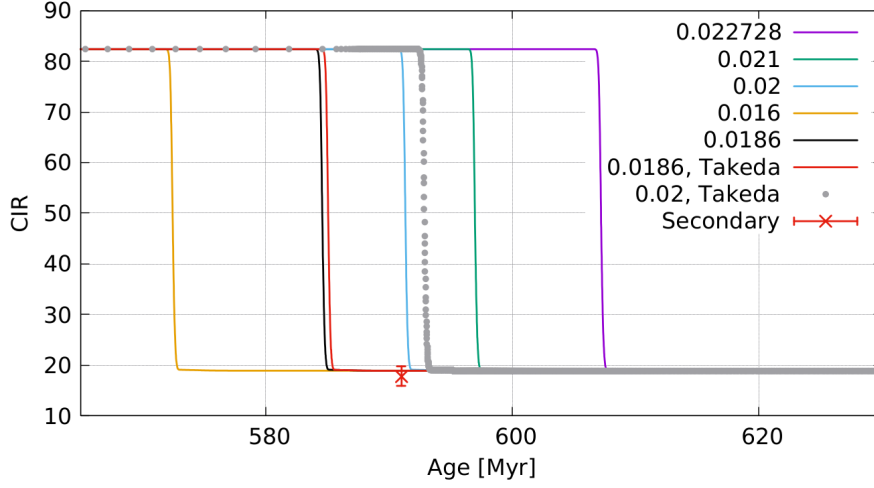


Figure 5.2.: Model predictions of the carbon isotope ratio of the primary of Capella. The data point corresponds to the determined value (Manuscript III).

A lower metallicity leads to a shift of the clump towards higher T_{eff} . However, this could be compensated for by a higher value for the overshooting. The track for the secondary within the Hertzsprung gap shifts only marginally towards lower luminosity. This in turn would enlarge the difference in age since the secondary would still require a lower value for the overshooting. The abundance determination by Fuhrmann (2011) was based on only eight Fe I lines and one Fe II. They performed a synthesis within the composite spectra, e.i., no spectral disentangling was performed. Since the secondary with its lower $v \sin i$ has much deeper and 'sharper' lines, the abundance determination is dominated by this component. However, they claim that the microturbulence they adopted ($\xi_t = 1.40$ and 1.80 km s^{-1}) might be too high. This can also be supported from the analysis in Chap. 4 where a lowering of the broadening parameters was necessary.

5.1.3. Optimised model

Computation of a grid of tracks and interpolation within the grid to find best common tracks was shown in the previous section. However, a more straight forward and efficient way is the combination of the model computation with a global optimisation on the adjustable parameters such as the mixing length, α_{MLT} , and the overshooting. To achieve this, a Nelder- and Mead global optimiser was written as part of the *CroCo* package (for *CroCo* see also Manuscript I). This algorithm allows the specification of variables within the *MESA* inlist file. It will use that file and passes it to *MESA*. After the computation of the track has finished, the point in the HRD on the track with the smallest residuum r to the measured values for a given star is computed

$$r = \min \left[\frac{|L_m - L_{tr}|}{L_m} + \frac{|T_{\text{eff},m} - T_{\text{eff},tr}|}{T_{\text{eff},m}} \right], \quad (5.1)$$

where the indices m and tr indicate the *measured* and the *track* values.

In case of a single star, that residuum is used as the minimisation criterion. An example for Capella B is shown in Fig. 5.4. The initial track to start the optimisation is shown at left ($\alpha_{MLT} = 1.800$ and $f = 0.01860$). The location of Capella B is indicated by the green rectangle. Only within that box, the residuum is computed to avoid mismatch with other

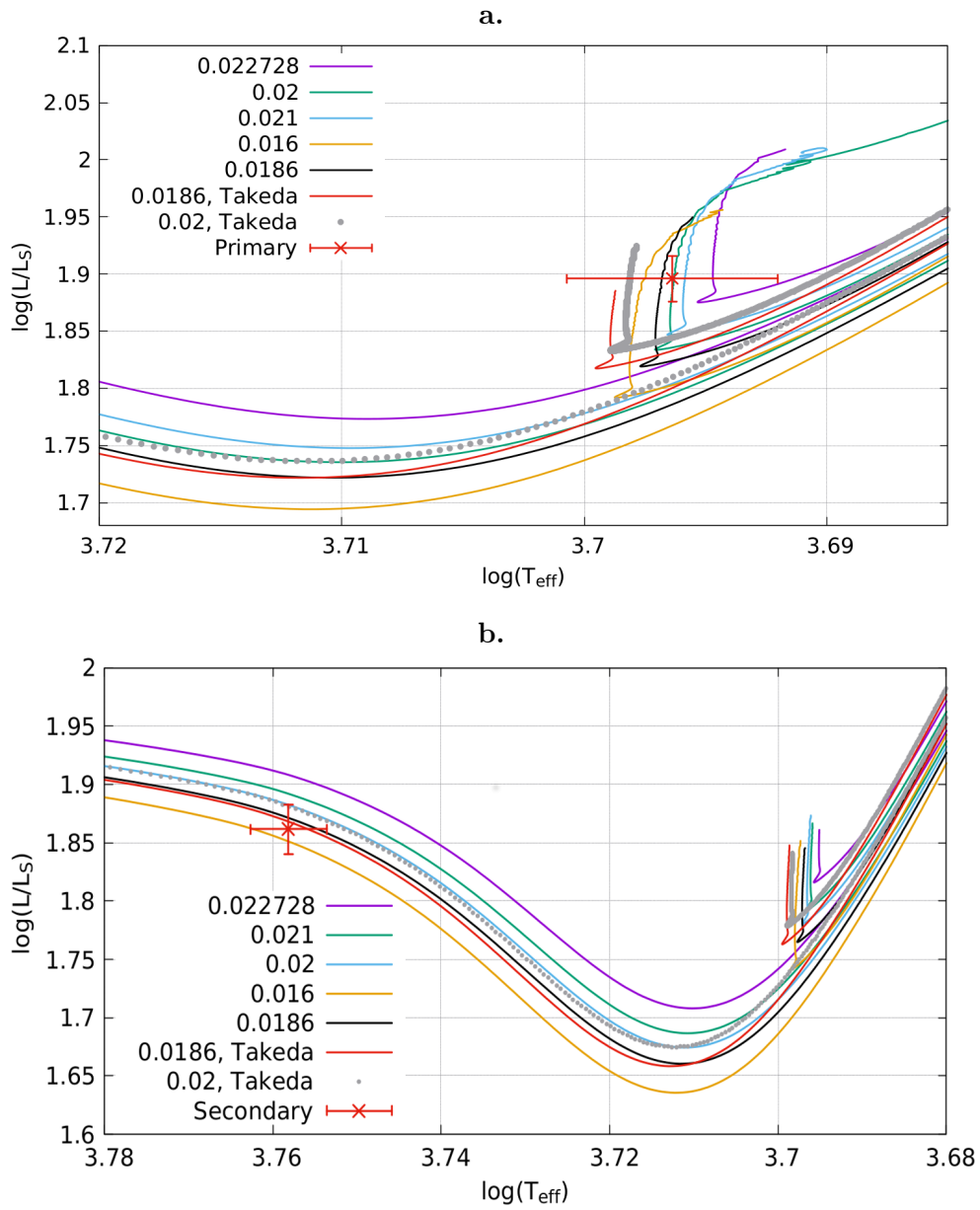


Figure 5.3.: Tracks for both components of Capella. **a:** For the primary and **b** for the secondary. Legend items refer to f . For $f = 0.022728$ it is $f_0 = 0.002728$ and for all other tracks $f_0 = 0.001$. Metallicity was applied from Torres et al. (2015).

f	f_0	α_{MLT}	$\log(T_{\text{eff}})$	$\log(L/L_{\odot})$	Age [Myr]	
Capella A			3.69636	1.89597		
0.022728	0.002728	1.80	3.69116	1.89834	583.62	
0.021	0.001	"	3.69233	1.89535	592.87	
0.020	"	"	3.69279	1.89562	597.64	
0.0186	"	"	3.69341	1.89585	604.05	
0.022728	0.002728	1.85	3.6947	1.89657	583.14	
0.021	0.001	"	3.69589	1.88902	588.89	
0.020	"	"	3.6963	1.89492	597.67	
0.0186	"	"	3.69669	1.90672	610.76	
0.016	"	"	3.69666	1.92533	633.05	
0.022728	0.002728	1.90	3.69807	1.89508	583.56	
0.021	0.001	"				
0.020	"	"	3.69952	1.89546	598.20	
0.0186	"	"	3.69977	1.90474		
Capella B			3.75846	1.861534		Diff [Myr]
0.022728	0.002728	1.80	3.75441	1.90699	608.73	-25.11
0.021	0.001	"	3.75654	1.8933	597.18	-4.31
0.020	"	"	3.75671	1.88618	592.64	5.00
0.0186	"	"	3.75705	1.87412	585.21	18.84
0.022728	0.002728	1.85	3.75505	1.89903	605.47	-22.33
0.021	0.001	"	3.75748	1.88903	595.12	-6.23
0.020	"	"	3.75766	1.8796	589.47	8.20
0.0186	"	"	3.75765	1.86854	582.66	28.10
0.016	"	"	3.75831	1.85071	570.47	62.58
0.022728	0.002728	1.90	3.75492	1.89354	603.69	-20.13
0.021	0.001	"				
0.020	"	"	3.75716	1.87174	587.16	11.04
0.0186	"	"	3.75802	1.86372	580.26	30.49

Table 5.1.: Time until first dredge-up and arrival at clump for Capella A and B (2.5687 and 2.4855 M) for different combinations of the overshooting parameter all giving $f_{ov} = 0.02$. $Z = 0.012$, $Y = 0.270$, and $\alpha_{MLT} = 1.85$.

close lines of the track, critical for example on the RGB (Capella A). The optimised values after two iterations are $\alpha_{MLT} = 1.886$ and $f = 0.01804$.

However, Capella as a binary gives another constraint for the optimisation. At their location in the HRD, they need to have the same age. Hence, the algorithm allows the optimisation of a binary as well. The residuum to be minimised in that case is

$$r_{\text{binary}} = \frac{g_A r_A + g_B r_B}{2} + \frac{|t_A - t_B|}{t_A + t_B} 2, \quad (5.2)$$

where r_A and r_B is the residuum of component A and B according to Eq. (5.1), weighted by the g 's and t_A and t_B the corresponding age from the tracks of component A and B, where the residuum is smallest, respectively. Furthermore, the algorithm allows to optimise the binary either by coupled or individual values. The coupled option assumes same values for the free parameters of both components.

Tracks not intersecting with the box in the HRD defined by the errors on L and T_{eff} were rejected. In a first optimisation, the track for the secondary was forced to the upper

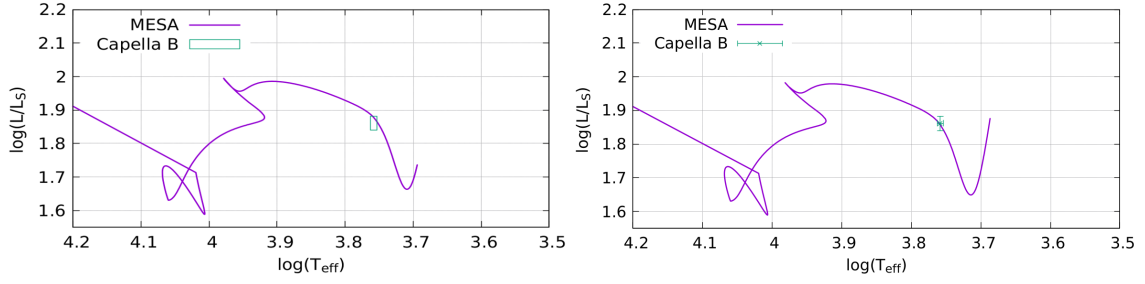


Figure 5.4.: Left: Initial track for Capella B computed by MESA. Right: Track after two iterations. Green box indicates the measured values of $\log(L/L_{\odot})$ and $\log(T_{\text{eff}})$ with the errors, Table 1.2 (Torres et al., 2015). See text for details.

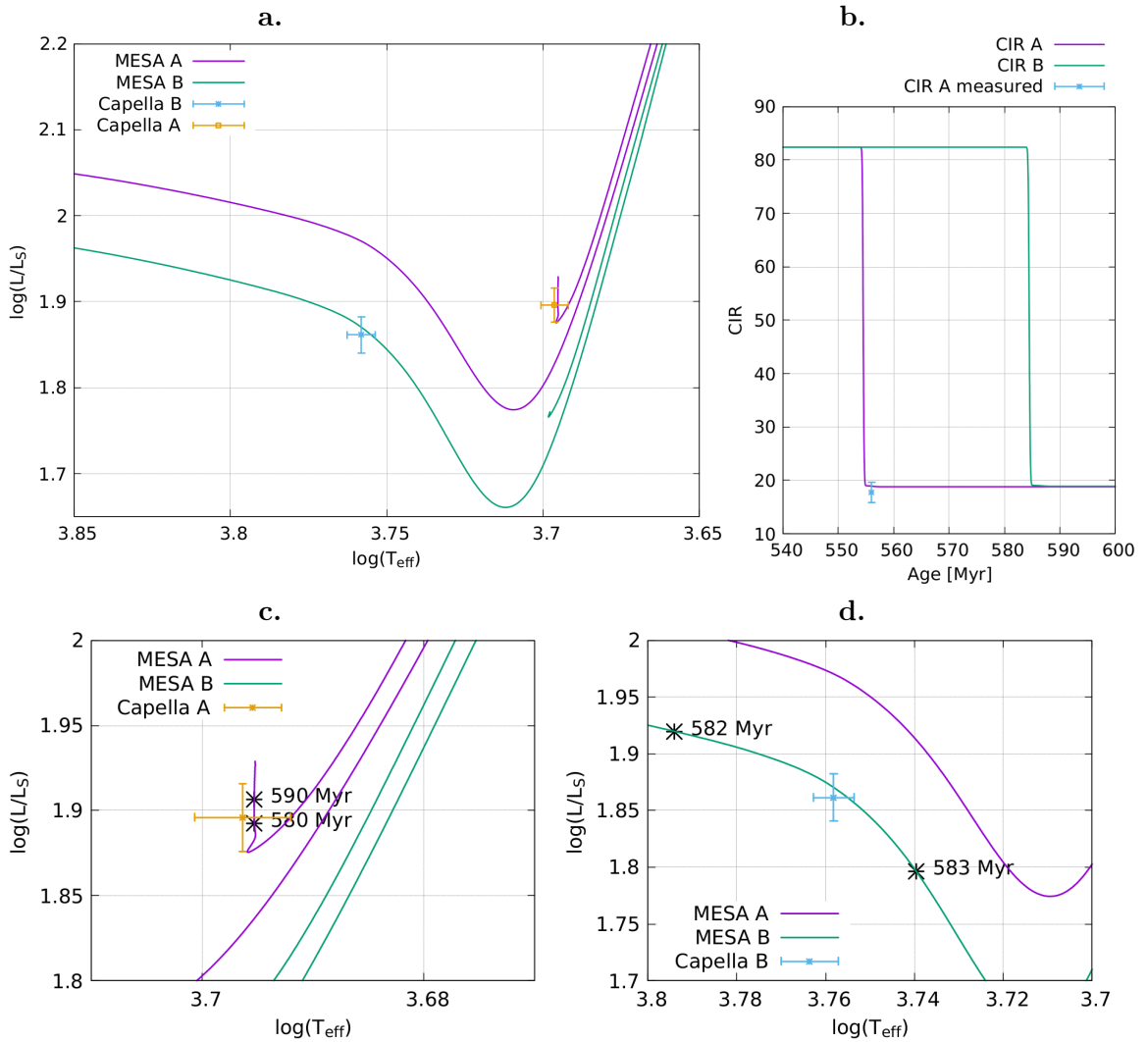


Figure 5.5.: **a:** Capella tracks from MESA derived with the optimisation algorithm described in text. Derived ages for the primary and secondary are 582.696 Myr and 582.609 Myr. **b:** Corresponding carbon isotope ratio. The measured value of 17.8 ± 1.9 (Manuscript III) and the model prediction from MESA. **c:** Detail for component A, **d** detail for component B.

Table 5.2.: Overview and grouping of observations. For the sets 1 to 13b, number of observations is without low SNR observations. For the three sets (13, 14 and 15) all single spectra used are counted.

Set	HJD start 245+	HJD end 245+	number of spectra	mean SNR at 5870 Å
1	4305	4426	25	55
2	4437	4582	25	75
3	4671	4823	25	70
4	4834	4945	19	75
5	5044	5169	22	65
6	5169	5326	21	75
7	5410	5797	25	50
8	5797	5895	22	70
9	5884	5992	27	60
10	5992	6362	12	70
11	6347	6571	18	80
12	6571	6779	24	75
13b	6779	7010	18	90
13	6779	7050	265	115
14	7354	7536	1,251	130
15	7595	7704	566	125

right corner of this box. This 'mismatch' may be due to the fast evolution within that short period of time in contrast to the long period a star spends within the clump. Hence, a second optimisation was performed with a stronger weight on the secondary's residuum in the HRD. The values finally used were $g_A = 0.5$ and $g_B = 2$. Optimised values for the primary are $\alpha_{MLT} = 1.859$, $f = 0.0234$ and for the secondary $\alpha_{MLT} = 1.861$, $f = 0.0188$. Figure 5.5 shows the corresponding tracks. The age difference is 0.087 Myr, with a residuum of $r_{\text{binary}} = 0.00129$, and unweighted $r_A = 0.000303$, and $r_B = 0.00107$. Compared to the derived values by the grid computations, the optimisation approach leads to much better fits, especially in age.

5.2. Rotation

The disentangling approach was applied to a large data set of observations over ten years in order to obtain the rotational periods of both stars. Supporting material and further descriptions can be found in Appendix D.

5.2.1. Observations, Data Reduction, and Disentanglement

Capella has been observed frequently with the STELLA echelle spectrograph (SES) mounted via fibre to the 1.2 m STELLA-I telescope, part of the STELLA robotized observatory on Tenerife (see Strassmeier et al., 2004; Strassmeier et al., 2012). The spectral resolving power is between R55 - 75k. The more than 2,000 single exposures are grouped into multiple data sets, all covering at least one orbital period and are listed in Table 5.2. The data reduction is based on an automated routine in IRAF. It includes the steps for image trimming, cosmic ray correction, bias, scattered light subtraction and flat-field correction by an equally treated master halogen flat-field.

Spectra taken after 2015 are grouped into three data sets, 13, 14, and 15. They have best SNR values and a high temporal resolution. Hence, it is not possible to use all of them for the disentangling, since it would require far too much RAM and time. Instead, only the best spectra were selected with a time difference corresponding to at least 2 km s^{-1} orbital motion. This value is about two times the spectral resolution expressed in velocities. This selection is shown for data set 14 in Fig. 5.6.

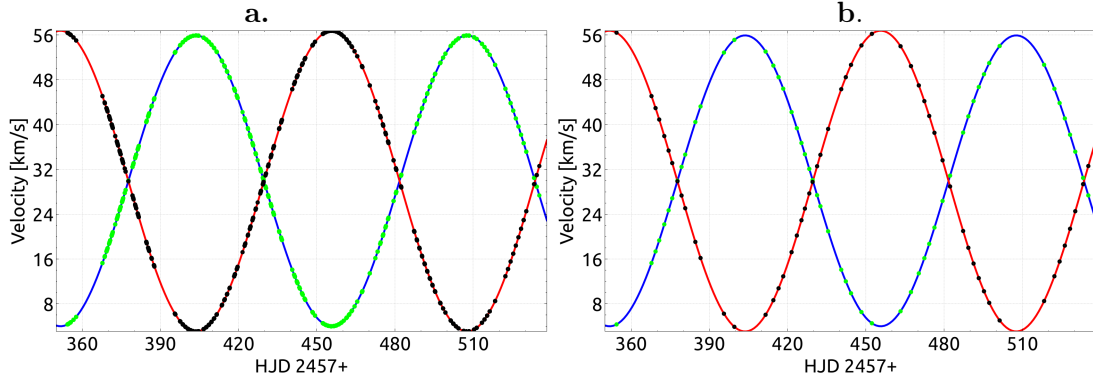


Figure 5.6.: An example for selecting data for disentangling. (a): All 1.251 spectra in data set 14; (b): 55 selected spectra used for disentangling.

Smaller subspectra were created for each spectral region of the used lines (see Appendix D). The regions in the red wavelength domain, starting with the Na I D doublet, suffer from strong telluric contaminations. Since these can challenge the frequency analysis, an attempt was made to remove these features in the following way: The disentanglement results in an average spectra for both components (due to the least-square nature of the singular value decomposition). Hence, features within the individual spectra are suppressed and visible in the observation - disentangled spectra (difference spectra). These are shown for data set 14 and the region around the Na I D line in Fig. 5.7. From this difference, the best ones (about ten) were selected and a master telluric was created. This telluric spectrum was used to correct each observed spectrum.

The disentangled spectrum of component A was subtracted from the individual spectra (the ones corrected from tellurics). These spectra were shifted to the rest-frame. Hence, the final product from the disentanglement procedure is a time series of spectra of component B. Same subtraction was done but with component B to create time series of spectra of component A. As already mentioned in the introduction of this thesis, the primary is believed to be less active, since the strong break in rotation has lead to a suppression of the dynamo effect. Hence, one can be certain that the main variability should originate from the gap giant. However, in order to support that, the disentangled chromospheric Ca II infrared triplet (IRT) lines are shown in Fig. 5.8. The solid black line shows an LTE synthesis by SME. The line wings and all blend lines in that region were fitted with the synthesis code. Since the core of the line is formed in higher layers of the atmosphere, were NLTE effects become significant (no equilibrium between radiative and collision processes), the differences between the synthetic and the measured profile reveal information about the activity, that is, the flux contribution from the chromosphere (e.g., Busà et al., 2007). The blue data points indicate that difference. The error bar results from the SNR of the disentangled spectrum. The difference of the equivalent widths (EW) of the synthetic and observed spectra vs the integration interval to compute the EW is shown in Fig. 5.9. It shows that this residual EW is significantly higher for the gap giant.

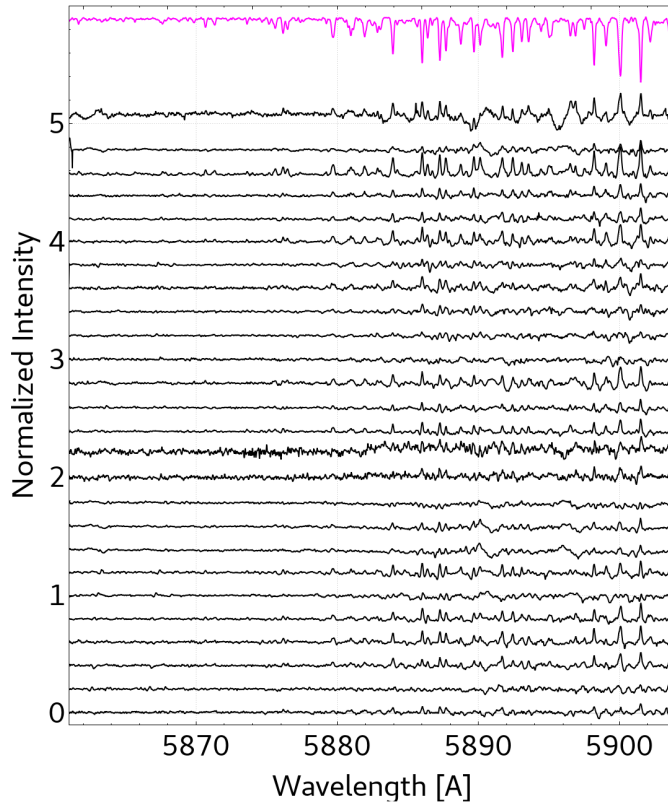


Figure 5.7.: Residual spectra between observed and disentangled spectra around the Na I D of data set 14. The purple spectrum at top is the master telluric created from ten best residual spectra and used to correct the individual observed spectra. It was multiplied by four for better visibility.

5.2.2. Frequency Analysis

From the time series of spectra, line moments were calculated. These line moments are used for a period search. Some data sets have been renormalized by two points (red and blue from line of interest) to assure a common continuum before computing line moments. In addition, to combine the measurements of the different data sets, quantities were corrected from biases. This was done by computing the median of each data set and correcting them to a common value. These differences result from slight differences in the continuum value of the disentangled spectrum. Furthermore, data points more than four sigma apart from the median were rejected.

The computed frequency spectra are based on a calculation of trial frequencies within the specified frequency range. Offset and sine functions are fitted for each frequency by weighted linear least-square minimisation. The statistical significance of the amplitude of a given frequency is defined by the false alarm probability (FAP). This FAP is calculated via F-statistics (Seber & Lee, 2003, p. 99) in combination with the incomplete beta function (Press et al., 1992, p. 226). This tool is part of the Spectroscopic Data Systems (SDS) package (Ilyin, 2019, in prep, priv comm. I. Iyin). The window function for a given frequency range is computed as well and plotted as purple curve in frequency plots. Significant peaks are fitted as well with weighted least-squares in order to determine the exact frequency.

Artificial spectra were created with same time-sampling and signal to noise as the ob-

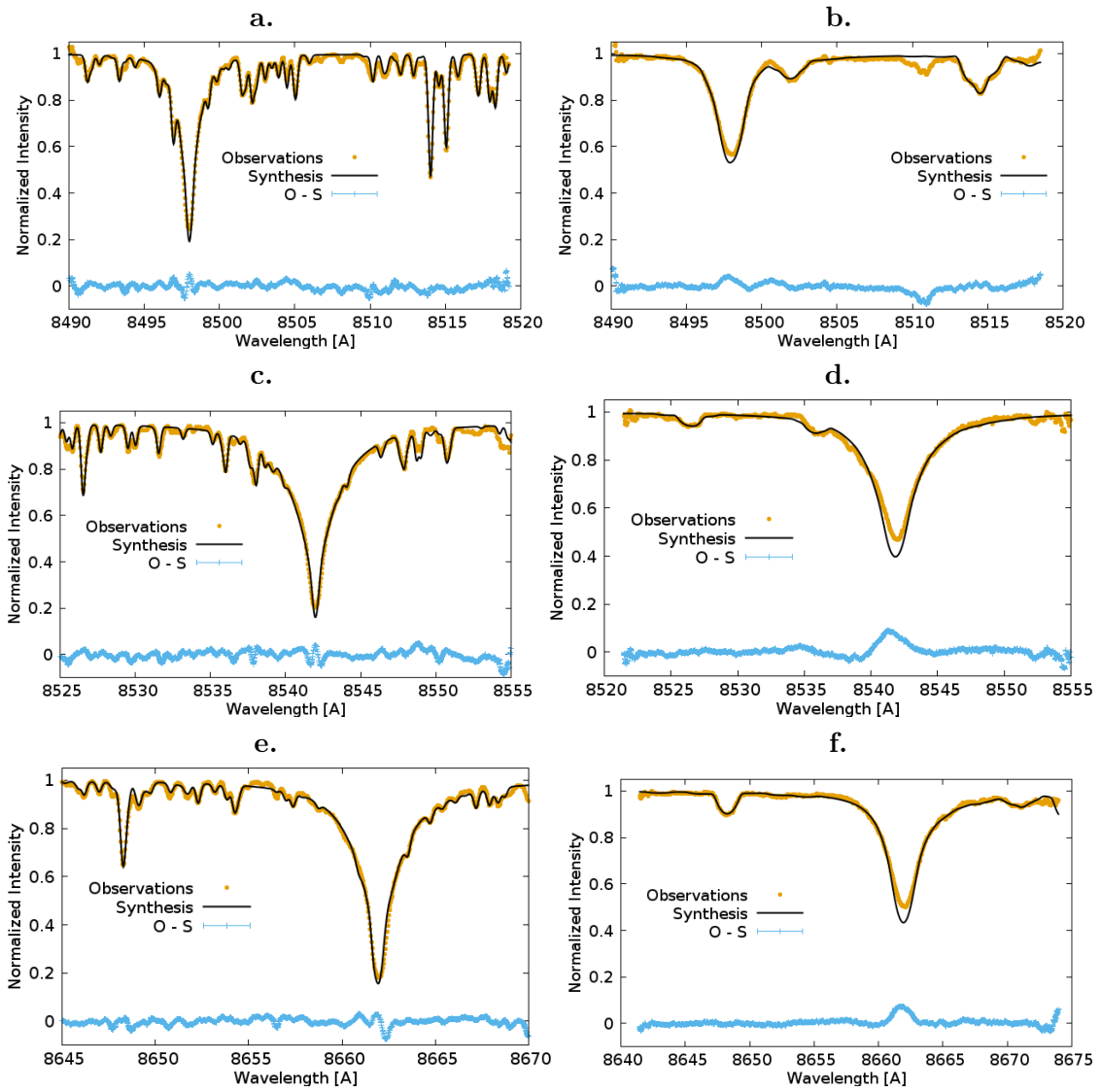


Figure 5.8.: LTE synthesis for the Ca II IRT of Capella A (left column) and B (right column).

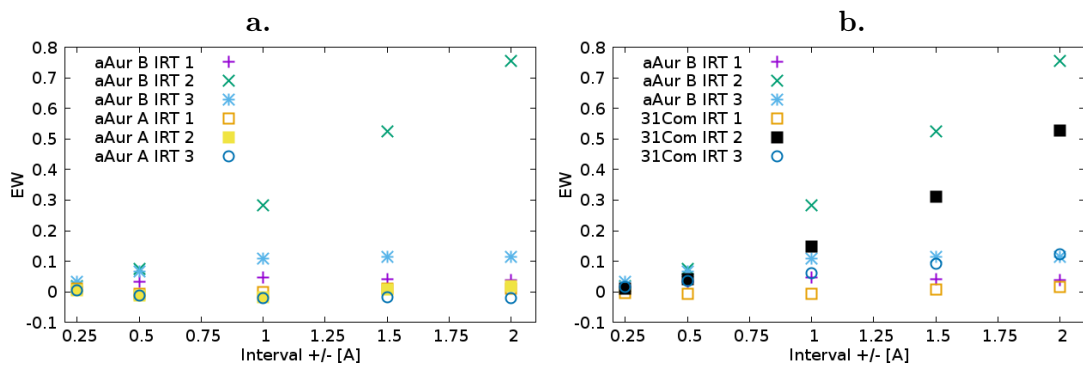


Figure 5.9.: Residual equivalent width vs integration interval of the Ca II IRT. **a:** Capella A and B, **b** Capella B and 31 Com. IRT1, 2, and 3 corresponds to λ 8498, 8542, and 8662.

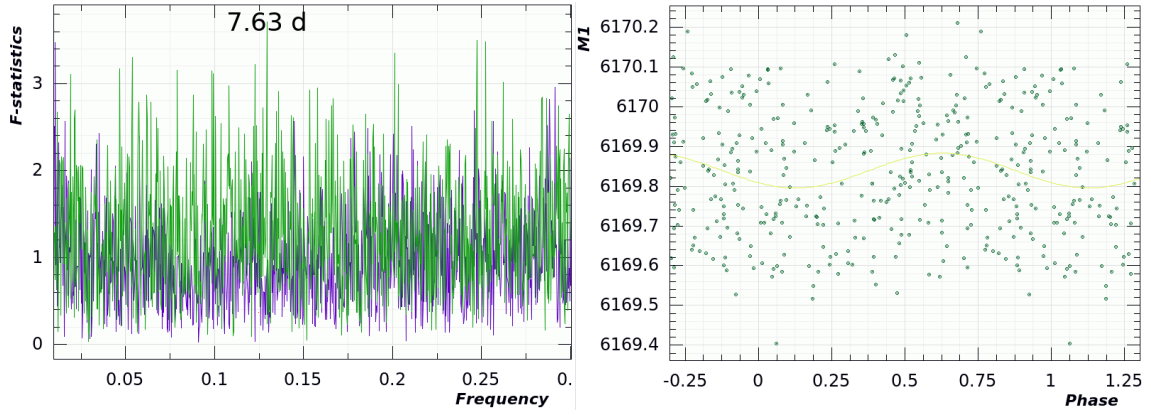


Figure 5.10.: Left: Frequency plot for the artificial data, right phase diagram for 7.63 days.

servations. A periodic distortion of the line-profiles were added to mimic a spot crossing the line-profile with a period of 8.16 days and an amplitude of 0.07. The detection limit of that value corresponds to a SNR of 14 in the line core and 50 in the continuum. The phase diagram and frequency spectrum is shown in Fig. 5.10. The reconstructed period based on a single line is $7.63 \pm 1.2 \times 10^{-4}$ (fit error) with a FAP of only 0.506. Hence, such peaks represent the detection limit and can not be considered as significant.

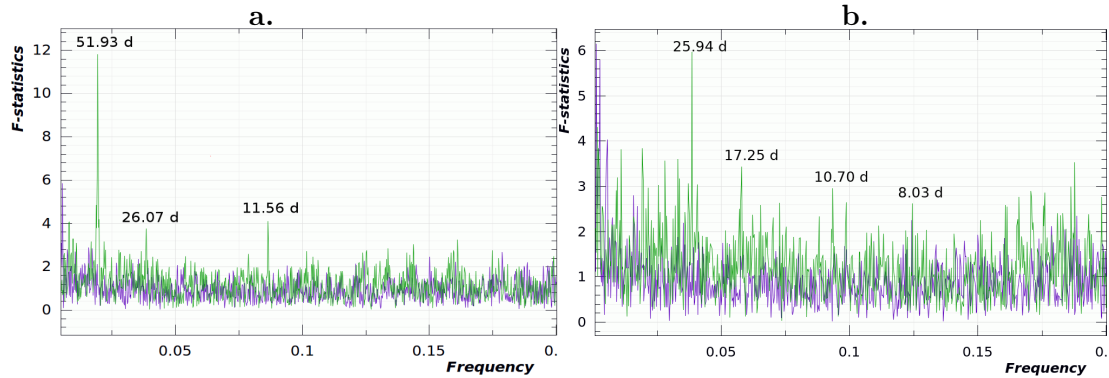


Figure 5.11.: An example of the period diagram. Green is the data, violet the window function. Shown is the data for the equivalent width of the blue Mg I b triplet. (a) Primary EW from Mg I b λ 5167 Å. The strong peak at the left is the half orbital period (52 d). Followed by a further harmonic of the orbit and the found 11 day period (second highest peak). (b) As a but for the secondary. Left two peaks may associated with the orbital period, followed by the 11 day period and a 8 day period. Latter one is also present in the window function.

An example of the frequency spectrum is shown in Fig. 5.11. This is based on the EW of the Mg I b triplet. The found periods for the computed line moments and are summarised in the Appendix D.2. As can be seen in Fig. 5.11b, the 8 day period is uncertain in this data, since the window function shows a peak there as well. From all the detections of the period around 11 days, a final value of 11.3 ± 0.6 is derived by a weighted average according to their FAP values. The difficulty in determining the period of the actually more active component may indicate, that its surface is spread with many small active regions (mentioned also by Wood & Ayres, 1995). This would smear the rotation signal in

the frequency analysis. Instead, the signal of the primary is clearly visible. Considering the errors, periods between the 11 days and 52 days (half orbital period) can be explained as further alias from the orbital period equal to the rotation period of the primary.

References

- Asplund, M., Grevesse, N., Sauval, A. J., & Scott, P. 2009, *ARAA*, 47, 481
- Busà, I., Aznar Cuadrado, R., Terranegra, L., Andretta, V., & Gomez, M. T. 2007, *A&A*, 466, 1089
- Fuhrmann, K. 2011, *ApJ*, 742, 42
- Ilyin, I. 2019, in preparation
- Paxton, B., Bildsten, L., Dotter, A., et al. 2010, *ApJS*, 192, 3
- Paxton, B., Schwab, J., Bauer, E. B., et al. 2018, *ApJS*, 234, 34
- Press, W., Teukolsky, S., Vetterling, W., & Flannery, B. 1992, *Numerical Recipes*, 2nd ed. (Cambridge University Press: Cambridge)
- Reimers, D. 1975, *Memoires of the Societe Royale des Sciences de Liege*, 8, 369
- Seber, G. & Lee, A. 2003, *Linear Regression Analysis*, 2nd ed. (WILEY)
- Strassmeier, K. G., Granzer, T., Weber, M., et al. 2004, *AN*, 325, 527
- Strassmeier, K. G., Weber, M., Granzer, T., & Järvinen, S. 2012, *AN*, 333, 663
- Takeda, Y., Hashimoto, O., & Honda, S. 2018, *ApJ*, 862, 57
- Torres, G., Claret, A., Pavlovski, K., & Dotter, A. 2015, *ApJ*, 807, 26
- Wood, B. E. & Ayres, T. R. 1995, *ApJ*, 443, 329

6. Summary and Outlook

A new scientific software package for spectral disentangling was presented (Manuscript I). It is based on singular value decomposition (SVD). This method to solve systems of linear equations has the advantage of the least-square nature of the solution. Hence, random variability such as noise is strongly suppressed in the disentangled spectra. Spectral disentangling is further defined as a template independent separation technique combined with an optimisation algorithm acting on the orbital elements of the spectroscopic binary (SB2). Hence, the solution of spectral disentangling consists of both the separated spectra and the orbital SB2 elements. Additionally, the impact of variability onto the results was studied as well (Manuscript II). This is particularly important, since all stars are variable in some amplitude. Hence, to understand the reaction of the technique under different kind of variability to improve the results, to interpret them and to gain knowledge about the variability itself it is of central importance. This was shown for several effects: (1) Flare as a sudden increase in continuum brightness, constant with wavelength. (2) Periodic variation of the line-width and the extraction of the period from the output of the disentangling. (3) A method to derive the flux-ratios of the components in each spectrum. Hence, two major differences of the presented code to other existing ones is (1) the possibility to optimise on the individual radial velocities (RV) in each spectrum and (2) to optimise on the flux-ratio of the two components within each observed spectrum. Point 1 is particularly advantageous to study disturbed systems. This disturbance can originate from a unknown or unseen third body or relativistic effects. In the case of optimisation on individual RVs, they do not have to be connected by an equation describing the orbital motion in dependence of time. Hence, it can account for several effects resulting in RV shifts of the component spectra. This may also include calibration errors on the wavelength axis. Point 2 on the other hand, makes it possible to account for shifts of the continuum axis. It provides the possibility to use the technique, e.g., on eclipsing systems. However, as long as the spectral region to be disentangled or the temperature variation is small, it can also account for irradiation/heating effects. This wavelength dependence of the flux-ratio is reserved for a future improvement of the code. However, despite all its advantages, SVD is a very time consuming method. Hence, a method to increase the speed of the optimisation process is necessary. This will be also part of further developments. It will be a combination of SVD and iterative subtraction as presented by González & Levato (2006). This approach however, needs an initial assumption of the spectrum for one component, say B. The computation is an iterative subtraction and as such much faster than SVD. Hence, the method to be implemented will be: (1) Initial spectra are computed from a first SVD. (2) The optimisation will proceed with these spectra and the iterative subtraction. (3) From time to time (after a significant number of iterations) another SVD will be performed to get better solutions for the disentangled spectra. Hence, the majority of the iteration of the optimisation process makes use of the fast iterative subtraction. (4) Only in a final run, the SVD is applied to derive the final orbital elements and disentangled spectra.

The revised carbon isotope ration (CIR) of 17.8 ± 1.9 of the primary of Capella (Manuscript III) is now in much better agreement with the model predictions by MESA (see Fig. 5.5) if an initial value of 82 is assumed and also with the predictions presented in Torres et al. (2015). Besides the computation of a whole grid of tracks by MESA a direct approach by

optimising on overshooting and mixing length lead to comparable results obtained by the grid calculation. However, it decreases the time for computation which is significant in case of Capella A, since the computation along the RGB is time consuming.

Optimisation rather than computing grids of tracks, leads to a more detailed derivation of the values for the overshooting and mixing length. The difference between the overshoot f of the two components may indicate a dependence on evolution or even on mass. Many studies have been undertaken to search for a dependence of the overshoot parameter value f_{ov} on mass or metallicity (e.g., Deheuvels, S. et al., 2016; Valle, G. et al., 2016, 2017; Schröder et al., 1997; Meng & Zhang, 2014). However, a clear answer on that question is still in strong debate. The used algorithm leads to similar values (difference of 0.1% only) for the mixing length of both components, $\alpha_{MLT,A} = 1.859$ for the primary and $\alpha_{MLT,B} = 1.861$, for the secondary, respectively. The difference of the overshoot parameter ($f_A = 0.0234$ and $f_B = 0.0188$, difference in age of 0.087 Myr) points towards a dependence on evolution, with a higher value for the more massive component A. If equal values are applied to both components, the optimisation leads to $\alpha_{MLT,A} = \alpha_{MLT,B} = 1.834$ and $f_A = f_B = 0.0208$ with an age difference of 0.494 Myr ($r_{\text{binary}} = 0.012591$, $r_A = 0.000417$, and $r_B = 0.011656$). These parameters are very close to those derived by Torres et al. (2015) of $\alpha_{MLT,A} = 1.85$, $\alpha_{MLT,B} = 1.80$, and $f_{ov,A} = f_{ov,B} = 0.020$. It has to be noted that in all cases, only overshooting during main sequence H-core burning was considered. Hence, the effect of the overshooting during the H-shell burning phase of the primary is neglected.

However, this can also relate to the evolutionary difference of both components. Nevertheless, these studies can strongly gain from a more precise determination of observables (L , T_{eff} , Z , M , R etc.) especially on brighter targets where high data quality can be achieved. This is particularly true for a precise determination of the initial value for Z , since it interferes strongly with the mixing length and overshooting, as stated in Sect. 5.1. However, one has to take in mind that the precision of masses of Capella was possible only by long-term observations over ten years. A necessity for facilities tuned to such observations of binaries exists in order to get a better understanding of the internal physics of stellar objects.

The determination of the rotation period of the secondary as performed in Sect. 5.2 is a rather expensive method, since the disentangling of such large data sets is a very time-consuming procedure. It finally depends strongly on the signal to noise ratio (SNR) of the individual observations. Most of the spectra used showed rather low SNR values for such a bright target (in the order of 50, see Table 5.2). However, for larger data sets, it could act as a method to provide 'observed' templates to improve the results from cross-correlation. As was also pointed out by Wood & Ayres (1995), the difficulty in determination of the rotation period of the more active secondary may be due to many active regions spread homogeneously over the surface.

The analysis in this thesis are based on high-resolution spectroscopic data. Applied to such a bright target as Capella, quality of the spectra used in Sect. 4 is excellent. It further demonstrates that observations of such bright targets with the best instruments can still contribute to the understanding of stellar physics. As demonstrated here by the very good agreement of the carbon isotope ratio revised in the mentioned article. However, since the results from observed data cannot be better as the data itself, the understanding of the behavior of the instruments to learn for future developments is also of central importance. Especially in view of its brightness and importance to stellar physics, Capella is an outstanding example. That is why there have also been great effort in instrumentation during the work on this thesis. This work is reflected by three publications

placed in the Appendix A. It is briefly summarised here. The simulation of the output of a planned instrument is important in order to proof if the instrument will perform such that it can tackle the science goal. Furthermore, this data can be used already in advance to create and test data reduction pipelines before the instrument is ready to observe. Besides the proof of specifications, this will lead to a more efficient use of the commissioning phase of the instrument. Hence, the work presented in Sect. A.1 describes a software package to simulate the output of spectrographs commonly used in astronomy. In Sect. A.2 this is put a step further and a high-resolution spectrograph is designed based on a new white pupil layout. This layout results from a consequent analysis of commonly used layout and logical improvements. The last section A.3 describes the fibre-link used to link PEPSI to the Vatican-Advanced-Technology-Telescope in order to make observations of bright targets possible. Work benefiting from this fibre-link was presented in Manuscript III and also in Strassmeier et al. (2018a). Finally, that work and significantly more resulted in a book publication, Sablowski & Schanne (2018).

References

- Deheuvels, S., Brandão, I., Silva Aguirre, V., et al. 2016, *A&A*, 589, A93
- González, J. F. & Levato, H. 2006, *A&A*, 448, 283
- Meng, Y. & Zhang, Q. S. 2014, *ApJ*, 787, 127
- Sablowski, D. P. & Schanne, L. F. 2018, *Astrophysikalische Instrumentierung und Messtechnik für die Spektroskopie*, 1st edn. (Selbstverlag, Mannheim, Germany)
- Schröder, K.-P., Pols, O. R., & Eggleton, P. P. 1997, *MNRAS*, 285, 696
- Strassmeier, K. G., Ilyin, I., & Weber, M. 2018a, *A&A*, 612, A45
- Torres, G., Claret, A., Pavlovski, K., & Dotter, A. 2015, *ApJ*, 807, 26
- Valle, G., Dell’Omodarme, M., Prada Moroni, P. G., & Degl’Innocenti, S. 2016, *A&A*, 587, A16
- Valle, G., Dell’Omodarme, M., Prada Moroni, P. G., & Degl’Innocenti, S. 2017, *A&A*, 600, A41
- Wood, B. E. & Ayres, T. R. 1995, *ApJ*, 443, 329

Acknowledgments

I would like to thank my supervisors, Klaus G. Strassmeier, Axel Schwope, and Michael Weber for their great support, time for discussions, and the opportunity to work free and independent.

There are more people I need to thank: Silva and Arto Järvinen, for support and help in many directions. Ilya Ilyin for all his time for discussions and support, especially in data reduction questions. Manfred Woche for his time for discussions about technical topics in optics. Gohar Harutyunyan, Christopher A. Sneden (MOOG), and, Nikolai Piskunov and Jeff Valenti (SME), for important support to get used to the synthesis codes. Matthias Steffen for his time for discussions about stellar atmospheres.

Last but not least, my family and friends not just to remind me that there is more than this thesis.

Selbstständigkeitserklärung

Hiermit erkläre ich, Daniel Patrick Sablowski, dass die an der Universität Potsdam eingereichte Promotionsarbeit

Spectroscopic analysis of the benchmark system α Aurigae

weder in vorliegender noch in abgewandelter Form an keiner anderen Hochschule eingereicht worden ist. Ebenso erkläre ich, dass die Arbeit nur mit den angegebenen Hilfsmitteln und Quellen selbstständig angefertigt wurde. Stellen die diesen Quellen und Hilfsmitteln dem Wortlaut oder dem Sinne nach entnommen wurden, sind kenntlich gemacht und in den Literaturverzeichnissen der einzelnen Kapitel aufgelistet.

Potsdam den

Daniel Patrick Sablowski

A. Contributions to Instrument Developments

A.1. SILENT: Spectrograph simuLation and EmulatioN Tool (Manuscript AI)

Daniel P. Sablowski¹ and Klaus Vollmann²

1: Leibniz Institute for Astrophysics Potsdam (AIP), An der Sternwarte 16, 14482 Potsdam, Germany
2: Deutsches Zentrum für Luft- und Raumfahrt e.V., Königswintererstr. 522, 53227 Bonn, Germany

Abstract

A software tool which was designed to compute basic optical parameters of spectrographs is presented. The idea is to find a first layout of the spectrograph by focusing on the science goal to which the instrument needs to be adapted. We focus on systems used in astrophysical instrumentation. These include classical, 3D and echelle spectrographs. The code also computes efficiencies of the specified systems, expected signal-to-noise ratios, layout of the spectral orders on the detector, etc. Furthermore, a complete image seen by the detector can be simulated. This artificial data are used to compare the performance of different designs and to test data reduction pipelines, before the system is being physically build. Some additional tools are implemented to characterise special optical devices, for example the telescope-spectrograph-interface and to support the design process. Hence, **SILENT** is a pre-design tool to determine the required optical paraxial parameters of the system to meet the science application.

A.1.1. Introduction

Since scientific measurements grow in their requirements on precision, it is of great importance to analyse the realistically simulated output of an instrument prior to physically building it. The common way to do this, is to create artificial data which reflects all know relevant impacts from the measurement chain. In astrophysical instrumentation this starts at the source, followed by intergalactic and interstellar medium, earth's atmosphere, telescope, instrument and ends at the digital output of the detector. Additionally, before performing detailed ray-tracing it is advantageous to compute overall parameters, e.g., wavelength coverage, spectral resolution, dispersion, sampling, grating anamorphism, etc., in a fast and simple way. This could already help to rule out designs which would not address the science case, the instrument has to be adapted for.

SILENT was designed to help the optical designer to find the correct design and to create realistic artificial data. This data can be used to inspect the spectral format on the CCD which is particularly important for 3D and echelle spectrographs. Furthermore, if the science case makes clear, that some spectral regions are of more importance than others, it is necessary to design such that these spectral regions are placed where maximum instrumental throughput is expected. This is especially important for echelle spectrographs, where these features need to be placed near the blaze maximum. Since all this can be done without taking into account all the details of aberrations and ray-tracing, **SILENT** uses basic

equations to compute all these parameters. The code is written in C++ and uses the Qt¹ library for the graphical user interface as well as OpenBLAS² for loop parallelisation.

We will first summarise the central equations as well as the output created by SILENT for the three implemented spectrograph types in Sect. A.1.2. In same section, equations to determine the necessary optical diameters in order to avoid vignetting are collected. The three main spectroscopic systems implemented are described in Sect. A.1.3. Further tools to support the pre-design process and for peripheral systems are discussed in Sect. A.1.7. Sect. A.1.8 is reserved for a design example of a simple spectrograph and a comparison with real data. The conclusion and discussion follow in the last Sect. 6.

A.1.2. Basic equations

In this section, the calculus and an overview of the equations implemented is given. This includes the calculation of the properties of the imaged spectrum as well as the sizes of the optical elements necessary to avoid vignetting.

The central equation is the equation for the reflective diffraction grating

$$\frac{m\lambda}{ng} = -\cos\gamma(\sin\alpha + \sin\beta), \quad (\text{A.1})$$

where m is the diffraction order, λ the wavelength, g the grating constant, n the refractive index of the surrounding medium, γ the off-plane angle, α and β the angles of incidence and diffraction, respectively. The minus sign results from a sign change by reflection. Sign convention is such that angles are measured towards the surface normal and are positive counter-clockwise. The proper use of transmission gratings is shown in Sect. A.1.8. The off-plane angle becomes important in some special spectrograph layouts (for example white pupil echelle).

Differentiating this equation with respect to the angle of diffraction, we get

$$\frac{d\lambda}{d\beta} = \frac{g \cos(\beta)}{m} \cos(\gamma) \quad (\text{A.2})$$

the angular dispersion, where we neglect the minus sign since we are interested in the absolute value. With the angular distance $p_x = f_{cam}d\beta$ of a pixel seen by the camera we get the linear dispersion per pixel on the detector (charge-coupled device, CCD)

$$D_x = \frac{p_x B_x g \cos(\beta)}{f_{cam} m} \cos(\gamma) \quad (\text{A.3})$$

when we use the focal length of the imaging camera, f_{cam} , the size, p_x , of a pixel in the direction of dispersion and the binning factor B_x on the CCD.

The two-pixel resolution is hence given by $d\lambda_{2p_x} = 2D$. In a similar way (differentiating with respect to α) we get the non-pixel-limited resolving power as

$$\frac{\lambda}{d\lambda} = f_{coll} \frac{m\lambda}{b_x g a \cos(\alpha) \cos(\gamma)}, \quad (\text{A.4})$$

where $a = \cos(\alpha)/\cos(\beta)$

is the anamorphism of the grating, b_x the width of the input slit and f_{coll} the focal length of the collimating optics. The Nyquist factor is defined as

$$N \equiv \frac{b'_x}{2p_x} \quad (\text{A.5})$$

¹<https://www.qt.io/>

²<https://www.openblas.net/>

the ratio between the size of the imaged slit width $b' = ba f_{cam}/f_{coll}$ and the size of two pixels. In order to avoid undersampling this ratio should be greater than unity.

These geometrical spectral parameters are computed by **SILENT** and written to local files. They can be plotted vs wavelength within the program. The modifications of the presented equations for the white pupil layout were presented in Sablowski et al. (2018).

Additionally, the program computes efficiency data. We use an analytical approximation for the blaze function (see Gray, 2005) and the user is free to set the peak value. The number of present optical surfaces is specified. The surface efficiency for each surface type will be interpolated for the computed wavelength points. The data can be easily replaced by custom data which should be provided by the manufacturer (see also Sect. A.1.2.4).

For all three types of spectrographs implemented, **SILENT** calculates the following parameters: resolving power, 2-pixel resolving power ($\lambda/d\lambda_{2px}$), spectral dispersion, anamorphism, imaged slit width, Nyquist sampling factor, transmission of earth atmosphere, Eq. (A.27), number of photons at the telescope entrance,

approximated CCD efficiency, efficiency of the diffraction grating, efficiency of all optical surfaces, efficiency of the instrument and overall efficiency (instrument + atmosphere). See also Table A.1 for an overview of all input parameters.

A.1.2.1. Basic design considerations

In this section, the question of the minimum achievable spectral resolution for a given telescope-spectrograph combination is discussed.

Given a telescope with an effective focal length of f_{tel} and a local seeing angle of σ , the size of a point source in the focal plane of the telescope is

$$d = f_{tel} \tan \sigma \quad (\text{A.6})$$

Let us interpret d as the full-width at half-maximum (FWHM) of the Gaussian intensity distribution of the point source in the focal plane. Hence, a slit of width d and infinite length vignettes about 24 per cent of the light. This is considered here as a good compromise between throughput and spectral resolution. If we further consider a grating of length e inclined at an angle of incidence α , the maximum allowed focal length of the collimator is given by

$$f_{coll} = F_{tel} e \cos \alpha, \quad (\text{A.7})$$

where $F_{tel} = f_{tel}/D_{tel}$ is the F-number, and D_{tel} the diameter of the telescope, respectively. The total angle $\Phi = \beta - \alpha$ at the grating is the angle between the incoming and diffracted beam. This is a user defined value (input parameter). The geometry at the grating has to be considered here such that the sign of Φ is properly chosen. With $K = m\lambda/g$ and Eq. (A.1), one gets

$$\alpha = \arcsin \left(\frac{K}{2 \cos(\Phi/2) \cos(\gamma)} \right) + \Phi/2. \quad (\text{A.8})$$

With the use of Eqs. (A.4), (A.6), and (A.7) one obtains

$$d\lambda = g \tan \sigma \frac{D_{tel}}{em} \frac{\Lambda_+}{\Lambda_-} \quad (\text{A.9})$$

an equation for spectral resolution, were

$$\Lambda_{+,-} = \sqrt{1 - \left(\frac{K}{2 \cos(\Phi/2) \cos(\gamma)} \right)^2} \pm \Phi/2. \quad (\text{A.10})$$

The important point in Eq. (A.9) is the factor D_{tel}/e . In high-resolution spectroscopy, a large telescope aperture has to be compensated by a large grating to achieve high spectral resolution. Further discussion of the influence of a fibre, image slicer, and sampling in the image plane can be found in Sablowski & Schanne (2018).

A.1.2.2. Aperture sizes

Besides the presented optical parameters, the sizes of the optical elements necessary to avoid vignetting is of central importance. This section describes how these values are determined in SILENT. Hence, the sizes of the apertures calculated here need to be taken as minimal values for the effective optical dimensions. Since the useful aperture of an optical element is often specified by 90% of its physical dimension, all apertures need to be enlarged by at least 10%. In addition, one also has to account for the mechanical mounting.

For the grating spectrometer the minimum diameter of the collimator is simply given by

$$d_{coll} = f_{coll}/F_{tel}. \quad (\text{A.11})$$

However, in case of a relay optic (e.g., after the fibre and/or image slicer) and the use of a fibre which will introduce focal-ratio-degradation (FRD, e.g., Clayton, 1989; Eigenbrot et al., 2012; Sablowski et al., 2016), one gets

$$d_{coll} = FRD f_{coll}/(F_{tel} V_{RO}), \quad (\text{A.12})$$

where V_{RO} is the magnification of the relay optic and $FRD = F_{in}/F_{out} > 1$ is the ratio between the F-number at the input and the exit of the fiber. The width of the grating corresponds to the given collimator diameter Eq. (A.12) and the necessary grating length results from the diameter of the collimated beam and the angle of incidence α at the grating,

$$d_g = FRD f_{coll}/(F_{tel} V_{RO} \cos \alpha). \quad (\text{A.13})$$

In the case of the classical spectrograph the angular dispersion of the grating Eq. (A.2) must be taken into account, i.e. the subsequent apertures must be larger than the collimator diameter d_{coll} . The minimum size of the camera aperture d_{cam} is therefore additionally dependent on the distance between the grating and camera front lens $\Delta l_{g,cam}$ and the size of the CCD (Eversberg & Vollmann, 2015, p. 166 Eq. (4.5)),

$$d_{cam} = d_{coll} + \Delta l_{g,cam} \cdot 2 \tan \left(\frac{N_x p_x}{2 f_{cam}} \right), \quad (\text{A.14})$$

where $N_x p_x = l_{x,CCD}$ is the length of the CCD in direction of echelle dispersion. Furthermore, the available wavelength range can be determined with the angular dispersion and the size of the CCD (Eversberg & Vollmann, 2015, p. 165 Eq. (4.4))

$$\Delta \lambda = \frac{d\lambda}{d\beta} \cdot \frac{N_x p_x}{f_{cam}} \quad (\text{A.15})$$

The same concept applies to the cross disperser of the classic echelle configuration. In this case, an additional dispersing element is inserted in front of the camera, which must also have a corresponding size in order to avoid vignetting. If a blazed grating is used as cross disperser, the minimum length l_{CD} is determined by the beam diameter d_{CD} and the grating angle of incidence $\alpha_{CD,g}$

$$l_{CD} = a_{max} d_{CD} / \cos(\alpha_{CD,g}), \quad (\text{A.16})$$

where $a_{max} = \max[\cos(\alpha)/\cos(\beta)]$ is the maximum value of the anamorphic magnification. In case of constant angle of incidence α , it corresponds to the maximum value of the angle of diffraction seen by the CCD

$$a_{max} = \cos(\alpha)/\cos(\beta_{max}) \quad (\text{A.17})$$

Since the anamorphic magnification alters the beam diameter in direction of dispersion only, the width of the grating w_{CD} is again given by the beam diameter

$$w_{CD} = d_{CD} = d_{coll} + \Delta l_{g,CD} \cdot 2 \tan\left(\frac{N_x p_x}{2f_{cam}}\right). \quad (\text{A.18})$$

In this case, the parameter $\Delta l_{g,CD}$ indicates the distance from the echelle grating to the cross disperser. If a prism acts as cross dispersing element, the angle of incidence $\alpha_{CD,p}$ is used in Eq. (A.16) to determine the necessary length of the cathet of the prism. The height of the prism is again determined by Eq. (A.18). The optimal angle of incidence on the prism can have large values. For example in the case of the frequently used F2 as glass material, values in the range of 50 to 55 degrees are used. Therefore, the prism must have correspondingly large dimensions. SILENT computes that angle in order to get symmetric path through an equilateral prism for the central wavelength, $\alpha_{CD,p} = \beta_{CD,p}$. Hence, the total deviation with respect to the input ray is $\Phi_{CD,p} = \alpha + \beta - 60^\circ = 2\alpha - 60^\circ$. By this assumption and with the law of refraction, one gets $\alpha_{CD,p} = \arcsin[n_{LZ,p} \sin 30^\circ]$, where $n_{LZ,p}$ is the index of refraction of the prism glass at the central wavelength λ_{LZ} . The aperture of the camera for the classical echelle is given again by Eq. (A.14).

In order to determine the required size of the CCD chip, the lengths of the orders must be calculated. From the grating equation Eq. (A.1), all central wavelengths of the specified orders can be determined by

$$\lambda_{LZ}(m) = -\frac{2g}{m} \cos \gamma \sin \Theta_B \cos(\Phi/2) \quad (\text{A.19})$$

using the addition theorem for $\sin(\Theta_B \pm \Phi/2)$ and the identities $\sin \alpha = \sin(\Theta_B + \Phi/2)$ for the angle of incidence and $\sin \beta = \sin(\Theta_B - \Phi/2)$ for the diffraction angle. The total angle Φ between the incident and the diffracted beam is predefined by the selected spectrometer setup. With the help of the angular dispersion, the CCD dimensions and the camera focal length, the spectrum in the focal plane can be fully simulated.

In the special case of an echelle spectrometer the available CCD area is completely filled with the imaged orders. The procedure for the calculation of the echellogram is described in more detail in section 3.2 and is in principle also valid for the classical spectrograph design with only one order. In a further step, SILENT checks whether there is enough space available on the CCD for the echelle orders. For this purpose, the edge wavelengths are determined from successive orders. This overlap is given by the difference of the red edge wavelength of order m and the blue edge wavelength of order $m + 1$. The overlap in units of wavelengths vs order number is shown graphically in the GUI. As long as this number is positive, overlap exists.

In case there is no overlap, a larger CCD chip must be selected. However, sufficient wavelength overlapping is essential to ensure that the separated orders can be merged as smoothly as possible. For this reason, the CCD chip gets generously dimensioned in echelle dispersion direction, i.e. from experience at least 10% larger than the order with the largest free spectral range would be required. According to (Eversberg & Vollmann, 2015, p. 200 Eq. (5.6)), the most extended order is the one with the smallest order number imaged on the CCD, that corresponds to the highest wavelength detectable.

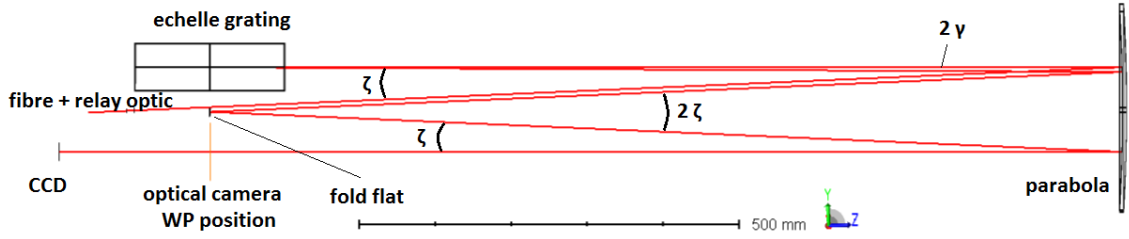


Figure A.1.: Layout of a WP echelle with one parabola acting as the main, 2nd, and transfer collimator. Only a central ray is drawn to visualize the main path clearly. The light is entering from left from the fibre, followed by a relay optic. Close to the relay optic is the fold-flat, see also Fig. A.2a.

The white pupil echelle configuration differs from the classic echelle by two additional optical elements that create an intermediate focus. The great advantage of the white pupil system is the largely suppressed spread of the beam behind the secondary collimator and the associated aperture reduction of the following optical elements. As a further result, the requirements for the correction of the imaging elements decrease considerably. As an example we consider the simple configuration III shown in (Sablowski et al., 2018) with only one paraboloid as collimator and $f_{coll1} = f_{coll2} = f_{trans} = 1200\text{mm}$, see also Fig. A.1 as reference for the following calculations. For this arrangement, the angle γ and thus the resulting distance between the fiber input and the intermediate focus must be as small as possible in order to keep the unavoidable off-axis errors of the parabolic mirror small. Due to the dispersion of the echelle, a spectral strip of overlapping orders is formed in the intermediate focus, whereby the length l_m of the m th order is given by the product of the angular order spread $\Delta\beta$ and the focal length of the transfer collimator

$$l_m = f_{trans} \cdot 2 \tan(\Delta\beta/2) \quad (\text{A.20})$$

As mentioned above not only the free spectral range but also the necessary overlapping regions of the orders must be taken into account for the angular extension. In order to image the echellogram completely on the CCD without vignetting, the geometric angular extent for the design of the folding mirror is therefore used for the angular spread

$$\Delta\beta = \Delta\beta_{CCD} = 2 \arctan\left(\frac{N_x p_x}{2f_{cam}}\right) \quad (\text{A.21})$$

In our example arrangement a 4524(H) x 3624(V) KAF16200M CCD with a pixel size of $6\mu\text{m}$ is used. The blaze angle of the echelle grating is $\Theta_B = 73^\circ$. With a camera focal length of $f_{cam} = 200\text{mm}$ the orders $m = 60$ to $m = 155$ can be imaged on the CCD with sufficient overlap. With $\gamma = 0.25^\circ$ a separation of 10.45mm between input and diffracted beam is generated. For the given parameters, SILENT gives the wavelength interval of the longest ($m = 60$) order on the CCD from $0.997153\mu\text{m}$ to $1.01803\mu\text{m}$ in the near infrared wavelength region. The corresponding diffraction angles are $\beta_{min} = 69.12^\circ$ and $\beta_{max} = 76.88^\circ$. Thus the 60th order has a length of 162.9mm in the intermediate focus according to Eq. (A.20), which is in good agreement with the corresponding ZEMAX calculation shown in Fig. A.2a. Subplot A.2b shows the footprint of that order on the transfer mirror part of the paraboloid. The change in shape of the beam cross-section is due to the grating anamorphism and modulates the extend of the beam in direction of dispersion, see Fig. A.2b. The required size for the transfer collimator is obtained from

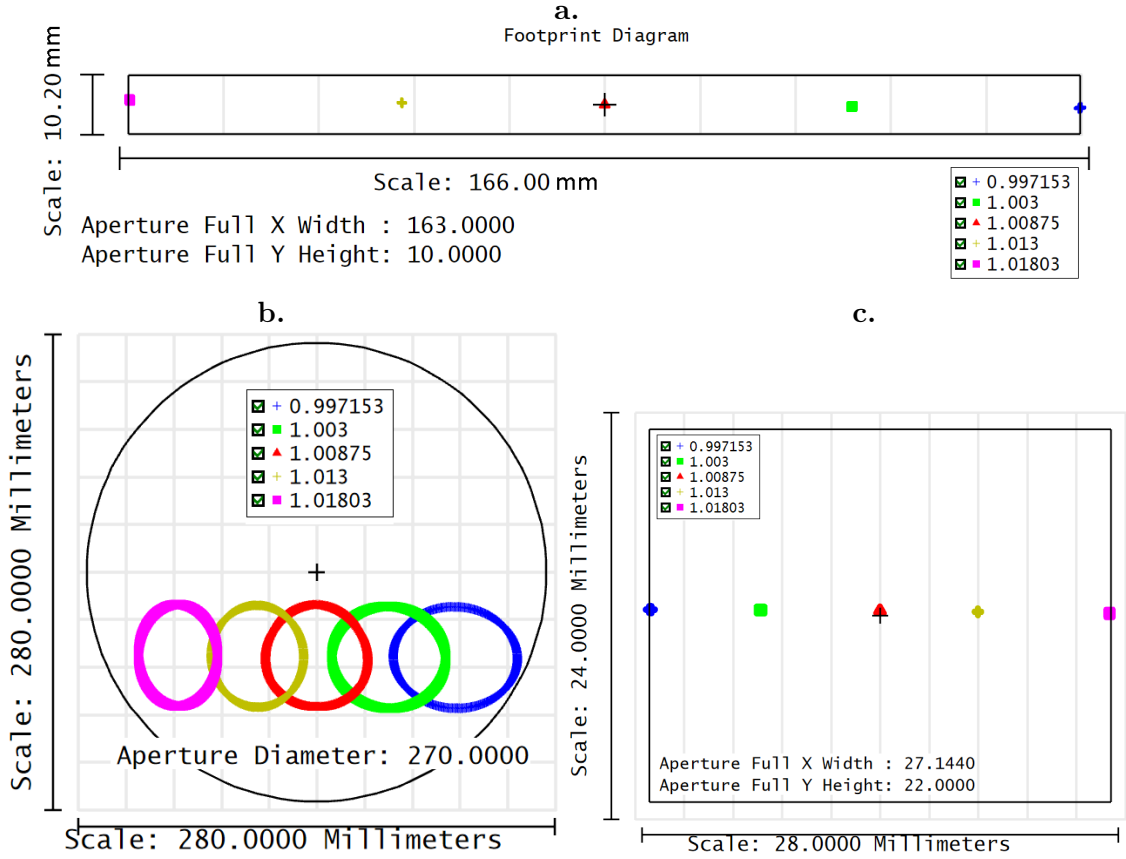


Figure A.2.: Footprints for the WP echelle. **a:** Shows the fold-flat near the intermediate focus between second-pass of main collimator and transfer collimator. **b:** For the transfer collimator. **c:** At the detector surface. Wavelengths are such that the CCD is completely filled. These wavelengths correspond to diffraction order $m = 60$ and are taken from SILENT output. See text for more details.

the length of the longest order and the expanded beam diameter again modulated by the anamorphic magnification (see Eq. A.17), $2a_{max}d_{coll}/2$

$$d'_{trans} = f_{trans} \cdot 2 \tan(\Delta\beta/2) + d_{coll}a_{max} \quad (\text{A.22})$$

which leads to the result $d_{trans} = 162,9\text{mm} + 60\text{mm} \cdot 1.29 = 240.3\text{mm}$. Note that the transfer collimator could be smaller, since the anamorphic magnification is < 1 for the red wavelength at the edge of the widened order. However, in order to center the central wavelength again on the center of that mirror, one has to use the maximum anamorphic magnification. Otherwise all following optical components would be displaced, which would unnecessarily increase the effort in mechanical design. Furthermore, the diameter is modulated by the off-axis distance of the beams from the mirror center. This angle is given by the angle of the beam emerging from the slit towards the central axis of the parabola. In this example, it was assumed to be $\zeta = 2.5^\circ$. Hence, the distance from the center is $y_1 = \tan(2.5^\circ) \cdot 1200\text{mm} = 52.39\text{mm}$. In addition, one also needs to consider the off-set, y_{fl} , of the fold-flat created by the off-plane angle $\gamma = 0.25^\circ$, $y_{fl} = 2 \tan(0.25^\circ) \cdot 1200\text{mm} = 10.47\text{mm}$. Therefore, the diameter of the mirror is given by

$$d_{trans} = 2\sqrt{(d'_{trans}/2)^2 + [f_{trans} \tan(\zeta) + f_{coll2} \tan(\gamma)]^2}, \quad (\text{A.23})$$

which yields 271.20mm for our example (see Fig. A.2b). For the more general case of different collimator focal lengths (e.g. design example in Sablowski et al., 2018), **SILENT** adjusts the focal length in Eq. (A.20). We note that in this configuration, the diameter of the parabola is primarily determined by Eq. (A.23). For other configurations, the diameters of the individual mirrors can be different. However, the shown equations can be used to calculate the diameters.

Recalling the great advantage of a WP echelle: The diffracted beam reflected at the transfer mirror will be combined at the pupil of that mirror (white pupil, WP). Hence, the beam size at that position is determined by the maximum value of the anamorphism and the monochromatic beam size at the transfer collimator. The maximum anamorphic magnification of the beam according to Eq. (A.17) yields for the diffraction angle given above $\cos(73^\circ)/\cos(76.88^\circ) = 1.29$. Therefore, the extend of the white pupil is simply given by

$$d_{WP} = d_{coll} a_{max}. \quad (\text{A.24})$$

The actual diameters necessary for the CD and optical camera depend on the angular dispersion and the distance from the WP. Let $\Delta l_{CD,WP}$ be the distance between the white pupil and the CD, hence

$$d_{CD} = d_{WP} + \Delta l_{CD,WP} \cdot 2 \tan(\Delta\beta/2). \quad (\text{A.25})$$

In case of a CD in transmission (e.g. prism), one needs to consider its thickness Δt_{CD} . The diameter of the entrance surface of the optical camera is obtained in the same way

$$d_{cam} = d_{WP} + \Delta l_{cam,WP} \cdot 2 \tan(\Delta\beta/2), \quad (\text{A.26})$$

where $\Delta l_{cam,WP}$ is the distance between the white pupil and the front surface of the optical camera.

In Fig. A.2c, the extend of the order on the CCD (without a CD) is shown and indicates a very good agreement between the ZEMAX results and the **SILENT** computed wavelength range covered by the CCD.

A.1.2.3. Target and telescope specification

The signal- to noise-ratio is of central importance for all measurements. Therefore, a stellar source approximated by Planck radiation can be specified in **SILENT**. The target specification takes several parameters into account: The transparency of the earth atmosphere in dependence of the angular distance z from zenith and the wavelength λ is approximated by (e.g., Wischnewski, 2018)

$$T_{earth} = 1 - 9.1224 \times 10^{-3} / (\lambda^4 (0.025 e^{-11 \cos z} + \cos z)) \quad (\text{A.27})$$

the contribution of Rayleigh scattering, $\propto \lambda^{-4}$, and the air mass. Further, the visual magnitude, m_{vis} , as a scale to the Planck radiation, $10^{-0.4(m_{vis})}$, the temperature, T_{eff} , of the black body and the exposure time, t_{exp} . In addition, the telescope parameters include: The diameter of the primary and the diameter of a vignetting aperture (e.g. secondary mirror), the effective focal length of the telescope, the seeing angle and the dimensions of the slit as circular, rectangular or slitless.

A.1.2.4. Efficiency calculation

To estimate the efficiency of the instrument, **SILENT** allows to specify the surface efficiency curves in dependence of the wavelength and the number of the surfaces present in the

system with this efficiency. Currently, the user can specify five different surface efficiency curves, which are reflective aluminium, reflective silver, reflective gold, reflective UV enhanced aluminium and anti-reflection coating. These files are simple ASCII files and can be replaced by user defined data. In addition, the user can use its own efficiency file, e.g. provided by a ray-trace software. This file could also represent internal transmission of the optical glasses, since they are not separately taken into account by **SILENT**.

Efficiency at the slit is calculated by the assumption of a Gaussian intensity distribution with a full-width at half-maximum (FWHM) corresponding to the seeing angle and the telescope focal length.

A.1.2.5. Detector

Detector response is simulated by taking several quantities into account: The pixel size, the number of pixels in x and y, the binning in x and y, bias (or offset) in ADU, noise in electrons, peak efficiency and wavelength and the gain factor. These parameters are saved for several common CCDs in an editable database file. The noise in the database refers to the manufacturer value of the read-noise. Hence, in real world application, the user may wish to manipulate that value according to its experience such that all additional noise sources are taken into account. Not taken into account is the dark current since it is usually very low, but could be indirectly accounted for with the CCD bias and noise level.

Since, the length of the detector in x (parallel to the spectral dispersion) will limit the spectral coverage, the calculation of the parameters is in dependence of the x coordinate rather than the wavelength. However, all parameters are functions of wavelength.

When calculating a full CCD frame, **SILENT** computes the contribution of flux to each pixel. Such an calculation can be very time consuming, especially for spectra with many lines (absorption or emission), since the contribution of each line to any pixel will be computed. That is why the computation of the frame is parallelised with the **OpenBlas** library.

A.1.3. Main systems

This section describes the three main spectroscopic systems implemented in **SILENT**. All the previous shown equations and procedures hold for them and the additions and differences are pointed out here. All necessary input parameters are summarised in Table A.1.

A.1.4. The classical spectrograph

All standard designs (Littrow, Czerny-Turner, etc.) with one diffraction element fall into this category. We have implemented standard diffraction grating and volume-phase-holographic grating (VPHG) as options for the diffractive element. In Fig. A.3 we show a CCD frame of 2048 x 1024 pixels with a Balmer absorption continuum. We have also applied an image slicer which generates the six spectra visible.

Devices like image slicer and relay optics are specified by the telescope-spectrograph interface (TSI, see Sect. A.1.7.3).

In addition to the calculated parameters as listed in Sect. A.1.2, one can calculate the spectrum of Neon, Balmer and Planck radiation. The line list of the first two can be modified by the user to calculate other spectra.

Furthermore, the SNR is simulated by Gaussian distributed noise. The width, w_y , of the spectrum perpendicular to the direction of dispersion (y -axis) is calculated. The number of photons, S , within the wavelength bin which corresponds to the size of a pixel in direction

Table A.1.: Summary of all input parameters for the calculation of spectrograph properties. Plus indicates applicable, minus not applicable to either the classical (C.), 3D, and echelle (E.) system.

Parameter	Unit	C.	3D	E.
Grating const., g	1/mm	+	+	+
Diffraction order, m		+	+	-
Blaze angle, θ_B	grad	+	+	+
Grating Peak efficiency, η_g		+	+	+
Total angle, Φ	grad	+	+	+
Wavelength range	nm	-	-	+
Central wavelength, λ_{LZ}	nm	+	+	-
Collimator focal length, f_{coll}	mm	+	+	+
Camera focal length, f_{cam}	mm	+	+	+
Transfer Coll. focal length, f_{trans}	mm	-	-	+
2nd Coll focal length, $f_{coll,2}$	mm	-	-	+
Cross-Disperser (CD) type		-	-	+
CD grating const., g_{CD}	1/mm	-	-	+
CD grating peak efficiency, η_{CD}		-	-	+
CD glass material		-	-	+
CD index of DCG layer, n_2		-	-	+
CD DCG layer index modulation, Δn		-	-	+
CD DCG layer thickness, d	mm	-	-	+
CD VPHG tune wavelength, λ_{tun}	nm	-	-	+
Number of Ag surfaces, N_{Ag}		+	+	+
Number of Al surfaces, N_{Al}		+	+	+
Number of Au surfaces, N_{Au}		+	+	+
Number of AR surfaces, N_{AR}		+	+	+
Number uncoated surfaces, N_{unc}		+	+	+
Object effective temperature, T_{eff}	K	+	+	+
Object zenith distance, z	grad	+	+	+
bolometric correction, BC	mag	+	+	+
Object visual magnitude, m_{vis}	mag	+	+	+
Exposure time, t_{exp}	sec	+	+	+
Seeing angle, σ	arcsec	+	+	+
Telescope focal length, t_{tel}	mm	+	+	+
Telescope diameter, D_{tel}	mm	+	+	+
Telescope vignetting diameter, D_{vig}	mm	+	+	+
Slit type		+	+	+
Slit width, b_x	mm	+	+	+
Slit length, b_y	mm	+	+	+
Number of pixels in x, N_x		+	+	+
Number of pixels in y, N_y		+	+	+
Pixel size in x, p_x	mm	+	+	+
Pixel size in y, p_y	mm	+	+	+
Binning in x, B_x		+	+	+
Binning in y, B_y		+	+	+
CCD bias	ADU	+	+	+
CCD read noise, R	e-	+	+	+
CCD peak efficiency		+	+	+
CCD peak wavelength		+	+	+
CCD gain	e-/ADU	+	+	+
Number of slitlets		-	+	-

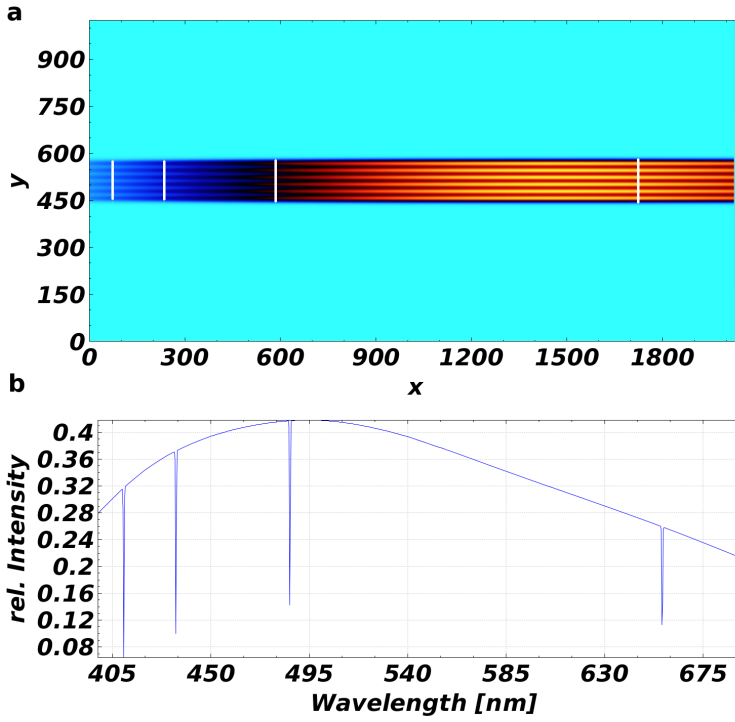


Figure A.3: **a:** Computed image of a balmer absorption spectrum on a Planck continuum as imaged by a classical spectrograph with a six-time image slicer. **b:** Spectrum of one slice from the image above. The spectrum is now shown vs. wavelength which allows an identification of the Balmer lines within the 2D image.

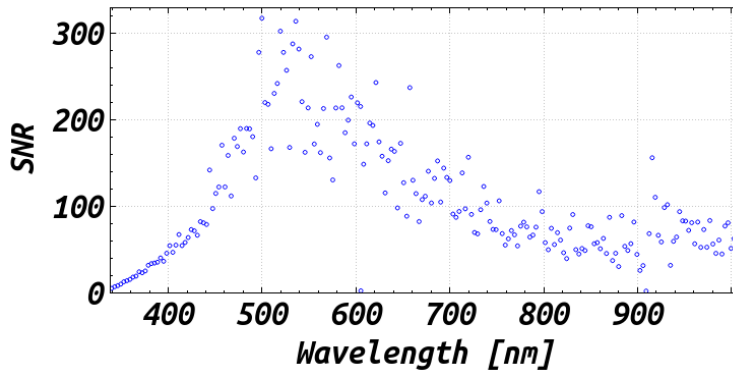


Figure A.4: Example output from the SNR simulation (see Text).

of dispersion (x -axis) is distributed over the width of the spectrum by a Gaussian normal distribution, $P_n(y)$. The amount of noise in each pixel is given by the $\sqrt{S_y} = \sqrt{SP_n(y)}$, where $S = S \int_{w_y} P_n(y)$. The read noise, R is added such that the whole noise contribution is given by $N = \sqrt{R^2 + S_y}$.

The program combines the rows (perpendicular to dispersion) by an weighted average and measures the SNR in spectrum pieces of 10 pixel width (in dispersion direction, can be changed by the user). The weights are again given by $P_n(y)$. An example of the output of that simulation is shown in Fig. A.4.

The equations presented in Sect. A.1.2.1 are also implemented. Given a grating size, the minimum reachable resolving power and the maximum focal length under the above made assumptions are calculated as a guide for the setting of the parameters. These calculations are not limited to the classical spectrograph. Hence, it may also be consulted in the design process of an echelle or 3D spectrograph.

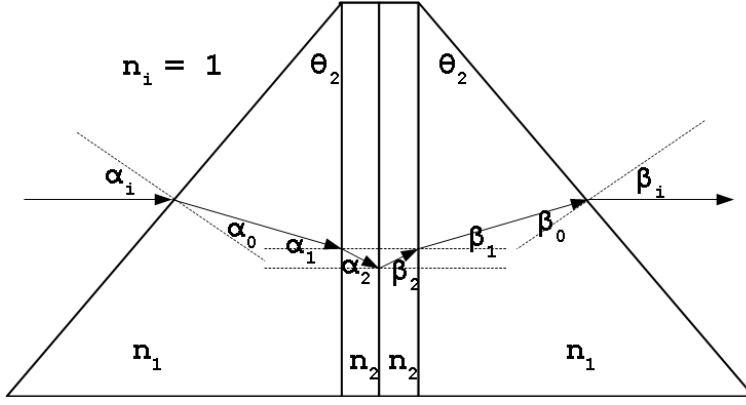


Figure A.5: Geometry at the VPH-Grism. Light is entering from left. It is assumed that both prisms are made from the same material and have same geometry.

A.1.5. The echelle spectrograph

The main window of the program is designed to set up the parameters of an echelle spectrograph. In addition to the equations given above, one has to consider two further aspects: (1) The cross-disperser (CD) and (2) the parameters of a white pupil layout (see e.g. Sablowski et al., 2018). There are four different elements implemented for the CD, a standard diffraction grating, a volume phase holographic grating (VPHG), a equilateral dispersive prism and a VPH-grism.

The grism is assumed to be in symmetric mode, such that the central wavelength λ_{LZ} passes through it without a deviation, see Fig. A.5. For symmetry at the grating $\alpha_2 = \beta_2 = \alpha_B$, the grating equation gives

$$\alpha_B = \arcsin \left[\frac{m\lambda_{LZ}}{2g_{CD}n_{2,LZ}} \right], \quad (\text{A.28})$$

where m and g_{CD} is the diffraction order and grating constant of the grating, and $n_{2,LZ}$ the index of refraction of the grating material at the central wavelength. Snell's law yields

$$\begin{aligned} n_{1,LZ} \sin \alpha_1 &= n_{2,LZ} \sin \alpha_2 \\ \alpha_1 &= \arcsin \left[\frac{m\lambda_{LZ}}{n_{1,LZ}2g_{CD}} \right] \end{aligned} \quad (\text{A.29})$$

the angle inside the prism. Furthermore, from the drawing one gets $\theta_2 = \alpha_i$. Again with Snell's law

$$\alpha_0 = \arcsin \left[\frac{n_{i,LZ}}{n_{1,LZ}} \sin \alpha_i \right]. \quad (\text{A.30})$$

Another relation from the drawing is $\alpha_1 = \alpha_i - \alpha_0$. Together with Eq. (A.30) and $\theta_2 = \alpha_i$ one finds

$$\alpha_1 = \theta_2 - \arcsin \left[\frac{n_{i,LZ}}{n_{1,LZ}} \sin \theta_2 \right]. \quad (\text{A.31})$$

Rearranging and use of Eq. (A.29) leads us to

$$\theta_2 = \arcsin \left[\frac{m\lambda_{LZ}}{n_{1,LZ}2g_{CD}} \right] + \arcsin \left[\frac{n_{i,LZ}}{n_{1,LZ}} \sin \theta_2 \right] \quad (\text{A.32})$$

the angle for the two prisms of the grism according to the specified glass (see also Sablowski & Schanne, 2018). Here, $n_{1,LZ}$ is the index of refraction of the prism at the central wavelength λ_{LZ} and $n_{i,LZ}$ the index of refraction of the surrounding medium. This

angle is computed by **SILENT** and printed to a text field in the GUI. The calculation of the VPHG efficiency is described in Sect. A.1.7.1.

The angle of diffraction β_i for a ray passing the VPH-grism is obtained by a surface-to-surface calculation. Hence

$$\alpha_0 = \arcsin\left(\frac{n_i}{n_1} \sin \alpha_i\right) \quad (\text{A.33})$$

and

$$\alpha_2 = \arcsin\left(\frac{n_1}{n_2} \sin \alpha_1\right) \quad (\text{A.34})$$

with $\alpha_1 = \alpha_i - \alpha_0 = \theta_2 - \alpha_0$ yields

$$\alpha_2 = \arcsin\left[\frac{n_1}{n_2} \sin\left(\theta_2 - \arcsin\left(\frac{n_i}{n_1} \sin \theta_2\right)\right)\right]. \quad (\text{A.35})$$

Furthermore, the grating equation yields

$$\beta_2 = \arcsin\left(\frac{m\lambda}{n_2 g_{CD}} - \sin \alpha_2\right) \quad (\text{A.36})$$

and again with Snell's law

$$\beta_1 = \arcsin\left(\frac{n_2}{n_1} \sin \beta_2\right) \quad (\text{A.37})$$

and

$$\beta_i = \arcsin\left(\frac{n_1}{n_i} \sin \beta_0\right), \quad (\text{A.38})$$

with $\beta_0 = \theta_2 - \beta_1$

$$\beta_i = \arcsin\left(\frac{n_1}{n_i} \sin(\theta_2 - \beta_1)\right). \quad (\text{A.39})$$

Putting Eqs. (A.37), (A.36), and (A.35) into Eq. (A.39) leaves us with

$$\beta_i = \arcsin\left\{\frac{n_1}{n_i} \sin\left[\theta_2 - \arcsin\left(\frac{m\lambda_{LZ}}{n_1 g_{CD}} - \sin\left(\theta_2 - \arcsin\left(\frac{n_i}{n_1} \sin \theta_2\right)\right)\right)\right]\right\}. \quad (\text{A.40})$$

Since the calculation of a whole echelle spectrum can be time consuming, a fast overview function is implemented to get a quick estimate of the wavelength coverage on the selected detector. The calculation of the parameter yields averaged efficiency, averaged signal, and averaged SNR for each spectral order imaged onto the detector. Furthermore, the central distance between neighbouring spectral orders is shown graphically as well as the overlap of orders in wavelengths units. This helps to make sure that the spectrum does not show gaps and orders do not suffer from cross-talk in the direction perpendicular to the direction of the echelle dispersion.

Furthermore, the echellogram can be computed to get a quick idea of the distribution of orders on the CCD. This calculation is identical with the calculation of the image frame and is carried out in the following manner: The central wavelength, λ_{LZ} , is computed and defines the angle of diffraction, β_{LZ} , towards the center of the CCD. The half angle of the image is hence given by $\beta_{CCD} = \arctan(l_{x,CCD}/2f_{cam})$ the half length of the CCD and the focal length of the optical camera. Hence, the calculation starts from $\beta_{LZ} - \beta_{CCD}$. The calculation runs in a loop for each pixel in direction of dispersion. In each iteration

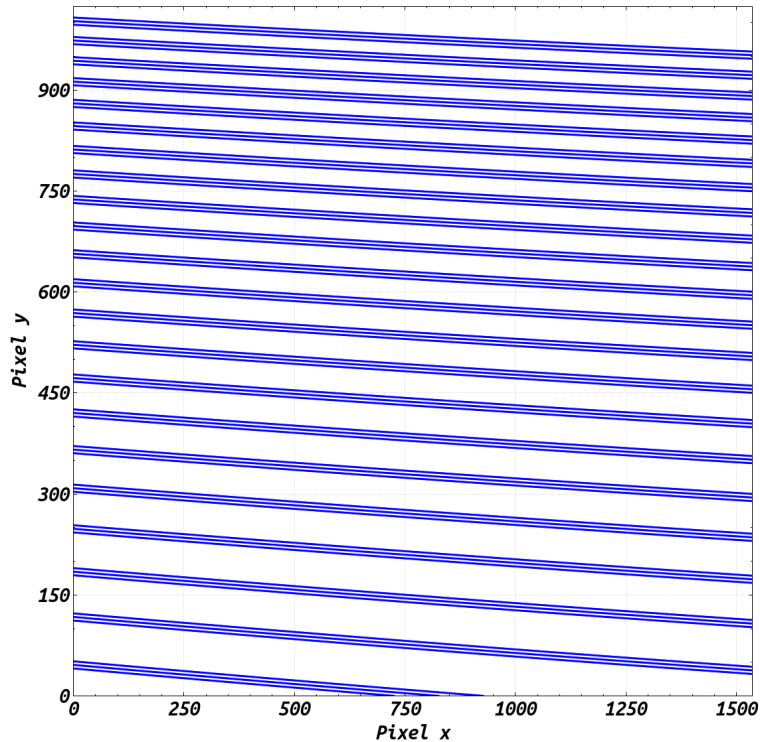


Figure A.6.: Example of an echellogram computed by SILENT. Parameters of the system are: $g = 79$ l/mm, blaze angle of 63.4 deg, $f_{coll} = 125$ mm, $f_{cam} = 120$ mm, lower and upper wavelength 400 and 700 nm, a grating with 300 l/mm for cross-dispersion and a CCD with 1536x1024 pixels each 9 μ m square.

of the loop, the new angle of diffraction towards the actual pixel is calculated from which in turn the wavelength is obtained via the grating equation etc. The position of the spectrum perpendicular to the echelle dispersion is calculated in the same way but with the properties of the CD. An example is shown in Fig. A.6. It draws three lines per order: The central position and the position \pm FWHM of the order. The FWHM is given by the size of the specified slit as imaged by the optics onto the detector. The data is saved to a file (echellogram.dat). It list relative and absolute order number, lower, central and upper wavelength of each order on the CCD and indicates with yes or no if there is overlap between adjacent orders.

A.1.6. The 3D spectrograph

3D spectrographs are used to study spatially extended objects such as galaxies and nebulae. Therefore, it is necessary to use an optical device (integral field unit, IFU) in the focal plane which transfers the 2-dimensional surface into a slit and feeds it to the spectrograph entrance. This can be, for example, achieved by a densely packed bundle of optical fibres. They can be easily rearranged to form an elongated slit. However, more sophisticated techniques such as the advanced image slicer are applied (Content et al., 2018). Many examples can be found in the literature, e.g., Dubbeldam et al. (2000); Kelz et al. (2006).

A similar approach is used for multi-object spectrographs. However, such an instrument needs to even rearrange the individual fibres in the focal plane of the telescope to target thousands of stars at the same time, e.g., Croom et al. (2012); de Jong et al. (2016).

The 3D spectrograph is basically just a multiplication of the classical one. The user can

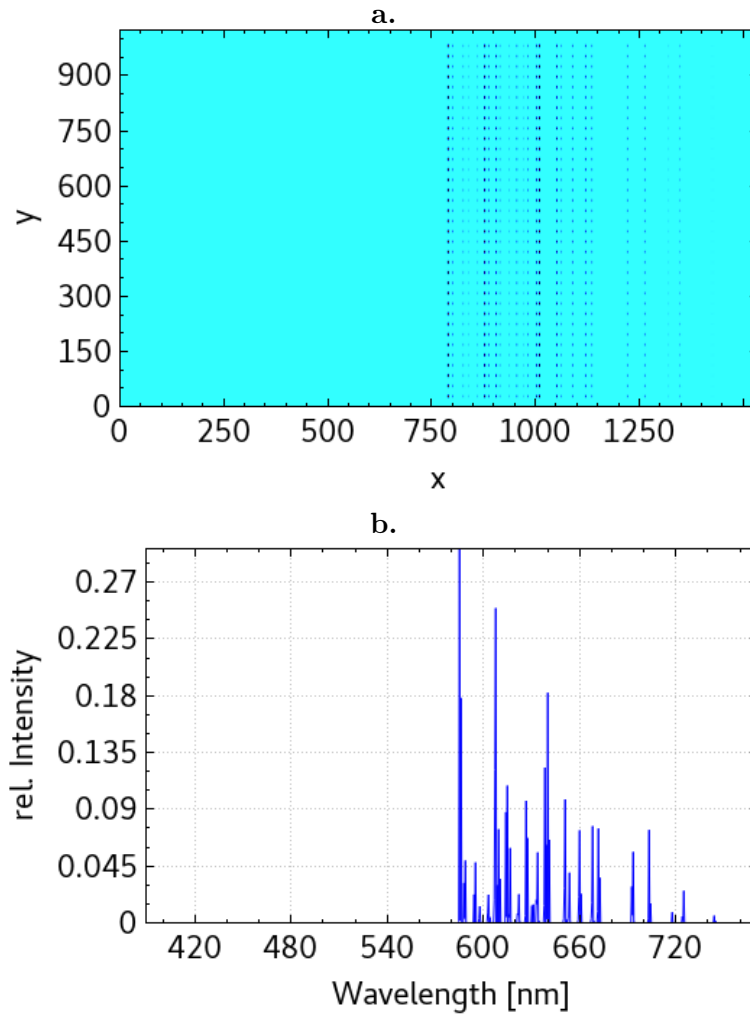


Figure A.7.: Example of an image **a** and a single spectrum **b** of an 3D spectrograph as calculated by SILENT. 35 single slitlets were computed for a neon emission spectrum.

specify the number of the slitlets to be computed. An example is shown in Fig. A.7. At top, the image on the CCD from 35 slitlets and fed with a neon lamp are shown. Bottom shows a single neon spectrum. It is worth noting that despite the tool is named 3D, it can also be interpreted as multi-object (single diffraction order) system.

A.1.7. Additional tools

This section will introduce the additional tools implemented in SILENT. They are dedicated to support the design process of the instrument and for peripheral sub-systems.

A.1.7.1. Volume phase holographic grating

VPH gratings can be of advantage in terms of peak efficiency. However, they are limited in bandwidth and show interesting polarization effects. Hence, it is important to specify the properties very well in order to get maximum performance parameters. The tool implemented here has two applications: The evaluation of the behavior of the efficiency for S, P and non-polarised light in dependence of the properties of the dichromated gelatine (DCG) layer and the behavior of the efficiency when the grating is tuned, that is, used in

wavelength ranges out of its initial design wavelength.

The efficiency calculation is based on the approximation by Kogelnik (1969). Which holds as long as

$$\frac{\lambda^2}{g^2 n_2 \Delta n} > \rho_{limit} \quad (\text{A.41})$$

is fulfilled, where n_2 is the mean index of refraction of the DCG layer and Δn its amplitude of modulation. The common value for the limit is $\rho_{limit} \approx 10$. Furthermore, the approximation is valid for the first diffraction order, $m = 1$. Hence, with $\beta = \alpha = \alpha_B$ the Bragg angle, Eq. (2.1) and (A.41) leads us to

$$\sin \alpha_B > \sqrt{\rho_{limit} \Delta n / (4n_2)} = \sin \alpha_{min}. \quad (\text{A.42})$$

One can see, that the Bragg angle depends on the properties of the DCG layer only. Beams with an incident angle far from the Bragg angle may pass the VPHG without diffraction, maximum diffraction efficiency peaks at the Bragg angle. Following the formalism of Kogelnik (1969), the diffraction efficiency is

$$\eta_S = \sin^2 \left(\frac{\pi \Delta n d}{\lambda \cos(\alpha_B)} \right) \quad (\text{A.43})$$

for S polarised,

$$\eta_P = \sin^2 \left(\frac{\pi \Delta n d}{\lambda \cos(\alpha_B)} \cos(2\alpha_B) \right) \quad (\text{A.44})$$

for P polarised, and

$$\eta = (\eta_S + \eta_P) / 2 \quad (\text{A.45})$$

for non-polarised light. We note that a slant ϕ can be introduced to the "grooves" of the VPHG, $\alpha_B = \alpha - \phi$. Such a slant leads to non-symmetric path and introduces anamorphism. It can be of advantage to suppress the occurrence of ghost images. In a transmission VPHG, the modulation is parallel to the grating surface. Reflection occurs for structures perpendicular to the grating surface. Reflecting VPHG are known to suffer from significantly smaller bandwidth and are hence less common (e.g., Barden et al., 2002).

The VPHG tool implemented calculates the

$$\alpha_B = \arcsin(\lambda / (2n_2 g)) \quad (\text{A.46})$$

Bragg angle and

$$\Delta n < \lambda^2 / (\rho_{limit} g^2 n_2) = \Delta n_{max} \quad (\text{A.47})$$

the maximum of the allowed amplitude of the index modulation such that the approximation by Kogelnik (1969) is fulfilled.

As an example, two illustrative cases are shown in Fig. A.8 and listed in Table A.2.

From the grating shown at top, the selection effect of a VPHG to polarisation is nicely visible. With a proper thickness, S and P polarised light can be separated. While one will be diffracted with 100 per cent efficiency, light with the perpendicular polarisation will be reflected. With a thickness of the DCG layer of around 11.6 μm , the grating shows 100 per cent diffraction efficiency for S polarised light. However, a glance to the right graph, which shows the efficiency for that thickness vs wavelength, demonstrates the limitation of bandwidth such a grating can be used.

The special case of the Dickson grating is shown at bottom in same Figure. The difference is a higher grating constant. It leads to 100 per cent diffraction efficiency for both polarisations at a thickness of the DCG layer of around 10.5 μm . The efficiency for S polarised light in dependence of wavelength is similar to the grating at top.

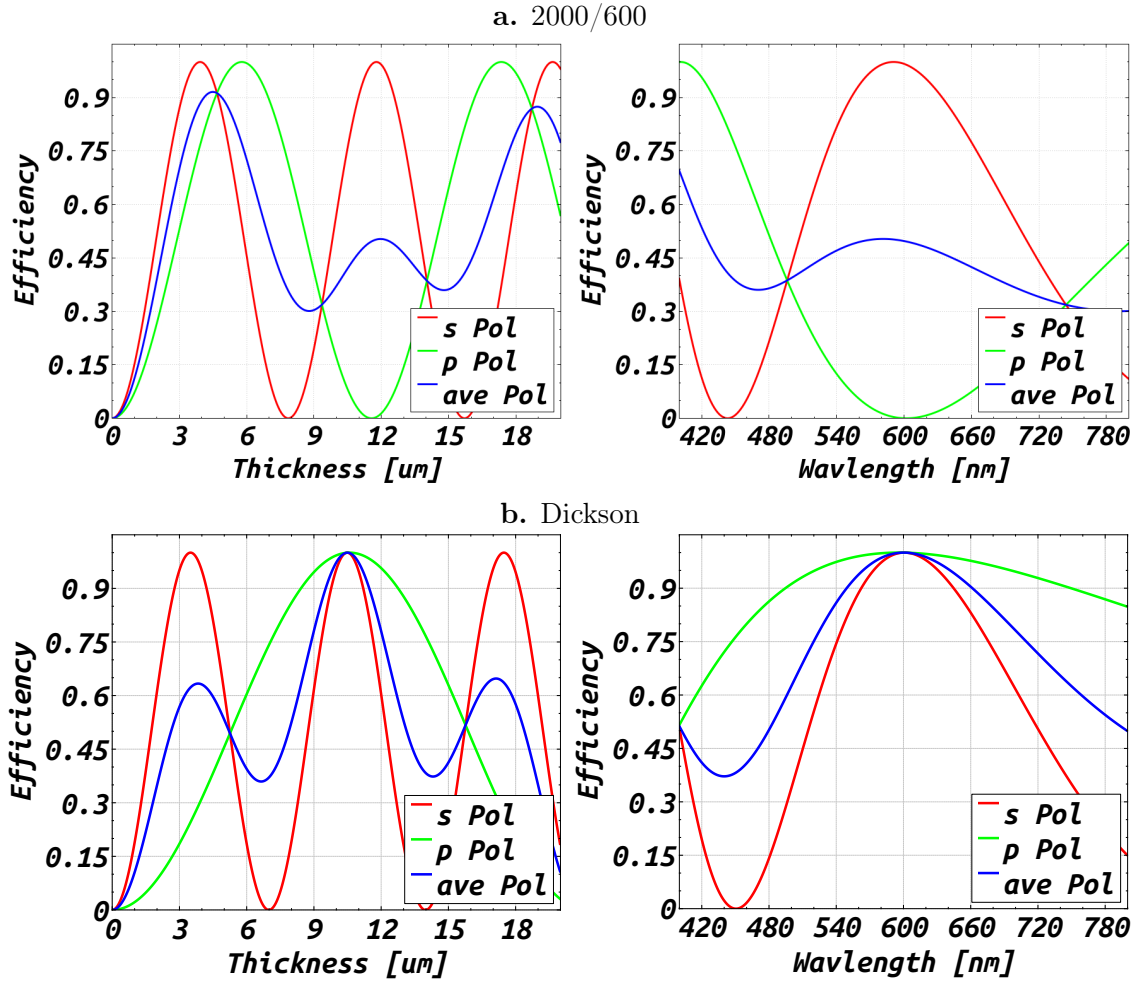


Figure A.8.: Example efficiency curves of VPHG. **a:** The special case of a grating with its polarizing selection effect is shown. It can achieve 100 per cent diffraction efficiency for one polarization, while the other light is reflected. Left vs thickness of the DCG layer and right vs wavelength for a thickness $d = 11.6\mu\text{m}$ of the DCG layer. **b:** The Dickson grating, as **a** but for a grating which peaks to 100 per cent for both polarizations at a thickness of $d = 10.5\mu\text{m}$.

	Dickson	2000/600
λ (nm)	600	600
g (1/mm)	2,890	2,000
n_2	1.4987	1.4987
α_B	35.36	23.61
α_{min}	20.00	20.00
λ_{min} (nm)	354	512
Δn_{max}	0.20	0.096
Δn	0.07	0.07
d (μm)	10.5	4.5

Table A.2: Parameters of the two example VPHG shown in Fig. A.8.

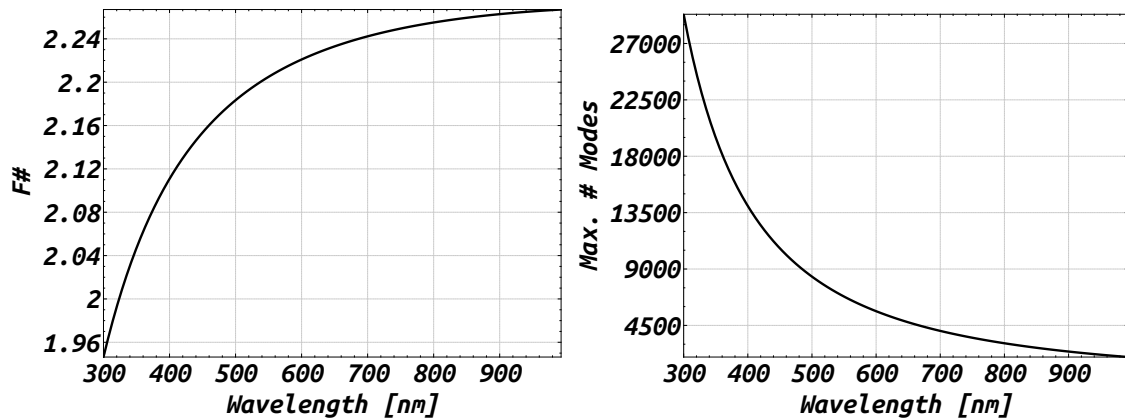


Figure A.9.: Left: The maximum accepted F-number vs. wavelength of an optical fibre with a silica core doped with 11.6 mol GeO₂. Right: For same doping but maximum number of excited modes vs. wavelength.

A.1.7.2. Optical fibres

Optical fibres are frequently used to link the telescope to a spectrograph and for peripheral applications such as calibration light coupling. The tool on optical fibres computes basic properties of optical fibres, such as numerical aperture, number of reflections, optical path length, number of excited modes and transmission based on user defined absorption data. It also gives the minimum allowed bending radius. The properties of the doped glasses in the catalog of fibre materials are from (Wehr & Wiechert, 1986; Butov et al., 2002) and cover 29 different materials doped with F, Cl, P, N, Al, B and GeO₂. As an example, the maximum accepted input F-number vs wavelength of a fibre with a silica 11.6 mol GeO₂ doped core is shown in Fig. A.9 left. The right graph of same figure shows the maximum number of excited modes for the same fibre type.

A.1.7.3. Telescope spectrograph interface

Is the spectrograph to be mounted via a fibre link, the design may make it necessary to add devices like image slicer and relay optics to adapt the fibre output to the collimating optics and the resolution of the spectrograph to the desired value. The telescope spectrograph interface (TSI) tool within SILENTis used to define these properties. The image slicer is currently implemented to be a Bowen Walraven (BW) type or a waveguide image slicer. In addition, the number of slices and the magnification of the fibre to image slicer relay optic can be specified. An example of the image formed by a five-way BW slicer is shown in Fig. A.10.

A.1.7.4. Fabry perot etalon

These devices have various applications. In high-resolution spectroscopy they can be used to record instrumentally induced shifts of the target spectrum to a high accuracy. Fed with continuous light, they provide a forest of intensity peaks in the spectrum. These peaks are equidistantly spread over wavelength. Hence, fitting these peaks provides an excellent statistic to determine internal drifts of the spectrograph. However, the interference spectrum is highly sensitive to the distance between the two mirrors of the Fabry perot etalon (FPE). Therefore, it has to be put into a stabilised environment.

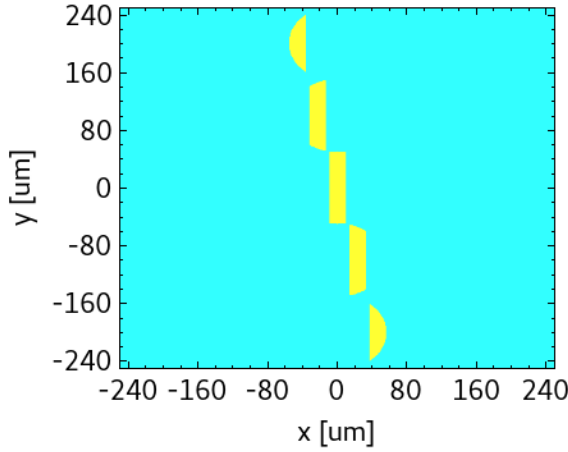


Figure A.10: Example of an image created by a five-way Bowen-Walraven type image slicer as created by the TSI tool. The user can specify the number of slices (up to seven), the magnification of the image onto the slicer and offsets in x and y between the slices.

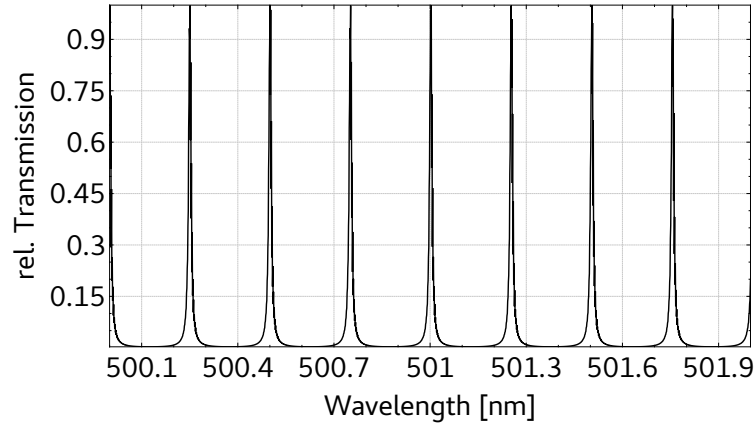


Figure A.11.: Fringe spectrum for a FPE with $d = 0.5$ mm, $R = 0.9$, and $\theta = 0$.

The FPE tool computes the fringe spectrum according to (e.g., Born & Wolf, 1999)

$$I_T = \frac{I_0}{1 + F_r \sin^2(OPD\pi/\lambda)}, \quad (\text{A.48})$$

were

$$OPD = 2d\sqrt{n^2 - \sin^2 \theta} \quad (\text{A.49})$$

is the optical path difference after double passing the medium with index, n , of thickness, d , between the mirrors under the angle, θ , and, $F_r = 4R/(1 - R)^2$, with the reflectivity, R , of the mirrors, (e.g., Sablowski & Schanne, 2018). An example of the computed fringe spectrum for a FPE with $d = 0.5$ mm, $R = 0.9$, and $\theta = 0$ is shown in Fig. A.11.

A.1.7.5. Czerny Turner

A very common spectrograph layout is the Czerny Turner (see Czerny & Turner, 1930, (CT)), which consists of the input slit, collimator mirror, diffraction grating, imaging mirror and detector. An exit slit is not considered here, since we are mainly interested in imaging rather than scanning systems. The literature about the CT spectrograph is very numerous (e.g., Lee et al., 2010; Austin et al., 2009; Pribram & Penchina, 1968).

Analytical studies of this design have shown, that it can be designed either for a coma corrected image (e.g., James, 2007) or a flat image plane (e.g., Beutler, 1945; Reader, 1969). To achieve this, the position of the grating with respect to the mirrors and the angles of

incidence on the mirrors need to be computed in a proper way. This tool will support that calculations to find an initial layout which can be further analysed and optimised within a sophisticated ray trace software.

For a coma-free image at a central wavelength λ_0 the

$$\frac{\sin \theta_2}{\sin \theta_1} = \left(\frac{R_2}{R_1} \right)^2 \left(\frac{\cos \alpha_0 \cos \theta_2}{\cos \theta_1 \cos \beta_0} \right)^3 \quad (\text{A.50})$$

Rosendahl condition has to be fulfilled (e.g., James, 2007).

Here, θ_1 and θ_2 are the angles at the mirrors, α_0 and β_0 the angle of incidence and diffraction at the grating corresponding to the wavelength of correction λ_0 , and R_1 and R_2 the radii of curvature of the mirrors, respectively.

For a flat image plane, one has to solve (see Reader, 1969)

$$C = -\frac{1}{4} \left[1 - 3 \left(\frac{Z}{R_2} \right)^2 \right] \theta_2^2 + \frac{1}{48} \left[1 - 30 \left(\frac{Z}{R_2} \right)^2 + 48 \left(\frac{Z}{R_2} \right)^3 - 27 \left(\frac{Z}{R_2} \right)^4 \right] \theta_2^4 \quad (\text{A.51})$$

for the angle at mirror 2, where Z is the distance between grating and mirror 2. This will give a constrain for Eq. (A.50) or vice versa. Two special cases are mentioned here. (1) $Z = R_2$ results in $\theta_2 = 0, \pm\sqrt{3}$. (2) $Z = 0$ is the use of a concave grating acting as diffractive element and camera and yields $\theta_2 = 0, \pm\sqrt{12}$. This layout is known as the Wadsworth configuration. Further discussion of the CT system can also be found in Sablowski & Schanne (2018).

A.1.7.6. Petzval lens

The Petzval lens is a simple optical system in the sense of the number of optical surfaces, which can be used to image the spectrum onto a detector. It consists of two achromatic lenses in some distance. Historically, however, the last doublet was also separated by a thin air gap. Nevertheless, since a large variety of achromatic doublets are available of the shelf, combinations of two glued doublets with sufficient optical quality may exist for a given application. Petzval lenses suffer from strong image curvature, which limits their applications. However, for slow spectrographs and small fields, the image may be imaged onto the detector with sufficient optical quality by such a lens.

The Petzval tool is basically a search algorithm to find the best combination of achromatic lenses available of the shelf. Constraints such as maximum and minimal diameters of the lenses, focal length and back-focus distance are set by the user. The database currently involves lenses from different well known manufacturers and can easily be modified by the user.

First step of the search is an analysis of possible combinations under assumptions of geometrical optics. In a second step, a full ray tracing of the found configurations can be performed. For this evaluation, the user can specify a set of wavelengths, fields and number of rays distributed evenly over the entrance aperture to create spot diagrams for each field. This results in a list of RMS spot values for the ten best systems found. The backfocus distance is also optimised by the use of the RMS value. The spot diagrams created by SILENTcorrespond to this optimised focus position.

Let us search for a Petzval with an entrance diameter of 40 mm, 135 mm focal length with a tolerance of 5 mm and a minimum back-focus distance of 40 mm. The following

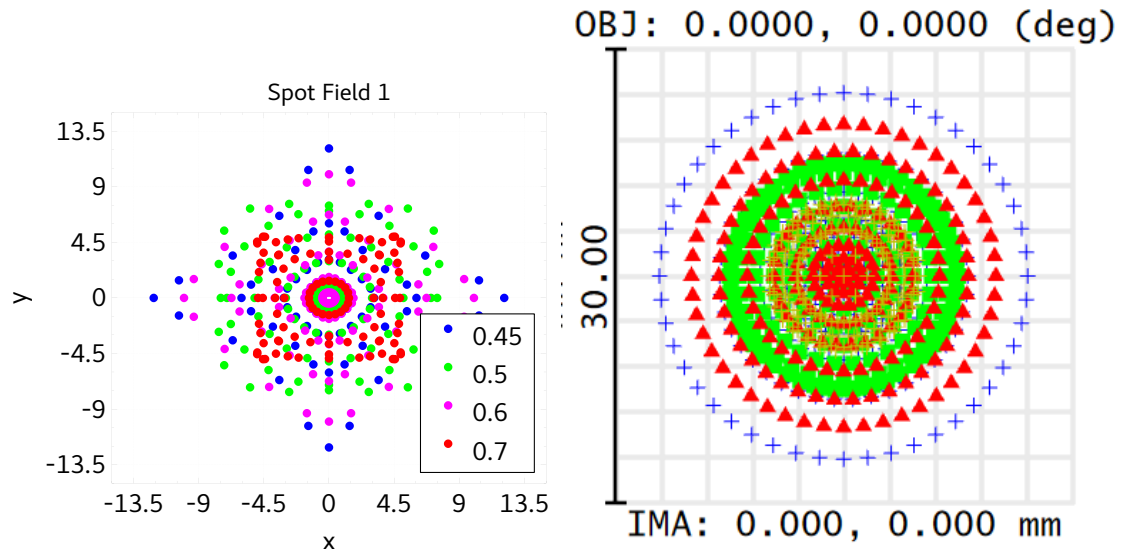


Figure A.12.: Spot diagrams on-axis for the example Petzval lens. Left from **SILENT** and right from **ZEMAX**. The legend refers to wavelength in units of micrometers. The overall size of the pattern is in very good agreement, The difference in shape originates from a different distribution of rays within the aperture.

constraints are applied to that search: Both lenses to be smaller than 51 mm. The front lens to be larger than 40 mm and the rear lens to be greater than 30 mm, respectively. The catalog of 284 achromatic lenses is a compilation of lenses from Thorlabs, Newport, Edmund Optics and Qioptiq. The search results in 1057 possible combinations. This number points out how helpless a search by a individual ray tracing would be. The ray tracing of all possible combinations leads to a best system in the sense of the on-axis RMS spot value averaged over wavelength. For the best combination found, the on-axis spot diagram calculated by **SILENT** and **ZEMAX** are shown in Fig. A.12.

It is worth noting, that this tool is not limited to find a lens for spectroscopic systems. It can be applied to any application, especially for test and evaluation set-ups within the optical laboratory.

A.1.7.7. Glass tool

In the design of refractive imaging systems, an important step is the selection of proper glasses to control aberrations. Therefore, that tool is used to find proper glass triples fulfilling the condition of superchromatism (see Herzberger, 1959). This condition is fulfilled if the partial dispersions, θ_b , for blue and, θ_r , red light of three glasses form a linear function in a θ_b - θ_r -diagram. Hence, the search algorithm picks two glasses and looks for a third one of all remaining glasses closest to the line defined by the two initial selected ones. The user can set constraints to combined transmission and a maximum deviation, d_{max}^2 , (squared difference, residuum) from the line by the third glass. In that way, only glasses with sufficiently high transmission in the blue and a good agreement with superchromatism are found. The combined transmission is computed in the following way: The user specifies a thickness t for the calculation of internal transmission based on the properties of the glass given in the glass database. The combined transmission of the glass triple is the transmission of light after it passes a block of each glass with each a thickness t . A combination is accepted if this combined transmission is above the specified value for all

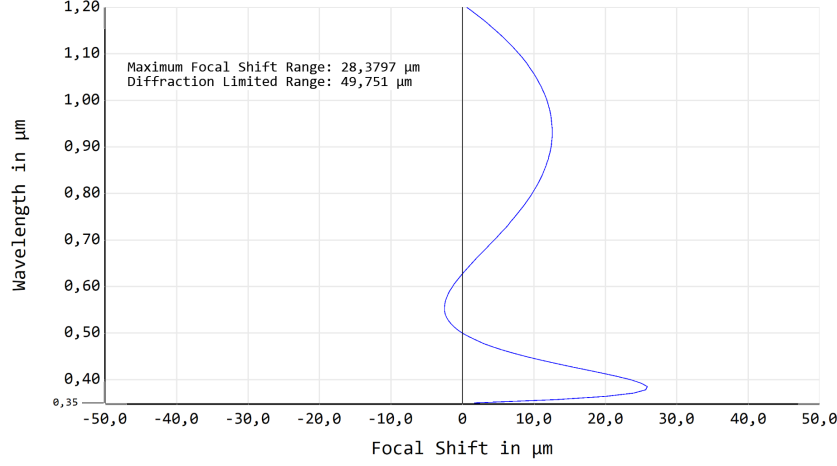


Figure A.13.: Focal shift of the superchromatic paraxial triplet described in text. The focal shift of 28.4 μm is well below the diffraction limit of 49.8 μm in the wavelength range of 350 to 1200 nm.

four user-specified wavelengths.

A good combination from a search within the catalogs of Schott and OHARA is N-BAF51, S-LAH55 and S-PHM52. For a given focal length, the tool computes the radii of an cemented paraxial triplet lens. For the first lens, it is assumed to have same radii but with opposite sign, $r'_1 = -r''_1$, and because of cemented lenses: $r'_2 = r''_1$ and $r'_3 = r''_2$. The effective power of the triplet is the sum of the single powers of the three lenses $F = F_1 + F_2 + F_3$, which one gets from the superchromatism boundary conditions to be (see Mehnert & Steinich, 2011)

$$\begin{aligned}
 F_1 &= \frac{v_1(\theta_3 - \theta_2)}{v_1(\theta_3 - \theta_2) + v_2(\theta_1 - \theta_3) + v_3(\theta_2 - \theta_1)} F \\
 F_2 &= \frac{v_2(\theta_1 - \theta_2)}{v_1(\theta_3 - \theta_2) + v_2(\theta_1 - \theta_3) + v_3(\theta_2 - \theta_1)} F \\
 F_3 &= \frac{v_3(\theta_2 - \theta_1)}{v_1(\theta_3 - \theta_2) + v_2(\theta_1 - \theta_3) + v_3(\theta_2 - \theta_1)} F,
 \end{aligned} \tag{A.52}$$

were $\theta_i = \theta_{b,i} = (n(350 \text{ nm}) - n_F)/(n_F - n_C)$ is the blue partial dispersion of glass i . The power is given by $F_i = (n - 1)(c_1 - c_2)$, were $c = 1/r$ is the curvature of the surface with radii r . It is further $\delta = \mu_F - \mu_C$ the main dispersion, were $\mu = n - 1$. With the assumptions above for the triplet and $F = 0.01\text{mm}^{-1}$ one obtains

$$\begin{aligned}
 r'_1 &= 2\delta_1/F_1 &= 16.2827 \text{ mm} \\
 r''_2 &= (-1/r'_1 - F_2/\delta_2)^{-1} &= 22.3999 \text{ mm} \\
 r''_3 &= (1/r''_2 - F_3/\delta_3)^{-1} &= 67.4236 \text{ mm}
 \end{aligned} \tag{A.53}$$

the three radii for the triplet. This system is corrected for chromatic focal shift from 350 nm to 1200 nm as can be seen from the focal shift diagram in Fig. A.13.

One should take in mind that this system is only corrected for color. All other aberrations are completely ignored. Hence, to control, e.g., spherical aberration it is necessary that the glasses span a wide range in dispersion given by the main Abbe number v . Therefore, a user-definable value to define the minimum value for the span in dispersion can be specified to that algorithm. For example, if a total transmission of $> 80\%$, a span in dispersion of > 40 and a minimum deviation of $d_{max}^2 < 10^{-5}$ is applied to a search within the Schott

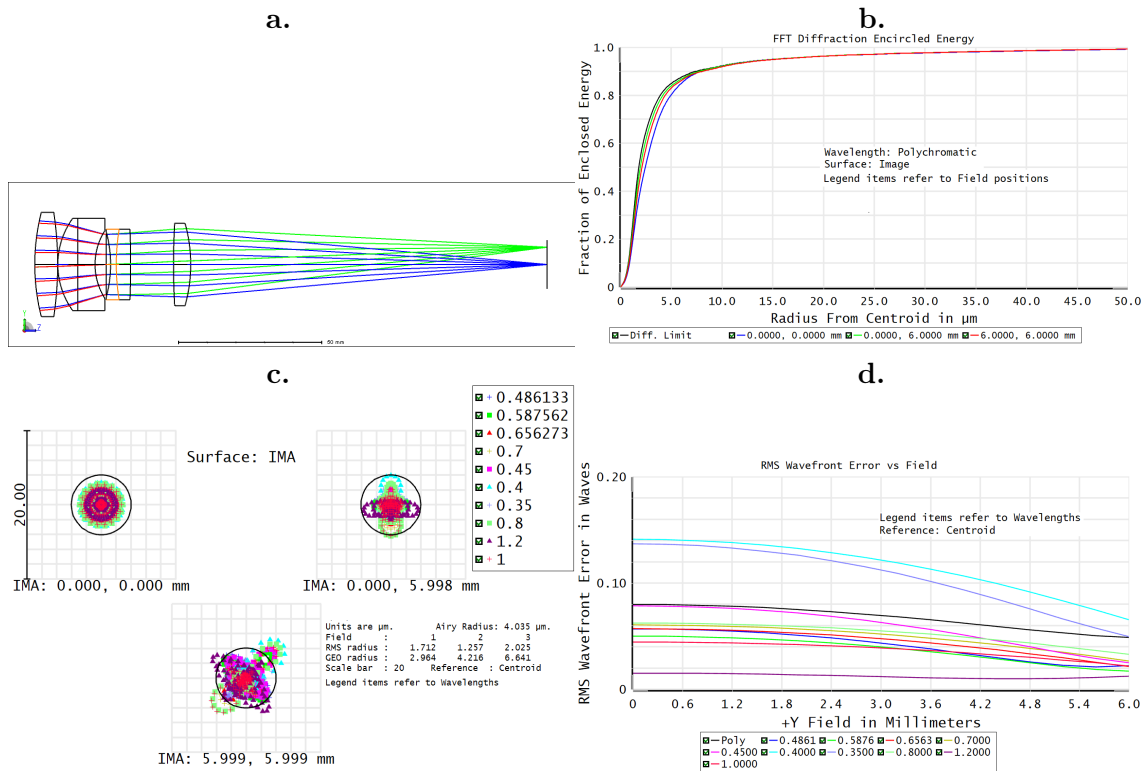


Figure A.14.: Optical performance of the double Gauss shown in Fig. A.14. **a:** Layout of the superchromatic double Gauss lens. **b:** Diffractive encircled energy for all colors and fields. The black line is the diffraction limit. **c:** Spot diagram for all colors. Airy disc is indicated by the black circle. **d:** Wavefront RMS plot again for all colors vs field.

and OHARA catalog, one gets about 20 combinations with available glasses. Hence, the tool can help to select initial glasses for a given design ansatz and to create glass catalogs. These catalogs can help to increase the convergence of the global optimisation process within an optical design software.

As an example, a superchromatic double Gauss lens was designed. The originally double Gauss lens consisted of two groups of two meniscus lenses, symmetrically arranged around the aperture and is also referred to as an anastigmatic system. Nowadays, this basic layout is used in many modified designs to achieve high image quality for higher F-numbers and fields. In comparison to the Petzval lens (discussed above), this lens combines surfaces with negative and positive optical power to reduce the influence of field curvature.

In this example, a modified version (historically the Summar from Leitz around 1930, see Brandt, 1956) with six lenses organised in four groups is used. The final layout is shown in Fig. A.14a and the listing in Table A.3. The optimisation of the system was carried out with a glass catalog of four superchromatic glass triplets (12 glasses). Wavelength range is from 350 nm to 1200 nm and the radius of the image is 6.0 mm. The performance of the system is summarised in Fig. A.14b-d and is diffraction limited in the considered wavelength range and field. The overall transmission of the system with applied antireflection coating is 79%. The peak value of 94% is at $\lambda 656.3$ nm, the lowest value of 60% at the highest wavelength of $\lambda 1,200$ nm, and the bluest of 70% at $\lambda 350$ nm. However, thicknesses were fine-tuned, especially for surface 6 (N-SSK2) to increase transmission at the far blue and pay with image degradation in the field. This design example shows the advantage of the use of a glass catalog limited to best glasses in the sense of color correction, transmission

Table A.3.: Listing for the superchromatic double Gauss as described in the text and shown in Fig. A.14.

Surface	Radius (mm)	Thickness (mm)	Material/Comment
0	72.943	8.000	S-FPL51Y
1	-119.997	0.050	AIR
2	27.270	7.000	N-FK58
3	-9172.944	6.000	S-BAL42
4	21.852	3.865	AIR
5	inf	1.560	STOP
6	-43.417	2.000	N-SSK2
7	75.088	5.000	PBL25Y
8	-346.717	15.000	AIR
9	263.632	6.000	N-FK58
10	-52.529	124.502	AIR
11	inf	-	image

and spread in dispersion to control aberrations.

In addition, basic properties of glasses can be visualised and glass catalogs from ZEMAX converted into SILENTreadable format. These internal catalogs are used by the Petzval tool and for the specification of the material of the echelle cross-disperser.

Another common task is to find a good alternative to replace an obsolete glass of an optical design. Therefore, an algorithm is implemented to search for good substituents within the given glass catalog. That search is based on the main index of refraction n_D and the main Abbe number v .

A.1.7.8. Peltier tool

Thermal stabilisation is of great importance for high-resolution spectrographs. For small volumes, Peltier elements combined with heat sinks and fans can be precisely control the air temperature. The required thermal resistance, σ_{th} , of the heat sink depends on the maximum allowed temperature difference and the properties of the peltier element (e.g., Buil, 1991). Cooling power, q_{th} , voltage, V , and current, A , of the element have to be specified by the user. The tool calculates, $q_j = VA$, the Jouls power, $COP = q_{th}/q_j$, the coefficient of performance, and the thermal resistance, $\sigma_{th} = dt/(q_j + q_{th})$, of the heat sink necessary. It is worth noting that the performance in reality depends strongly on the thermal conduction between the different elements. That is usually increased by the use of special glue or paste. However, since these have a much lower heat conductivity compared to metals (e.g. aluminium) commonly used for heat sinks, it is important to keep the gaps thin and the surfaces with a quality polished finish.

A.1.8. A Design Example

The applicability of the software and its output is demonstrated in this section. A comparison between obtained data by the real instrument will also be given.

In order to avoid uncertainties originating from the losses at the slit due to the quality of the auto guiding of the telescope, a slitless system was chosen. Parameters of the experimental set-up are summarised in Table A.4 and the optical layout is shown in Fig. A.15. The system makes use of a collimator with negative focal length to keep the lever

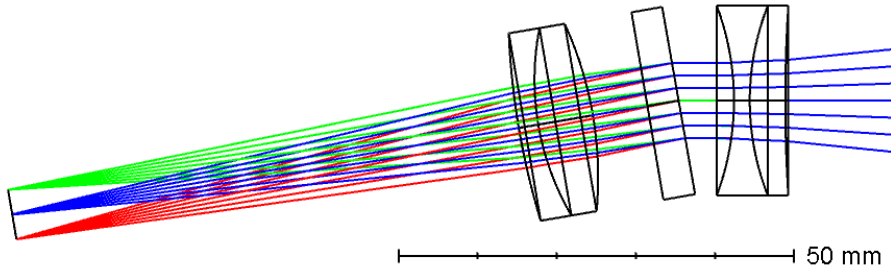


Figure A.15.: Layout of the slitless spectrograph with a transmission grating and a collimator of negative focal length to keep the lever arm at the telescope short. Parameters are summarised in Table A.4.

Table A.4.: Parameters of the example slitless spectrograph shown in Fig. A.4.

Quantity	value	quantity	value
f_{coll}	-50	f_{cam}	75
g	300 l/mm	Φ	5
ϕ	17.5	θ_B	4.47
D_{tel}	152	f_{tel}	750
σ	4 arcsec	AR surf.	9
Al surf.	2	Pixel	2052x2062
Pixel size	7.5 μm	Read noise	7 e^- RMS
CCD gain	0.5 e^-/ADU		

arm at the telescope short. A Newtonian telescope with a diameter of eight inch was used for the observations. The grating works in transmission. Hence, the manufacturer value of the groove angle ϕ has to be used to calculate the blaze angle (e.g., Loewen & Popov, 1997)

$$\theta_B \approx \phi(n_g - n_s)/2, \quad (\text{A.54})$$

where n_g and n_s is the refractive index of the grating and surrounding material, respectively.

The wavelength coverage calculated by SILENTis in very good agreement with both the results from ZEMAX and the real measurement. It extends from 340 to 1,000 nm. Further, the measured spectrum of that star is shown in Fig. A.16 in comparison with the balmer spectrum as calculated by SILENT. The continuum is calculated by a Planck distribution with the user specified values for temperature etc. The line width is obtained by the magnification of the slit width due to the spectrometer optics and is assumed as the FWHM of a Gaussian line. To compute such spectra within SILENTa user-defined line list is used, which also allows the specification of line-depth, since SILENTdoes not compute a full synthetic spectrum. This spectra can be used to get an idea of the spectrum to be measured and to identify the positions of important lines. This helps to ensure that lines of special scientific interest are place where maximum efficiency is expected.

The estimated SNR of a Vega spectrum with an assumed grating efficiency of 50% and the properties of a KAI-4022M detector is shown in Fig. 2.2. In an exposure of one second, a SNR of ≈ 130 was measured at 700 nm, ≈ 150 at 450 nm, and ≈ 160 at 640 nm which is in very good agreement with the simulation. Further application to white pupil echelle system was presented in (Sablowski et al., 2018).

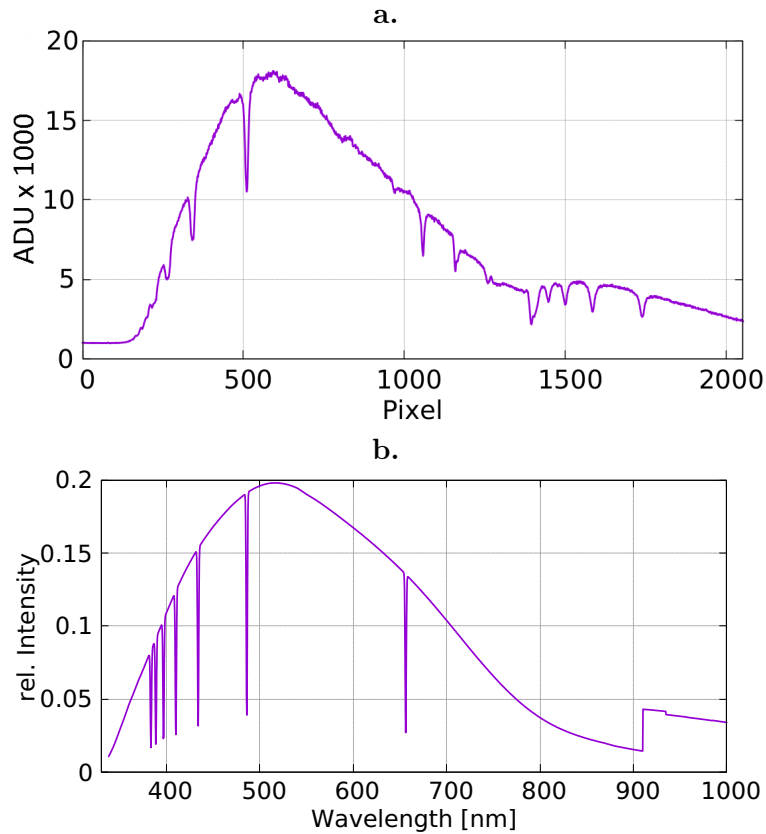


Figure A.16: **a:** Measured spectrum of Vega. Wavelength increase with pixel number. The second maximum in intensity at around pixel 1600 is due to the second diffraction order and shows another balmer sequence. **b:** Calculated balmer spectrum. The second order is not taken into account, line width are determined by the seeing and strength is arbitrarily chosen, since they are used for line identification only. The y axis reflects the efficiency of the overall system folded with a Planck radiation of 10,000 K.

A.1.9. Conclusion and Outlook

A software to support the optical designer in pre-design steps and in the design of peripheral sub-systems was presented. The only alternative to this software, to the knowledge of the authors, was presented in Barnes (2012) but is not available to the public and limited to echelle systems.

To obtain more realistic outputs from SILENT, the optical aberrations of the systems should be taken into account. In a future version of the software, it is planned to incorporate that based on aberration function in dependence of wavelength and field. This tool will finally have the possibility to use output from an optical design software and a definition of the aberration function by the user.

A method based on the chromatic coordinate introduced by Buchdahl (1968) to correct for at least $n + 1$ wavelengths with n glasses was presented by Robb (1985). Hence, this approach will be implemented in the glass tool in a later version of the code.

Since reimaging (e.g., of the fibre exit at the spectrograph input to feed an image slicer) is a very common task in instrumentation as well as in daily lab work, for relay systems based on a pair of achromatic lenses, a tool similar to the Petzval tool will be implemented to search for the best combination for a given magnification within a catalog of suitable lenses.

The applicability of the software was shown by a comparison of the simulated output and real data. The signal to noise calculation is, however, a rather uncertain estimate, since it strongly depends on the atmospheric conditions. Nevertheless, the single observation compared here, showed an acceptable agreement with the simulation.

Whenever possible, the **SILENT** computation output was compared with a sophisticated ray-trace software (**ZEMAX**). These comparisons showed a very good agreement. Hence, the overall goal of that package for pre-design spectroscopic systems in order to compare them is demonstrated. This will also provide a tool to help in design review processes.

Code Availability

The code is available open source under the Apache 2.0 licence. It can be downloaded from the github page of the developer³. An exe version for Windows 64bit (tested on Win7 and Win10) and the source code (to compile on any other machine) is stored there. It is recommended to use the **Qt creator** to load the project file and compile the program. The available folder containing the Windows version should contain all the necessary .dll driver files such that compiling the program should not be necessary.

Acknowledgements

We thank our colleagues Roger Haynes, Manfred Woche, Michael Weber and Klaus G. Strassmeier for their support, time for discussions, and comments on the text.

References

- Austin, D. R., Witting, T., & Walmsley, I. A. 2009, *Appl. Opt.*, 48, 3846
- Barden, S. C., Arns, J. A., Colburn, W. S., & Williams, J. B. 2002, in *Proc. SPIE*, Vol. 4485, 4485 – 4485 – 10
- Barnes, S. I. 2012, in *Proc. SPIE*, Vol. 8550, 8550 – 8550 – 8
- Beutler, H. G. 1945, *J. Opt. Soc. Am.*, 35, 311
- Born, M. & Wolf, E. 1999, *The Principles of Optics*, seventh edn. (Cambridge University Press)
- Brandt, H.-M. 1956, *Das Photo Objektiv*, 1st edn. (Springer Fachmedien Wiesbaden GmbH, Germany), p. 76
- Buchdahl, H. A. 1968, *Optical aberration coefficients* (Dover Publications)
- Buil, C. 1991, *CCD Astronomy*, 1st edn. (Willmann-Bell, Inc.), chapter 3
- Butov, O., Golant, K., Tomashuk, A., van Stralen, M., & Breuls, A. 2002, *Optics Communications*, 213, 301
- Clayton, C. A. 1989, *A&A*, 213, 502
- Content, R., de Ugarte Postigo, A., Thöne, C., & Sheinis, A. 2018, in *Proc. SPIE*, Vol. 10706, 10706 – 10706 – 9
- Croom, S. M., Lawrence, J. S., Bland-Hawthorn, J., et al. 2012, *Monthly Notices of the Royal Astronomical Society*, 421, 872
- Czerny, M. & Turner, A. F. 1930, *Zeitschrift für Physik*, 61, 792

³<https://github.com/DPSablowski/silent>

- de Jong, R. S., Barden, S. C., Bellido-Tirado, O., et al. 2016, in Proc. SPIE, Vol. 9908, 9908 – 9908 – 18
- Dubbeldam, C. M., Content, R., Allington-Smith, J. R., Pokrovski, S., & Robertson, D. J. 2000, in Proc. SPIE, Vol. 4008, 4008 – 4008 – 12
- Eigenbrot, A. D., Bershady, M. A., & Wood, C. A. 2012, in Proc. SPIE, Vol. 8446, 8446 – 8446 – 10
- Eversberg, T. & Vollmann, K. 2015, Spectroscopic Instrumentation, 1st edn. (Springer), p. 165
- Gray, D. F. 2005, The Observation and Analysis of Stellar Photospheres, 3rd edn. (Cambridge University Press), p. 62
- Herzberger, M. 1959, Opt. Acta, 6, 197
- James, J. 2007, Spectrograph Design Fundamentals, 1st edn. (Cambridge University Press), p. 81
- Kelz, A., Verheijen, M. A. W., Roth, M. M., et al. 2006, Publications of the Astronomical Society of the Pacific, 118, 129
- Kogelnik, H. 1969, The Bell System Technical Journal, 48, 2909
- Lee, K. S., Thompson, K. P., & Rolland, J. P. 2010, Opt. Express, 18, 23378
- Loewen, E. G. & Popov, E. 1997, Diffraction Gratings and Applications (Marcel Dekker Inc)
- Mehnert, H. & Steinich, T. 2011, PHOTONIK, 5
- Pribram, J. K. & Penchina, C. M. 1968, Appl. Opt., 7, 2005
- Reader, J. 1969, J. Opt. Soc. Am., 59, 1189
- Robb, P. N. 1985, Appl. Opt., 24, 1864
- Sablowski, D. P., Plüschke, D., Weber, M., Strassmeier, K. G., & Järvinen, A. 2016, AN, 337, 216
- Sablowski, D. P. & Schanne, L. F. 2018, Astrophysikalische Instrumentierung und Messtechnik fÄCÄr die Spektroskopie, 1st edn. (Selbstverlag, Mannheim, Germany), p. 221
- Sablowski, D. P., Woche, M., Weber, M., Järvinen, A., & Strassmeier, K. G. 2018, in Proc. SPIE, Vol. 10706, 10706 – 10706 – 15
- Wehr, H. & Wiechert, D. 1986, Materials Research Bulletin, 21, 559
- Wischniewski, E. 2018, Astronomie in Theorie und Praxis, eight edn. (Selbstverlag, Kaltenkirchen, Germany), Band 1 p. 53

A.2. A study of white-pupil configurations for high-resolution échelle spectrographs (Manuscript AII)

Daniel P. Sablowski¹, M. Woche¹, M. Weber¹, A. Järvinen¹, K. G. Strassmeier¹

Proc. of SPIE Vol. 10706

1: Leibniz Institute for Astrophysics Potsdam (AIP), An der Sternwarte 16, 14482 Potsdam, Germany

Abstract White pupil arrangements using parabolic off-axis mirrors are commonly used by instrument designers of high-resolution spectrographs. Their advantage is a non-chromatic, spherical free collimation, an intermediate focus providing the possibility for stray light apertures, and the compression of the beam diameter using a second, a transfer, collimator. However, these arrangements suffer from off-axis aberrations in the field. Many configurations create the intermediate focus, after double-passing the primary collimator, in the vicinity of the spectrograph input. This makes it necessary to introduce small angles at the main collimator, further increasing off-axis aberrations. Furthermore, image curvature is high and requires toroidal surfaces to be added near the spectrograph focus in front of the CCD. In high-precision radial velocity measurements, it is of great importance to properly model the spectrographs transfer function in order to derive exact line positions. Therefore, clean and very well defined spots, even when working near the sampling limit, which can simply be represented by gaussians will benefit such measurements. This point is usually considered less by instrument designers. We have studied several possible off-axis mirror arrangements for white pupil spectrographs and discuss our results here. We focus on the image quality generated by the mirrors, on-axis as well as in the field. We come to the conclusion that a fairly uncommon arrangement provides best performance in the sense of image quality and focus accessibility.

high-res spectroscopy, spectrographs, off-axis mirrors, white pupile, échelle

A.2.1. Introduction

White pupil (WP) echelle arrangements are widely used for high-resolution spectrographs. In contrast to a classical design with collimating and imaging optics, in a WP additional optics are used between the echelle and the cross-disperser, see Fig. A.17. Commonly, the diffracted beam from the echelle is reimaged by the main collimator and recollimated by a so-called transfer collimator. An advantage is the possibility for a beam compression. Using a transfer collimator with shorter focal length than the main collimator will result in a smaller beam size at the cross-disperser (asymmetric design). However, this makes a higher dispersion of the cross-disperser necessary. An example for a symmetric design is the STELLA Echelle Spectrograph (SES) attached to a 1.2 m robotic telescope on Tenerife (Weber et al. (2012)). In contrast, the Potsdam Echelle Polarimetric and Spectroscopic Instrument (PEPSIStrassmeier et al. (2015)) at the Large Binocular Telescope on Mt. Graham is an example for an asymmetric setup.

Since these instruments become rather large footprints due to the large focal lengths, they are fibre-connected to the telescope. Hence, a relay-optic is used to adapt the focal ratio of the fibre output to the main collimator. Usually, that relay system is used to create an intermediate focus where an image slicer can be placed. As shown in Fig. A.17, the beam reflected by the echelle is refocussed by the second collimator. This collimator is usually the same as the first one (double pass).

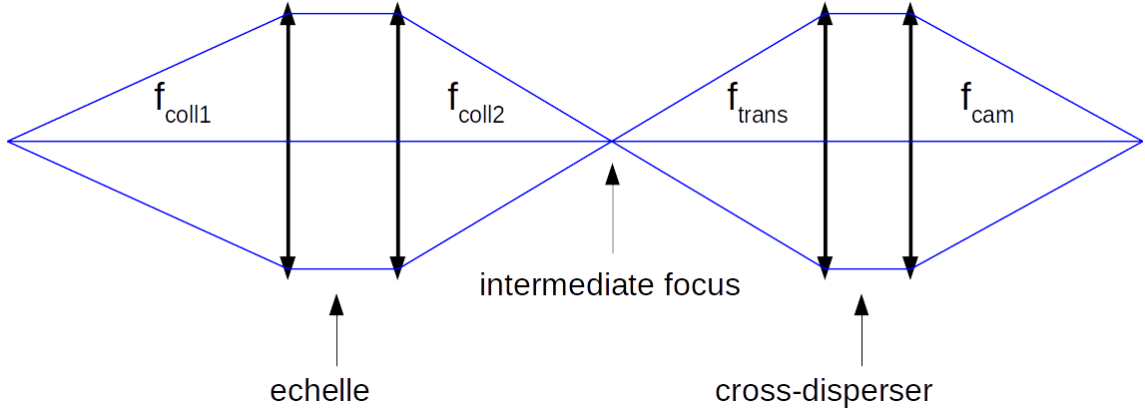


Figure A.17.: Schematic layout of a WP arrangement. The beam (from either telescope or fibre) is collimated by collimator one of focal length f_{coll1} , dispersed by the echelle, reimaged by the second collimator (which is often the first in double-pass) with focal length f_{coll2} , recollimated by the transfer collimator with focal length f_{trans} and imaged by a camera with a focal length of f_{cam} after passing through the cross-disperser.

We want to compare different arrangements of such a main-and-transfer-collimator system in terms of image quality. For a fairly uncommon setup, we will also show a more detailed design example.

A.2.1.1. Main parameters

Before starting a detailed analysis we want to show the general impact of a WP arrangement on the spectroscopic properties of the spectrograph. The equation for a reflective grating is given by

$$\frac{m\lambda}{ng} = -\cos(\gamma)[\sin(\alpha) + \sin(\beta)], \quad (\text{A.55})$$

where m is the diffraction order, g the grating constant, n the index of refraction of the surrounding medium, λ the wavelength, γ the off-plane angle and α and β the angle of incidence and diffraction, respectively. The dispersion is given by

$$\frac{dl}{d\lambda} = f_{cam} \frac{d\beta}{d\lambda}, \quad (\text{A.56})$$

where f_{cam} is the focal length of the imaging optics. The derivative at the right-hand side is obtained from the grating equation and leads us to

$$\frac{dl}{d\lambda} = \frac{m}{gn} \frac{f_{cam}}{\cos \beta \cos \gamma}, \quad (\text{A.57})$$

where dl is the linear element occupied by $d\lambda$. In accordance to the WP arrangement shown in Fig. A.17, we have to take the WP magnification $\phi_{WP} = f_{coll2}/f_{trans}$ into account:

$$\frac{dl}{d\lambda} = \frac{m}{gn} \frac{f_{cam}}{\cos \beta \cos \gamma} \phi_{WP}. \quad (\text{A.58})$$

In a similar way, we obtain

$$\frac{\lambda}{d\lambda} = \frac{m\lambda}{gbn} \frac{f_{coll1}}{\cos \alpha \cos \gamma} \quad (\text{A.59})$$

an equation for the resolving power, where b is the slit width. In order to calculate the width of the slit image in the image plane of the spectrograph, we have to take the anamorphic magnification of the grating into account. In widely used γ -configurations it is $\alpha = \beta$ and anamorphic magnification a is unity for the order's central wavelengths. However, for other wavelengths the factor can be derived from the grating equation as well and is given by

$$a = \frac{d\beta}{d\lambda} \left(\frac{d\alpha}{d\lambda} \right)^{-1} = \frac{\cos(\alpha)}{\cos(\beta)} \quad (\text{A.60})$$

and we obtain

$$b'_d = ba \frac{f_{cam}}{f_{coll1}} \phi_{WP} \quad (\text{A.61})$$

the width of the slit image in the direction of echelle dispersion (denoted by d). For the common case $f_{coll1} = f_{coll2} = f_{coll}$ and $f_{trans} < f_{coll}$, the width of the imaged slit is larger compared to a classical (non-WP) arrangement. Note that this anamorphic magnification has not to be confused with anamorphism of the beam size.

Since the angles of incidence and diffraction at the grating are in general not equal, the beam diameter in the dispersion direction will not be conserved after diffraction. This anamorphism can easily be seen by geometry to be $\cos(\beta)/\cos(\alpha)$. We further note that the anamorphic magnification of the cross-disperser has to be taken into account for proper calculation of the slit height in the image plane. Further properties and merits of a spectrograph are discussed in [Sablowski & Schanne (2018)], [Eversberg & Vollmann (2015)] and [Schroeder (2000)].

A relay-optic with magnification ϕ_{relay} is almost always necessary for fibre-linked instruments and is used to adjust the input focal number to the image slicer and collimator. For the above made assumptions, the final geometric width of the slit image is given by

$$b'_d = ba \frac{f_{cam}}{f_{trans}} \phi_{relay}. \quad (\text{A.62})$$

or

$$b'_d = ba \frac{f_{cam}}{f_{coll1}} \phi_{WP} \phi_{relay}. \quad (\text{A.63})$$

This is independent from the focal length of the collimator if used in double pass.

A.2.1.2. Design constraints

Besides the above shown equations, we have to consider the sampling of the spectrograph in order to maintain the resolving power. Referring to Eq. A.63, and setting $\alpha = \beta$ we can write for

$$\frac{n_{pix}p}{b} = a \frac{f_{cam}}{f_{coll1}} \phi_{WP} \phi_{relay} \quad (\text{A.64})$$

or with Eq. A.62 ($f_{coll1} = f_{coll2}$)

$$\frac{n_{pix}p}{b} = a \frac{f_{cam}}{f_{trans}} \phi_{relay}, \quad (\text{A.65})$$

where n_{pix} is the number of pixels occupied by b' and p is the pixel size. To maintain the analogous resolution on a discrete detector, the Nyquist criterion is often cited, which states in that context that $n_{pix} \geq 2$. Basically, Eq. A.64 sets a limit to the achievable resolution. Since the focal length of the optical camera and the transfer collimator is set by the wavelength range to be covered by a CCD with given size, the maximum focal length

of the collimator is set by the size of the pixels and the necessary number of pixels covered by the image of the slit. This shows that for higher resolution one need to reduce the pixel size or increase the size of the detector. As noted above, a transfer collimator with smaller focal length creates larger slit images which supports the use of larger pixels.

Consider an example with a camera with 200 mm and a collimator with 1500 mm focal length, respectively. For reasonable focal number at the camera of $f/3$ the beam size has to be 66 mm which would give a focal number of 22.5 for the collimator. In case of $f/4$ fibre input, a magnification of 5.6 would be necessary. Hence, a fibre of $50 \mu\text{m}$ would have a width of approx. $37.3 \mu\text{m}$ in the image plane (Eq. A.61). If one use a WP arrangement with a transfer collimator of 1000 mm focal length the image would be enlarged by that factor to $56 \mu\text{m}$. This makes the use of an image slicer practicable. However, the dispersion of the spectrum will be enlarged by the same factor, i.e., larger detectors required.

Since echelle spectrographs are used for broadband spectroscopy we need an optical design free of chromatic aberrations to maintain high image quality over the entire wavelength range. Furthermore, due to the mentioned increase of detector size for higher resolution, field angles can be large and off-axis aberrations as well as field curvature are crucial. In addition, to achieve high-resolution we have to deal with rather large beam diameters and spherical aberration of the camera system has to be corrected as well. For good modelling of the spectrographs transfer-function, it is of advantage to create a diffraction limited system. Off-axis parabolic mirrors are perfect for an axial beam but suffer from strong off-axis aberrations and field curvature. The goal is therefore to find an arrangement which limits these aberrations and provides an almost perfect image quality before the beam enters the cross-disperser and the optical camera.

A.2.2. White pupil arrangements

In this section we are going to discuss the image quality of commonly used (e.g. Raskin, G. et al. (2011); Strassmeier et al. (2015); Weber et al. (2012); Kaufer et al. (1999)) off-axis parabola arrangements. We will focus on the image quality without considering the optical camera. The next section will then, exemplarily, discuss a new setup in more detail.

For the following discussion, we will show the layout and spot diagrams for different off-axis parabola (OAP) arrangements. The spots refer to a central diffraction order. The black circle in the spot diagrams show the Airy disc (diffraction limit). The numbers above the boxes are wavelengths in micrometers. The cross-disperser (CD) is not considered and we use a paraxial lens to create the image. Hence, as mentioned, we will discuss the intermediate image quality provided by the OAPs. Furthermore, we use paraxial lenses for the relay system. We note here, that there are two ways of using a focusing (here parabolic) mirror as an OAP (see Fig. A.18). The correct way is to illuminate the off-axis part of the mirror by a divergent beam emerging from the focus of the parabola. A second OAP is used to reimagine that parallel beam to the focus point of that second OAP. Such an arrangement compensates the path differences of all rays for an axial bundle and creates a perfect image on-axis. The second way is the inverse use: creation of the parallel beam towards the focal point of the parabola. The latter way should be avoided, since it does not provide good image quality. Fast systems with high off-axis angles are very sensitive to field aberrations such as coma. Hence, it is necessary to keep the focal numbers high and with that, it is practicable to realise small off-axis angles.

In Fig. A.19, we show the layout and spots for a central diffraction order of arrangement I. The input is at the focus of the main collimator. A small angle at the grating in γ leads to a separation between input and diffracted beam. The collimator is used in double-pass and creates an intermediate focus near the fibre input. The transfer collimator is at the

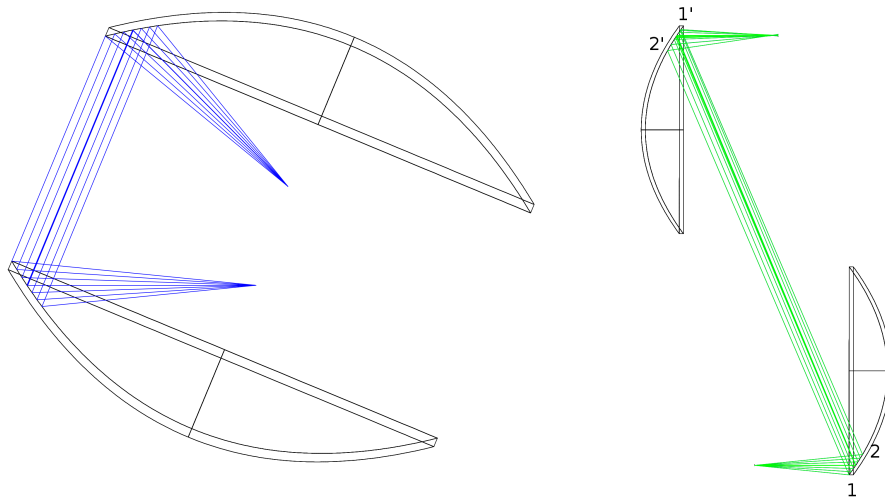


Figure A.18.: Two ways to arrange OAPs. Left: Correct arrangement, the divergent and convergent beams emerging from and focusing to the focal point of the parabola, respectively. Right: Inverse arrangement. The inverse mounting has another issue: the ray reflected from point 1 hits point 2' instead of 1' as in the left mounting.

left and recollimates the beam. One can see, that this system suffers from strong off-axis aberrations. They are mainly caused by the small angle at the grating to separate the beams. Without that, the image would be perfect on the optical axis. However, this arrangement I is widely used for high-resolution and high-precision radial velocity echelle spectrographs.

Second arrangement shown in Fig. A.20 is related to the well known Ebert-Fastie configuration in which the grating is placed at the focus of the main collimator. It has the advantage of good focus accessibility for the incoming and diffracted beam. The intermediate focus is at the focus of the transfer collimator. However, it is possible to optimise on the off-axis angles to reduce the off-axis aberrations but residuals will remain in the final image. This is due to the inverse use of the main collimator as an OAP.

Arrangement III is shown in Fig. A.21. The input is now placed at the focus of the main collimator and we have a mixed situation of arrangement I and II. A small angle at the grating is necessary to separate input and intermediate focus. However, using the main collimator a third time for recollimation and having a correct off-axis arrangement (input at focus of main collimator), the path differences can be compensated in the field and the image is near to the diffraction limit on axis. The next arrangement shown in Fig. A.22 is basically the same, but demonstrates the use of a transfer collimator with shorter focal length. The image quality is not affected by that change, but the system magnification changes accordingly.

Our preferred and more uncommon arrangement is shown in Fig. A.24. The input is placed at the focus of the main collimator. However, we use a second (physically) main collimator, but the opposite side of it to create the intermediate focus. The transfer collimator has a shorter focal length and its focus is at the intermediate focus. The image is free from off-axis aberrations and field curvature is the main contribution to the blurring of the spots. However, even the spots in the field are near the size of the Airy disc. The main collimator can be made from one mirror, since both sides are used. This arrangement has the advantage of good focus accessibility of both, the input and the intermediate one. It is not necessary to introduce small angles for beam separation and since all three

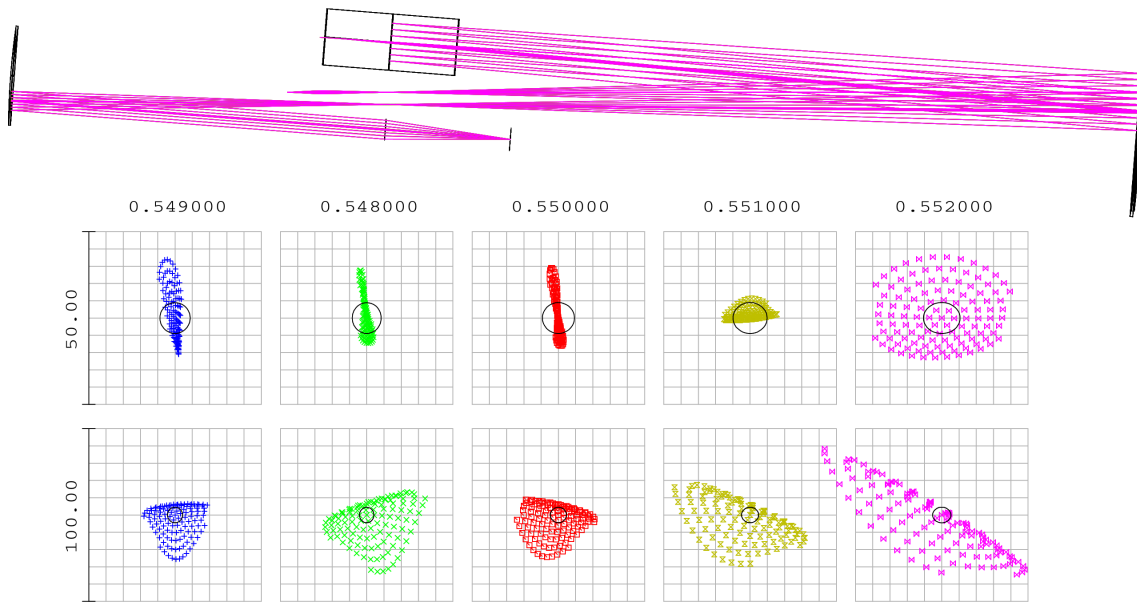


Figure A.19.: Layout and spot diagrams for arrangement I. Spots at top are in the image plane, bottom at the intermediate focus between main and transfer collimator.

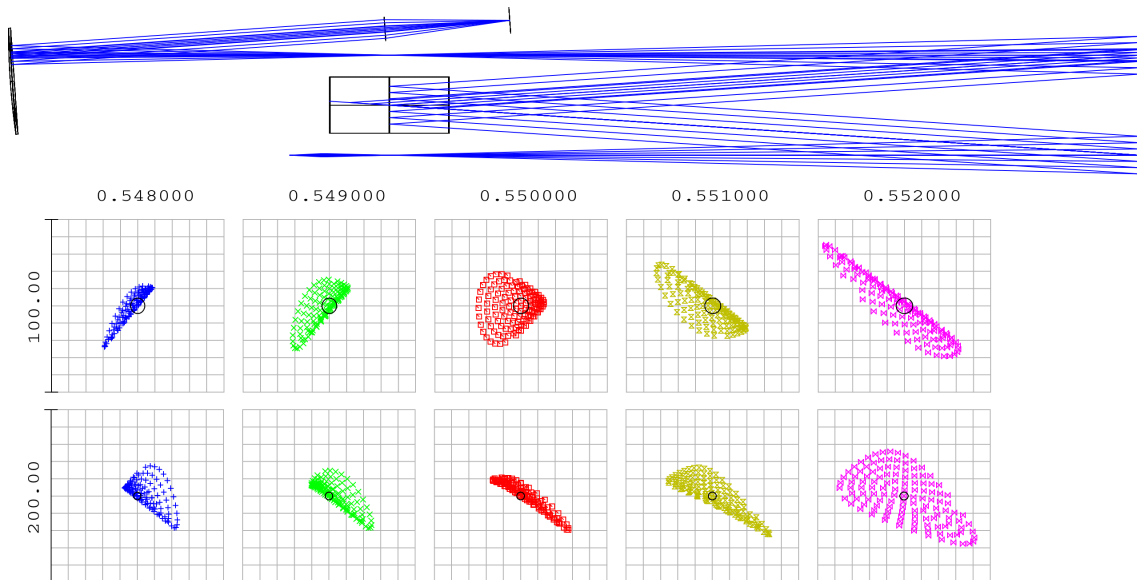


Figure A.20.: Layout and spot diagrams for arrangement II. Spots at top are in the image plane, bottom at the intermediate focus between main and transfer collimator.

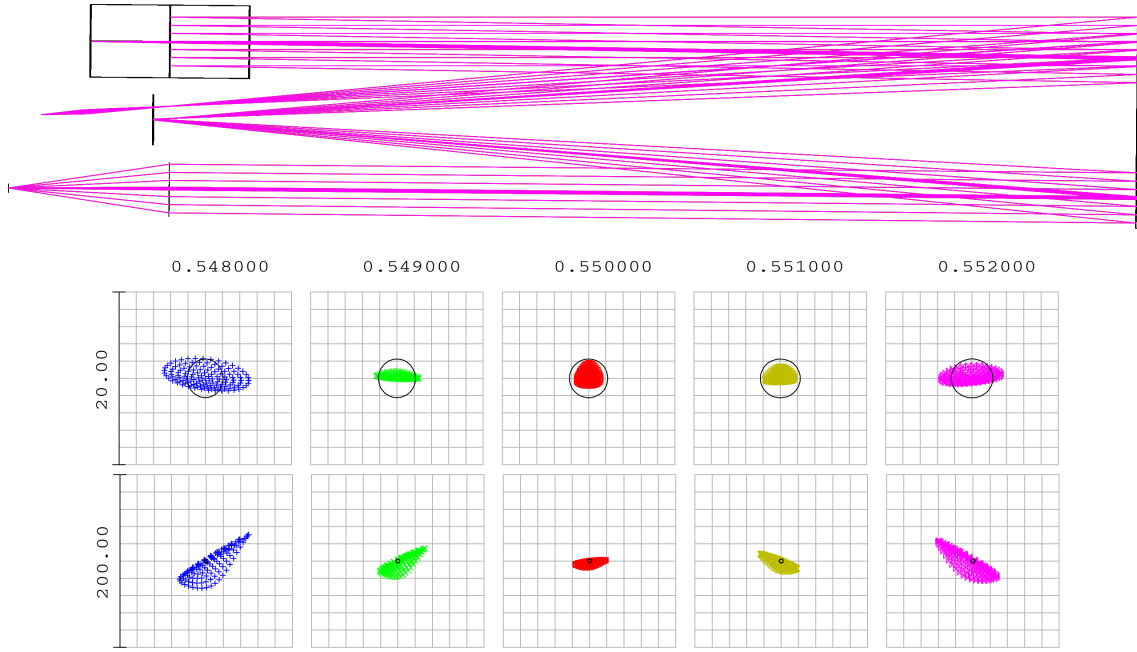


Figure A.21.: Layout and spot diagrams for arrangement III. Spots at top are in the image plane, bottom at the intermediate focus between main and transfer collimator.

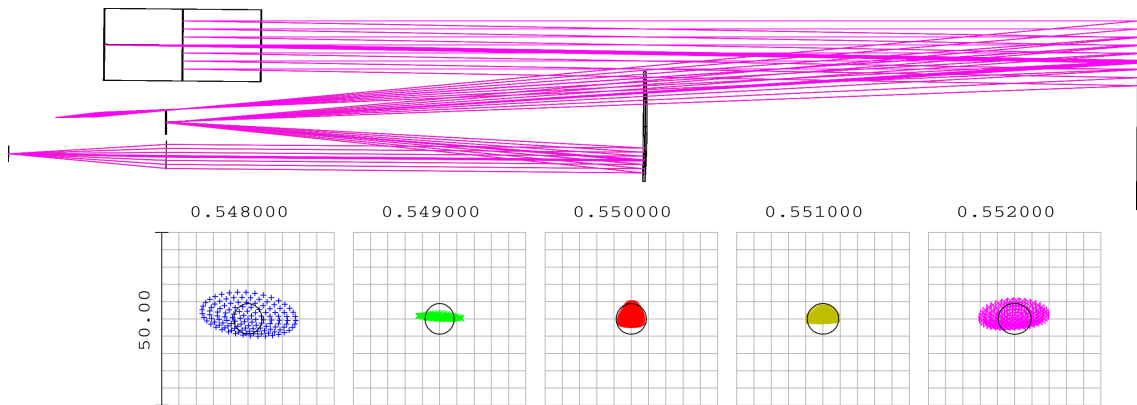


Figure A.22.: Layout and spot diagrams for arrangement IIIb. Spots are in the image plane.

OAPs are illuminated in the correct way (from the focus point), off-axis aberrations are already compensated to a high extend. This leads to symmetric spots, which support the determination of line positions, i.e., accurate RV measurements and detailed line-profile analysis. In other arrangements it is often necessary to use toroidal optics near the CCD (to reduce their influence on chromatism) to compensate for the remaining field aberrations. This is not necessary for our arrangement IV. However, setup II and IV need larger angles at the grating. When working in the γ configuration (tilt about γ to separate input from diffracted beam), line tilt ζ is introduced. Due to geometry, the minimum of that angle γ is given by the focal length of the collimator and the half-width of the grating (or beam radius) to

$$\tan(\gamma) = \frac{W/2}{f_{coll}}. \quad (\text{A.66})$$

The line tilt is calculated from the grating equation by

$$\tan(\zeta) = \frac{d\beta}{d\gamma}, \quad (\text{A.67})$$

which gives for $\alpha = \beta = \theta$

$$\tan(\zeta) = 2 \tan(\theta) \tan(\gamma) = 2 \tan(\theta) \frac{W/2}{f_{coll}}, \quad (\text{A.68})$$

where θ is the blaze angle. We plot this relation in Fig. A.23 for an R2 (red) and R4 (green) echelle grating, respectively, where the number refers to the tan of the blaze angle. The R2 grating will introduce a line tilt by about four times of the value of γ and for R4 already eight times. The advantage of using an R4 grating is the increase of the resolving power (larger α , see Eq. A.59) at the same beam diameter. However, to keep the off-plane angle γ small in configurations II and IV, it is possible to reduce the beam size by a factor of 0.5 and keep the resolving power. This will decrease the minimum required angle Eq. A.66. However, substitution of Eq. A.66 into Eq. A.68 and writing W_{R2} and $W_{R4} = W_{R2}/2$ for the beam size, respectively, we find that $\tan(\zeta_{R2}) = 2 \cdot 2W_{R2}/2f_{coll} = 2 \cdot 4W_{R2}/4f_{coll} = 2 \cdot 4W_{R4}/2f_{coll} = \tan(\zeta_{R4})$. As long as we keep the projected resolving power, for such a configuration line tilt is independent from the choice of the grating.

Furthermore, a larger blaze angle leads to higher dispersion and larger detectors are required. It is therefore necessary to find a compromise between the introduced value of line tilt and dispersion. To reduce the size of the detector, the focal length of the optical camera could be reduced, leading to a faster optical system which in general increase the number of required elements and costs. Additionally, higher dispersion in the end means larger fields which further increase the challenges for the optical camera design.

An advantage of the white pupil arrangement is the compensation of the linear dispersion in the pupil of the transfer collimator. This is shown in Fig. A.25. The off-axis wavelengths dispersed by the echelle and refocused by the collimator (right) hit the transfer collimator (left) at a distance from the optical axis. This results in a reflection of all recollimated beams towards the pupil of the transfer collimator. Hence, the cross-disperser placed in that distance from the transfer collimator can be made rather small.

Another basic aberration we need to consider is field curvature. The Petzval surface radius of curvature for such a mirror system can be easily calculated by the focal lengths of the single mirrors by

$$C_P = (f_{coll1}^{-1} + f_{coll2}^{-1} + f_{trans}^{-1}) = r_P^{-1}, \quad (\text{A.69})$$



Figure A.23.: Line tilt introduced by off-plane angle γ . Red is for an R2 grating ($\theta = 63.4\hat{\text{A}}^\circ$) and green for R4 ($\theta = 76\hat{\text{A}}^\circ$).

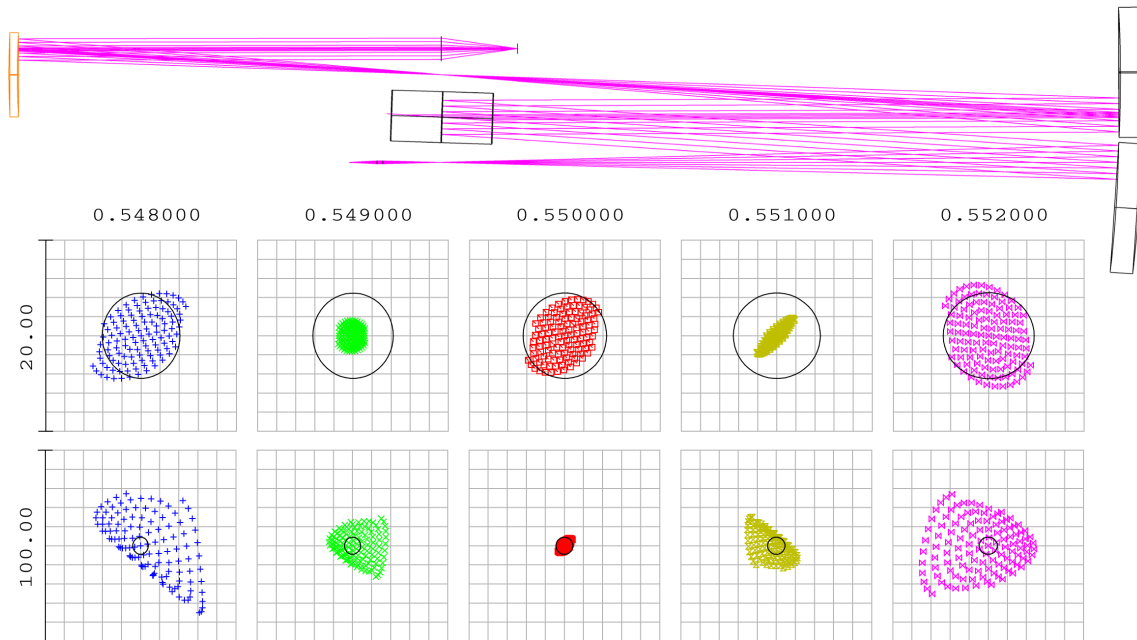


Figure A.24.: Layout and spot diagrams for arrangement IV. Spots at top are in the image plane, bottom at the intermediate focus between main and transfer collimator.

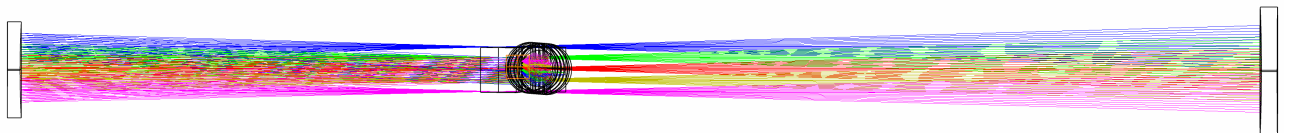


Figure A.25.: Side view of the WP layout. The dispersed beams focused by the collimator (right) are recollimated by the transfer collimator (left). These parallel beams overlap in the pupil of the transfer collimator. Hence, the beam size is smallest in the pupil and the cross-disperser is placed here.

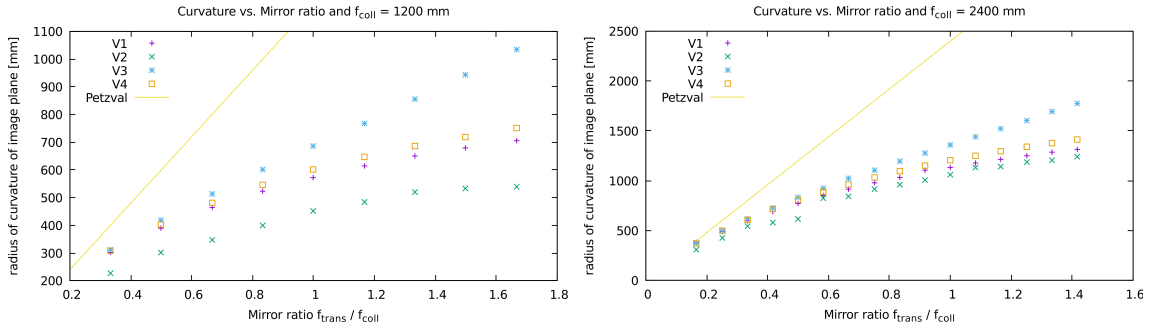


Figure A.26.: Radius of curvature of image plane vs. the ratio of focal lengths of transfer and main collimator for the four discussed WP arrangements. Left: for a main collimator focal length of 1200. Right: for 2400 mm.

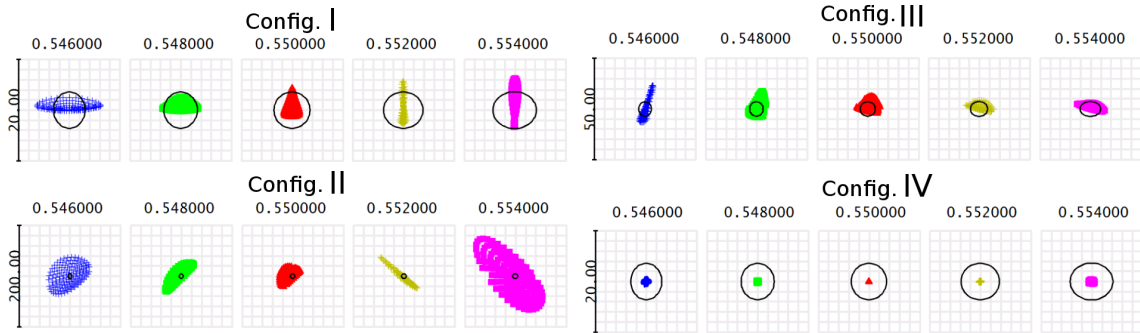


Figure A.27.: Spot diagrams for the presented configurations on a spherical curved image surface to test when the systems have eliminated field curvature. Configuration one is close to diffraction limit but still suffers by off-axis aberrations. In contrast, configuration four displays perfect spots over the whole diffraction order (field).

which gives a radius of curvature of 300 mm for 1200 mm collimators and 600 mm transfer collimator. It shows that surface curvature becomes a problem for large ratios of f_{coll}/f_{trans} and may be less a problem for large focal length spectrographs (high resolution).

Field curvature is one of the main aberrations of such mirror systems. Therefore, we have analysed the dependence of the image curvature of the presented systems in dependence of the focal lengths of both mirrors (main and transfer). We used ZEMAX to optimise on the back focal distance of the paraxial camera and the radius of curvature of the image plane. The obtained values of the curvature are shown in Fig. A.26 together with the calculated Petzval radius (r_p). We can see that image curvature becomes important for small ratios f_{trans}/f_{coll} but is less severe for long focal length spectrographs (high resolution). Or: For high-res spectrographs we can achieve higher beam compression while maintaining the value for image curvature.

An interesting behavior of these systems is the image quality after optimising on the image plane radius. Or asking: eliminating surface curvatures, which aberrations remain. Therefore, we show the spot diagrams of the four systems in Fig. A.27 where we have allowed for a curved image plane.

It is obvious that all configurations, except configuration IV, show distorted spots by off-axis aberrations. However, configuration I is very close to a diffraction limited image on a curved image surface. Configuration IV would leave us with a perfect image even in the field if we can compensate surface curvature with the optical camera.

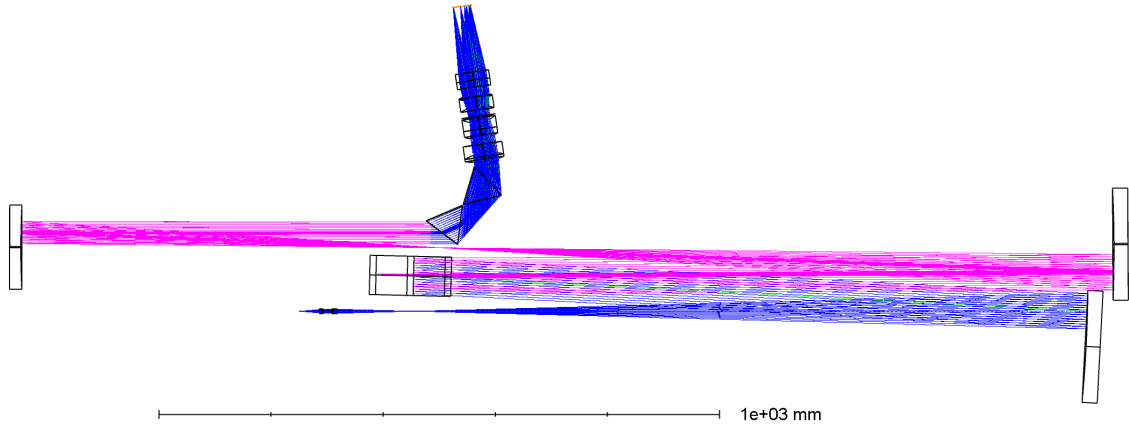


Figure A.28.: Layout of the discussed design example for a high-resolution diffraction limited broadband echelle spectrograph.

A.2.3. Design example

This section will briefly discuss an example for a design with the WP arrangement IV as shown in the previous section. Our goal is to increase the image quality to diffraction limit over the wavelength range from 400 to 800 nm. The spectrum should fit on a 4K detector with $6 \mu\text{m}$ pixels (KAF16200). The relay system can be made from OAPs as well, which will work for small input fields (one or two fibres). This will maintain the chromatic free image. Due to the broad wavelength range, we use two equilateral dispersion prisms made from F2 glass to cross-disperse the spectrum. Due to the magnification by the transfer collimator and the possibility to implement a second fibre (sky or simultaneous calibration fibre) or an image slicer, higher cross-dispersion is required compared to a system with $f_{trans} = f_{coll}$.

The main collimators are from standard telescope 8 inch diameter parabolic mirrors with 1200 mm focal length. The transfer collimator is also a standard parabola with a focal length of 750 mm and 6 inch diameter. Due to the small beam, the prisms as well as the optical camera can be rather small. For the prisms a size of about 70 mm is sufficient. To fit the spectrum onto the targeted detector size, a focal length of 200 mm for the optical camera is used. Hence, a standard photographic lens working at $f/2.8$ would already make a good job in imaging. The layout of the whole spectrograph is shown in Fig. A.28.

To better handle chromatic aberrations, we use a refractive relay system of two doublets shown in Fig. A.29 and the ansatz is listed in Tab. A.5. With these additional degrees of freedom, it is easier to correct the final image from field aberrations and to maintain our goal of a diffraction limited image. Since these lenses can be made rather small, they provide very good imaging quality over a broad wavelength range. OAPs with small focal lengths are also more difficult in alignment.

As mentioned in the previous section, this configuration requires larger angles at the echelle grating for proper separation of the beams. The line tilt is independent from the blaze angle as long as we keep the projected resolving power. Hence, to reduce the off-plane angle we have used mirrors with rather large focal lengths. This will also suppress the impact of field curvature as discussed above.

The optical camera is based on a double Gauss lens with a focal length of 200 mm made of four doublets. A doublet design reduces coating costs, since all lenses need to be coated only on one side. The layout of the camera and the listing is shown in Fig. A.30 and Tab. A.6, respectively. Double Gauss lenses are used for photographic lenses for a larger field.

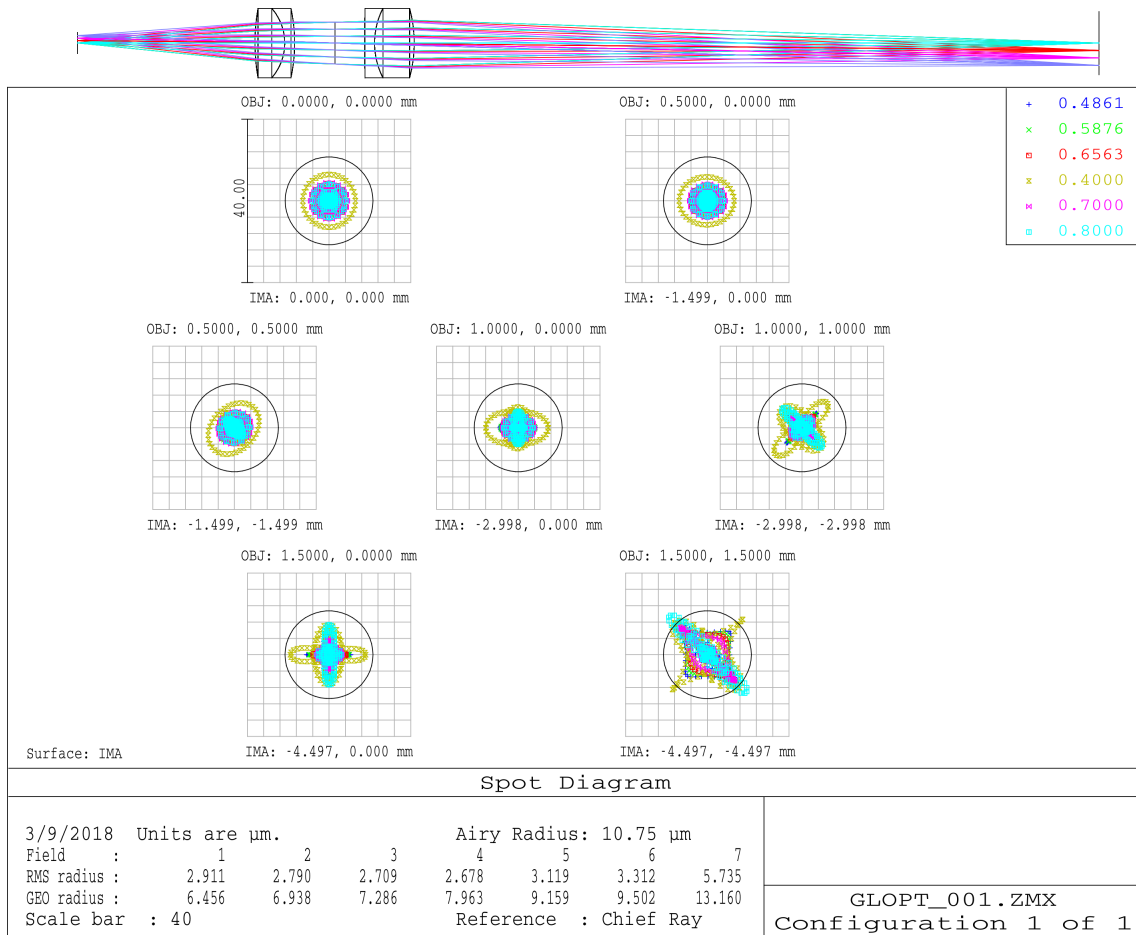


Figure A.29.: Relay system for object fields of 3 mm diameter from 400 to 800 nm at diffraction limit.

They can provide good field correction and high speeds can be reached when breaking the symmetry. The problem of designing such a lens in view of proper glass selection is twofold: first of all, one wants to reduce the chromatism of aberrations and chromatic focal shift to an acceptable or better diffraction limited value. Secondly, the transmission in the blue region should be maximised. The latter became a more severe problem since older glasses showed a much higher transmission for blue wavelengths compared to new ones and is more pronounced for high-index glasses (naturally, since they are connected by the complex index of refraction).

The shown system was first designed independent from the spectrograph. Constraints on glass thicknesses and distances were properly applied as well as constraints to three curvatures: zeroth forced to be positive, the one before (surface 5) and after aperture (surface 7) to be positive and negative, respectively. As shown above, field curvature is the main aberration we have to deal with. Therefore we have applied a curved image plane to the camera design but with opposite sign as the curvature of the spectrograph (see Fig. A.30). This allows to already compensate for the curvature and makes a final adjustment in the overall system more easy. As soon as a diffraction limited configuration was found, we replaced low-transmission glasses by available ones. To find a good replacement, we used an algorithm which browses through the available glasses and compares main index of refraction n_d and Abbe number V_d of the glass to be replaced and gives a set of closest

Table A.5.: Listing of design ansatz for the relay system shown in Fig. A.29 for magnification of 1:3.

surface	radius of curvature [mm]	thickness [mm]	glass
0	-	35.860	air
1	42.500	6.000	S-FPL55
2	-12.740	2.000	N-BK7
3	-33.628	8.162	air
4	stop	5.982	air
5	503.881	2.000	N-BK7
6	13.579	8.000	S-FPL55
7	-25.453	138.200	air

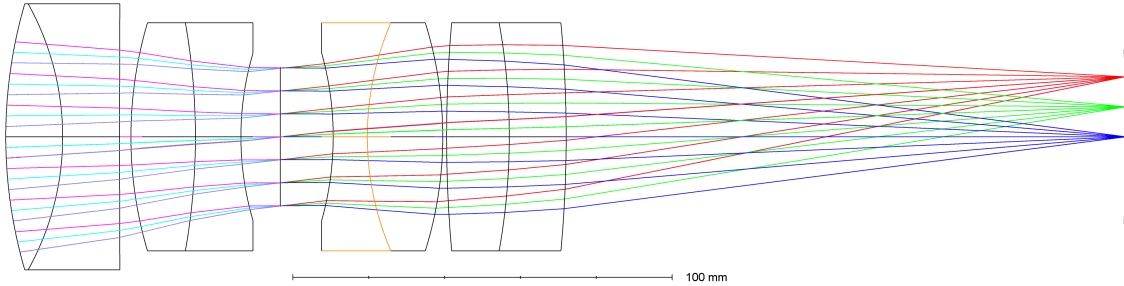


Figure A.30.: Layout optical camera based on double Gauss design as listed in Tab. A.6.

replacements, for which the merit

$$\delta = |((n_d - n'_d)/n_d + (V_d - V'_d)/V_d)/2| \quad (\text{A.70})$$

is smallest, where $'$ denotes the substituent. The listing in Tab. A.6 corresponds to that optimisation stage and can be used as a design ansatz for the optimisation within the whole optical system.

Our goal was to create a diffraction limited system over the range of 400 to 800 nm. Therefore, we show the spots for the bluest (#142), middle (#103) and upper (#69) diffraction order in Fig. A.31. The wavelengths were selected with sufficient overlap for adjacent orders. For the bluest order, we calculated about twice the free-spectral range. The black circle corresponds to the Airy disc (diffraction limit). We have optimised on the peak-to-valley of the spots rather than the rms values. This will better correct for inhomogeneous spot shapes. The Airy radius for the blue order (#142) is $2.1 \mu\text{m}$. The geometrical radius for the bluest and reddest wavelength of that order (as shown in the mentioned figure) is $2.5 \mu\text{m}$ and $2.9 \mu\text{m}$, respectively. The RMS values are much smaller and well below the Airy disc with $0.9 \mu\text{m}$ and $1.5 \mu\text{m}$ for the bluest and reddest wavelength, respectively. The Strehl value for the bluest wavelength is 0.9, i.e., diffraction limited in practice. In the two other diffraction orders shown, the geometrical size is very close to the Airy radius ($2.6 \mu\text{m}$ for #103 and $3.7 \mu\text{m}$ for #69).

To calculate all parameters and the spectral format on the CCD, we made use of the open-source software SILENT (Spectrograph sImuLation and EmulatioN Tool), which is a graphical UI based c++ program for classical, echelle, and 3D spectrographs available on github⁴. The glass replacement algorithm mentioned above is also implemented. This software can compute complete CCD frames to show interorder gaps and the position of

⁴<https://github.com/DPSablowski/silent>

Table A.6.: Listing of lens data for the optical camera shown in Fig. A.30. The system is tuned to a curved image plane to compensate for the field curvature of the whole optical system. Thicknesses are not fine tuned.

surface	radius of curvature [mm]	thickness [mm]	glass
0	124.994	15.000	N-PSK53A
1	-71.878	12.360	N-SK4
2	8130.099	1.000	air
3	105.337	18.000	S-BAL42
4	-171.867	13.000	S-NBH56
5	77.727	15.105	air
6	stop	10.760	air
7	-81.254	18.000	N-KZFS11
8	75.775	24.746	N-BASF2
9	-99.990	9.565	air
10	337.277	15.000	N-SF6HT
11	-169.399	15.000	N-ZK7A
12	-323.739	110.710	air
13	-450.000	-	air

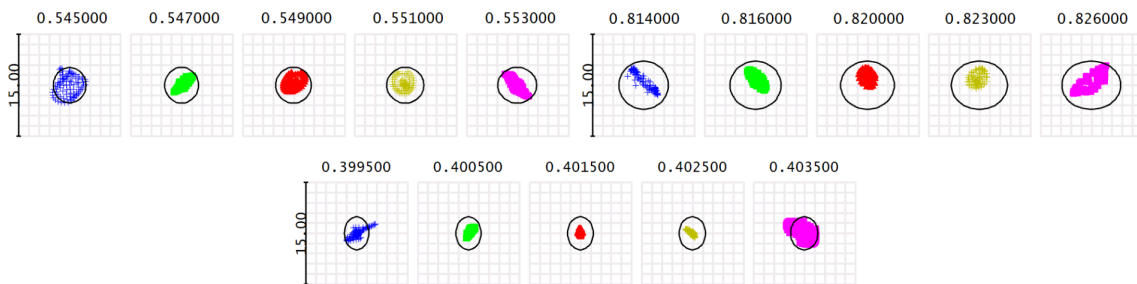


Figure A.31.: The spots of the final optimised spectrograph. The lower corresponds to the bluest diffraction order, the spots above are for a central order (left) and the reddest order imaged on the detector (right).

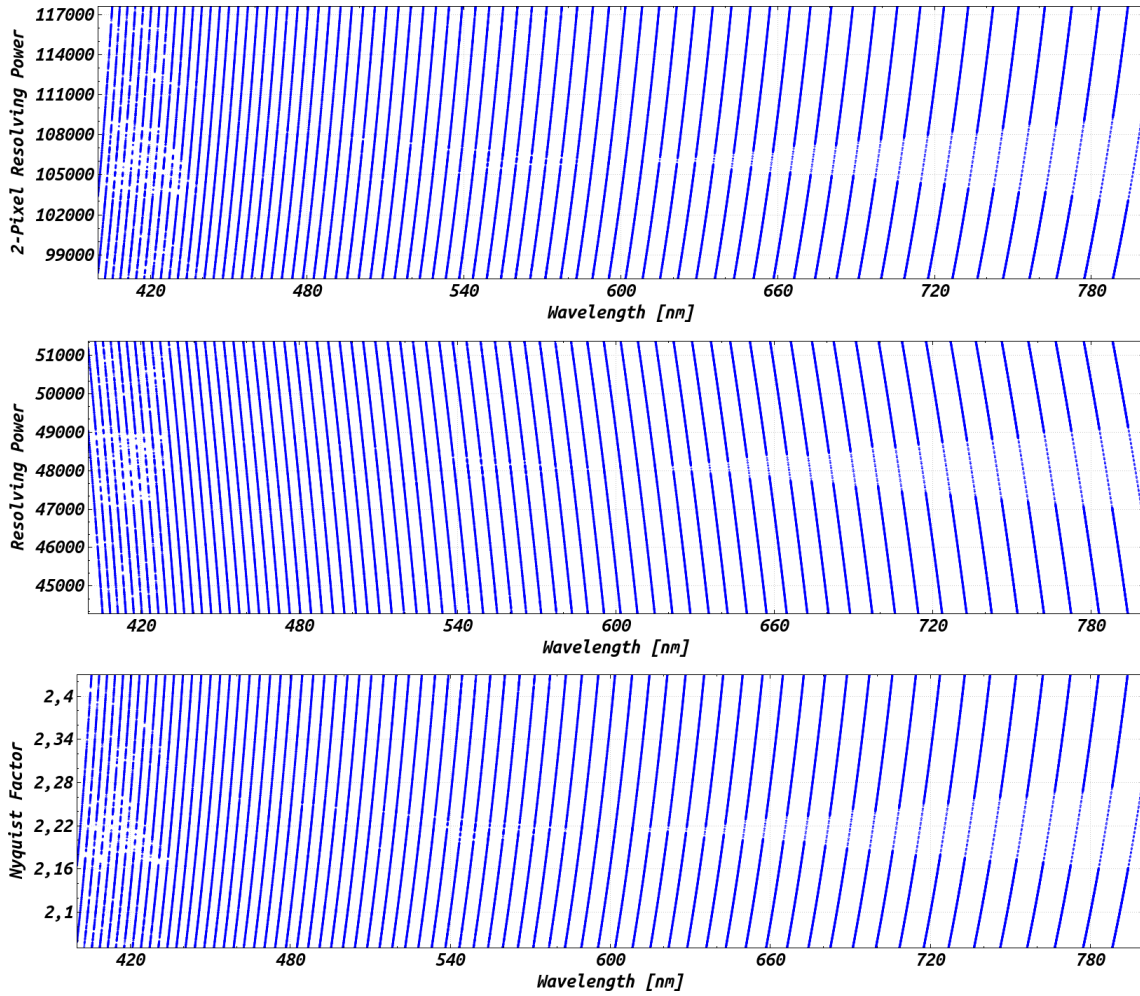


Figure A.32.: Some parameters for the presented system plotted for all diffraction orders between 400 and 800 nm. At top is the two-pixel limited resolving power, middle graph shows the resolving power achieved with a $67 \mu\text{m}$ fibre sliced once and at bottom the Nyquist factor ($= 1$ for two pixel sampling).

important lines which should be near the blaze peak for higher signal to noise ratio. We show a continuum (Planck) spectra and the thorium argon spectrum as would be imaged on a KAF16200 detector in Fig. A.33. We used a height of the image of the fibre after the relay-system of $400 \mu\text{m}$. This corresponds to a fibre of around $67 \mu\text{m}$ diameter and sliced one time. Shown is the coverage of wavelengths from 400 to 800 nm.

The KAF16200 has $6 \mu\text{m}$ pixels which results in a 2-pixel limiting resolving power of approx. 100k. The resolving power with a $67 \mu\text{m}$ fibre and sliced once peaks at approx. 51k. This provides good sampling of 4 pixels per resolution element. The spots shown above are well below the size of a pixel. Therefore, the slit-spread-function will not be degraded by image aberrations. Hence, the shape of the image will be well represented by a gaussian function. This in turn will make the precision of line fitting and determination of the center of gravity more precise. On the other hand it would support even smaller pixel sizes and with that higher 2-pixel-resolution or better sampling of the resolution element for even better fitting at the resolution.

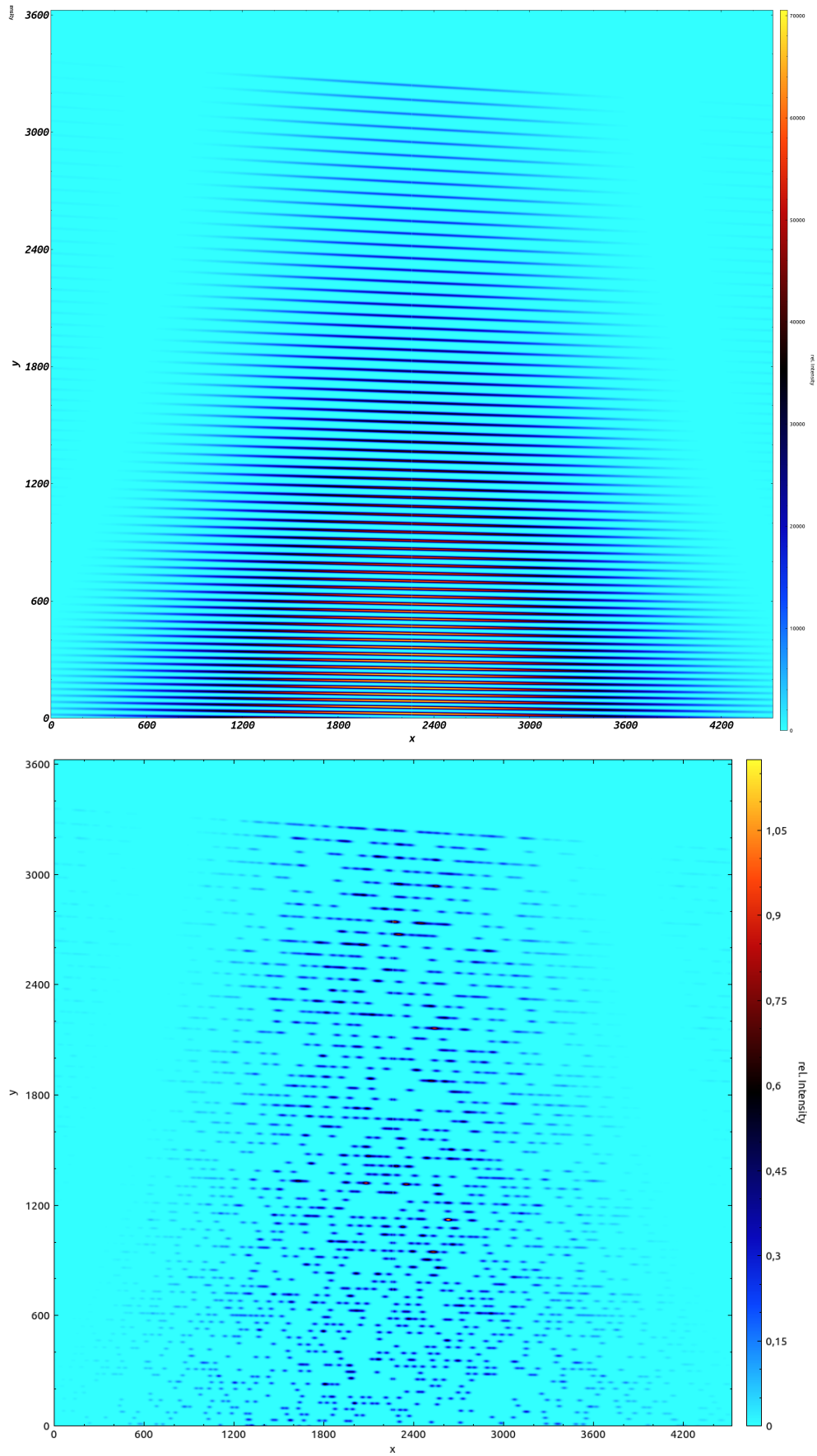


Figure A.33.: Simulated CCD frame with continuous (flat, left) and thorium-argon spectrum. The order width is such that a one-time slicer is allowed and to have still sufficient inter-order separation.

A.2.4. Conclusion

In the light of field curvature and off-axis aberrations, we have compared several commonly used off-axis parabola arrangements for white pupil high-res echelle spectrographs. A more uncommon setup was presented as well, which is arranged such that main collimators are used in the correct way and to eliminate off-axis aberrations. This arrangement has the advantage over all other systems of creating a perfect image on a curved image plane. Hence, we also showed an optical camera and the design process, capable of correcting for the image curvature. However, the disadvantage is the higher off-plane angle γ at the grating, causing stronger inclination of the slit image on the detector. Nevertheless, this angle can be kept small for long focal length systems. Higher image curvature of such a system may be compensated by a different optical camera layout, e.g., a Petzval system. They are known to suffer from stronger image curvature and often combined with a Piazz-Smyth field flattner (Smith & Genesee Optics Software, Inc. (1992)) to achieve speeds of up to $f/2$. This is a very common approach to correct for it in many up-to-date WP echelle systems (Raskin, G. et al. (2011); Strassmeier et al. (2015); Weber et al. (2012); Kaufer et al. (1999)). However, these components have to be placed very close to the detector surface to minimise the influence of chromatism introduced by the lens. This makes it difficult to access the lens for alignment, i.e., its alignment needs to be carefully verified during assembling.

We finally conclude that our presented echelle design version IV is comparable to the widely used version I. The image quality of both systems is dominated by field curvature. However, eliminating for this aberration, version I still suffers from off-axis aberrations, leading to distorted spots. This can be completely compensated for in version IV. In the view of precise radial velocity measurements and detailed line-profile analysis, a homogeneous and well defined point-spread-function is to be preferred. Such distorted spots influence the slit-spread-function when working with spot sizes close to the size of a pixel and close at the Nyquist two-pixel-resolution limit. This will add to a unknown variable in the data-reduction process, especially when we think of temperature dependence of image quality, hence, temperature dependence of the slit-spread-function.

Our design example demonstrates that diffraction limited image over the whole wavelength range from 400 to 800 nm can be achieved over the whole detector. This example eliminated the influence of optical aberrations to the final image of a unresolved spectral line and will support the precision of the instrument. Additionally, the optical complexity of the overall system is comparatively low.

References

- Eversberg, T. & Vollmann, K. 2015, Spectroscopic Instrumentation (Berlin, Heidelberg: Springer)
- Kaufer, A., Stahl, O., Tubbesing, S., et al. 1999, The Messenger, 95, 8
- Raskin, G., Van Winckel, H., Hensberge, H., et al. 2011, A&A, 526, A69
- Sablowski, D. P. & Schanne, L. F. 2018, Astrophysikalische Instrumentierung und Messtechnik für die Spektroskopie (Mannheim, Germany: self-published)
- Schroeder, D. J. 2000, Astronomical Optics (San Diego, California: Academic Press)
- Smith, W. J. & Genesee Optics Software, Inc. 1992, Modern Lens Design (USA: McGraw-Hill Inc.)

- Strassmeier, K. G., Ilyin, I., Järvinen, A., et al. 2015, *Astronomische Nachrichten*, 336, 324
- Weber, M., Granzer, T., & Strassmeier, K. G. 2012, The STELLA robotic observatory on Tenerife

A.3. PEPSI-feed: linking PEPSI to the Vatican Advanced Technology Telescope using a 450m long fibre (Manuscript AIII)

D. P. Sablowski¹, M. Weber¹, M. Woche¹, I. Ilyin¹, A. Järvinen¹, K. G. Strassmeier¹ and P. Gabor²

Proc. of SPIE, 99125H, 2016

1: Leibniz Institute for Astrophysics Potsdam (AIP), An der Sternwarte 16, 14482 Potsdam, Germany
2: Vatican Observatory, The University of Arizona, USA

Abstract Limited observing time at large telescopes equipped with the most powerful spectrographs makes it almost impossible to gain long and well-sampled time-series observations. Ditto, high-time-resolution observations of bright targets with high signal-to-noise are rare. By pulling an optical fibre of 450m length from the Vatican Advanced Technology Telescope (VATT) to the Large Binocular Telescope (LBT) to connect the Potsdam Echelle Polarimetric and Spectroscopic Instrument (PEPSI) to the VATT, allows for ultra-high resolution time-series measurements of bright targets. This article presents the fibre-link in detail from the technical point-of-view, demonstrates its performance from first observations, and sketches current applications.

high-res spectroscopy, fibre optics, fibre-feed, PEPSI

A.3.1. Introduction

It is common that large telescopes are used to feed a suite of instruments. This limits the maximum time for observations for each individual instrument. Long and dense time-series of data from a single target are almost impossible to obtain. However, if a high-resolution spectrograph is connected to a small sized telescope, it is possible to gain time-series data with high quality of bright stars. We have established a 450 m long fibre connection from the 1.8m VATT to feed the PEPSI Strassmeier et al. (2015) spectrograph located in the basement of the LBT building. A comparable project was carried out at the Gemini Telescope and the CFHT ESPaDOnS Spectrograph Chene et al. (2014). A good example for science on bright stars is the binary Capella Torres et al. (2015) with an orbital period of 104d. Ultra-precise orbital parameters for binaries are of great importance, e. g. for the determination of stellar masses which are very sensitive to the evolutionary status but also for color-surface brightness relations which are important for the calibration of the cosmic distance ladder. Dense time-series observations are essential for these kind of studies.

Three main issues on fibre optics need always be considered when designing fibre-coupled instruments. Firstly, focal-ratio-degradation (FRD) is the effect of faster output beam compared to the input. It is explained by disturbance of the microstructure between core and cladding as well as macroscopic bending of the fibre itself. Secondly, modal noise is the result from interference inside the waveguide which leads to an angular-discrete intensity distribution of the output beam Sablowski et al. (2016). Thirdly, low transmission is most critical in the blue region towards the near ultra violet in visual applications. Modal noise for long fibres is effectively reduced by the imperfect intersurface between core and cladding which in turn increases FRD. Working with fast input ratios will reduce both modal noise and FRD. The fibre system for PEPSI is designed to work at an input f-ratio of $f/3.2$ which

is near the limit to prevent any losses at the total reflection intersurface between core and cladding due to small bedding radii of the fibre cable.

In Sect. A.3.2 we describe the fibre-link from the VATT to PEPSI via the Permanent Fibre Unit (PFU) of PEPSI. We demonstrate the performance of the link with measurements on bright stars in Sect. A.3.3 and draw our conclusions in the last section.

A.3.2. The measurement chain

The light collected by the VATT is coupled into a $200\mu\text{m}$ circular FBP fibre from Polymicro. The transmitted light after 450 m of fibre is coupled into the octagonal FBP fibre inside the permanent fibre units (PFUs) mounted on the LBT. At the spectrograph input, the output beam is transformed to $f/13.9$ and injected to the waveguide image slicer. The slicer provides three different modes of spectral resolution Strassmeier et al. (2015).

A.3.2.1. Fibre link

We show the optical layout of the fibre-injection in Fig. A.34. The $f/9$ beam provided by the VATT is collimated by a commercial achromatic lens with a focal length of 150mm. The parallel beam passes a beam splitter with an ratio of 99:1 between transmitted and reflected light. The reflected light is directly imaged by a second achromatic lens (50mm focal length) onto the CCD of the guide camera. The transmitted part is imaged by a third lens (100mm focal length) onto the fibre core. The fibre core is positioned behind a reflective pinhole. The light reflected from the pinhole passes the beam splitter again and is reflected by a slightly tilted mirror towards the guide camera. The spot diagrams for all three configurations are shown in Fig. A.35

We use a custom $200\mu\text{m}$ FBPA200240280400 fibre ($200\mu\text{m}$ core, $240\mu\text{m}$ cladding, $280\mu\text{m}$ polyimide, and an extra $400\mu\text{m}$ acrylate for protection) to transport the light from the VATT to the LBT. At the LBT, the fibre is connected to the PEPSI permanent focal station (PFU) at the calibration light input, see Fig. A.36. The VATT fibre is attached to an achromatic rod lens to provide an equal output as for the calibration fibre. A mirror can be rotated into the beam and reflects the light to a triplet lens which transforms the diverging beam into a converging beam to match the LBT input. Then using two optional folding mirrors, one of the three available octagonal science fibres can be selected which provide the three different resolution modes. It is also possible to bypass the calibration optics to avoid re-imaging losses, in that configuration the fibre is directly attached to the $200\mu\text{m}$ sky fibre using a fibre-switch inside the left (LBT-SX side) PFU.

The original FBP fiber was directly shipped to the LBT, therefore it was not possible to measure it. However, we measured transmission with a sample FBP fibre and FRD as well as modal noise for a 420m long STU fibre from the same manufacturer. The measurement system used to perform the measurements described below has been described elsewhere Sablowski et al. (2016).

Modal noise measurement Due to interference inside the fibre, the output beam is discrete in space. This intensity structure leads to noise in the spectral measurements. The noise is increased if spatial filters, e.g., input slits are used. It is reduced for fast input beams and towards smaller wavelengths where more modes are excited. Scattering caused by impurities inside the glass and at the interface between core and cladding leads to a decrease of this structure. Hence, it also depends on the length of the fibre. A study (Sablowski et al., 2016) on modal noise from short pieces of fibres verified that it

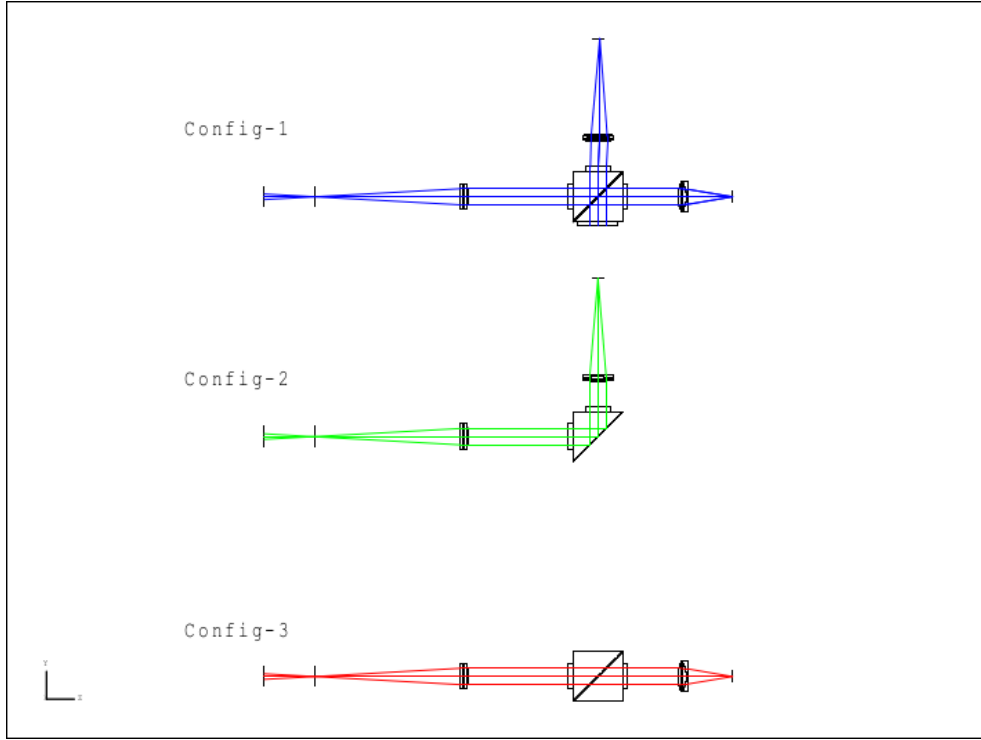


Figure A.34.: Layout configurations of the fibre link. Configuration 1 shows the full path reflected at the fibre pinhole and imaged onto the guider camera slightly offset in respect of the direct reflection. Configuration 2 shows the direct reflected path towards the guider camera and configuration 3 shows the path entering the fibre.

is proportional to the number of modes. The modal parameter V is a measure for the number of bound modes $N_M \approx 4V^2/\pi^2$. For circular symmetric fibres, it is given by

$$V^2 = \frac{4\pi^2}{\lambda^2} (NA)^2 \rho^2, \quad (\text{A.71})$$

where λ is the wavelength, NA the numerical aperture of the input beam and ρ the radius of the fibre core. If we assume poisson statistics, the signal-to-noise ratio SNR is proportional to the square root of the number of excited modes, $SNR \propto V$. Hence, it increases with decreasing wavelength, fibre core diameter and numerical aperture. The wavelength dependence of the input f-ratio and the maximum number of modes is shown in Fig. A.37a and A.37b for a core-doped GeO_2 (11.2 mol %) fibre Butov et al. (2002). The f-ratio increases (decreases) towards longer (shorter) wavelength, i.e., it is possible to couple blue light with even faster input f-ratios. Figure A.37c shows the number of modes for the same fibre for constant input f-ratio of 3.2.

The overall noise N in the spectrum is given by

$$N^2 = B^2 + M^2 + P^2 \quad (\text{A.72})$$

the square-sum of the background noise B , the photon noise P and the modal noise M . The background noise was reduced by using an average of ten images. Furthermore, we measured that noise in the mean image and compute the modal noise from the measured overall noise in the spectrum according to

$$M = \sqrt{N^2 - B^2 - P^2}, \quad (\text{A.73})$$

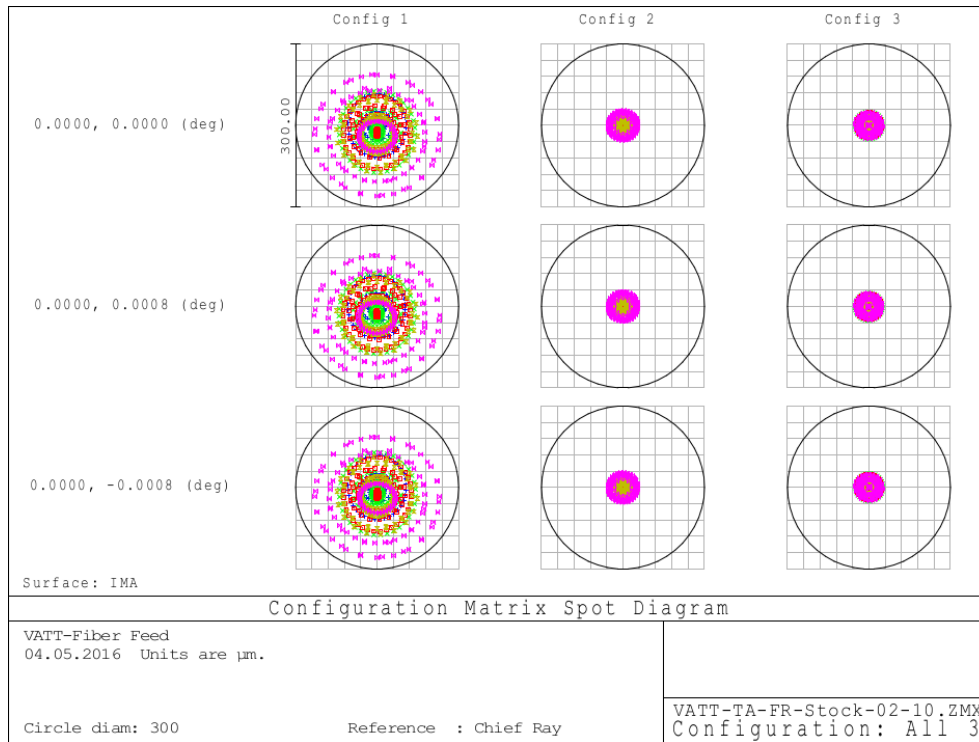


Figure A.35.: Spot diagram for all three configurations. The circle has a diameter of $300\mu\text{m}$. After back-reflection from the pinhole, the beam suffers from stronger aberrations. However, since the direct reflected image is used for guiding and the image quality at the pinhole surface is sufficient, commercial lenses were used.

where we determined P from the count rate in the spectrum. The SNR measurements shown in Fig. A.38a have been performed with a transportable Czerny-Turner spectrograph. The spectrograph suffers from astigmatism, which causes the spectrum to expand several times as geometrically expected. Hence, the interference structure of the spectrum is pronounced and well measurable. We have performed the SNR measurements in the spectral region between 674 and 698nm. Resolving power of the spectrograph is 20.000 for a $50\mu\text{m}$ input slit width and the dispersion is $0.0157\text{nm}/\text{pix}$ at a pixel size of $9\mu\text{m}$. Hence, we need to note that these measurements are comparable to among themselves, but do not set overall limits.

We measured the SNR of the fibre on and off the spool, which is plotted in the aforementioned figure. The values for the fibre on the spool are higher except for the measurement at $f/10$ input. For the fast input at $f/4$ and $f/5$ the measurements are photon noise limited, i.e., modal noise is not present. However, if these measurements are compared with those in Sablowski et al. (2016) (Fig. 7) modal noise is strongly reduced even for the measurements off the spool, which is the more realistic case. An increase of ≈ 4.6 is achieved if we compare the value for $f/4$ input in Fig. 7 for the $200\mu\text{m}$ circular fibre of the aforementioned paper with our measurements.

Focal-Ratio-Degradation We have measured the 420m long sample of a STU fibre for input f-ratios of 3.2, 4, 5, 7 and 10 and show the results in Fig. A.38b. We also plot the relation input f-ratio equal to output f-ratio. The measurements were performed for the six central wavelengths of the cross-dispersers of PEPSI, but there is no hint for a wavelength dependence of the FRD. These measurements show strong FRD even for slow input ratios.

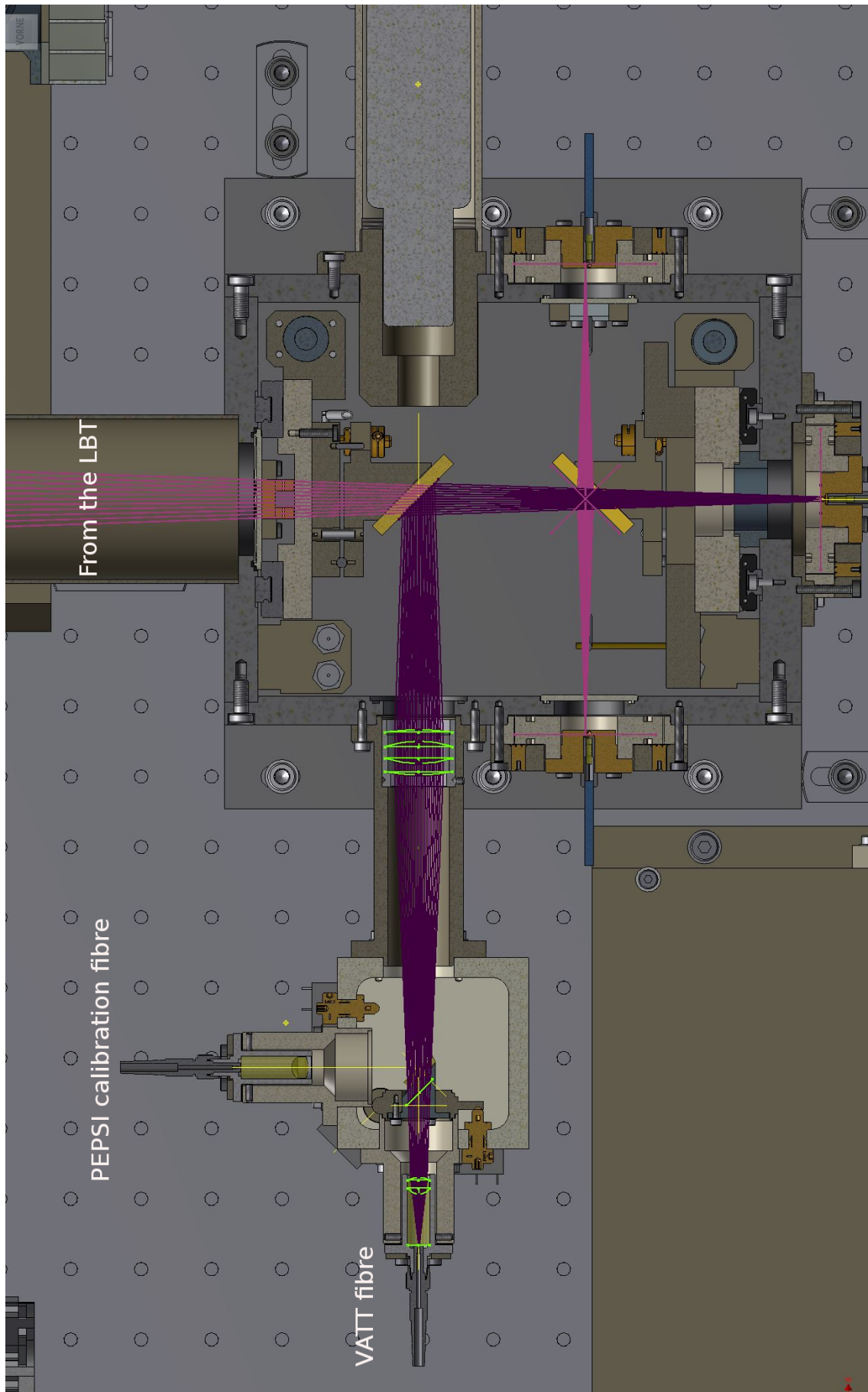


Figure A.36.: Connection of the VATT fibre (top left) at the calibration input at the PFU. The output is transformed to match the LBT f-ratio and is reflected towards the octagonal science fibres.

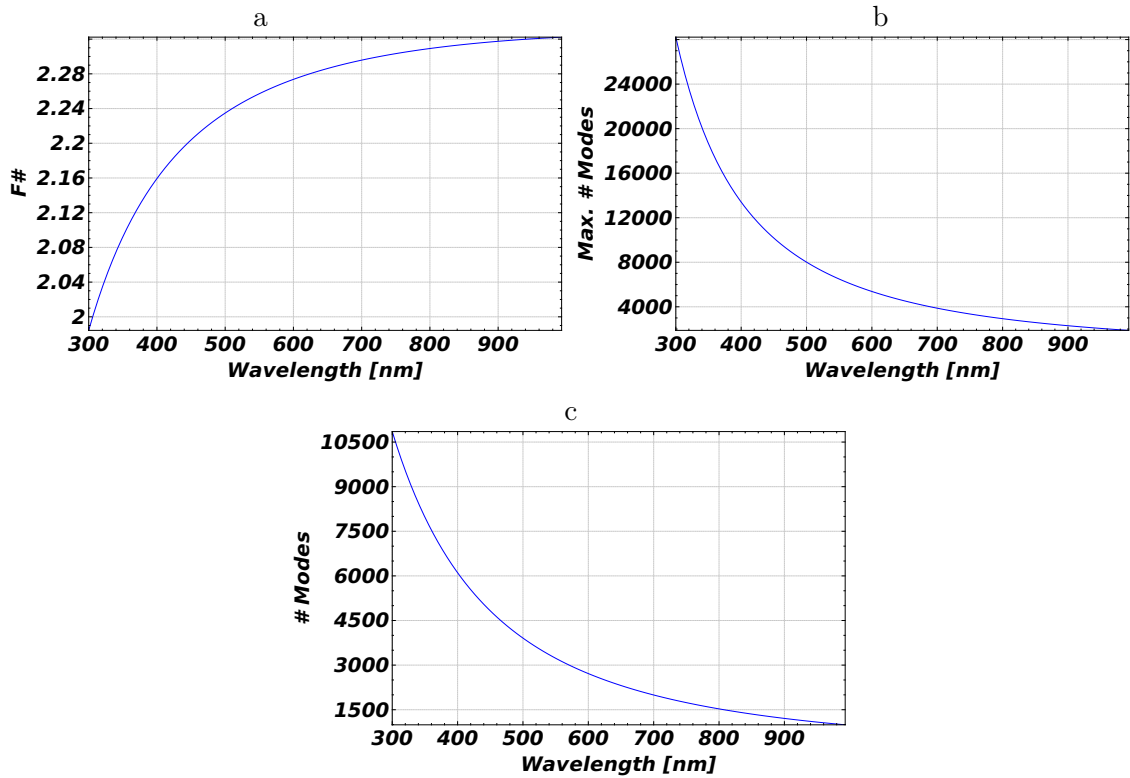


Figure A.37.: (a): Input f-ratio for a core-doped GeO₂ (11.2 mol %) fibre. (b): Maximum number of modes calculated with the wavelength dependent f-ratio. (c): Number of modes for a constant input f-ratio of 3.2.

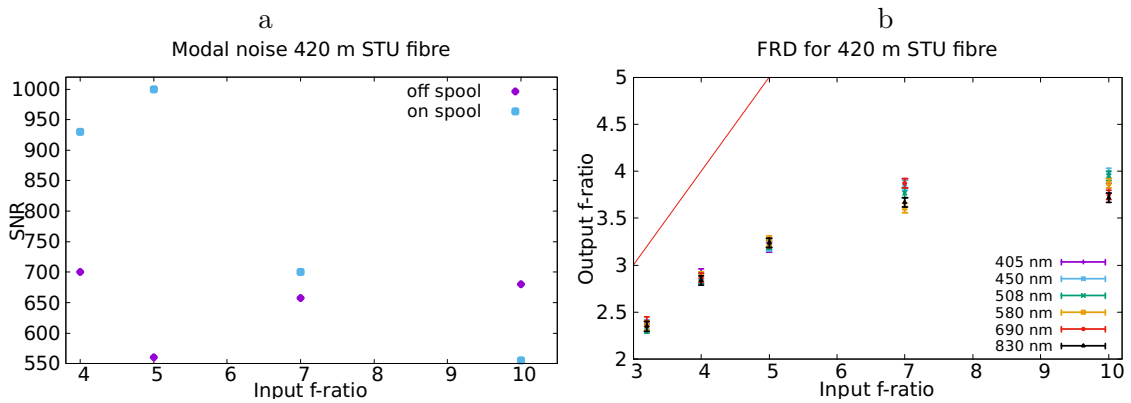


Figure A.38.: (a) Measured modal noise of 420 m STU fibre on and off the fibre spool; (b) FRD for a 420m long sample of STU fibre. Also shown is the relation input f-ratio equal to the output f-ratio.

F/4 input, e.g., yields and output of around F/2.8 which is around 0.3 lower than the ratio in Fig. 10 in Sablowski et al. (2016).

Transmission In broadband applications in the visual range of the spectrum, transmission is critical in the blue region towards the ultra violet. This is caused by Rayleigh scattering as well as scattering caused by impurities inside the glass and the non-ideal interface between core and cladding. Additionally, absorption caused by the hydroxide anion affects the transmission towards the near infrared. Therefore we have measured the transmission of three different types of fibres and show the results in Fig. A.39. The STU sample was 420m long, the FBP sample we used had a length of 50m and the WF fibre was 500m long. We extrapolated the FBP measurements. The data provided by the manufacturer for the WF fibre was for a $200\mu\text{m}$ core fibre and we performed the measurements with a $72\mu\text{m}$ fibre.

The measurements were done in the following way. Both ends of the fibre were glued to connectors and polished. We used interference filters (405, 450, 508, 580, 690 & 830nm) with a bandwidth of 10nm to get the transmission in dependence of the wavelength. We measured the throughput of the fibre and at the same time we recorded the fluctuations of the illumination source to correct for them afterwards. Then we cut down a piece of 1m from the sample fibre, connectorized and polished it again and measured the throughput of that short fibre under the assumption that it is only affected by coupling losses. We did not disconnect the other fibre end from the illumination system while preparing the bare fibre end. This was repeated five times for each fibre to get the errorbars as plotted. We conclude for these measurements, that the provided values from the manufacturer are in good agreement with our measurements.

A.3.2.2. Guiding and PEPSI interface

The PEPSI VATT telescope adapter is equipped with a Basler acA1600-20gm/gc guiding camera which has the Sony ICX274 $1600 \times 1200 \times 4.4\mu\text{m} = 7.04 \times 5.28\text{mm}$ CCD. The scale factor on the CCD is 0.11 arcsec/pix.

The camera is a GigE Vision closed-source standard interface which requires a 1GB Ethernet link. A separate local computer server Dell R220 is used to provide the high-speed Ethernet link to the camera and hosts the graphical user-interface to the guider application. The PEPSI control program is then linked to the guider GUI via LBTO general-purpose network over an X11-forwarding `ssh` socket.

To communicate with the Basler, we use the third party open-source software library Aravis (wiki.gnome.org/Projects/Aravis) which is a vision library for GeniCam technology based cameras.

The Graphical User Interface and Numerical Template Library is part of the Spectroscopic Data Systems (SDS) which is written in C++ and uses multi-threaded event-driven graphical communications to a single X11 server via native `Xlib` calls in the same application.

The camera has a single RJ45 connector and is powered over Ethernet link with a separate standard power supply. As the power consumption may grow high during continuous CCD readouts, the temperature of the camera may rise as high as 60C, hence, the camera is equipped with a custom made heat sink to reduce any thermal noise on the CCD during integration.

The camera is not equipped with a mechanical shutter, but is using a global electronic shutter. The exposure times are limited to the range of $1\mu\text{s} - 1\text{s}$. In the case of faint targets

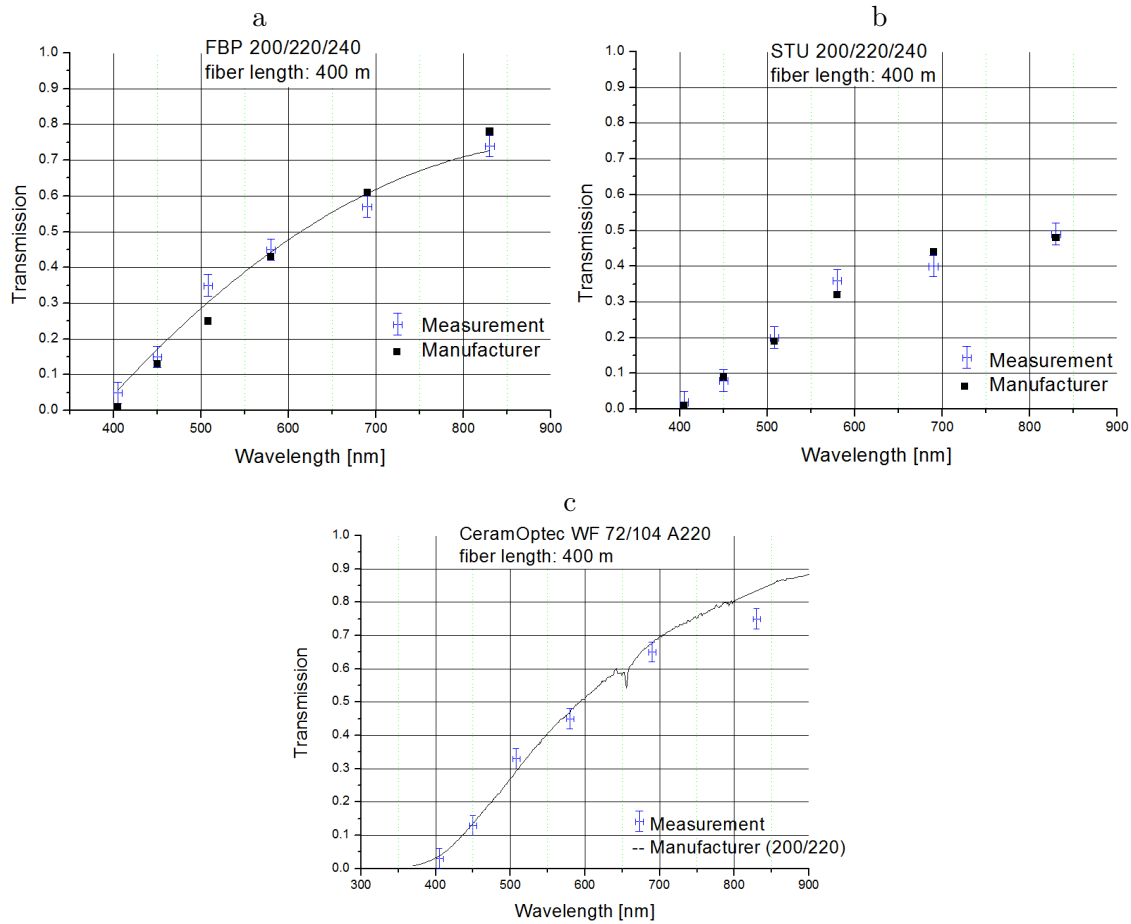


Figure A.39.: Transmission for the three measured fibres compared to values from the manufacturers. For the PEPSI-VATT link we used the FBP fibre shown in panel (a). Panel (b) shows the transmission data for the STU fibre (measured with 420m) and (c) shows the data for the WF measured with 500m from 72 μ m (manufacturer values for a 200 μ m WF fibre.)

when 1 s integration time is not sufficient to get enough light, a special accumulation mode is used where a specified number of short exposures are summed up into the resulting image for further analysis of the target position.

The communication with the VATT telescope control system (TCS) is implemented with a dedicated Internet socket which accepts a number of interface commands. The PEPSI VATT control interface uses the commands to point the telescope to a target with the specified equatorial coordinates, to apply a small guiding corrections in RA/Dec, and to obtain status information of the current position of the telescope and its environment. The PEPSI VATT adapter is mounted in a fixed position in the Cassegrain focus flange with no de-rotator being used during observations, therefore, the guiding CCD offset corrections in XY of the Alt/Az frame are always converted into the equatorial coordinate system as required by the TCS (Fig. A.40b).

The observing targets are stored and subsequently selected from the catalog stored as a FITS Binary table and managed by a separate graphical application (Fig. A.40c). Alternatively the observing target can be retrieved from the observing blocks of the PEPSI control program. The observing catalog application has a capability to retrieve coordinates and other attributes from SIMBAD database via Internet socket, as well as to display a

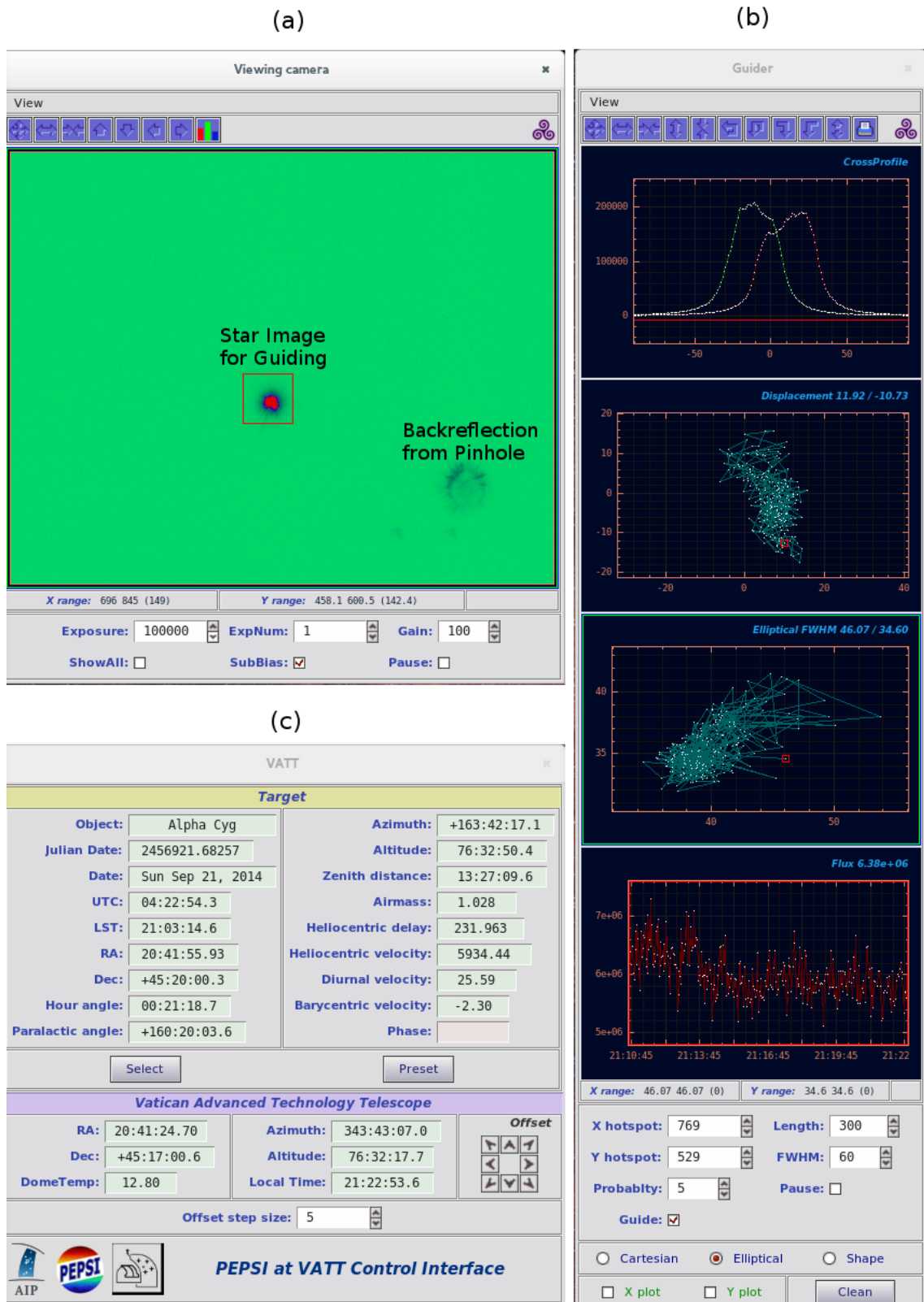


Figure A.40.: The Graphical Interface to control VATT by presetting telescope to the selected star (c) and guiding on the direct reflected guider image (at the center of the image, b). The back-reflected fiber pinhole image is seen at the bottom right part of the image (a).

visibility plot of the selected targets. Once the next observing target is selected, the observer can initiate the telescope to slew to the new position. Once the new target appears on the CCD camera at about its center, the observer can start guiding on the target. In case the target appears too far from the CCD center due to pointing errors, its position can be corrected by GUI buttons to move the star in Alt/Az coordinate system closer to the CCD center.

The guiding is done on the direct-reflected image of the observing target and the back-reflected image from the mirrored pinhole of the 200 μm fiber is merely used to verify that the star is well centered on the pinhole (Fig. A.40a). This configuration is achieved with a gray beam-splitter which has a mirrored wedge on one side to offset the back-reflected image on diagonal of the CCD. The direct-reflected guider image takes a few percent of the target light. The guider application keeps the target at the specified hotspot position on the CCD by applying small corrections to the TCS to ensure that the star is well centered on the pinhole. The pinhole position can be otherwise interactively modified especially after mounting and dismounting the adapter in the Cassegrain focus.

Prior to the image processing to obtain the guiding offsets, the raw CCD image has to be de-trended to avoid any gradients due to illumination and thermal effects. The background surface is removed with two-pass iterations in CCD columns first, then in rows. The image is first partitioned in 128 stripes in columns where the median value for each stripe is calculated. A spline fit of the specified smoothing factor through these 128 background estimates is used to evaluate and subsequently subtract from every column of the CCD image. Then, the same procedure is repeated but in CCD rows since the background gradient may have bi-directional slope.

A Gaussian windowed center of gravity is used to determine the offset of the direct-reflected image of the star from the hotspot position. A typical FWHM of the Gaussian window is about $7'' - 10''$ on sky and can be alternated depending on the seeing conditions. The use of the windowed function is justified as it gives a more precise position of the source via iterative process of re-adjusting of the position of the window function to the final position and eliminates any side effects which may take place in the field of view. The second moment of the gravity center gives estimates of the FWHM of the seeing profile and its covariance from which the Cartesian or elliptical seeing conditions are calculated. The finite width of the Gaussian window affects the FWHM of the seeing profile as they are added in reciprocal quadratures as the result of the product of two Gaussian profiles, hence, the window function FWHM has to be excluded from the final estimate of the width.

When calculating the first moment of the center of gravity, we also use the variances of the photon noise with the assumption of the Poisson noise distribution for each CCD pixel. The variances, properly scaled with the Gaussian window function, allow for the errors and covariance estimate of the determined center of gravity. Subsequently, as the guider camera collects a number of such estimates, we calculate the mean offset and covariance matrix of the random variables correlated in XY , from which we derive the total accumulated offset distance and its variance. As the next step, we evaluate its statistical significance with the F -test. If the statistical significance is lower than specified level (a typical False Alarm Probability (FAP) level is $10^{-3} - 10^{-5}$), we continue to collect more guider images and accumulate more accurate mean center of gravity estimate. Once it becomes statistically more significant, then the correction in XY are applied and the accumulation of the mean offset is started over. If we want more frequent corrections of the guide star, then we need to rise the level of FAP, and the opposite is true, so that with the lower FAP level the guiding offset are applied less frequently.

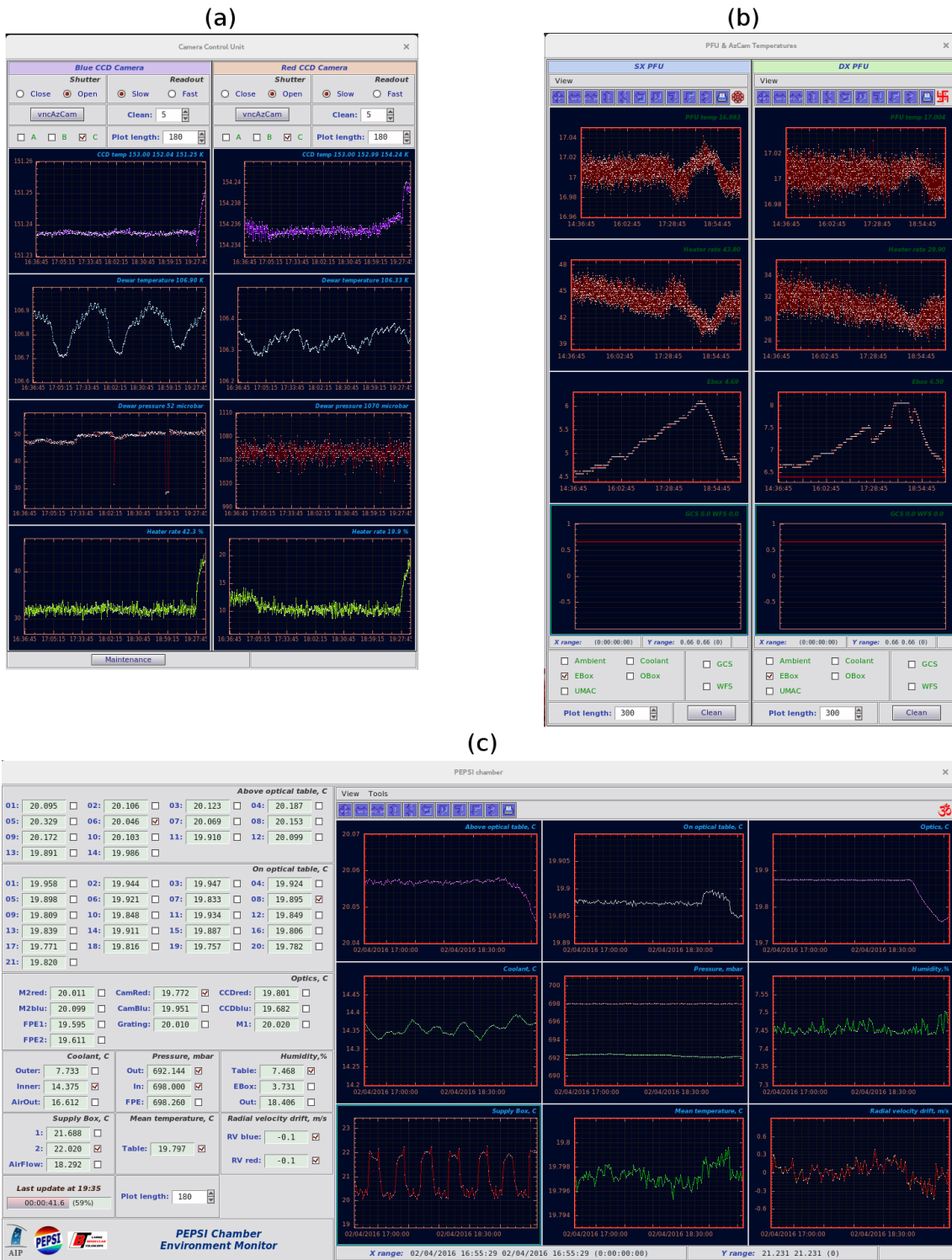


Figure A.41.: The environmental data displayed via the PEPSI control program. (a) shows the temperature and pressure value for the blue and red CCDs. (b) are the values of the PFUs and (c) shows the environment of the PEPSI spectrograph chamber.

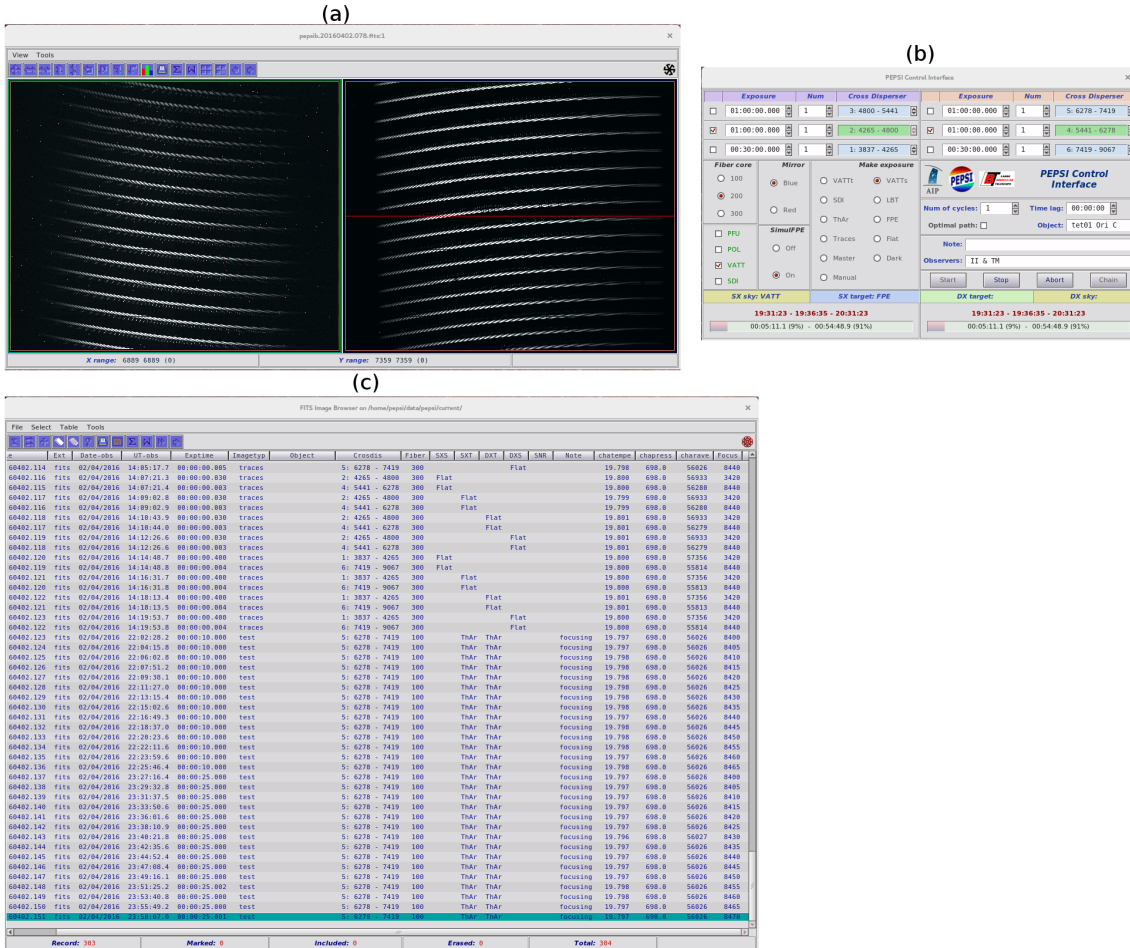


Figure A.42.: The windows for PEPSI set-up and data visualization via the PEPSI control program. (a) shows the raw fits frames and allows to use and plot regions of the frame in x and y. The window (b) is to choose the proper configuration for the exposure (cross-disperser, exposure time etc.) and (c) collects all frames in a table from where they can be loaded.

A.3.3. Observations

The observations using the VATT are divided into several runs per semester of 7–10 nights each, usually during bright time. Bright targets are chosen to get data with high SNR at highest possible resolution. However, also some fainter targets such as θ^1 Ori C (magnetic brake candidate) and the Nova Sqr 2015b (V5668 Sqr)Wagner et al. (2016) were observed. Additionally, 10 nights of simultaneous observations were made on Capella to cover the rotation period of the secondary component. This system is of particular interest, since both components are evolved stars. The secondary, however, is still within the Hertzsprung gap towards the RGB. It shows a higher lithium surface abundance since convective mixing has not affected it yet. The masses of both components are very precisely determined Weber & Strassmeier (2011), such that analysis of the evolution were performed with high accuracy Torres et al. (2015). Hence, dense and high-resolution of spectra for Doppler imaging of the secondary Hertzsprung gap star were obtained.

In Fig. A.43 we show some statistics of obtained observations with PEPSI linked to VATT in dependence of the used cross-dispersers. Due to the 450m of fibre in between,

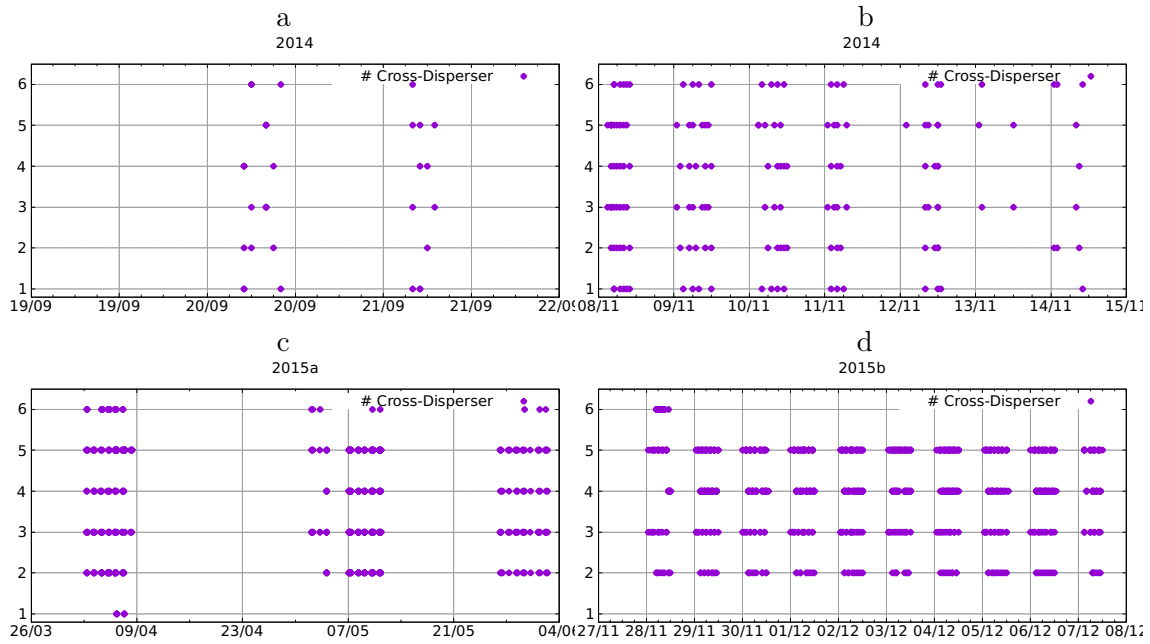


Figure A.43.: Observations vs. time plotted for all six cross-disperser for (a) semester 2014 A, (b) semester 2014 B, (c) semester 2015 A and (d) semester 2015 B.

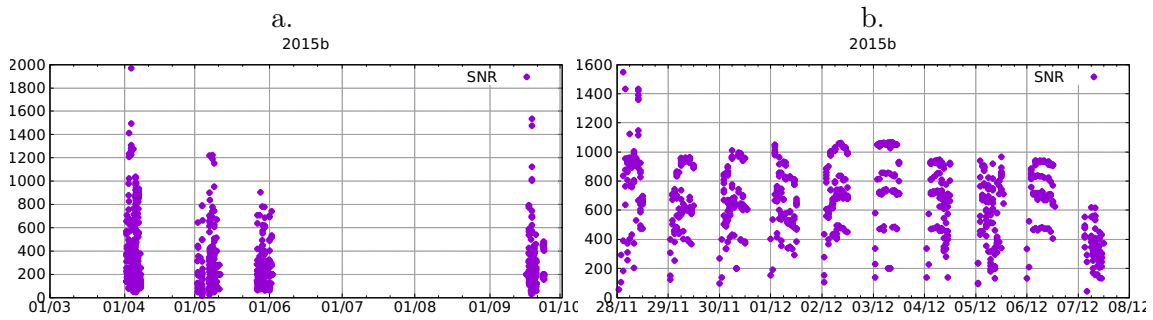


Figure A.44.: Signal-to-noise ratio vs. time for observations in (a) semester a 2015 and (b) semester b 2015.

measurements in the blue region (CD I) were not continued in 2015.

We show the signal-to-noise ratio of the measurement of 2015 in Fig. A.44. Again, the fibre limits signal-to-noise in the blue, therefore high values are only obtained in the red spectral regions.

Epsilon Eridani (Fig. A.45) is among the bright stars that are mildly magnetically active and where a planet detection had been claimed (but still actively discussed). It is also a case that exhibits cyclic magnetic activity of its chromosphere and even its photosphere albeit with a much shorter period than the Sun (≈ 3 years Metcalfe et al. (2013); Lehmann et al. (2015)). Well-sampled spectroscopic observations over such a long period are usually only possible with smaller telescopes and small spectrographs but ideally suited for a telescope-spectrograph combination like the VATT and PEPSI.

A.3.4. Future work and conclusion

A new image slicer for PEPSI is in construction and will provide an additional stack for the VATT fibre. The VATT fibre will be removed from the PFU and connected to a

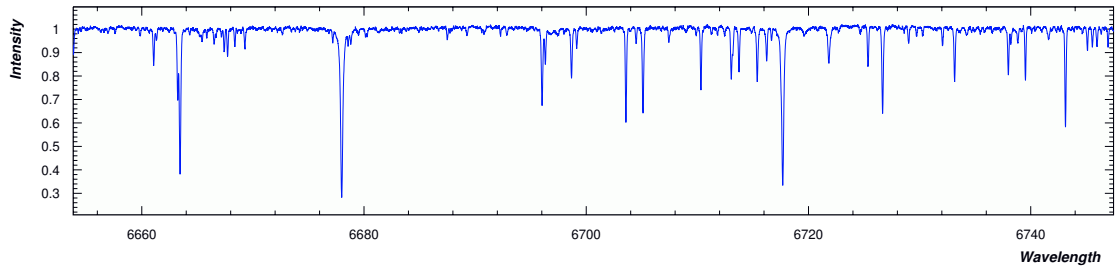


Figure A.45.: $R \approx 250,000$ spectrum of the bright K-dwarf epsilon Eridani. Shown is an excerpt around the Li I 6708 line. S/N ratio in the continuum is around 300:1, exposure time was 20min. The spectrum was taken on Sept. 24, 2015, UT12:31 with the 100- μm fibre connection from the PFU into the spectrograph adding considerable losses due to the geometric mismatch with respect to the long VATT (200- μm core) fibre.

fibre switch near the spectrograph. From that switch, a dedicated fibre is attached to the transformation optics at the spectrograph input which feeds the image slicer. Using the 200 μm fiber but filling the space normally used for the target and sky individual spectra from the LBT SX or DX telescopes, this will give a resolution comparable to the ultra-high-resolution mode usually provided using the 100 μm fibres. It will also increase throughput since re-coupling inside the PFU is no longer necessary, and the total fibre length is shortened by 40 m.

References

- Butov, O., Golant, K., Tomashuk, A., Van Stralen, M., & Breuls, A. 2002, *Optics Communications*, 213, 301
- Chene, A.-N., Padzer, J., Barrick, G., et al. 2014, GRACES: Gemini remote access to CFHT ESPaDOnS spectrograph through the longest astronomical fiber ever made: experimental phase completed
- Lehmann, L. T., Künstler, A., Carroll, T. A., & Strassmeier, K. G. 2015, *Astronomische Nachrichten*, 336, 258
- Metcalf, T. S., Buccino, A. P., Brown, B. P., et al. 2013, *The Astrophysical Journal Letters*, 763, L26
- Sablowski, D. P., Plüschke, D., Weber, M., Strassmeier, K. G., & Järvinen, A. 2016, *Astronomische Nachrichten*, 337, 216
- Strassmeier, K. G., Ilyin, I., Järvinen, A., et al. 2015, *Astronomische Nachrichten*, 336, 324
- Torres, G., Claret, A., Pavlovski, K., & Dotter, A. 2015, *ApJ*, 807, 26
- Wagner, R. M., Woodward, C. E., Starrfield, S., et al. 2016, in *American Astronomical Society Meeting Abstracts*, Vol. 227, American Astronomical Society Meeting Abstracts, 239.10
- Weber, M. & Strassmeier, K. G. 2011, *Astronomy and Astrophysics*, 531, A89

B. Appendix of Manuscript III

B.1. Correction of tellurics and flux ratio

Because the correction of the telluric lines in the wavelength range under consideration is crucial for the analysis, some details of this procedure are described here. A forthcoming paper by Sablowski et al. (2019) will discuss these disentangling problems in more detail.

The residual spectrum between the separated spectra and an observation is shown in Fig. B.1a. The identified tellurics are approximated by spline fits shown by dots. These splines were used to correct for the telluric lines in the observations. Special care was taken to identify the telluric lines such that no stellar signatures were affected. This was ensured by an iterative process: Only one line (we took the strongest) at a time was removed. The disentangling was performed again, and the next line with the highest contribution to the residuals was corrected. In this way, we corrected for all the telluric lines indicated by the dots in Fig. B.1a in all 12 observed spectra. The same residuals for the fully corrected observations after the final disentangling run is shown in Fig. B.1b.

Measurements of the light ratio for Capella are summarized in Table B.1 and plotted in Fig. B.2. The black solid line is the ratio r given by dividing two Planck relations $r = aP(T_{\text{eff,p}})/P(T_{\text{eff,s}})$ with temperatures as given in Table 4.2. A multiplication factor $a = 1.04$ is needed to adapt to the data.

B.2. Spectrum of the secondary

To ensure that the disentangling is not affected by the tellurics or by the limited sampling of the orbit, further tests were performed. First, three spectra that show the smallest signal from tellurics were selected from the 12 spectra listed in Table 4.1. As pointed out by Sablowski & Weber (2017), at least 3 spectra are required because SVD has to be performed on an overdetermined system of equations, that is, for two components present in the spectra, at least three observations are required. Furthermore, these spectra should correspond to distinctive orbital phases. The separated spectra obtained from that data set are in excellent agreement with the spectra used for the synthesis (see Fig. B.3a). Second, to show that the orbital sampling by the observations is sufficient for the disentangling, 12 spectra were created by the use of synthesized spectra covering the same orbital phases as the observed spectra listed in Table 4.1. The excellent agreement between the templates (the synthesized spectra) and the separated spectra is shown in Fig. B.3b.

The weak feature around the 8004 Å lines can almost entirely be reproduced by the blend lines (Fe I 8002.6 Å, 8003.2 Å, Al I 8003.2 Å, and Ti I 8003.5 Å) and with a carbon abundance as derived for the primary. However, we show the separated spectrum together with a theoretical spectrum in Fig. B.3c. We used the parameters given in Table 4.2 and a macroturbulent velocity of 7.0 km s⁻¹. The used line list is a combination of the list provided by Carlberg et al. (2012) and selected lines (with significant strengths) from VALD-3. The blue-side line to the strong Fe I 7998.944 Å could not be identified. It is too strong for a ¹²CN line (it would disagree with lines at 8004 Å). VALD-3 lists a central depth of the fitted Fe I 7998.944 of 0.534. There are only two lines listed in VALD-3 with

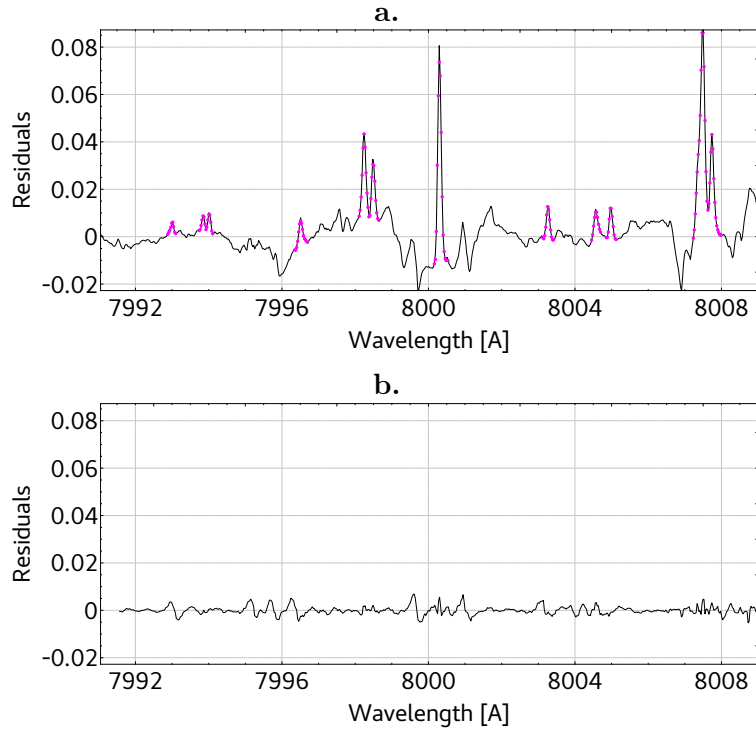


Figure B.1.: Residual spectrum between separated spectra of the two components and an observation with strong telluric lines. **a.** Residuals before correction. The dots represent the spline used to approximate the telluric lines. **b.** Residuals to the final corrected spectrum.

Table B.1.: Relative light ratio measurements for Capella.

Reference	Wavelength [\AA]		$k = l_{GS}/l_{G0}$
	start	end	
Bagnuolo & Sowell (1988)	3996.5	4219.5	0.61 ± 0.02
Griffin & Griffin (1986)	3931	4919	0.69
Hummel et al. (1994)	4400	4600	0.77 ± 0.07
Bagnuolo & Sowell (1988)	4568	4770	0.82 ± 0.02
Torres et al. (2009)	5165.5	5210.5	0.677 ± 0.023
Hege et al. (1983)	5150	5250	0.64 ± 0.03
Torres et al. (2009)	4086	6464	0.854 ± 0.041
Bagnuolo & Sowell (1988)	5351.5	5604.5	0.93 ± 0.02
Bagnuolo & Sowell (1988)	5351.5	5604.5	0.87 ± 0.02
Bagnuolo & Sowell (1988)	5351.5	5604.5	0.92 ± 0.02
Bagnuolo & Sowell (1988)	5351.5	5604.5	0.91 ± 0.02
Hummel et al. (1994)	5383	5583	0.87 ± 0.04
Hege et al. (1983)	5450	5550	0.82 ± 0.02
Hege et al. (1983)	5420	5620	0.89 ± 0.01
Griffin & Griffin (1986)	5095	5993	0.87
Huby et al. (2013)	6112	8430	λ -dependent
Hummel et al. (1994)	8003	8203	1.05 ± 0.05

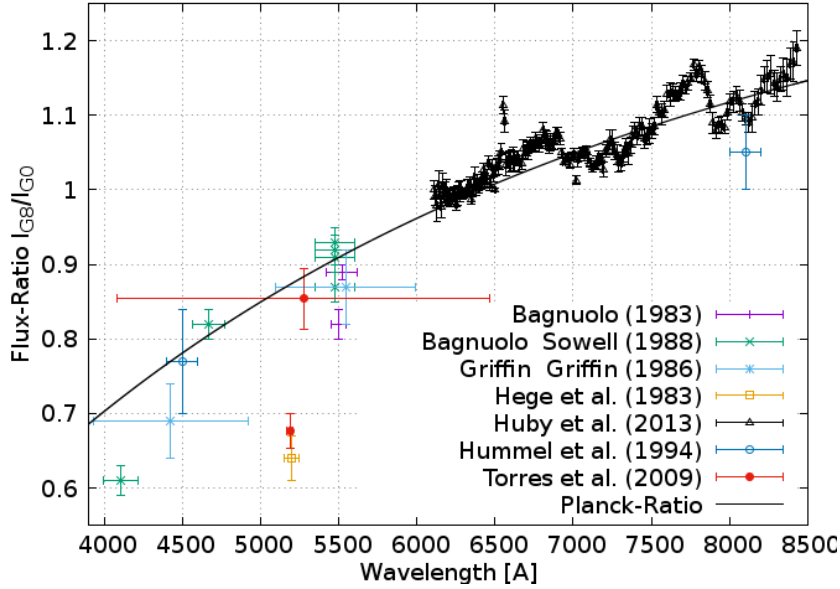


Figure B.2.: Visual presentation of the measurements of the light ratio for Capella (see also Table B.1).

significant depth: Fe I 7996.8156 Å with a depth of 0.026 and Ti I 7996.4350 Å with a depth of 0.072, but they are too weak to fit the observation. The NIST atomic line data base (Kramida et al., 2018) lists only one further and rather exotic possibility of an Th I line with unknown $\log gf$ value. A synthesis would lead to unrealistic abundance and high $\log gf$ value for that line. Furthermore, we plot the synthetic spectrum of the ^{13}C N lines (blue line, abundance as derived for the primary).

References

- Bagnuolo, Jr., W. G. & Sowell, J. R. 1988, *AJ*, 96, 1056
- Carlberg, J. K., Cunha, K., Smith, V. V., & Majewski, S. R. 2012, *ApJ*, 757, 109
- Griffin, R. & Griffin, R. 1986, *JApA*, 7, 45
- Hege, E. K., Hubbard, E. N., Cocke, W. J., et al. 1983, *LowOB*, 9, 185
- Huby, E., Duchêne, G., Marchis, F., et al. 2013, *A&A*, 560, A113
- Hummel, C. A., Armstrong, J. T., Quirrenbach, A., et al. 1994, *AJ*, 107, 1859
- Kramida, A., Ralchenko, Y., Reader, J., & NIST ASD Team. 2018, NIST Atomic Spectra Database (ver. 5.6.1), [Online]. Available: [2018, December 17]. National Institute of Standards and Technology, Gaithersburg, MD.
- Sablowski, D., Järvinen, S., & Weber, M. 2019, *A&A*, accepted
- Sablowski, D. P. & Weber, M. 2017, *A&A*, 597, A125
- Torres, G., Claret, A., & Young, P. A. 2009, *ApJ*, 700, 1349

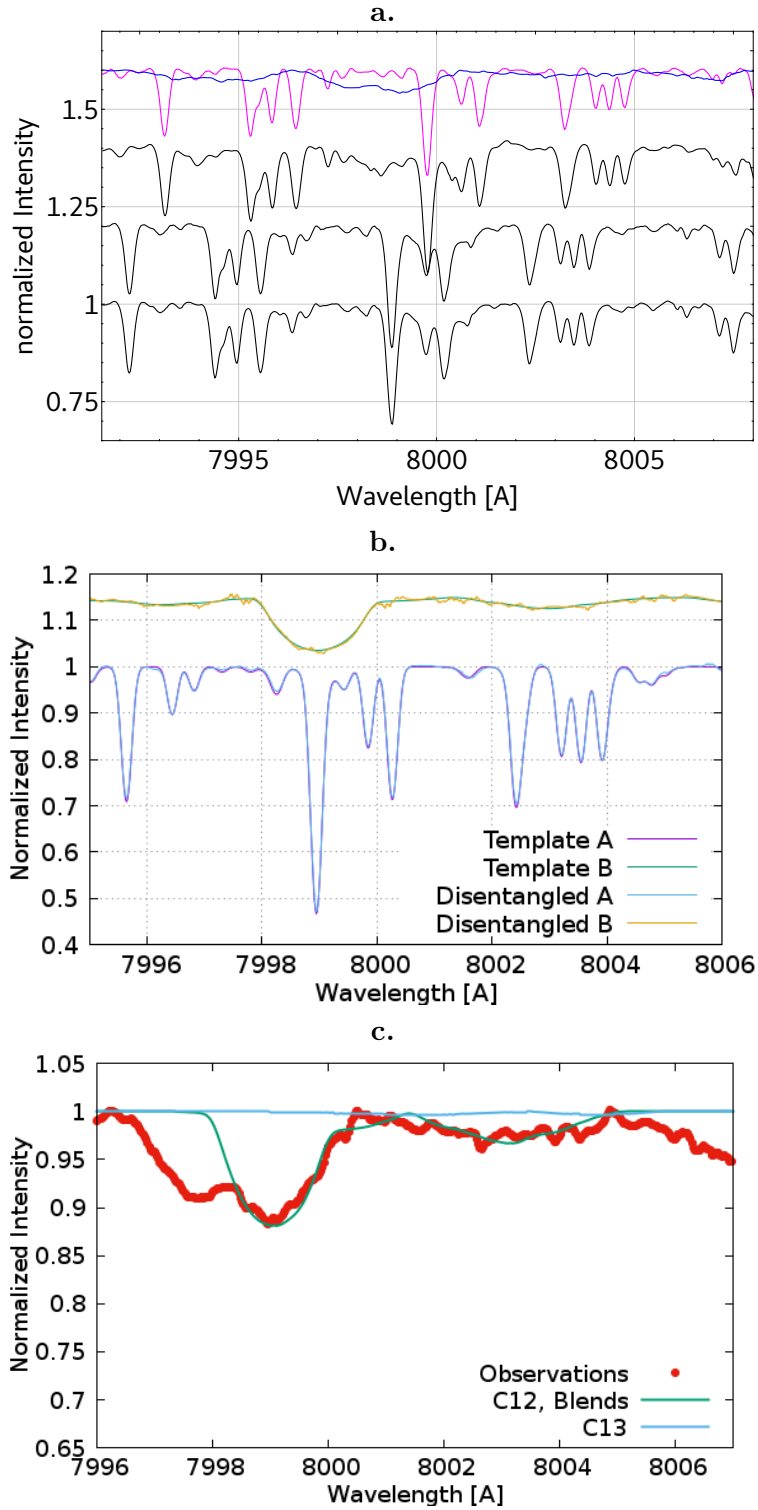


Figure B.3.: **a:** Three selected observations (each shifted on y by 0.2 for better visibility) with the weakest telluric feature (black) and the separated spectra (purple and blue) from these observations. The separated spectra are shifted in wavelength to match the topmost observation. The separated spectra are scaled such that the line strength matches the strengths in the observations. **b:** Synthetic spectra (used as templates to create an artificial binary data set) in comparison with the separated spectra (see Text). **c:** The separated spectrum (red) of the G0III secondary of Capella with a synthetic spectrum (green). This was derived with the stellar parameters as listed in Table 4.2 and the line list given in Table B.2. It shows predominantly only the strong FeI 7999 Å line. The blue line is a synthetic spectrum based on the ^{13}CN lines as with an abundance as derived for the primary.

Table B.2.: Line data for the synthesis of the secondary. Compiled with data from Carlberg et al. (2012) and VALD-3.

Species	λ (\AA)	χ (eV)	$\log gf$ (cgs)
^{12}CN	7990.388	1.380	-2.0585
^{12}CN	7990.790	1.450	-1.6234
^{12}CN	7991.583	1.470	-1.6216
^{12}CN	7992.297	0.090	-2.0114
^{12}CN	7992.297	0.180	-1.5143
Ti I	7993.600	1.873	-2.4970
^{12}CN	7994.018	1.420	-1.6326
Fe I	7994.459	5.946	-2.242
^{12}CN	7994.694	0.110	-1.9666
Ni I	7994.775	5.481	-1.175
^{12}CN	7995.640	0.060	-2.9172
^{12}CN	7995.640	0.290	-1.6556
^{12}CN	7995.640	0.310	-1.6615
Ti I	7996.435	3.337	0.2660
Fe I	7996.8156	4.5844	-2.505
Sc I	7997.372	5.900	-5.489
Ti I	7997.481	4.515	-2.311
^{12}CN	7998.312	1.540	-1.2480
Fe I	7998.944	4.371	0.1489
^{12}CN	7999.214	1.400	-2.0287
^{12}CN	7999.214	1.600	-1.8041
^{12}CN	7999.846	0.100	-1.9830
^{12}CN	8000.261	0.190	-1.4962
^{12}CN	8000.316	1.470	-1.6091
Fe I	8000.317	5.538	-2.878
Fe I	8000.396	6.038	-1.194
Nd II	8000.757	1.091	-1.2220
^{12}CN	8001.524	1.420	-1.6253
^{12}CN	8001.652	1.480	-1.6091
^{12}CN	8002.412	0.180	-1.4962
Fe I	8002.576	4.580	-2.2400
Al I	8003.185	4.087	-1.8790
^{12}CN	8003.213	0.120	-1.9431
Fe I	8003.226	5.539	-1.7630
Ti I	8003.485	3.724	-0.2000
^{12}CN	8003.553	0.311	-1.6440
^{12}CN	8003.213	0.120	-1.9431
^{12}CN	8003.910	0.3300	-1.6478
^{12}CN	8004.036	0.0600	-2.9245
Fe I	8005.049	5.5869	-5.518
Zr I	8005.248	0.623	-2.1901
Si I	8006.459	6.261	-1.7220
Fe I	8006.702	5.067	-2.2820
^{12}CN	8006.925	1.600	-1.7878
Co I	8007.242	4.146	-0.1159

C. Contributions to the high-mass regime

C.1. The Tarantula Massive Binary Monitoring project: II. A first SB2 orbital and spectroscopic analysis for the Wolf-Rayet binary R145

T. Shenar¹, N. D. Richardson², D. P. Sablowski³ et al.

Astronomy & Astrophysics, 2017, 597, A125

1: Institut für Physik und Astronomie, Universität Potsdam, Karl-Liebknecht-Str. 24/25, D-14476 Potsdam, Germany

2: Ritter Observatory, Department of Physics and Astronomy, The University of Toledo, Toledo, OH 43606-3390, USA

3: Leibniz Institute for Astrophysics Potsdam (AIP), An der Sternwarte 16, 14482 Potsdam, Germany

We present the first SB2 orbital solution and disentanglement of the massive Wolf-Rayet binary R145 ($P = 159\text{d}$) located in the Large Magellanic Cloud. The primary was claimed to have a stellar mass greater than $300 M_{\odot}$, making it a candidate for the most massive star known. While the primary is a known late type, H-rich Wolf-Rayet star (WN6h), the secondary could not be so far unambiguously detected. Using moderate resolution spectra, we are able to derive accurate radial velocities for both components. By performing simultaneous orbital and polarimetric analyses, we derive the complete set of orbital parameters, including the inclination. The spectra are disentangled and spectroscopically analyzed, and an analysis of the wind-wind collision zone is conducted.

The disentangled spectra and our models are consistent with a WN6h type for the primary, and suggest that the secondary is an O3.5~If*/WN7 type star. We derive a high eccentricity of $e = 0.78$ and minimum masses of $M_1 \sin^3 i \approx M_2 \sin^3 i = 13 \pm 2 M_{\odot}$, with $q = M_2/M_1 = 1.01 \pm 0.07$. An analysis of emission excess stemming from a wind-wind collision yields a similar inclination to that obtained from polarimetry ($i = 39 \pm 6^{\circ}$). Our analysis thus implies $M_1 = 53_{-20}^{+40}$ and $M_2 = 54_{-20}^{+40} M_{\odot}$, excluding $M_1 > 300 M_{\odot}$. A detailed comparison with evolution tracks calculated for single and binary stars, as well as the high eccentricity, suggest that the components of the system underwent quasi-homogeneous evolution and avoided mass-transfer. This scenario would suggest current masses of $\approx 80 M_{\odot}$ and initial masses of $M_{i,1} \approx 105$ and $M_{i,2} \approx 90 M_{\odot}$, consistent with the upper limits of our derived orbital masses, and would imply an age of $\approx 2.2\text{Myr}$.

C.2. The Wolf-Rayet binaries of the nitrogen sequence in the Large Magellanic Cloud - Spectroscopy, orbital analysis, formation, and evolution

T. Shenar¹, D. P. Sablowski², R. Hainich³ et al.

in preparation

- 1: Institute of Astrophysics, KU Leuven, Celestijnlaan 200D, 3001 Leuven, Belgium
- 2: Leibniz Institute for Astrophysics Potsdam (AIP), An der Sternwarte 16, 14482 Potsdam, Germany
- 3: Institut für Physik und Astronomie, Universität Potsdam, Karl-Liebknecht-Str. 24/25, D-14476 Potsdam, Germany

Context. Massive Wolf-Rayet (WR) stars dominate the radiative and mechanical energy budget galaxies and probe a critical phase in the evolution of massive stars prior to their core-collapse. It is currently not known whether classical WR (cWR) stars form primarily through wind-stripping (w-WR) or binary stripping (b-WR). In contrast to single WR stars, analysis of WR binaries were so far largely avoided due to their complexity. In this study, we focus on the virtually complete population of the 44 WR binaries / binary candidates of the nitrogen sequence (WN) in the sub-solar metallicity environment of the Large Magellanic Cloud (LMC).

Aims. Relying on a diverse spectroscopic database, we aim to derive the physical and, when possible, improved orbital parameters of all WN binary candidates in the LMC. Our goal is to provide an unprecedented statistical test for evolution models of evolved massive stars at low metallicity, and to determine the impact of binarity in forming observed populations of WR stars.

Methods. The spectral analysis is performed using the Potsdam Wolf-Rayet (PoWR) code. Radial velocities are measured via cross-correlation, and disentanglement is performed using the code `Spectangular` or the shift-and-add technique. The evolution of the systems is interpreted using the Binary Population and Spectral Synthesis (BPASS) code, exploring binary interaction as well as chemically-homogeneous evolution.

Results. Of the 44 WN binary candidates, 29 are identified as SB2 and analyzed as such. Eight systems are potential SB1 systems, two of which (BAT99 99 and 112) are potential candidates for WR + compact-object systems. We cannot confirm the binarity of the remaining candidates. About 2/3 of the WN components in binaries are identified as core He-burning (cWR), while 1/3 are hydrogen-burning WR stars. We estimate that $45 \pm 30\%$ of the cWR stars in our sample have interacted with a companion via mass-transfer (45% b-WR or wb-WR). However, based on BASS tracks, only $\approx 12 \pm 7\%$ of the cWR stars in our sample formed purely due to stripping via a companion (12% b-WR). No obvious differences in the distribution of single and binary WN stars on the Hertzsprung-Russel diagram (HRD) are apparent, whose luminosities extend down to $\log L \approx 5.2 [L_{\odot}]$. With the exception of a few systems (BAT99 19, 49, and 103), the equatorial rotational velocities of the OB-type companions are moderate ($v_2 \sin i \lesssim 250 \text{ km s}^{-1}$) and challenge standard formalism of accretion of angular momentum. For most of our targets, chemically-homogeneous evolution can be rejected for the secondary, but not for the WR progenitor. If the apparently single WN stars are not binary products, the only $4 \pm 2\%$ of the WN stars are pure binary-stripped WR stars - about ten times less than expected.

Conclusions. No dichotomy is observed in the HRD positions of single and binary WN stars. If the apparently-single WR stars truly evolved as single stars, the pre-WR mass-loss rates and/or mixing are largely underestimated in evolution codes. Otherwise, it must follow that virtually all apparently-single WN stars in the LMC were stripped by an undetected companion.

We conclude that there are two distinct alternatives. According to the first, binary interaction does not govern the formation of WN stars at low metallicity, and current evolution models strongly underestimate the wind/eruptive mass-loss prior to the WR phase. Otherwise, one is forced to conclude that most apparently single WN stars are, in

fact, products of binary interaction.

D. Individual lines and periods

D.1. Individual lines

D.1.1. Ca II IRT

The infrared triplet (IRT) of ionized Ca II with its lines at 8498, 8542, and 8662 Å is one of the most prominent spectral feature in the near IR (NIR) of G, K, and M stars. Its cores are formed in the chromosphere whereas the wings have photospheric origin (e.g. Andretta et al., 2005), this coupling between different regions of the atmosphere leads to a less localization of the line itself. The triplet is formed by radiative de-excitation from 3^2P to the metastable 3^2D state. Filled-in absorption and core emissions in deep cores are observed for stars with a high activity level (e.g. Linsky, 2017; Zhang & Gu, 2008; Soderblom et al., 1993; Dempsey et al., 1993) Moreover, compared to the near UV H & K lines, the IRT region is less blended and the continuum is much better defined, making the analysis of the line-profile and its changes easier.

Connection between the IRT line $\lambda 8542$ Å and the more established chromospheric diagnostic lines Ca IIH and K as well as the NUV Mg II h & k (for the Wilson-Bappu effect of that line see e.g. Elgarøy et al., 1999) have been studied by, e.g., Linsky et al. (1979). They also found an correlation of the Wilson-Bappu effect. This has been questioned in the case of Capella, e.g. by Linsky et al. (1995), where the authors found that more than 60 % of the Mg II flux emerging from the Hertzsprung gap star. However, since the luminosity of both components differ only by 8 % (e.g. Torres et al., 2015) the fluxes in the Ca IIH & K and Mg II h & k should be equal as well. The result of the disentanglement of the two blue lines of the IR triplet is shown exemplarily in Fig. D.1a.

D.1.2. H α and H β

The H α line shows a relation between line width and luminosity (e.g. Linsky, 1980). The line formation in chromospheres of cool stars were studied, e.g., by Cram & Mullan (1985). They found that in cool and low gravity stars ($T_{\text{eff}} = 4,000$ K, $\log g = 2$) H α gets deeper and wider (compared to a purely photospheric line). A high gravity model ($\log g = 4$) at same T_{eff} gave a weak collision dominated absorption with only residual emission for high activity. Models with higher T_{eff} (5,000 to 6,000) show an almost insensitivity to gravity were the line fills-in and widens. As shown, for example, by Andretta et al. (2005), the Hydrogen Balmer lines are formed in higher layers of the chromospheres.

An example for the disentangled profiles of H α and H β are shown in Fig. D.1b and Fig. D.1c, respectively.

D.1.3. Mg I b triplet and 4571 Å line

As discussed in Sasso et al. (2017), the core of the Mg I b triplet is formed in the low chromosphere while the wings originate from the photosphere. Furthermore, the opacities and the source function are affected by photoionization (NLTE). Hence, the line is less localized.

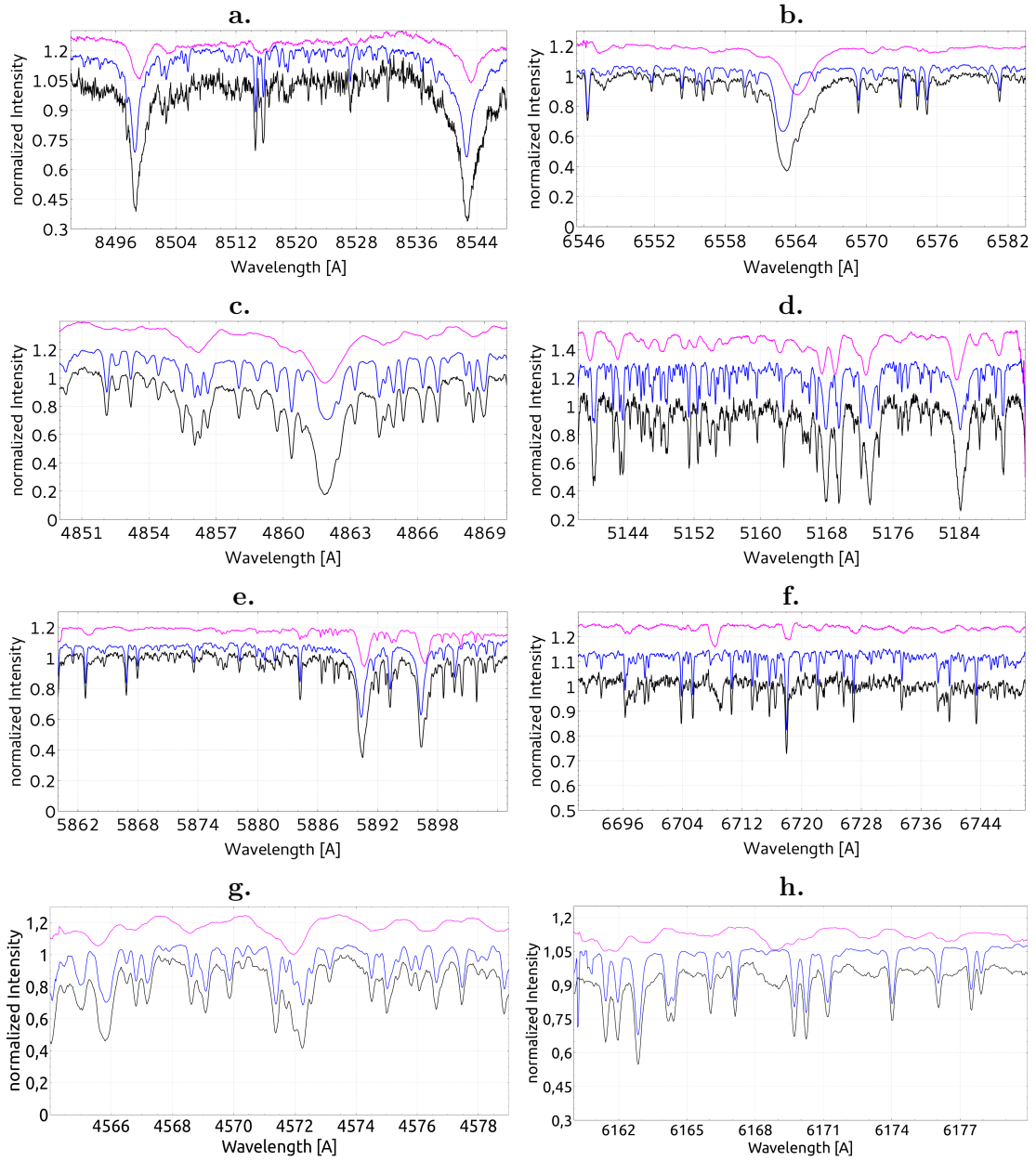


Figure D.1.: Result of the disentangled spectra. An arbitrary chosen spectrum is shown in black. Blue and purple are the disentangled spectra for the primary and secondary, respectively. The disentangled spectra are shifted on y-direction for better visibility and on x-direction to match to the observation for better comparison. **a** Ca II IRT from data set 4. **b** H α from data set 6. **c** H β from data set 3. **d** Mg Ib lines from data set 1. **e** Na I D resonance doublet from data set 5. **f** Li I λ 6707 Å from data set 5. **g** Mg I λ 4571 Å from data set 15. **h** Fe I λ λ 6165.36, 6170.51, 6173.34 Å from data set 15.

Table D.1.: Further photospheric lines studied.

Ion	λ [Å]	g
Fe I	6173.34	2.50
Fe I	6165.35	0.69
Ca I	6162.17	1.25
Ca I	6166.40	0.50
Ni I	6175.36	1.00

In contrast, the 4571 Å line (intersystem forbidden between 3^1S and 3^3P_1 , dominated by collisions) source function is in thermodynamical equilibrium (Sasso et al., 2017). They conclude, that the line is particularly sensitive to changes of activity in solar-like stars at the temperature minimum (where this line is formed). Hence, it can be used as a temperature probe on the lower chromosphere and it is tighter bound to the local temperature (Langangen & Carlsson, 2009). Further information about line formation and 1D modelling can also be found in, e.g., Osorio et al. (2015) and Osorio & Barklem (2016)

D.1.4. Na i D resonance doublet

Short & Doyle (1998) showed that for M dwarfs the Na i D lines behave similar to Ca II H & K. With increasing level of activity, the Na i D lines fill-in, then showing emission, and at very high activity levels the emissions display reversals.

D.1.5. Li i $\lambda 6708$ Å and photospheric lines

As a thermonuclear sensitive element, the Li I $\lambda 6708$ Å line is an important indicator for studies on the evolution of stars. As successors of A- or B-type stars, the envelopes of the components of Capella were radiative during the main sequence phase and mixing of elements was less efficient than in stars with convective envelopes. However, rotationally induced meridional circulation and diffusion can cause mixing in these stars. Nevertheless, assuming identical abundances, the destruction of Li within the clump giant is obvious. Due to the importance of that line and the particular interest in element spots on the stellar surface, we performed the disentangling also in that spectral region. Furthermore, it has been shown, e.g., by Mishenina et al. (2012); Houdebine & Doyle (1995) that even such 'photospheric' lines can show signatures of activity. For high active ($H\alpha$ in emission) stars (M and K dwarfs), they showed that additional non-photospheric UV radiation would lead to a weakening of the lines EW.

The EW of Li I 6708 Å line is also very sensitive to temperature and with that to active regions on the stellar surface. Hence, it can also be used for activity studies.

As an example, we show the result from the disentanglement of this line for the data set 5 in Fig. D.1f. The blue and purple spectra are the disentangled spectra of the primary and secondary, respectively, and black is a composite spectrum from that data set. Most prominent line in that region is the Ca I $\lambda 6717.681$ Å line. The Li abundance in the secondary is about two orders of magnitude higher than in the further evolved primary (e.g. Torres et al., 2015).

D.2. Periods

As an example, we show the frequency spectrum (FS) obtained by the EW of the blue Mg I b triplet of the primary and secondary in Fig. 5.11. Top figure shows the FS for the primary. The strongest peak at the left is the first harmonic of the orbital period (52 d, FAP $4.92\text{e-}23$) followed by another harmonic. The second highest peak to the right corresponds to a period of 11.57 days (FAP of $5.63\text{e-}4$). We summarize all 50 detections of the 11 day period in Table D.2. The mean is at 11.3 ± 0.6 days. These were obtained from the data sets 1 to 12 and 13b. The bottom graph in the mentioned figure shows the case for the secondary. The two peaks at the left can be associated with the orbital period of the system. Also present is a 8 day period but it can not be considered as real, since the window function shows a peak here as well. The peak at 10.7 days is within the error of the 11.3 day period detected in the data of the primary. A possible five day period was also detected by Horner (1996) but ill sampled by their observing run of 10 days only. Hence, the listed detections of a five day period are considered as first harmonic of the 11 day period here.

In addition, the 80 day period detected by Krisciunas & Guinan (1990), which is also present in our data ($P = 78.9$) of the Li I line with a very low FAP of $10\text{e-}141$. However, the data for the Li I photospheric line shows additional information (see Fig. D.2). The strongest peak is at 11 days, followed by two strong peaks at 8 and 6 days with further peaks in between. In the chromospheric lines, some data shows periods within the same range, but with much lower significans. The 8 day period here is again rejected due to the peak of the window function.

A different threatement was necessary for the data sets 13, 14 and 15 with much higher time-resolution. As mentioned, we selected around 25 spectra from these data sets which are of good SNR. The result from the performed disentangling on these reduced sets were used for a two dimensional cross correlation (CC) in CroCo to obtain the RV for all spectra in the sets. These RVs were used to subtract the disentangled components to get the time-resolved single component spectra, which where also shifted to a common frame with the RVs from the CC. The subtraction of the spectra for these data sets is more critical than for the previous data sets. This is because the system was observed primarily in quadrature before 2015, hence line separation is at its maximum and residuals from subtraction and variability of the subtracted component have less influence. Therefore, relatively more data points were rejected. To conclude, from our extensive data, we can confirm the 11 day period (FAP = $10\text{e-}10$). All detections are summarized in Table D.3.

The observations were scheduled for every night, which creates strong frequency peaks with itself a period of one day in the frequency spectrum. Hence, the search for high-frequency variations ($100 \mu \text{ Hz}$) is challenged by these one-day harmonics. As shown, for example, by Huber et al. (2010), pulsations of giants are within that range of frequencies. As pointed out by Chaplin & Miglio (2013), these frequency spectra start to increase in complexity when the star leaves the main sequence. Our data shows a crowded frequency spectrum in that region, Fig. D.3. Due to the strong blending of the one day period peaks and uncertain contributions from artifacts (from subtraction, signal to noise variation, and normalisation differences), we were not able to identify any frequency complexes connected to pulsations in that domain.

References

- Andretta, V., BusÀ , I., Gomez, M. T., & Terranegra, L. 2005, A&A, 430, 669
- Chaplin, W. J. & Miglio, A. 2013, ARAA, 51, 353

Table D.2.: Detections of the 11 day period of the primary for all chromospheric lines studied. The periods of 5 days are considered as a harmonic of the 11 day period. The error is the error of the fit of the peak in the frequency spectrum. Quantities are: EWA and EWB, equivalent width, sumA and sumB sum under line, M1 first M2 second line moment of component A and B, respectively.

Line	Period [d]	Error [d]	Quantity	FAP
Ca II 8498	11.4148	0.0002	EWA	3.58e-4
Ca II	10.1153	0.0002	sumB	5,78e-3
Ca II	11.4237	0.0004	M2A	7.03e-3
Ca II	11.6481	0.0002	M2B	2.36e-2
Ca II	10.2046	0.0002	EWB	1.48e-4
Ca II	11.4137	0.0003	M1A	3.86e-3
Ca II	11.6552	0.0002	M1B	2.36e-2
Ca II 8542	5.5598	0.0002	EWA	2.19e-3
Ca II	5.6310	0.0003	M2A	4.59e-3
Ca II	5.2151	0.0002	EWB	1.31e-3
Ca II	5.2773	0.0003	M2B	4.24e-3
Ca II	10.2370	0.0002	sumA	3.44e-2
Ca II	5.4371	0.0004	M1A	3.42e-3
Ca II 8662	11.2370	0.0002	sumA	2.38e-2
Ca II	11.4041	0.0008	EWA	2.96e-2
Mg I 4571	12.3659	0.0001	M1A	1.60e-2
Mg I	10.8206	0.0002	M1B	4.76e-3
Mg I	11.0632	0.0001	EWA	1.52e-2
Mg I	5.9771	0.0001	EWB	2.20e-4
Mg I	10.5771	0.0002	M2B	3.55e-4
H α	11.4256	0.0001	EWB	8.32e-4
H α	5.3420	0.0001	EWA	6.21e-3
H β	11.7328	0.0001	sumA	2.07e-2
H β	10.6840	0.0001	sumB	3.82e-2
H β	12.0920	0.0001	M1A	1.58e-3
H β	5.7708	0.0002	M2B	5.69e-3
H β	12.2272	0.0001	M2A	1.18e-3
Mg Ib 5167	11.5667	0.0001	EWB	5.63e-4
Mg Ib	10.5310	0.0002	M1B	2.35e-3
Mg Ib	10.4025	0.0002	M2B	2.35e-3
Mg Ib	11.1614	0.0001	M1A	2.34e-2
Mg Ib 5173	11.1106	0.0001	M2A	2.35e-2
Mg Ib	11.6438	0.0002	EWB	8.19e-4
Mg Ib	11.5655	0.0002	M2B	5.12e-3
Mg Ib	11.1613	0.0002	M1A	3.25e-4
Mg Ib	10.5953	0.0002	sumB	1.19e-3
Mg Ib	11.3323	0.0001	M1B	5.12e-3
Mg Ib 5184	10.5569	0.0002	M1A	3.25e-4
Na ID 5890	11.7225	0.0005	M1B	1.04e-2
Na ID	11.8104	0.0003	M1A	5.80e-3
Na ID	11.8230	0.0002	M2B	1.04e-2
Na ID 5896	11.0594	0.0002	sumB	1.52e-2
Na ID	11.0601	0.0001	sumA	6.06e-3

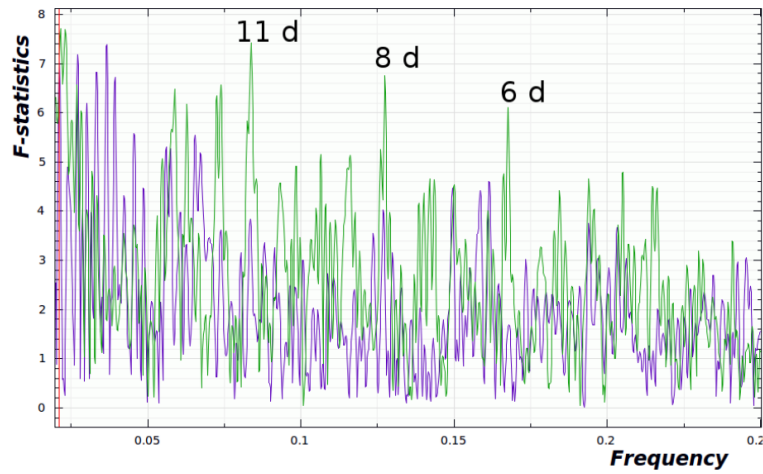


Figure D.2.: Frequency spectrum of the Li I high cadance data. Visible are three strong peaks: the rotation of 11 days of the secondary followed by a peak at 8 and 6 days.

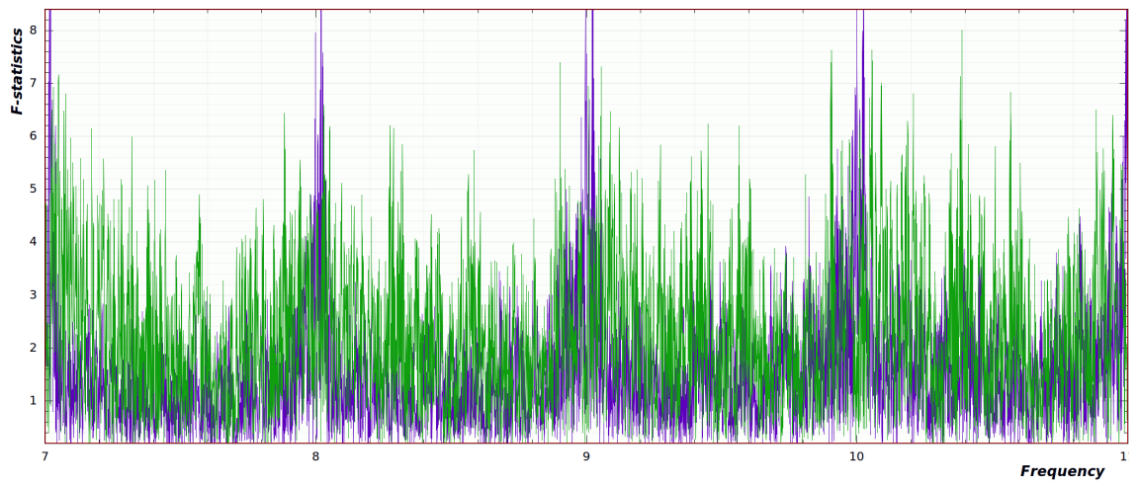


Figure D.3.: Frequency spectrum for small periods (80 to 130 μ Hz) with data from the Mg I b triplet. Periods at around one day (observational bias) are subtraced.

Cram, L. E. & Mullan, D. J. 1985, *ApJ*, 294, 626

Dempsey, R. C., Bopp, B. W., Henry, G. W., & Hall, D. S. 1993, *ApJS*, 86, 293

Elgarøy, Ø., Engvold, O., & Lund, N. 1999, *A&A*, 343, 222

Horner, S. 1996, *ApJ*, 460, 449

Houdebine, E. R. & Doyle, J. G. 1995, *A&A*, 302, 861

Huber, D., Bedding, T. R., Stello, D., et al. 2010, *ApJ*, 723, 1607

Krisciunas, K. & Guinan, E. 1990, *IBVS*, 3548

Langangen, Ø. & Carlsson, M. 2009, *ApJ*, 696, 1892

Linsky, J. L. 1980, *ARAA*, 18, 439

Table D.3.: Further periods found in data sets 13, 14, and 15 for photospheric lines.

Line	Period [d]	Error [d]	Quantity	FAP
Li I	10.408	0.0002	sumA	2.58e-11
Li I	12.721	0.0003	EWA	5.46e-18
Li I	13.528	0.0004	sumB	3.3e-10
Fe I 6173	5.8167	0.0002	EWA	2.07e-6
Fe I	11.841	0.0001	sumA	2.87e-17
Fe I	20.555	0.0001	M1A	9.98e-24
Fe I	11.620	0.0001	sumB	2.03e-29
Fe I	5.745	0.0001	EWB	1.95e-97
Fe I	5.529	0.0001	M1B	1.37e-15
Fe I 6165	11.587	0.0001	EWA	2.27e-12
Fe I	10.755	0.0001	M1A	1.48e-17
Fe I	10.576	0.0001	sumB	2.65e-9
Ca I 6162	13.025	0.0001	sumA	3.61e-28
Ca I	11.267	0.0002	EWA	3.92e-11
Ca I	11.6077	0.0002	EWB	5.16e-6
Ca I 6166	10.1302	0.0001	EWA	1.35e-15
Ca I	11.4240	0.0002	M1A	4.58e-17
Ca I	11.5850	0.0001	sumB	1.53e-38
Ca I	10.1140	0.0001	EWB	1.50e-29
Ca I	11.5871	0.0002	M1B	3.99e-5
Ni I 6175	10.5767	0.0001	sumA	3.05e-16
Ni I	10.4624	0.0002	EWA	1.63e-8
Ni I	10.6010	0.0001	sumB	4.51e-17
Ni I	11.6830	0.0001	EWB	1.17e-28

Linsky, J. L. 2017, ARAA, 55, null

Linsky, J. L., Hunten, D. M., Sowell, R., Glackin, D. L., & Kelch, W. L. 1979, ApJS, 41, 481

Linsky, J. L., Wood, B. E., Judge, P., et al. 1995, ApJ, 442, 381

Mishenina, T. V., Soubiran, C., Kovtyukh, V. V., Katsova, M. M., & Livshits, M. A. 2012, A&A, 547, A106

Osorio, Y. & Barklem, P. S. 2016, A&A, 586, A120

Osorio, Y., Barklem, P. S., Lind, K., et al. 2015, A&A, 579, A53

Sasso, C., Andretta, V., Terranegra, L., & Gomez, M. T. 2017, ArXiv e-prints

Short, C. I. & Doyle, J. G. 1998, A&A, 336, 613

Soderblom, D. R., Stauffer, J. R., Hudon, J. D., & Jones, B. F. 1993, ApJS, 85, 315

Torres, G., Claret, A., Pavlovski, K., & Dotter, A. 2015, ApJ, 807, 26

Zhang, L.-Y. & Gu, S.-H. 2008, A&A, 487, 709

E. MESA Inlist-file for Capella

```
! Capella Revisited: New Binary Orbit, Physical Properties
! and Evolutionary State
! by G. Torres, A. Claret, K. Pavlovski, & A. Dotter, 2015, ApJ, 807, 26
! http://adsabs.harvard.edu/abs/2015ApJ...807...26T
! inlists by Aaron Dotter 2015
! this inlist works with MESA r7385
! it is intended to be run in the test_suite 'multimass'
! because it runs a grid of tracks with different masses
! for the same physics
!
! Adapted to MESA r10398 in singlemass environment
! for this thesis.
!
! inlist for Capella

&star_job
  show_log_description_at_start = .false.
  history_columns_file = 'history_carbon.list'
  change_net = .true.
  new_net_name = 'pp_and_cno_extras.net'
  set_rates_preference = .true.
new_rates_preference = 2
  auto_extend_net = .false.
  kappa_file_prefix = 'a09'
kappa_lowT_prefix = 'lowT_fa05_a09p'
!kappa_Type2_logT_lower_bdy = 4.5d0
kappa_CO_prefix = 'a09_co'

  !save a model at the end of the run
  save_model_when_terminate = .true.
  save_model_filename = 'CapellaB_at_680Myr.mod'
  !begin with a pre-main sequence model
  !create_pre_main_sequence_model = .true.#

  !start from a model
  load_saved_model = .true.
  saved_model_name = 'CapellaB_at_TAMS.mod'
  !display on-screen plots
  pgstar_flag = .true.
/ !end of star_job namelist

&controls
```

```

    log_directory = 'LOGS/m2_4855_a1_85_f0_01'
initial_mass = 2.4855
    ! starting specifications
initial_z = 0.012
initial_y = 0.27
    photo_interval = 20000
    history_interval = 1
    ! write_profiles_flag = .false.
    ! stop when the center mass fraction of h1 drops below this limit
xa_central_lower_limit_species(1) = 'he4'
xa_central_lower_limit(1) = 1d-6
    ! max_model_number=2000
    mixing_length_alpha = 1.85
    MLT_option = 'Heneyey'

!overshoot_f_above_nonburn_core = 0
!overshoot_f_below_nonburn_core = 0
!overshoot_f_above_nonburn_shell = 0
!overshoot_f_below_nonburn_shell = 0

overshoot_f_above_burn_h_core = 0.03
overshoot_f0_above_burn_h_core = 0.01

overshoot_f_above_burn_h_shell = 0.03
overshoot_f0_above_burn_h_shell = 0.01

overshoot_f_above_burn_he_core = 0.03
overshoot_f0_above_burn_he_core = 0.01

conv_bdy_mix_softening_f0 = 0.003 ! 0.003
conv_bdy_mix_softening_f = 0.001 ! 0.001
conv_bdy_mix_softening_min_D_mix = 1d-3 ! 1d-3
which_atm_option = 'grey_and_kap'

!'photosphere_tables'
    cool_wind_RGB_scheme = 'Reimers'
Reimers_scaling_factor = 0.2
    varcontrol_target = 1d-4
mesh_delta_coeff = 0.5
mesh_delta_coeff_pre_ms = 1

    do_element_diffusion = .false.
diffusion_min_T_at_surface = 1d3
cubic_interpolation_in_X = .true.
cubic_interpolation_in_Z = .true.

    use_Type2_opacities = .true.
Zbase=0.012
    kap_Type2_full_off_X = 1d-2

```



```

kap_Type2_full_on_X = 1d-3
  tol_correction_norm = 1d-5
tol_max_correction = 1d-3

  !timesteps
dH_limit_min_H = 1d-2
dH_limit = 0.01
dH_hard_limit = 0.015
dH_decreases_only = .true.

  dH_div_H_limit_min_H = 1d-5
dH_div_H_limit = 1d-1
dH_div_H_hard_limit = 5d-1

  dHe_limit_min_He = 1d-2
dHe_limit = 0.01
dHe_hard_limit = 0.015
dHe_decreases_only = .true.

  dHe_div_He_limit_min_He = 1d-5
dHe_div_He_limit = 1d-1
dHe_div_He_hard_limit = 5d-1

  delta_HR_ds_L = 1
delta_HR_ds_Teff = 4
delta_HR_limit = 0.02
delta_HR_hard_limit = 0.04

  ! stop when the star nears ZAMS (Lnuc/L > 0.99)
! Lnuc_div_L_zams_limit = 0.99d0    ! stop_near_zams = .true.

  max_age=680000000

/ ! end of controls namelist

```